University of Strathclyde

Department of Physics

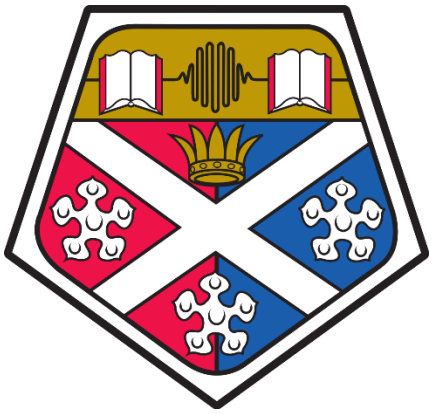

Two-Dimensional Periodic Surface Lattice High Power Millimetre Wave Experiment

Alan Richard Phipps

(B.Sc (Hons) University of Strathclyde)

A thesis presented in fulfilment of the requirements for

the degree of Doctor of Philosophy

2016

Copyright

Dedication

I would like to dedicate this thesis to someone who has always offered me the strength and protection that I have needed. You made it possible for this PhD to be undertaken and completed. I will always love you.

Table of Contents

Acknowledgments

Primarily I would like to thank my supervisor Prof. A.W. Cross. I would also like to thank Prof. A.D.R. Phelps who provided much needed help over the years. I would also like to thank them both for offering me the opportunity to conduct this research under their expert tutelage.

I would like to acknowledge the contributions of Dr L. Zhang and Dr C. Donaldson who were very helpful during the experimental phase and without whom this work would not have been possible. I wuld like to thank Dr. Ivan Konoplev for his assistance wth the theory of the thesis. I would also like to thank Dr. Craig Robertson for his assistance in the construction of the aluminium formers for the electrochemical deposition of copper on the periodic surface lattice.

I would like to thank the rest of the University of Strathclyde's Atoms, Beams and Plasmas group for their various contributions over the years, especially Mr D. Barclay who manufactured many of the experimental components.

Abstract

Millimetre wave radiation generation from a free electron maser based on a two-dimensional (2D) periodic surface lattice has been demonstrated. Second harmonic Gyrotron Backward Wave Oscillator (BWO) interaction with a two dimensional periodic surface lattice (PSL) has been observed. The major achievements in the thesis are the 1) design, 2) simulation, 3) construction and 4) operation of the experiment.

Two different methods were used to manufacture two different types of 2D periodic surface lattice. The first method used 1) electrochemcial deposition of copper on an aluminium former with the alumium subsequently removed by dissolving in strong alkali solution. The second method used a 2) 3D additive manufacturing technique resulting in a silver 2D PSL.

For construction method 1): four different copper 2D PSLs with the same inner diameter of 20 mm and the same number of longitudinal corrugations (7), period (3.0 mm) and azimuthal variations (20) but with different peak to peak amplitudes of 0.5 mm; 0.6 mm; 1 mm and 1.6 mm were manufactured. A W-band (75GHz to 110GHz) Vector Network Analyser was used to measure the transmission of millimetre waves through the 20 mm inner diameter copper 2D PSLs in order to investigate the effect of the amplitude of the perturbations (0.5 mm; 0.6 mm; 1 mm; 1.6 mm) has on the coupling of the surface and volume fields. By comparing the measured transmission of millimetre waves through the four copper 2D PSLs with different amplitude of corrugations it was shown that an increase in the peak-to-peak perturbation amplitude resulted in excitation of surface fields by an obliquely incident wave and the excitation of an eigenmode of the PSL.

For the 3D additive construction method 2): a silver high contrast structure defined as having a peak-to-peak amplitude of corrugation of 1.6 mm (from top to bottom of the grating) that is larger than a quarter of the operating wavelength was manufactured. A G-band (140GHz to 220GHz) Vector Network Analyser was used to measure the transmission of millimetre waves through the silver 2D PSL of 7.2 mm inner diameter having 16 longitudinal periods each period of length 1.6 mm having a perturbation amplitude of 1.6 mm (peak to peak) and an azimuthal period of 3.5mm. In VNA millimetre wave measurements a resonance of the 1st harmonic at 171.1 GHz due to electromagnetic wave interaction with the 3.5 mm azimuthal period which corresponded to a W-band resonance at zero axial wavenumbers of ~85 GHz was observed.

Theoretical, numerical and experimental investigation of a proof of principle 2nd harmonic gyrotron BWO based on the silver 2D PSL was carried out. An electron gun that used a velvet cathode was designed and constructed. Experiments were conducted using the velvet cathode electron gun with the electron accelerating voltage produced by a cable Blumlein generator. The electron beam formed and transported through the 7.2 mm inner diameter silver 2D PSL beam-wave interaction region within an 18 mm bore 1.8 T solenoid was measured. An 80 kV, 100 A electron beam with a beam outer diameter of 4 mm and inner diameter of 2mm which was approximately 1.8 mm away from the inner surface of the 2D PSL corrugation was measured. Numerical simulations predicted an electron beam of longitudinal velocity of 0.46c which excited an electromagnetic wave on the 2D PSL with a longitudinal (period 1.6 mm) and azimuthal (3.5 mm period) corrugations. Propagating the electron

beam through the 2D PSL a possible 2nd harmonic gyrotron BWO was identified at a frequency of ~80GHz from measurements of the frequency using high pass cut off filters and the mode pattern as compared to numerical simulation and the electron beam wave dispersion calculations. Millimetre wave radiation at a frequency of ~80GHz at an output power of 134 ± 5 kW corresponding to an operating efficiency of ~1.7 % was measured. Measurements of the frequency and mode pattern indicate that individual scatterers from the 2D PSL may have been synchronized by the lattice resulting in different parts of the electron beam interacting with the coherent Surface Field (SF) via the 2nd harmonic gyrotron Backward Wave Oscillator instability. Evidence indicates possible electron beam excitation of a cavity eigenmode consisting of the superposition between a $TM_{0,2}$ incident Volume Field (VF) and a structurally induced $TE_{5,1}$ Surface Field (SF). Alternative interactions include a 2nd harmonic gyrotron Backward Wave Oscillator with a pure $TE_{5.1}$ mode, 2nd harmonic gyrotron Backward Wave Oscillator with a pure $TM_{0,2}$ mode (~75GHz) and a BWO interaction operating with the first spatial harmonic of the $TM_{0,2}$ volume mode (~75GHz) or a combination of all four. For for a high contrast periodic surface lattice (corrugation depth of 1.6 mm is greater than $\lambda/4$) a hybrid EH type mode can be excited within the structure. To conclusively prove experimentally which interaction is dominating a more accurate 1) frequency measuremnet using a heterodyne frequency diagnostic and 2) mode pattern measurement achieved by automating the scan are required and is part of the future work.

The results of the experiment have been used to inform the design of a Cherenkov Maser which couples a $TM_{0,6}$ volume field with a $HE_{16,1}$ surface field on a 20 mm diameter 2D PSL structure with 20 longitudinal corrugations of period 3.2 mm and 16 azimuthal variations of peak to peak amplitude of 1 mm. The beam-wave interaction in the 20 mm inner diameter 2D PSL was modelled using the particle in cell code Magic 3D. In the simulations an axial magnetic field of 6 T was used to guide a 1.6 kA, 300 kV annular electron beam with a mean radius of 8.5 mm and beam thickness of 1 mm through the 2D PSL where the beam was located 0.5 mm away from the inner diameter of the 2D PSL. Numerical simulations predict excitation of the 2D PSL by this electron beam will generate 150MW of power at an operating frequency of 97 GHz corresponding to an electronic efficiency of 30 %.

Nomenclature

2D PSL – Two Dimensional Periodic Surface Lattice

Δm = Azimuthal period

Δr = Perturbation amplitude

A = Cross-sectional area

A_+ = Amplitude of incident wave

A_- = amplitude of reflected wave

B = Magnetic field vector

$\mathbf{B_z}$ = z component of magnetic field

BWO – Backward Wave Oscillator

c = The speed of light = $2.99792458 \times 10^{8} ms^{-1}$

D = Diameter of waveguide aperture

d_z = Period of the perturbation in the z direction

e = Electric charge = $1.602 \times 10^{-19} C$

E = Electric field vector

E_x = x component of the electric field

E_y = y component of the electric field

E_z = z component of the electric field

E_r = radial component of the electric field

E_φ = azimuthal component of the electric field

FDTD = Finite Difference Time Domain

FEM – Free Electron Maser

FEM = Finite Element Method

FFT = Fast Fourier Transform

FIT = Finite Integration Technique

$f_{cut\text{-}off}$ = The cut-off frequency of a waveguide

HT – High Tension

I_{beam} = Beam current

J = Thermionic current density

J_i = Root of the Bessel function

$\boldsymbol{k}_+$ = Wavevector of the incident wave

$\boldsymbol{k}_-$ = Wavevector of the reflected wave

$\boldsymbol{k}_{ti}$ = transverse component of wavevector of incident wave

$\boldsymbol{k}_{ts}$ = transverse component of wavevector of scattered wave

$\boldsymbol{k}_z$ = z component of the wavevector

m = Number of azimuthal variations

m_0 = Electron rest mass

m_1 = Azimuthal variations of the volume field

m_2 = Azimuthal variations of the surface field

P = Power

PBA = Perfect Boundary Approximation

PEC = Perfect Electrical Conductor

PiC = Particle in Cell

RVA = Rotary Vane Attenuator

r_0 = Unperturbed waveguide radius

R = Resistance

r_{min} = Minimum perturbation radius

r_{max} = Maximum perturbation radius

SF – Surface Field

STL = Stereolithograph

SWS – Slow Wave Structure

TWT – Travelling Wave Tube

V = Accelerating Voltage

VF – Volume Field

VNA = Vector Network Analyser

Z = Impedance

Greek:

α = Coupling coefficient

γ_0 = The relativistic correction factor

ε = Permativity

ε_r = Relative permativity

ε_0 = Permativity of free space ($8.85 \times 10^{-12} Fm^{-1}$)

λ = Radiation wavelength

μ = Permeability

μ_r = Relative permeability

μ_0 = Permeability of free space ($4\pi \times 10^{-7} Hm^{-1}$)

v_z = Electron velocity in the z direction

v_{perp} = Electron velocity in the transverse direction

ω = Angular Frequency

ω_b = Plasma frequency of the electron beam

1 Introduction

1.1 Historical Review

Coherent, high power, frequency tuneable microwave radiation sources are used in a wide variety of applications. Plasma heating [1.1], particle accelerators [1.2] and satellite communications have all benefited from the push into the millimetre and THz range. In recent years the demand for devices operating at MW and sub – MW powers in the frequency range of 30 to 300 GHz and beyond has significantly increased [1.3-1.7].

At powers on the scale of tens of Watts there already exists a number of highly developed solid state sources at Ka-band (26.5 GHz to 40 GHz) frequencies and solid state devices up to 3 Watts at W-band (75 GHz to 110 GHz) frequencies. However there exists applications where high power output (kW to MW) and frequency tunability are essential and for these, the vacuum electronic device has historically been the frontrunner that is capable of producing high output power at high frequencies. This involves the interaction of an electron beam in a vacuum with an electromagnetic wave, and a number of devices, both amplifiers and oscillators are already in use around the world. Problems arise however when we try to increase the operating frequency of the device since this results in a corresponding decrease in the structural dimensions. If the power density becomes large then electrical breakdown within the interaction region can occur. This issue can be addressed by the use of an oversized interaction region that allows for higher power densities but at the cost of working with a higher order waveguide mode. The oversized nature of the cavity region is relative to the wavelength of operation [1.8, 1.9] but the use of a 2D periodic surface lattice enables single mode excitation at a moderate power density within the device while simultaneously avoiding the formation of beam instabilities due to a high beam charge density [1.10]. To achieve such frequency selectivity two – dimensional distributed feedback can be applied to the interaction region [1.11-1.13] providing spatial and temporal coherence of the radiation from the bunched electrons in the active medium [1.14-1.16].

This chapter begins with a short overview of microwave vacuum electronic devices before introducing periodic surface lattices and summarising previous 2D PSL studies at Strathclyde and finally detailing the aim of the research and the layout of the thesis.

1.2 PSL Background & Applications

The history of the Two-Dimensional Periodic Surface Lattice (2D PSL) begins in Nizhny Novgorod at the Institute of Applied Physics of the Russian Academy of Sciences (IAP RAS) in 1995. Dr Ivan Konopolev was studying for his undergraduate degree under the expert tutelage of Professor

Naum Ginzburg, head of the high-frequency relativistic electronics group. They were working on a mildly relativistic beam-wave interaction within a planar 2D PSL structure which had produced promising results [1.17]. Ivan chose to relocate to Glasgow, Scotland to undertake his PhD at Strathclyde University under the supervision of Professor Alan Phelps continuing his work on 2D PSLs. Through the mathematical framework of 'conformal mapping' Dr Konoplev converted the planar 2D PSL to cylindrical and coaxial form and completed his PhD in 2001 by investigating theoretically and numerically the use of PSL structures to provide distributed feedback in a high power Free Electron Maser (FEM) [1.18].

The work continued with Dr Konoplev taking up a post at Strathclyde as a research assistant in the Atoms, Beams and Plasmas group (ABP) and as the second supervisor of Paul McGrane working with Adrian Cross the first supervisor and Alan Phelps the 3rd supervisor, developed a 2D PSL input reflector and a 1D PSL output reflector to define the cavity of a Free Electron Maser. The FEM when driven by a 7 cm diameter, high current 500 A annular electron beam of energy 450 keV generated 15 MW of output power at a frequency of 37.3 GHz with 6 % energy conversion efficiency. Drs. Konoplev, Cross and Phelps then went on to supervise Philip MacInnes who was tasked with re-designing the FEM utilising the same cylindrical, coaxial 2D PSL input mirror and 1D PSL output mirror to define the cavity of the FEM used previously but to increase the microwave output power. This was achieved by re-designing the cold cathode electron gun to increase the current in the annular electron beam from 500 A to 1.5 kA. The FEM when driven by a 7 cm diameter, high current 1.5 kA annular electron beam of energy 450 keV generated 60 MW of output power at a frequency of 37.5 GHz with 10 % energy conversion efficiency. [1.19,1.20]. This work resulted in the award of a PhD for Philip MacInnes in 2009.

The next step was taken by PhD student Lorna Fischer who came to Strathclyde in 2006 and began work on both a Ka and W-band 2D PSL beam-wave interaction region that utilised the cylindrical 2D PSL but incorporating the removal of the inner conductor. After successful millimetre wave measurements of a Ka-band 2D PSL structure, electron beam-wave interaction simulations were carried out using CST PS and ATK's Magic 3D. Positive results were obtained demonstrating numerically successful production of high power microwaves at Ka (26.5-40 GHz) and W-band (75-110 GHz) frequencies [1.21-1.23]. The successful modelling of this device in the numerical code marked the successful completion of Lorna's PhD in 2010 [1.24] with the torch past to myself when I started a PhD studying 2D PSLs.

My PhD involved the design, analysis, construction and testing of a W-band Surface Wave High Power Microwave source based on a 2D PSL that was cylindrical in nature, building on the work of Lorna Fisher to remove the inner conductor that was present in previous experiments. My design was to investigate the mode production and control in a beam-wave interaction without the use of the inner

conductor at W-band frequencies. Successful completion of the electron beam experiments was achieved in April 2015 where it was found that the 2D PSL was indeed capable of supporting a relativistic beam-wave interaction and controlling the mode in the interaction region.

The main application for this device is plasma diagnostics in tokamak based nuclear fusion systems. The measurement of density fluctuations by way of coherent scattering of electromagnetic waves at microwave and millimetre wave frequencies is a useful tool in analysing the cause of a turbulent plasma [1.23]. The controlled heating of fusion tokamak plasmas is also of interest for a device such as this [1.24]. Electron Cyclotron Resonance Heating (ECRH) of fusion plasmas has made rapid progress where state of the art sources such as the gyrotron oscillator can produce 1 MW continuous wave radiation at a frequency of 170 GHz. Tens of gyrotron oscillators are required for the ECRH system for the International Thermonuclear Experimental Reactor (ITER) which will come online in 2025. However higher frequency 263 GHz, 2 MW continuous wave sources are required for the ECRH heating system for the Demonstration Fusion Power Plant (DEMO) It is difficult to increase the frequency of operation of the 170 GHz gyrotrons as they already use a very high order $TE_{28,12}$ mode and although it is possible to place a thin annular electron beam in the optimum position in the 170 GHz gyrotron cavity to excite a single mode this becomes increasingly challenging as the mode index increases for higher frequency operation. The 2D PSL has the potential to provide additional mode control to enable the cavity to become even more oversized with respect to the wavelength as the mode index increases with frequency. The 2D PSL therefore could play an important role in providing additional mode stability in high power 2 MW, 263 GHz microwave sources required for DEMO. There are many other potential applications of 2D PSL in high power millimetre wave sources for communications and spectroscopy, for the security and medical industries. Further development of the 2D PSL interaction region may in the future result in more applications being uncovered through the development of electrodynamic structure.

1.3 My Main Contributions

In the course of this project I have made many important contributions which include, for example: the optimisation of the Magic 3D beam – wave interaction code [Appendix B], the design and manufacture of the experimental components that are suitable for installation in a vacuum system and compatible with a high current electron beam guided by an existing magnetic coil. I also studied the potential to use Periodic Surface Lattices (PSL) at frequencies moving towards the THz range. The main contributions that I have made to this project however would have to be the use of Additive Manufacturing or 3D Printing in fabricating the 2D PSL interaction region for the electron beam experiments [1.25,1.26] and the design, numerical analysis, manufacture and testing of the W-band

and G-band [TE_{11}-TM_{01}-TEM] mode conversion system for use in the cavity eigenmode formation process that was measured using a Vector Network Analyser (Anritsu ME7808).

Those two aspects of the project stand out as the main achievements I made to the project, For example the mode conversion system, resulted in the successful measurement of the cavity eigenmode formation within the interaction region, allowing us to move on to the numerical modelling of the beam – wave interaction. The use of 3D Printing allowed the interaction region to be manufactured quickly and cheaply without the need for the various steps involved in the time consuming process of copper electrodeposition. Both steps were originated, analysed and implemented by myself alone and contributed to the successful completion of the project.

1.4 Beam-Wave Microwave Interactions Relevant to this Thesis

The microwave generation process generally involves an interaction between an active media which in this case is an electron beam with an electromagnetic wave. This corresponds to resonant interactions between the normal electromagnetic modes of a cavity or waveguide and the natural modes of oscillation in a beam of electrons. The natural modes of oscillation in an electron beam are generally formed by either longitudinal spatial bunching or rotational phase bunching. Both of these cavity modes and beam modes can be described by specific dispersion relations relating angular frequency ω to axial wave number k_z.

In chapter 2, the general dispersion relations of waveguide modes and electron beam modes for different types of Free Electron Maser (FEM) devices are described. The two generic interactions relevant to this thesis are Cherenkov slow wave interaction including interaction with backward and forward waves and Cyclotron Resonance Maser or Gyrotron and Gyrotron Backward Wave Oscillator interactions are reviewed. Finally at the end of chapter 2 the saturation mechanism in microwave generation is described.

1.5 Periodic Structures

Periodic structures have been implemented in a number of systems in optics [1.36] and vacuum electronics over a broad frequency range from millimetre through to optical wavelengths [1.37-1.40]. These structures can offer frequency selection for systems and is only limited by the fabrication technology required to manufacture them. Distributed feedback due to Bragg scattering has been successfully employed in a variety of devices, where it is used to provide coherent radiation by synchronisation of the transverse components of an oversized active medium, in return allowing for specific mode selection and control. There are two distinct types of periodic corrugation relative to

this work; they are one dimensional structures, having variation in only the longitudinal coordinate, and two-dimensional, or 'doubly periodic' structures, consisting of perturbations not only along the length but across the transverse dimension also.

1.5.1 1D & 2D Periodic Structures

Two dimensional periodic structures can be manufactured by machining shallow corrugations on the inner surface of an annular waveguide and may be represented analytically as:

$$r = r_0 + \Delta r cos(\boldsymbol{k}_z z + m\varphi) \qquad (1.1)$$

where r_0 is the radius of the unperturbed waveguide, Δr is the amplitude of the corrugation, $\boldsymbol{k}_z = 2\pi/d_z$, d is the period of the corrugation along the z direction and m is the number of lattice variations. The wave propagating through the waveguide will reflect from each small perturbation of the waveguide wall, where, due to the periodicity of the wall perturbations, only waves which satisfy the Bragg resonance conditions [1.38] will be effectively coupled on such a corrugation

$$\boldsymbol{k} = \boldsymbol{k}_+ - \boldsymbol{k}_- \quad m = \pm(m_1 - m_2) \qquad (1.2)$$

where $\boldsymbol{k}_\pm$ are the longitudinal wavenumbers of the incident (forward) and scattered (backward) waves respectively and $m_{1,2}$ are the azimuthal numbers . Assuming azimuthal symmetry, that is to say, m = 0, coupling between the forward and backward waves is possible. The coupling coefficient is proportional to the corrugation amplitude Δr and if the amplitude of the perturbation tends to zero no coupling will exist. An increase in the amplitude will result in increased wave coupling.

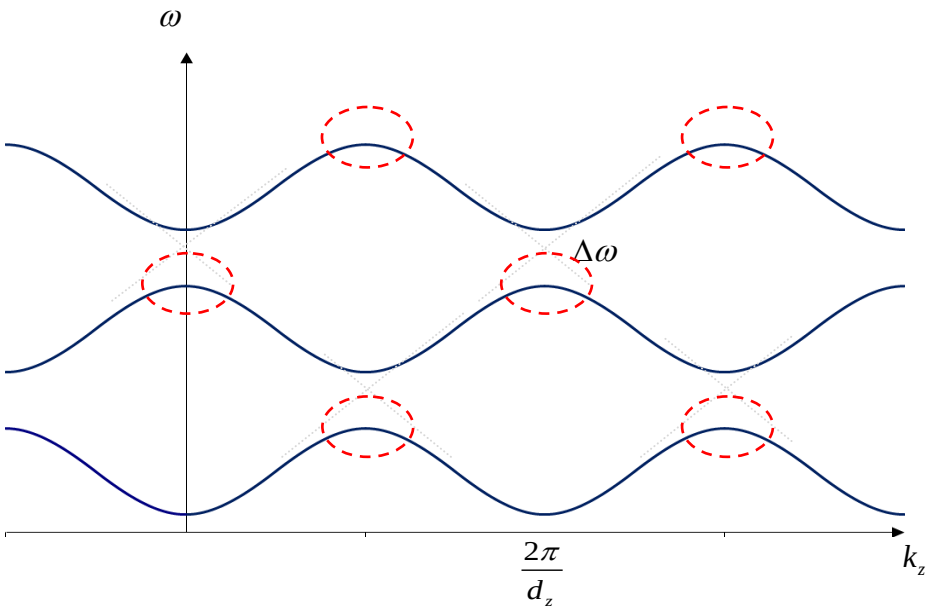

Figure 1.1: Brillouin diagram illustrating a finite corrugation which leads to mode coupling, where the coupled mode regions are outlined via red dashed circles.

This effect, known as Bragg scattering, can be visualised in a Brillouin diagram such as that seen in figure 1.1. The spatial harmonics of the waveguide modes are shifted along the k- axis according to the equation $k_n = 2\pi n/d_z$, where n is an integer.

In order to obtain spatially coherent radiation from the oversized electron beam and to improve mode control, the use of two-dimensional feedback has been successfully implemented [1.41-1.50]. This type of 2D structure offers coupling of an incident Volume Field (VF) and an induced Surface Field (SF) and hence the creation of a cavity eigenmode that is the superposition of both of these components. Only waves satisfying the Bragg conditions (equation 1.2) will couple at the corrugation.

1.6 Previous Studies & Statement of Problem

Previous studies have shown both 1D and 2D Bragg structures offer a highly efficient method of providing feedback in an oversized system [1.47-1.50]. These studies implemented the 1D and 2D structures in either a planar or coaxial configuration. This coaxial geometry has limitations, in that we are restricted to the fact that coupling can only occur for waves having zero radial variations as the presence of the inner conductor limits the generation of the modes, even in the presence of the 2D structure, we can still only achieve mode selectivity over the azimuthal index.

1.7 Experimental Observations at Strathclyde

Strathclyde University has conducted a number of experiments that utilised two – dimensional distributed feedback, one of which is a Free Electron Maser (FEM) experiment that produced up to 60 MW of pulsed output power at a frequency of 37.2 GHz [1.31-1.35]. This experiment involved an oversized ($D/\lambda > 10$) co-axial 2D periodic surface lattice, where D represents the diameter of the waveguide aperture and λ the operating wavelength with an annular electron beam used to drive the maser. The design incorporated a coaxial cavity with two individual 2D corrugated inner conductors separated by a region of plane conductor. Frequency diagnostics measured an operating frequency of 37.2 GHz and the efficiency of the Free Electron Maser was found to equal approximately 10 % [1.50].

A previous study at Strathclyde University by former PhD student Lorna Fisher investigated the effects a doubly periodic corrugation has upon removal of the central line and found that the removal of this additional surface did not affect the enhanced mode coupling, due to the additional modes being present, whilst still maintaining the coherence and selectivity representative of the coaxial setup [1.51].

1.8 Thesis Structure

This thesis will focus on a Cherenkov interaction operating at 103.6GHz and a second harmonic gyrotron backward wave oscillator that utilises a structure similar to that described in in section 1.4 operating at ~80 GHz. Chapter 2 and chapter 3 are primarily devoted to the theoretical analysis of the 2D periodic surface lattice and the mode coupling and cavity eigenmode formation process. Beginning from first principles, this analysis will refer to waveguide, coupled mode and Bragg reflection theory as it applies within a bounded conducting region. Chapter 4 presents numerical simulation of the PSL cavity which is then linked to the mm-wave measurements conducted using an Anritsu ME7808B Vector Network Analyzer (VNA) with 75 GHz to 110 GHz and 140 GHz to 220 GHz millimetre wave extender heads. PSL cavity structures were made in copper and silver with varying perturbation amplitudes to investigate the cavity formation process and how it is affected by changes to the dimensions and geometry of the corrugations. Chapter 5 describes the experimental design used in the beam-wave interaction. Chapter 6 describes the electron beam and millimetre wave diagnostics. Chapter 7 contains the measured beam parameters and results of the beam-wave interaction experiments with regard to the mm-wave measurements of the output frequency, mode patterns and power. Chapter 8 gives the conclusions where we discuss the overall results of the research and future work.

2

Electromagnetic and Electron Beam Theory

2.1 Introduction

This chapter shall comprise of an overview of the fundamental physics involved in the beam-wave interaction [2.1], starting with the flow of electromagnetic radiation in free space, through the propagation of the electromagnetic waves within a waveguide structure and ending with an analysis of the coupling between surface and volume fields within the interaction region within a periodic surface lattice. An analysis of electron beam dynamics will also be presented here, specifically the Cherenkov instability in a dielectric lined waveguide with a forward wave and the Cherenkov instability with a backward wave in a periodic structure as well as the Electron Cyclotron Maser (ECM) or gyrotron and gyrotron beackward wave oscillator interaction.

2.2 Maxwell's Equations & the Wave Equation

The motion of the electric and magnetic fields of an electromagnetic wave follow distinct laws that govern their behaviour as they evolve in time and space. James Clark Maxwell was responsible for combining three previously established laws, namely, Gauss's Law, Gauss's Law for Magnetism, Faraday's Law, with a fourth law, Ampere's Law, to which he added a charge density component. These laws have since been collectively known as Maxwell's equations and they are the basis for all research & development into electromagnetic theory for the past 100 years. These laws are given by equations (2.1 – 2.4) [2.2, 2.3]:

Gauss's Law $$\boldsymbol{\nabla} \circ \boldsymbol{D} = \rho \tag{2.1}$$

Gauss's Law for Magnetism $$\boldsymbol{\nabla} \circ \boldsymbol{B} = 0 \tag{2.2}$$

Maxwell-Faraday Law $$\boldsymbol{\nabla}\, x\, \boldsymbol{E} = -\frac{\partial \boldsymbol{B}}{\partial t} \tag{2.3}$$

Maxwell-Ampere Law $$\boldsymbol{\nabla}\, x\, \boldsymbol{B} = \mu_0 \left(\boldsymbol{J} + \varepsilon_0 \frac{\partial \boldsymbol{E}}{\partial t} \right) \tag{2.4}$$

Here, **D** is the electric displacement field (**D**=ε**E**), ρ is the charge density (relative to free space in this instance), **B** is the magnetic flux density, **E** is the electric field strength, **H** is the magnetic field strength (**B**=μ**H**),, and **J** is the current density (again in this instance relative to free space). These equations are valid for all space, time and are applicable to any type of media, in so much as, the relative permeability and permittivity are taken into account. This means that for a linear material the electric and magnetic field terms can be calculated using the 'constitutive relations', given by

equations (2.5) and (2.6). Here ε_r and μ_r represent the relative permittivity and permeability, respectively, of the medium in question, while ε_0 and μ_0 are the permittivity and permeability of free space. For a non-linear media, the relations hold but ε_r and μ_r are not scalars. A third constitutive relation is often used for the case of a good metallic conductor. In such a case, the current density is linked to the electric field, through the conductivity of the metal, σ, as given by equation (2.7).

$$\mathbf{D} = \boldsymbol{\varepsilon_0}\varepsilon_r \boldsymbol{E} \tag{2.5}$$

$$\boldsymbol{H} = \frac{1}{\mu_0 \mu_r}\boldsymbol{B} \tag{2.6}$$

$$\boldsymbol{J} = \sigma \boldsymbol{E} \tag{2.7}$$

From Maxwell's equations, further expressions can be derived for the electric and magnetic fields which describe their propagation. These inhomogeneous wave equations are given below by equations (2.8) and (2.9), for the electric and magnetic fields, respectively. For the case of a medium with no free EM field sources, the right hand sides of both equations can be set to zero, leaving equations which hold for homogenous media.

$$\nabla^2 E - \mu\varepsilon\frac{\partial^2 E}{\partial t^2} = \boldsymbol{\nabla}\rho + \mu\frac{\partial \boldsymbol{J}}{\partial t} \tag{2.8}$$

$$\nabla^2 H - \mu\varepsilon\frac{\partial^2 H}{\partial t^2} = -(\boldsymbol{\nabla} \times \mathbf{J}) \tag{2.9}$$

The solution to these wave equations take a general form as shown by equation (2.10) which depicts the solution for the electric field in Cartesian geometry. These equations assume that the oscillations of the electric and magnetic field components are harmonious in time and that the direction of propagation is parallel to that of the z – axis. The transverse and axial components of the electric field are given by $\boldsymbol{E}_{trans}$ and $\boldsymbol{E}_z$, respectively, where ω is the angular frequency of the signal and is equivalent to $2\pi f$, where f is the frequency. Additionally, k represents the wave-number of the particular wave, these two values are related through equation (2.11):

$$\boldsymbol{E}(x, y, z, t) = [\boldsymbol{E}_{trans}(x, y) + \hat{z}E_z(x, y)]\exp[j(\omega t - kz)] \tag{2.10}$$

$$\omega^2 = \frac{k^2}{\mu\varepsilon} \tag{2.11}$$

2.3 Waveguide Theory

In the scenario where a wave is subject to 'boundary conditions', such as those imposed by a metallic waveguide, these conditions state that particular rules must be applied at the boundary surface. For example, the tangential **E** should reduce to zero within the waveguide walls through the concept of skin depth, where the amplitude of the field is evanescent with a reduction coefficient that is dependent on both the frequency of the wave and the physical properties of the waveguide walls. Therefore the tangential component of the electric field will be zero at the wall boundary. Due to the perpendicular nature of the two field components, the normal component of the magnetic field will also be zero at the wall boundary. In the current investigation, only hollow waveguides are considered. As a result, only the Transverse Electric (TE) and Transverse Magnetic (TM) modes are examined. The TE mode has an axial magnetic field component and conversely the TM mode has an axial electric field component. A third type of mode, the TEM or Transverse Electromagnetic mode has no axial field components at all, however the TEM mode will not be considered since it can only propagate with the existence of an inner conductor and in this thesis only hollow waveguides were studied.

In the presence of a dielectric or a corrugated metal surface which can be assumed to be an effective dielectric then the so called HE hyrbrid mode can be exist in the structure [2.4]. The introduction of the waveguide induced boundary conditions results in a modification of the wave – number and wavelength of the propagating radiation. This modification manifests itself as an upper limit on the wavelength of the radiation that can propagate within the waveguide structure. The axial wave – vector, k_z, of such a confined signal is given by equation (2.12), where k is the previously defined wave – number relative to free space, and k_c is the cut – off wave – number, which is dependent on the physical parameters of both the waveguide and the field. When the wave – number is less than k_c of a particular waveguide, the signal is said to be 'cut – off' and hence will not propagate. A corresponding cut – off frequency, $f_{cut\text{-}off}$, can also be defined, and is shown in equation (2.13). The wavelength of the radiation as it moves along the waveguide is given by equation (2.14).

$$k_z = \sqrt{k^2 - k_c^2} \tag{2.12}$$

$$f_{cut-off} = \frac{c}{2\pi} k_c \tag{2.13}$$

$$\lambda_{guide} = \frac{2\pi}{k_z} \tag{2.14}$$

As previously described, Maxwell's equations are valid for their application to time – varying electric and magnetic fields in any media. However, in so – called HILS media (one which is Homogenous,

Isotropic, Linear and Stationary), the source terms can be negated. Maxwell's third and fourth equations can be therefore rewritten, this time in phasor notation, as shown in equations (2.15) and (2.16) below:

$$\nabla x \boldsymbol{E} = -j\omega\mu\boldsymbol{H} \tag{2.15}$$

$$\nabla x \boldsymbol{H} = j\omega\varepsilon\boldsymbol{E} \tag{2.16}$$

By utilising the general form of the solution of the wave equation, previously given by (2.10), the individual components of the electric and magnetic fields can be given by equations (2.17) – (2.22):

$$\frac{\partial E_z}{\partial y} + jk_z E_y = -j\omega\mu H_x \tag{2.17}$$

$$-jk_z E_x + \frac{\partial E_z}{\partial x} = -j\omega\mu H_y \tag{2.18}$$

$$\frac{\partial E_y}{\partial x} + \frac{\partial E_x}{\partial y} = -j\omega\mu H_z \tag{2.19}$$

$$\frac{\partial H_z}{\partial y} + jk_z H_y = j\omega\varepsilon E_x \tag{2.20}$$

$$-jk_z H_x - \frac{\partial H_z}{\partial x} = j\omega\varepsilon E_y \tag{2.21}$$

$$\frac{\partial H_y}{\partial x} + \frac{\partial H_y}{\partial y} = j\omega\varepsilon E_z \tag{2.22}$$

Typically the transverse components are solved in terms of the axial electric and magnetic field components. Therefore, the resulting field components are given by equations (2.23) – (2.26), below:

$$E_x = -\frac{j}{k_c^2}\left(k_z\frac{\partial E_z}{\partial x} - \omega\mu\frac{\partial H_z}{\partial y}\right) \tag{2.23}$$

$$E_y = \frac{j}{k_c^2}\left(-k_z\frac{\partial E_z}{\partial y} + \omega\mu\frac{\partial H_z}{\partial x}\right) \tag{2.24}$$

$$H_x = \frac{j}{k_c^2}\left(\omega\varepsilon\frac{\partial E_z}{\partial y} - k_z\frac{\partial H_z}{\partial x}\right) \tag{2.25}$$

$$H_y = -\frac{j}{k_c^2}\left(\omega\varepsilon\frac{\partial E_z}{\partial x} + k_z\frac{\partial H_z}{\partial y}\right) \tag{2.26}$$

For a given electromagnetic signal; flowing within a bounded region, the power passing through a cross – section of the geometry can be obtained. This is obtained through integration of the Poynting vector, over the area of interest, as shown by equation (2.27).

$$P_0 = \frac{1}{2}\int \boldsymbol{E}\, x\, \boldsymbol{H}\, .\, d\boldsymbol{A} \tag{2.27}$$

2.3.1 Rectangular Waveguide Theory

Consider a section of metallic waveguide with rectangular cross – section as shown in figure 2.1. In such a case, the waveguide is of width, b, and height, a, which are aligned with the x and y axes, respectively, while propagation occurs along in the z direction. In a hollow waveguide, transverse electric and magnetic modes, TE and TM, respectively, can propagate. A pure TE mode has no axial electric field component, E_z, while a pure TM mode has no axial magnetic component, H_z. The modes allowed by the boundary conditions can be characterised by integer indices, m and n. For the rectangular case, these integers represent the number of half – wave variations in the x and y directions of the y and x polarised field components, respectively, yielding a form of $TE_{m,n}$ and $TM_{m,n}$.

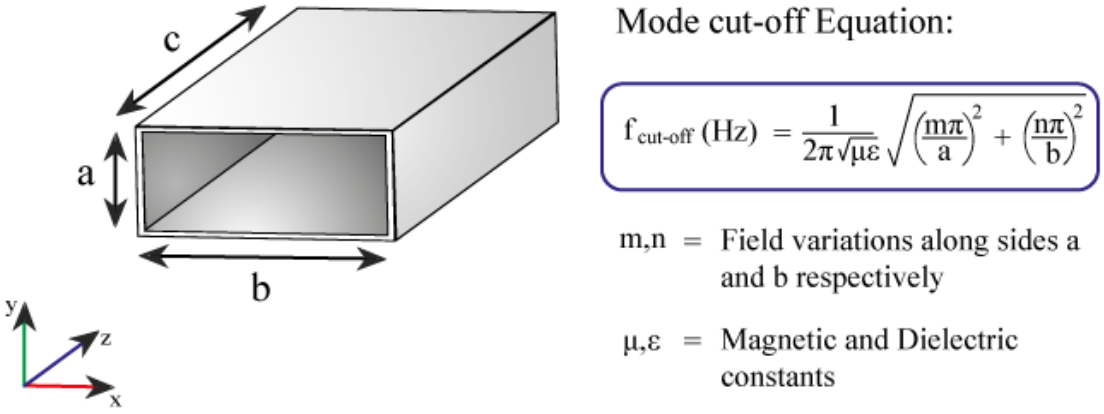

Figure 2.1: The entrance to the rectangular waveguide with the relevant mode cut – off equation.

This thesis will primarily focus on $TE_{m,n}$ and the $TM_{m,n}$ modes and mainly in the circular waveguide which will be the focus of the next section. However, the general form of the E_z component of the $TM_{m,n}$ mode take the form shown in equation (2.28), where B is the amplitude of the signal, and the temporal evolution $\exp(j\omega t)$ is assumed.

$$E_z = B sin\frac{m\pi x}{b} sin\frac{n\pi y}{a} exp(-jk_z z) \tag{2.28}$$

2.3.2 Cylindrical Waveguide Theory

Consider a section of metallic waveguide, this time of circular cross – section, as represented in figure 2.2. The waveguide is of radius, r, with circular section of the waveguide aligned in the x and y planes, with radiation propagating along the z axis. Consider the vector, **ρ**, which is comprised of x and y components, and is located a distance, r, from the x and y axis, and is rotated by an angle, φ.

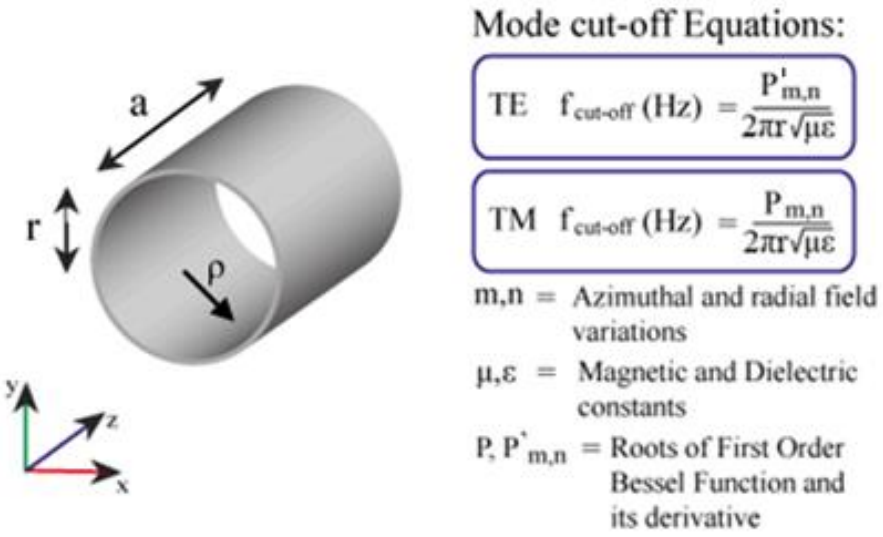

Figure 2.2: A cylindrical waveguide with mode cut – off equations.

As with the rectangular waveguide, in cylindrical waveguide only the $TE_{m,n}$ and $TM_{m,n}$ modes can propagate. However, in this instance, m and n indices refer to the number of full – wave variations of the radially polarised field around the azimuth and half – wave variations in the azimuthally polarised field across the radial direction, respectively. The fundamental mode for cylindrical geometry is the $TE_{1,1}$ mode. In this investigation the TM modes are of primary importance in a cylindrical waveguide. Therefore, the axial electric field component for the TM mode is given by equation (2.29), where A is the field amplitude. As described previously, all transverse field components can be obtained by manipulation of the axial components. However, given the use of a cylindrical coordinate system, a transform must be performed on equations (2.23) – (2.26) to obtain ρ and φ components.

$$E_z = Asin(m\varphi)J_m(k_c\rho)\exp(-jk_cz) \qquad (2.29)$$

The cut – off wave – number of a cylindrical waveguide mode becomes more subtle due to the use of cylindrical coordinates. The general form is given by equation (2.30), below, where $p_{m,n}$ refers to a specific value for a given mode. For a TM mode, $p_{m,n}$ is the n^{th} root of the Bessel function of the first

kind $J_m(x)$. Similarly, $p'_{m,n}$ for a TE mode is the n^{th} root of the derivative of such a Bessel function, $J'_m(x)$, and is usually written as $p'_{m,n}$. As a result, for the TM modes

$$k_c = \frac{p_{m,n}}{r} \tag{2.30}$$

and for the TE modes

$$k_c = \frac{p'_{m,n}}{r} \tag{2.31}$$

2.3.3 Waveguide Dispersion

In a regular or smooth bore circular waveguide, a given waveguide mode behaves in a certain manner when its frequency and wave – number are considered. Such behaviour is conveniently represented through the use of dispersion relations For simple, unperturbed, rectangular and cylindrical waveguide, the dispersion relation for a $TE_{m,n}$ or $TM_{m,n}$ modes are given by equation (2.32). Here, the first term on the right hand side of equation 2.32 is equivalent to the cut – off frequency of the mode in question.

$$\omega^2 = c^2 k_c^2 + c^2 k_z^2 \tag{2.32}$$

$$\omega = c k_z \tag{2.33}$$

On plotting the hyperbolic equation 2.32, a form similar to that in Figure 2.3 is obtained. The point at which the curve crossed the frequency axis is equal to the cut – off frequency for that mode. In figure 2.3, the linear curves represent the dispersion of a wave in free space, given by equation (2.33), to which the far from cut – off guided signal is asymptotic. At any point on the dispersion curve, the phase, v_{phase}, and group, v_{group}, velocities of the wave can be obtained through the equations (2.34) and (2.35), respectively.

$$v_{phase} = \frac{\omega}{k_z} \tag{2.34}$$

$$v_{group} = \frac{\partial \omega}{\partial k_z} \tag{2.35}$$

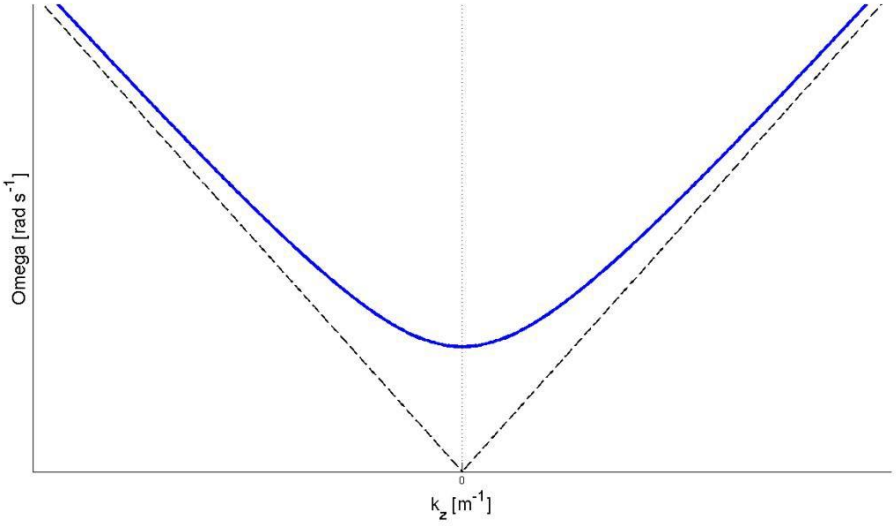

Figure 2.3: A typical example of a waveguide dispersion plot, showing the speed of light lines (dotted lines), to which the dispersion lines of the waveguide are asymptotic.

2.3.4 Natural Modes of a Waveguide

The following equation describes the behaviour of an electromagnetic wave inside a smooth walled waveguide:

$$\omega^2 = \omega_{co}^2(n,m) + k_z^2 c^2 \tag{2.36}$$

where $\omega_{co}^2(n,m)$ is the cutoff frequency of the $TM_{n,m}$ and $TE_{n,m}$ modes in a given waveguide, n is the number of azimuthal variations and m is the number of radial variations of the modes. A plot of this dispersion is shown in figure 2.4 where both the phase velocity and the group velocity are plotted, with the phase .velocity given by $v_{ph} = \omega/k_z$ and the group velocity by $v_g = \partial\omega/\partial k_z$.

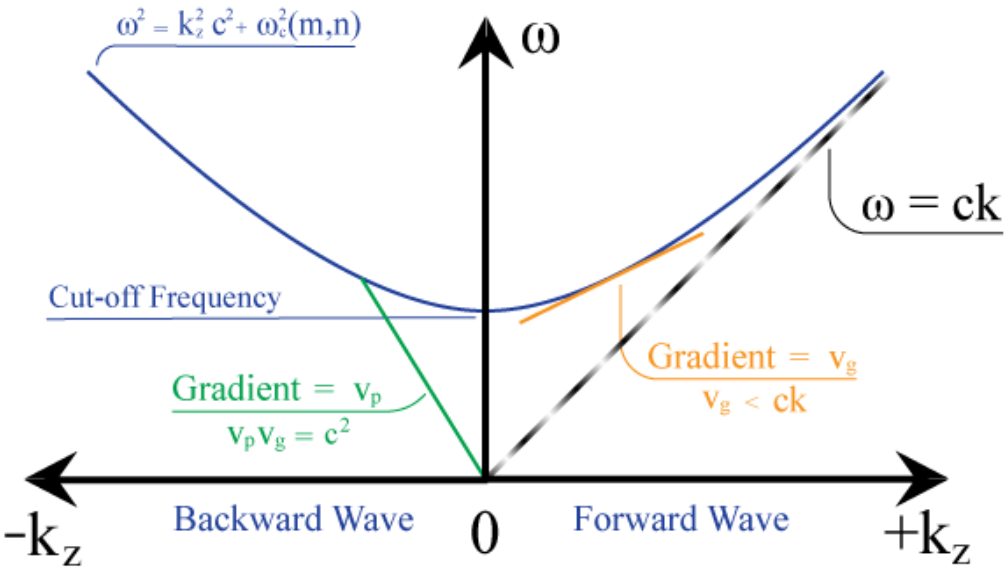

Figure 2.4: A dispersion diagram for an electromagnetic wave inside a cylindrical waveguide demonstrates the relationship between frequency and axial wavenumber.

Due to the relationship $v_p v_g = c^2$ the phase velocity must always be greater than c and the group velocity must always be smaller than c. By making changes to the structure of the wave guide wall via either the insertion of a corrugation or a dielectric material, the phase velocity of the waveguide modes can be reduced to a value less than c.

2.3.5 Electron Beam Modes

In this section, the dispersion relations (ω, k_z diagram) governing both the normal waveguide modes and the natural electron beam modes are described. The conditions for their interaction are described and the mechanisms involved for microwave generation are discussed.

The dispersion curves describing the oscillation in a beam of electrons are dependent on the motion of these electrons and also their oscillating mode. An oscillation mode for an electron beam is its space charge oscillation wave. In its most simple situation, without any consideration for the radial boundaries, the dispersion relation describing the space charge wave for a beam propagating along the *z*-axis, can be expressed by:

$$\omega = k_z v_z \pm \frac{\omega_b}{\gamma^{\frac{3}{2}}} \tag{2.37}$$

where k_z is the wavenumber, v_z is the drift velocity of the electron beam, ω_b is the plasma frequency of the electron beam given by

$$\omega_b = \sqrt{\frac{n_b e^2}{\varepsilon_0 m_0}} \tag{2.38}$$

and γ_0 is the relativistic factor given by

$$\gamma_0 = \left(1 - \frac{v^2}{c^2}\right)^{-\frac{1}{2}} \tag{2.39}$$

The $\pm$ in equation (2.37) allows us to distinguish what are known as fast waves, where the "+" sign is used, and slow waves, where the "-" sign is used. In equation 2.38. n_b is the beam density, e is the electronic charge, ε_0 is the permittivity of free space, and m_e is the electronic mass and c is the speed to light. In figure (2.5) the dispersion relation for space charge waves in an electron beam is plotted along with the dispersion relation of electromagnetic wave propagation in a waveguide, given by

$$\omega = c\sqrt{k^2 + k_c^2} \tag{2.40}$$

Where k_c is the cut-off wavenumber.

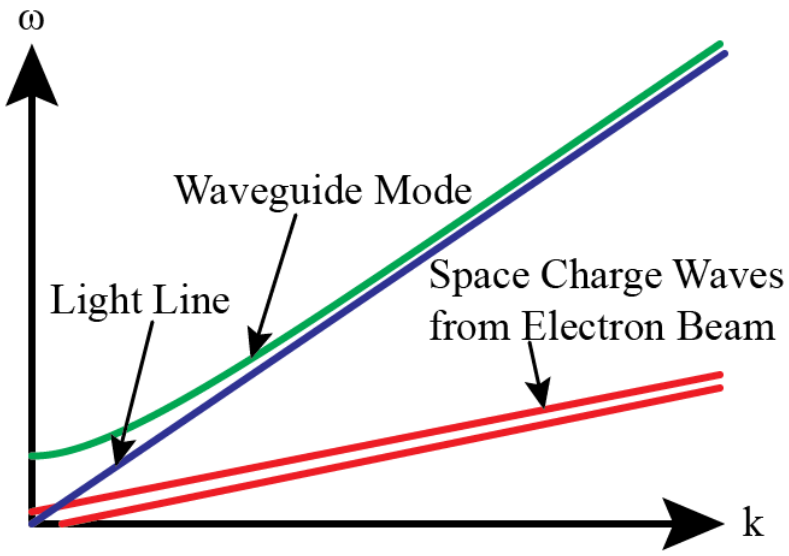

Figure 2.5: Plots of dispersion relations of space charge waves and waveguide

Note that in figure 2.5, the slow space charge wave lines and the waveguide dispersion curve never intersect. Without an intersection in these curves, none of the radiation produced by the oscillations in the electron beam can propagate and be extracted in the waveguide. Another way of looking at this

situation is that the phase velocity of the space charge waves is less than the speed of light while the phase velocity of the waveguide mode is larger than the speed of light. With no match in the velocities, no interaction is possible.

2.3.6 Slow Wave Beam Interaction

If a corrugation is introduced in a waveguide wall, the radius of the waveguide varies axially as

$$r_w = r_0 - \Delta r \sin(k_0 z) = r_0[1 - \varepsilon_r \sin(k_0 z)] \tag{2.41}$$

then the waveguide dispersion relation becomes periodic with a period, k_0, in k-space which is related to the waveguide corrugation length by

$$k_0 = \frac{2\pi}{d_z} \tag{2.42}$$

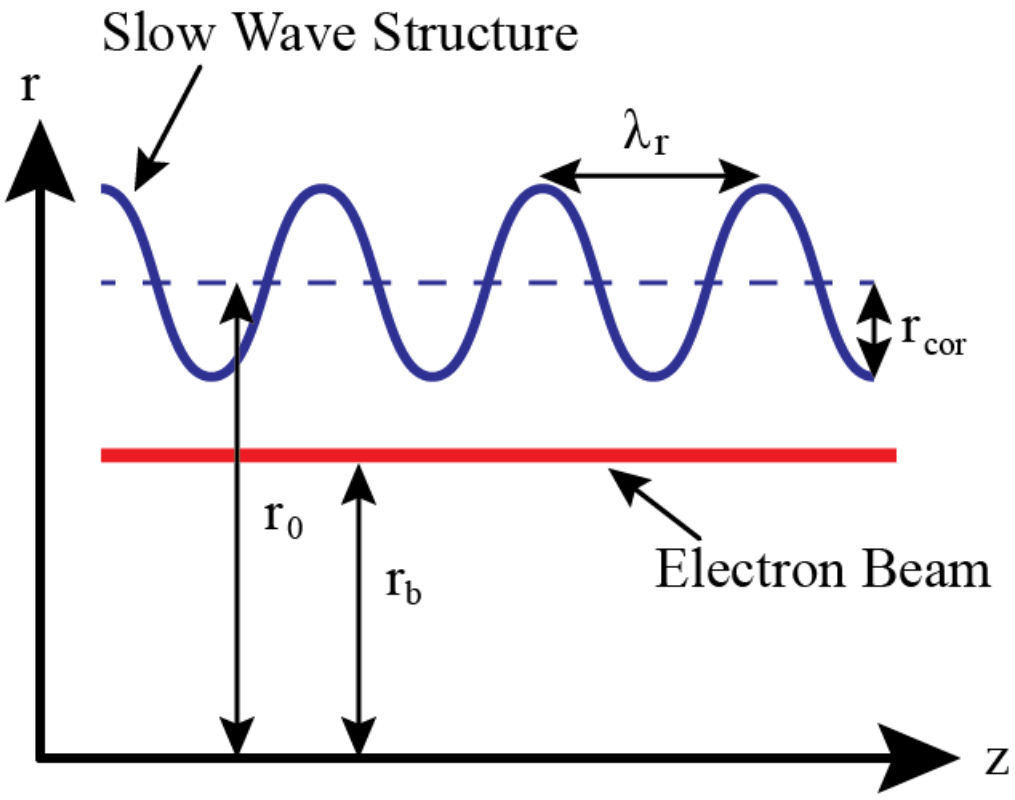

Figure 2.6 Electron beam flowing in a corrugated waveguide

In equations 2.41 and 2.42, r_o is the average waveguide radius, r_{np} is the corugation amplitude, d_z is the corrugation period, ε_r is the ratio of the corrugation amplitude to the average waveguide radius and k_o is the wavenumber related to the corrugation period. The corrugated wall structure is illustrated in Figure 2.6. In this figure, r_b is the radius of the thin annular electron beam. This periodic waveguide relation is illustrated in Figure 2.7, along with the space charge wave dispersion relation.

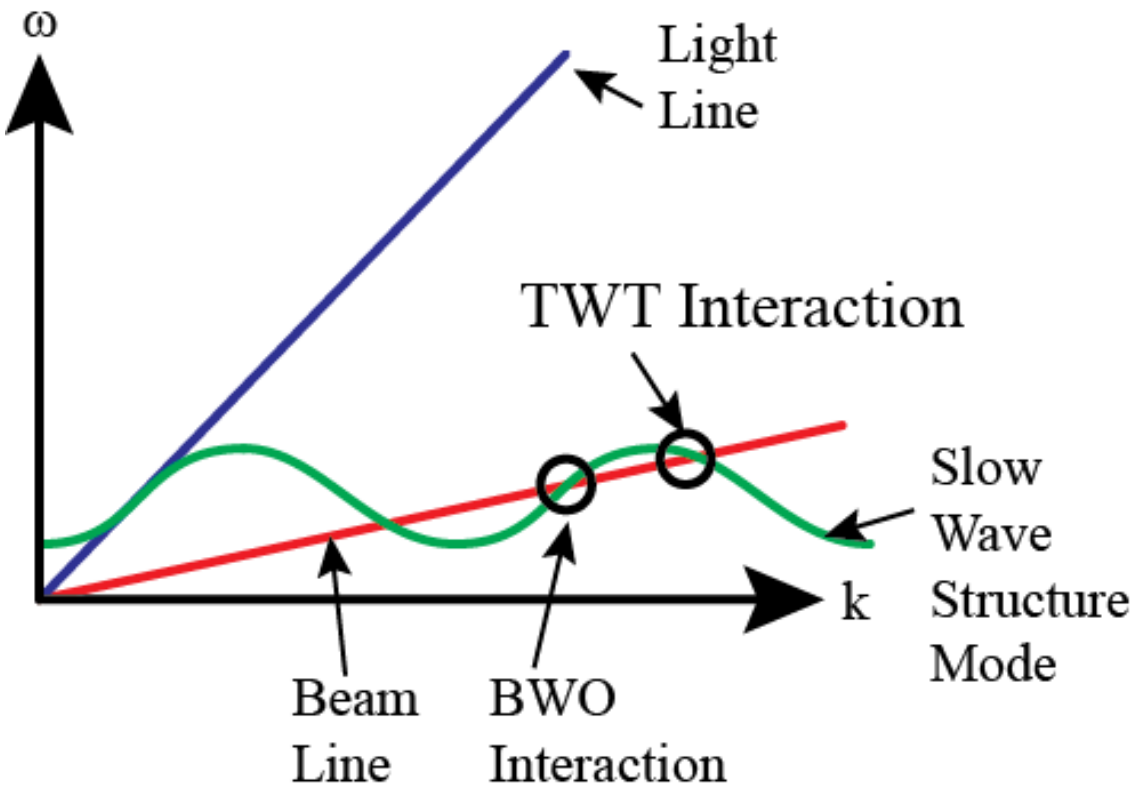

Figure 2.7: Plots of beam line space charge wave curves and a SWS curve

From this plot, it is clear that the space charge waves from the beam line can intersect with corrugated waveguide waves, allowing for the extraction of radiation . The presence of the corrugation reduces the phase velocity of the waveguide allowing the electron beam and the waveguide modes to interact. Such a corrugation in the waveguide is known as a Slow Wave Structure for this reason.

On Figure 2.7, the TWT interaction and the BWO interaction are marked. A TWT interaction with the space charge waves will amplify a periodic disturbance in the electron beam, but will not cause background "signal" oscillations to grow. For this reason, a TWT is considered an amplifier in the grouping of microwave devices. In the BWO interaction, the "noise" oscillations will grow to produce

microwaves. A BWO is, therefore, categorised as an oscillator since it does not require an input signal.

Note that the group velocity of the wave, which is the slope of the SWS dispersion curve at the intersection point, is positive for the TWT and negative for the BWO. A positive group velocity implies a wave in which energy is carried in the same direction as the electron beam, while a negative group velocity implies a wave whose energy propagates in the opposite direction to the electron beam, which is why this interaction is known as a Backward Wave Oscillator.

2.3.7 Cherenkov Beam-Wave Interaction Mechanisms

An alternative way of slowing the wave is to use a dielectric medium which will enable a Cherenkov interaction when the electron is propagating faster than the speed of the wave in the medium. To realise a Cherenkov interaction between an electron beam and an electromagnetic wave, it is again necessary to satisfy the synchronism between the electron beam and the electromagnetic wave. The synchronism conditions are met at the cross point between an electromagnetic (EM) wave dispersion curve, defined as:

$$\omega = \upsilon_{ph}\sqrt{k_z^2 + k_\perp^2} \tag{2.43}$$

and an electron beam line:

$$\omega - k_z\upsilon_z = s\Omega_{eff} \tag{2.44}$$

where ω is the angular frequency of the EM wave, k_z is the axial wave number, and $k_\perp$ is the transverse wavenumber, υ_{ph} is the phase velocity of the wave, υ_z the axial velocity of the electron, s is the harmonic number and Ω_{eff} is an effective frequency corresponding to oscillatory motion of the electrons.

Cherenkov radiation occurs when electrons move in a dielectric medium whose refractive index is greater than one, n > 1 and the electron velocity is greater than the phase velocity of light in that medium, $\upsilon_z > \upsilon_{ph}$ where $\upsilon_{ph} = c/n$. The idea here is that for a sufficiently large refractive index the phase velocity of a propagating EM wave will be reduced enough so that the velocity of the electrons will be larger and hence there will be resonant energy exchange, going from the electrons to the wave.

We note that when $v_z \approx v_{ph}$ the electrons have no transverse momentum so $\Omega_{\text{eff}} = 0$ and so the synchronism condition can be written as:

$$\omega = k_z v_z \tag{2.45}$$

In order to obtain coupling, the beam must pass near the effective dielectric and couple through the exponential tail of the EM surface field, as shown below:

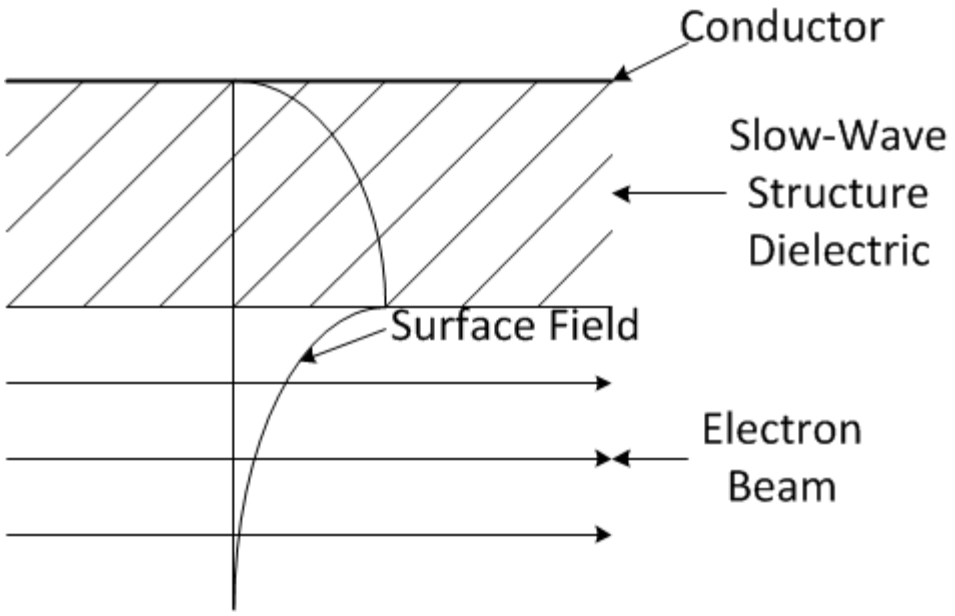

Figure 2.8: The interaction between the evanescent surface field penetrating into both the dielectric and the centre of the waveguide and the electron beam.

The bunching process itself occurs because of the acceleration and deceleration of the electrons by the electromagnetic wave with the electrons increasing speed in the positive part of the wave and hence taking energy from the wave and other electrons slowing in the negative portion of the wave and giving energy to the wave. Thus allowing bunches to form at the point of zero field.

2.3.8 Bunching Mechanisms

The process of bunching itself can be thought of by considering the electron distributions, where initially, they are uniformly distributed over the distance of the waveguide wavelength λ_z; half of the electrons are accelerated and the other half decelerated by the electric field, thus allowing bunches to form as illustrated in Figure 2.9. If the axial velocity is allowed to equal to the phase velocity, $v_z = v_{ph}$, the bunches will form in the vicinity of zero field which does not allow for transfer of energy. If however the velocity of the electron beam is made slightly greater, i.e. $v_z > v_{ph}$, it will

travel faster than the wave resulting in the bunch centre to advance into the decelerating phase of electric field and therefore resulting in a net transfer of the beam energy to the wave.

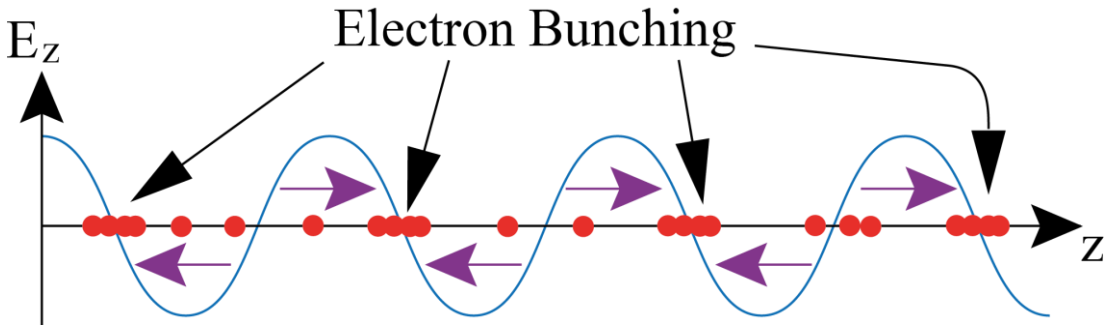

Figure 2.9: Bunching of an electron beam in a linear beam source, by the axial electric field of a synchronized travelling wave.

Radiation sources based on this type of interaction are the Travelling Wave Tube (TWT) and the Backward Wave Oscillator (BWO), these are linear beam devices (have no transverse momentum). The TWT is an amplifier and follows a convective instability, such that in addition to the waves growing they also convect away from the location at which they were created, shown in Figure 2.10. The BWO is an oscillator which uses an absolute instability, i.e. the instability grows as time progresses without moving from the point of origin, shown in Figure 2.11. Alternatively, the waveguide modes can be slowed down by modifying the shape of the confining walls by some kind of 'loading'. This 'loading' effect may be achieved by introducing a periodic variation in the radius of a cylindrical waveguide or by applying a dielectric layer.

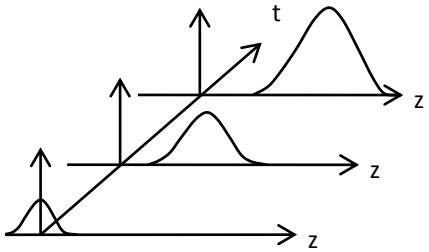

Figure 2.10: Convective instability

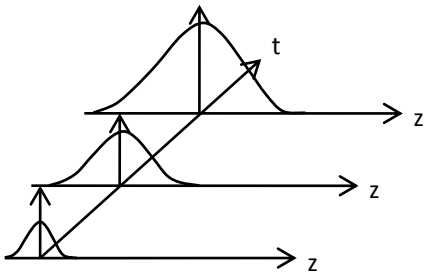

Figure 2.11: Absolute instability

For the devices that utilises these instabilities, the type of device depends on where the interaction coincides with a section of the waveguide mode dispersion that has positive or negative group velocity [2.5]. TWTs operate with positive group velocity and BWOs operate with negative.

2.3.9 Free Electron Devices

There are several aspects to be considered in the beam – wave interaction: (1) waveguide and cavity modes, (2) electron motion and oscillation modes, (3) the beam – wave interaction mechanism, (4) the electron beam intensity and (5) any operational effects. Microwave sources are either fast – wave or slow – wave devices. A fast – wave interaction involves a waveguide mode with a phase velocity greater than the speed of light, whilst a slow – wave interaction involves a waveguide mode whose phase velocity that is less than the speed of light.

With regard to electron motion, microwave devices fall into three categories: O – type devices in which the electrons drift axially along an external applied magnetic field and the field helps to guide the beam through the device. M – type devices in which the electron drift is perpendicular to crossed electric and magnetic fields and the third type of device known as Space Charge devices, where the interaction is intrinsically traceable to an intense space charge interaction such as in a virtual cathode oscillator [2.6].

With regard to the mode of operation of the device, microwave devices fall into two categories: the first is the amplifier device which produce an output signal that is a larger amplitude version of a given input signal and the second type of device called the oscillator where the output signal grows from background noise after the gain in the device overcomes the losses. These devices usually require some form of feedback.

According to the beam current density there are also two categories for microwave devices. The Compton regime involves low beam current and because of this space charge effects are negligible and the electrons behave and emit coherently. The Raman regime involves the use of high electron densities with beam currents approaching a significant fraction of the space – charge limit. Here, the modes of oscillation of the electrons play an important role in the generation of microwaves.

2.3.10 The Electron Cyclotron Maser Interaction

There are different ways to achieve the required coupling by either reducing the phase velocity of the wave mode for a slow wave interaction which has been described in section 2.3.6, or operating close to the cut-off of the electromagnetic wave for a fast wave interaction as described in this section 2.3.10.

Electron Cyclotron Masers (ECMs) are high power microwave sources that produce coherent millimetre and sub – millimetre radiation. They take advantage of the interaction between a fast

electromagnetic wave and electrons to transfer energy from electrons gyrating in a strong guiding magnetic field to an electromagnetic wave. The use of the fast wave interaction to generate millimetre-wave power has great potential as the supporting structures can be oversized waveguides.

2.3.10.1 Energy Transfer in an Electron Cyclotron Maser

The Electron Cyclotron Maser is generally a fast wave device that incorporates electron bunching due to the combined effect of both axial and transverse electromagnetic fields. By considering an electron beam travelling through a relatively strong magnetic guide field B_0 we can see that the electrons will have a transverse velocity component and so they will execute a small Larmor rotation about their guiding center at the cyclotron frequency, $\omega_c = \frac{eB_0}{m\gamma}$ where γ is the relativistic Lorentz factor. The output frequency can be tuned by either adjusting the magnetic field strength or the electron beam voltage therefore promoting spontaneous emission of cyclotron radiation where the frequency is determined by:

$$\omega = k_z v_z + s\omega_c \tag{2.46}$$

Where s is a non-zero integer. Electrons involved in this interaction can interact resonantly with faster waveguide modes and as the cyclotron frequency is energy dependent, the rotating electrons will become bunched in their rotational motion, this is visualised in figure 2.12 below. Microwave generation in ECM devices is therefore based upon the extraction of the electrons rotational energy in a magnetic field.

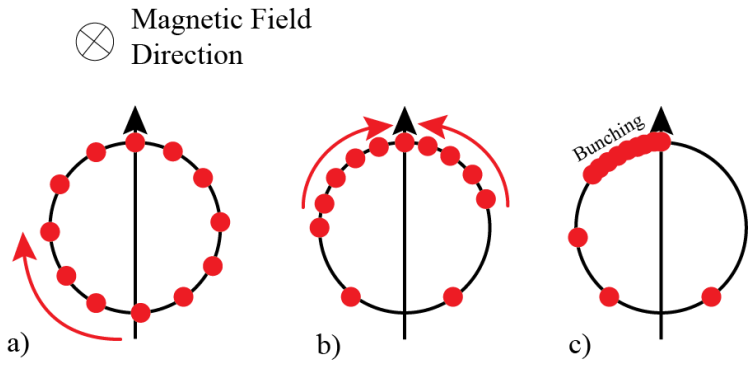

Figure 2.12: Schematic of orbital bunching in CRM devices showing, a) the initial position of the uniformly distributed electrons, b) interaction between the electron beam and the wave and c) the phase slippage between the formed electric bunch and the electric field.

a) At time t = 0 the electrons gyrating in a circular orbit are evenly distributed by azimuthal position and they interact with the electric field, either absorbing or radiating EM radiation.

b) The action of the electromagnetic field on the electrons causes them to bunch due to the dependence of the electron gyration frequency on the electron energy and hence their mass. After several rotations, a phase bunch is formed. Electrons that are decelerated increase in gyro frequency therefore advance in phase, and electrons that are accelerated decrease in gyro frequency and retard in phase.

c) If the electron cyclotron frequency is less than the frequency of the electromagnetic field, the position of the bunches are delayed with respect to the phase of the electric field, this is known as phase slippage and as a result the net kinetic energy of the particles will decrease resulting in an increase in the amplitude of the electromagnetic wave.

Radiation sources based on the Cyclotron interaction include; the Gyrotron, Figure 2.13 [2.7, 2.8], the gyro-BWO Figure 2.14 [2.9, 2.10] and the gyro-TWT Figure 2.15 [2.11], which are all gyro-devices driven by annular electron beams.

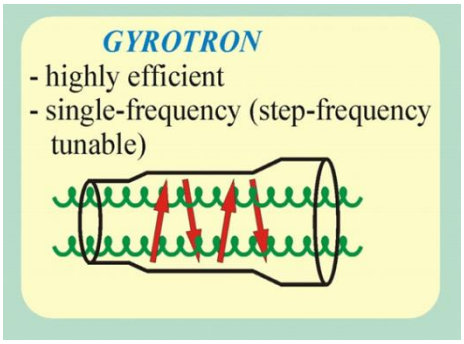

Figure 2.13 Schematic diagram of a gyrotron oscillator

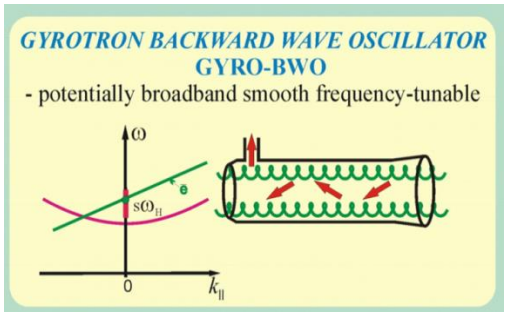

Figure 2.14 Schematic diagram of a gyrotron backward wave oscillator

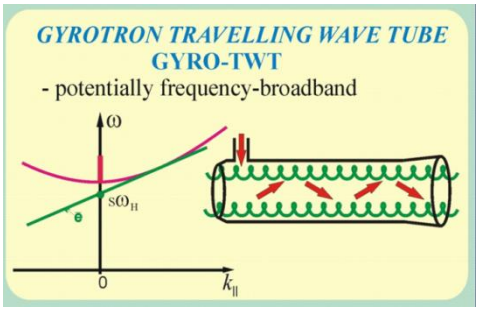

Figure 2.15 Schematic diagram of a gyrotron travelling wave amplifier

The different gyrotron type beam wave interactions are summarised in ω, k dispersion diagram of figure 2.16

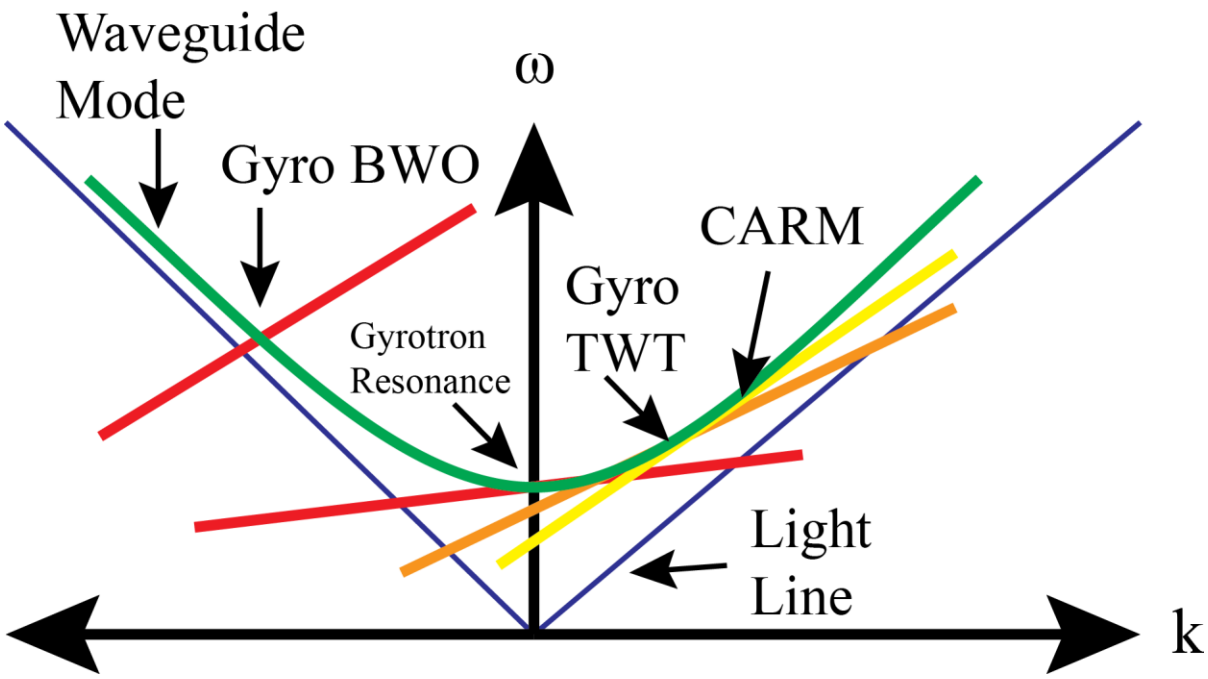

Figure 2.16 Dispersion curves for a selection of common gyro-type beam wave interactions

2.3.11 Saturation Mechanism

In microwave devices bunching is an important factor in producing a coherent output signal, before bunching occurs in the system the output waves are spontaneously emitted. After bunching occurs the signal becomes coherent from stimulated emission of all the electrons in the bunch. This stimulated emission occurs because all of the electrons in the bunch are in a similar energy state and act collectively under the influence of any electromagnetic fields. When the beam is strongly bunched, for stimulated emission the microwave output power is proportional to the number of bunches, N_b, and the square of the number density of electrons within the bunches , n_b:

$$P \propto N_b n_b^2 \qquad (2.47)$$

The growth of the output signal cannot continue indefinitely, as the electrons as well as giving energy to the wave can also absorb energy from the wave, the process will reach saturation and growth will cease at that point. There are a number of mechanisms that will lead to saturation, the two most common ones are: the excess kinetic energy of the electrons is exhausted and the electron oscillations are no longer resonant with the wave and secondly the electron bunches becomes trapped in the strong potential wells of the wave and begin to reabsorb energy from the wave. These saturation mechanism result in

$$P \propto N_b n_b^{\frac{4}{3}} \qquad (2.47)$$

All these types of device have one (or more) things in common. They all possess an interaction region, i.e. a place where the energy can be generated. One of the main goals of this thesis is to demonstrate the possibility of obtaining high power output of W-band radiation (75 - 110 GHz). Currently the output power limitation is the restriction in transverse size of the interaction space which is required so as to avoid the excitation of parasitic modes. This limitation of the interaction space may result in either: breakdown due to the high power density, or electron beam instabilities due to the high space charge density. An increase in the transverse size is therefore necessary in order to maintain a low beam current density as well as to keep down the field strength as the microwave power is increased, but this generally leads to a loss of mode selectivity (single mode operation is desired). The use of distributed feedback is suggested to overcome the problems associated with mode control inside the oversized region and to help achieve single mode operation.

2.3.12 Gyro BWO Theory

When electrons are moving through a slow-wave structure, electron bunches form since there is a feedback mechanism and beam-wave synchronism. The wave phase velocity and electron beam velocity must be close to Cherenkov resonance

$$\omega - k_{para} v = 0 \tag{2.48}$$

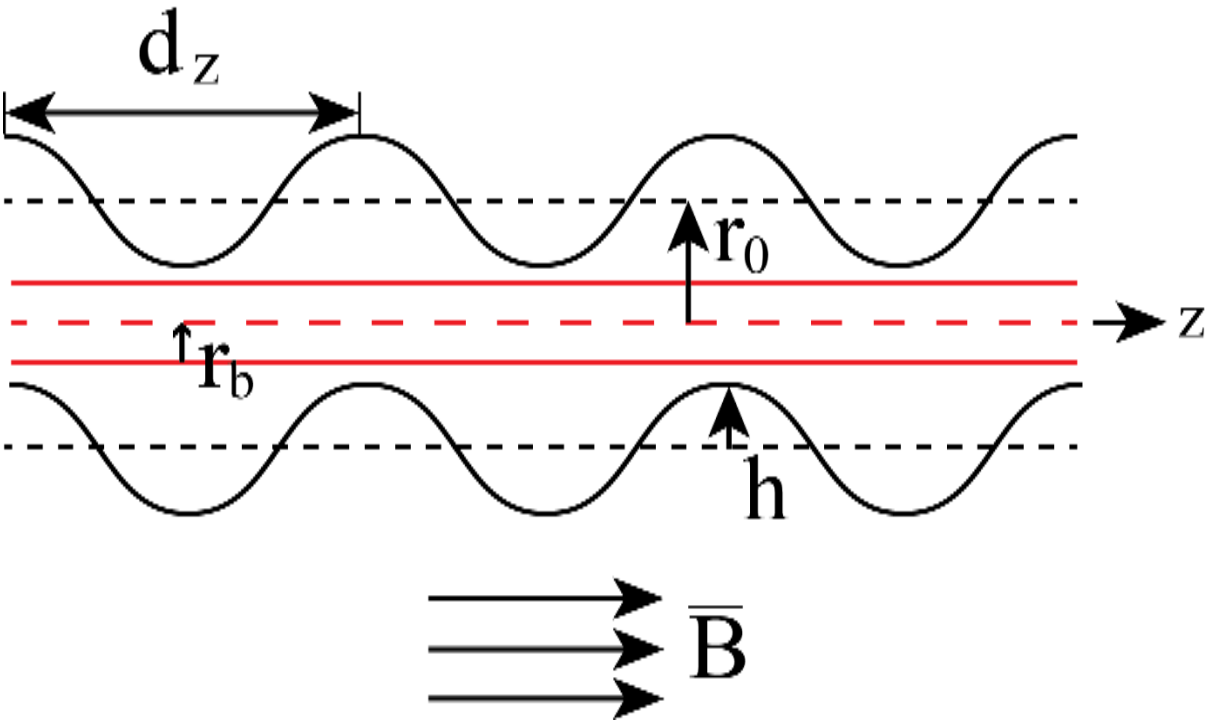

Figure 2.17: A slow wave structure used for a BWO interaction.

Backward Wave Oscillators are an absolute instability which generates microwaves from noise when the beam current I_b exceeds the start current I_{start} [2.12]

$$I_{start} = \frac{0.124\,V}{RN^3} \tag{2.49}$$

where V is the applied voltage, R-coupling impedance given by

$$\mathrm{R} = \frac{E_z^2}{2k_z^2\ P} \tag{2.50}$$

where $k_z = \omega/v_{ph}$, P is the power, E_z is the z-component of the electric field, N –electric length given by equation

$$N = \frac{L\,c}{\lambda v_{ph}} \tag{2.51}$$

where λ operating wavelength, c is the speed of light, L the length of the slow wave structure. When I_{beam} is greater than I_{start} the minimum length results in some specific wavenumber becoming unstable where the effect of E_z is to perturb and modulate the beam which becomes bunched and then the bunches are decelerated. More detailed theory of the BWO can be found in Appendix E

3 Periodic Surface Lattice Analytical Theory

3.0 Introduction

Periodic structures have been used to provide distributed feedback in optics [3.1] and in vacuum electronics over a broad spectral range, from the millimetre through to optical wavelengths [3.2-3.5]. The advantage of using these structures is that they can provide selective feedback where the performance is limited only by the technology available to obtain the periodic perturbation of either the waveguide walls or refractive index of the dielectric material.

The method of two dimensional distributed feedback via Bragg scattering has been successfully employed in a variety of devices, where it is used to provide coherent radiation by synchronization of transverse components of an oversized active medium, in return allowing for specific mode selection and control. There are two distinct types of periodic corrugation relevant to this work; they are one dimensional structures, having variation in only the longitudinal coordinate, and two-dimensional, or 'doubly periodic' structures, consisting of perturbations not only along the length but across the transverse direction also. This chapter will describe the mode coupling phenomenon that occurs within these structures and will begin with Floquet's Thereom [3.6, 3.7].

3.1 Periodic Structures & Floquet's Theorem

The two-dimensional perturbation can be realised by machining a shallow corrugation on the surface of an annular waveguide and may be presented analytically as:

$$r = r_0 + \Delta r cos(\boldsymbol{k}_z z + m\varphi) \tag{3.1}$$

where r_0 is the radius of the unperturbed waveguide, Δr is the amplitude of the corrugation, $\boldsymbol{k}_z = 2\pi/d_z$, d is the period of the corrugation along the z direction and m is the corrugation azimuthal index. The wave propagating through the waveguide will reflect from each small perturbation of the waveguide wall, where, due to the periodicity of the wall perturbations, only waves which satisfy the Bragg resonance conditions will be effectively coupled on such a corrugation. The wave transformation takes place via an interaction with a distributed structure usually represented by a periodic lattice. The distributed feedback studied in this thesis is due to Bragg scattering that takes place in the vicinity of the Bragg frequency determined by the following relationship [3.8-3.10]:

$$\boldsymbol{k} = \boldsymbol{k}_+ - \boldsymbol{k}_- \qquad m = \pm(m_1 - m_2) \tag{3.2}$$

Where $\boldsymbol{k}_+$ is the wave - vector of the incident wave, $\boldsymbol{k}_-$ is the wave - vector of the scattered wave and $m_{1,2}$ are the azimuthal numbers of the incident and scattered waves respectively and **k** is the structure

eigenvector representing the periodicity of the scattering structure given by $\boldsymbol{k}_z = 2\pi/d_z$ where d is the period of the scattering structure.

Assume that the electromagnetic field is a harmonic function of time:

$$\boldsymbol{E}(\boldsymbol{r}, t) = \boldsymbol{E}(x, y, z)e^{i\omega t} \tag{3.3}$$

Consider a structure that is periodic along z with period L. Then a modulus of the field will also be a periodic function with the same period: $|\boldsymbol{E}(x, y, z + L)| = |\boldsymbol{E}(x, y, z)|$. Hence, the complex amplitude after a shift by one period along z gets the phase multiplier $e^{-i\varphi}$, where φ is a real constant:

$$\boldsymbol{E}(x, y, z + L) = \boldsymbol{E}(x, y, z)e^{-i\varphi} \tag{3.4}$$

Now consider the function of coordinates $\boldsymbol{F}(x, y, z) = \boldsymbol{E}(x, y, z)e^{i\beta_0 z}$, where $\beta_0 = \varphi/L$. It is readily verifiable that this function is periodic:

$$\boldsymbol{F}(x, y, z + L) = \boldsymbol{F}(x, y, z) \tag{3.5}$$

Thus, a field in a periodic system with period L is a periodic function of z with the same period L up to the factor $e^{i\beta_0 z}$:

$$\boldsymbol{E}(x, y, z) = \boldsymbol{F}(x, y, z)e^{i\beta_0 z} \tag{3.6}$$

Equations (3.5) and (3.6) express Floquet's theorem. According to equation (3.3) we can write this theorem as:

$$\boldsymbol{E}(x, y, z, t) = \boldsymbol{F}(x, y, z)e^{i(\omega t - \beta_0 z)} \tag{3.7}$$

Spatial Harmonics

Using the periodicity of the function **F**(x,y,z) let us write it as a Fourier series:

$$\boldsymbol{F}(x, y, z) = \sum_{-\infty}^{\infty} \boldsymbol{F}_n(x, y)e^{-i\left(\frac{2\pi}{L}\right)nz} \tag{3.8}$$

Substituting equation (3.8) into equation (3.7), we obtain

$$\boldsymbol{E}(x,y,z,t) = \sum_{-\infty}^{\infty} \boldsymbol{F}_n(x,y) e^{-i(\omega t - \beta_0 z)} \tag{3.9}$$

Where

$$\beta_n = \beta_0 + \frac{2\pi}{L} n, \qquad n = -\infty, \dots, -1, 0, 1, \dots, \infty \tag{3.10}$$

So the field in the periodic structure is a superposition of wave type: $\boldsymbol{F}_n(x,y)e^{-i(\omega t-\beta_0 z)}$. These waves have equal frequencies but different spatial structures. In particular, they have different wavelengths $\lambda_n = 2\pi/\beta_n$. They also have different transversal distributions. The function $\boldsymbol{F}_n(x,y)$ is obtained by solving Maxwell's equations with the corrrsponding boundary conditions. These waves are called *spatial harmonics*. Below we describe informally the key properties of spatial harmonics.

1. Wavelength:

$$\lambda_n = \frac{2\pi}{\beta_n} = \frac{2\pi}{\beta_0 + 2\pi n/L}, \qquad n = -\infty, \dots, -1, 0, 1, \dots, \infty \tag{3.11}$$

2. Phase Velocity:

$$v_{ph,n} = \frac{\omega}{\beta_n} = \frac{\omega}{\beta_0 + 2\pi n/L} \tag{3.12}$$

3. Group Velocity:

$$v_g = \frac{\delta\omega}{\delta\beta_n} = \frac{\delta\omega}{\delta\beta_0} \tag{3.12a}$$

As we see the group velocity is the same for all harmonics. It can be shown that in systems without losses, $v_g = v_{en}$ where v_{en} is the velocity of an energy motion: $v_{en} = \frac{P}{\overline{W}}, P = \int_S [E\ x\ H]_z d\sigma$, and $\overline{W} = (1/2L)\int_{\Omega_L} (\varepsilon_0 E^2 + \mu_0 H^2)\, d\tau$ are the energy flux through a cross section of the structure and the average energy stored over unit length, respectively, Ω_L is a volume of one cell of the structure.

4. The field of each harmonic satisfies the Maxwell equations but the period of harmonic λ_n does not equal a multiple of the structure period, L. Only the total field (Eq. 3.9) satisfies the boundary condition. Thus, if we excite any single harmonic (e.g. by interaction with a synchronous electron beam), all other harmonics would emerge with amplitude and phase relationships that are determined by the geometry of the structure and frequency. A specific

set of harmonics determines a certain mode. In general, an infinite number of modes are possible for any periodic structure.

5. For sufficiently large, *n*, harmonics are slow waves. This follows from (Eq. 3.12).

6. All slow harmonics $(v_{ph,n} < c)$ have properties of surface waves. It may be shown that the field of the nth harmonic decreases with distance *x* from the boundary of the periodic structure as

$$e^{-\sqrt{\beta_n^2 - k^2}x} = e^{-(2\pi x/\lambda_n)}\sqrt{1 - \left(v_{ph,n}/c\right)^2}$$

So the field of the slow wave harmonic diminishes by a factor of $e^{-2\pi\sqrt{1-\left(v_{ph,n}/c\right)^2}}$ along a distance of λ_n. Thus, the energy of the slow harmonic propagates in the *skin layer*,

$$\Delta_{sk} = \frac{\lambda_n}{2\pi\sqrt{1 - \left(v_{ph,n}/c\right)^2}} = \frac{\lambda}{2\pi}\frac{v_{\varphi n}}{c}\frac{1}{\sqrt{1 - \left(v_{ph,n}/c\right)^2}} \qquad (3.13)$$

For a large delay $(v_{ph,n} \ll c)$,

$$\Delta_{sk} = \frac{\lambda_n}{2\pi} = \frac{\lambda}{2\pi}\frac{v_{ph,n}}{c}$$

7. The function $\omega = \omega(\beta_0)$ is periodic with period $2\pi/L$. If we increase β_0 by $2\pi/L$, β_n takes the place of β_{n+1}. As a result, the label of each β_n is changed, but the full set of harmonics is not changed. For the same reason, we can conclude that ω is an even function of β_0: Inverting the sign for β_0 together with the rest of the harmonics β_{-n}, gives the same wave travelling in the –z direction. In principle, the frequency domain of any periodic system consists of separate transmission bands divided by attenuation bands (i.e. any periodic structure similar to some bandpass filter).

8. Taking into account the properties of the dispersion function $\omega = \omega(\beta_0)$ indicated above, we can deduce that the propagation constant of the zeroth harmonic β_0 is enclosed in the range

$$0 \le \beta_0 L \le \pi \qquad (3.14)$$

So the maximum phase shift of the zeroth harmonic per period is equal to π. The group velocity v_g for the range boundaries $\beta_0 = 0, \pi$ is obviously zero.

9. According to Eqs. (3.10) and (3.14), we find that the module of the propagation constant (-1)th is within the range $\pi/L \leq |\beta_{-1}| \leq 2\pi/L$. As such , the modules of the propagation constant can be arranged as

$$|\beta_0| \leq |\beta_{-1}| \leq |\beta_1| \leq |\beta_{-2}| \leq |\beta_2| \leq \cdots \quad (3.15)$$

It can be shown that the fields of the harmonics decrease with $|\beta_n|$. Therefore Eqn (3.15) gives the law of harmonic amplitude decrease. The zeroth harmonic has the greatest amplitude. Recall that the field of the harmonic decreases with distance *x* from the boundary as $e^{-\beta_n x}$. So at a sufficient distance from the boundary we see only the zeroth harmonics (i.e. the field has the structure of a regular waveguide field).

10. All harmonics with $n \geq 0$ have a positive phase velocity. Assume that the curve $\omega = \omega(\beta_0)$ has a positive slope for the first mode in the range of Eqn (3.14). We find that all positive harmonics have coinciding directions of phase and group velocities, so they are forward waves. All negative harmonics having phase and group velocities in the opposite direction are backward waves. When the phase and group velocities of a fundamental harmonic of a structure have the same directions the structure is said to have positive dispersion. In a structure with negative dispersion the zeroth harmonic and all positive harmonics in the fundamental mode, the phase and group velocities have opposite directions. Note that the group velocity of the nth spatial harmonic can be represented as

$$\frac{1}{v_{g,n}} = \frac{d\beta_n}{d\omega} = -\frac{2\pi}{\lambda_n^2}\frac{d\lambda_n}{d\omega}$$

Therefore, for structures with positive dispersion, the wavelengths of the zeroth and all positive spatial harmonics are decreased with frequency.

3.1.1 1D Periodic Structures

The structures studied in this section utilise one-dimensional (1D) distributed feedback realized via wave scattering on a corrugation on the surface of a waveguide. The corrugation can be situated on any surface within the waveguide or on multiple surfaces in a multi-conductor waveguide. The 1D Bragg structures studied have periodicity of the corrugations varying along one coordinate. We

assume that the amplitude of the corrugation is small enough not to affect the transverse structure of the interacting wave.

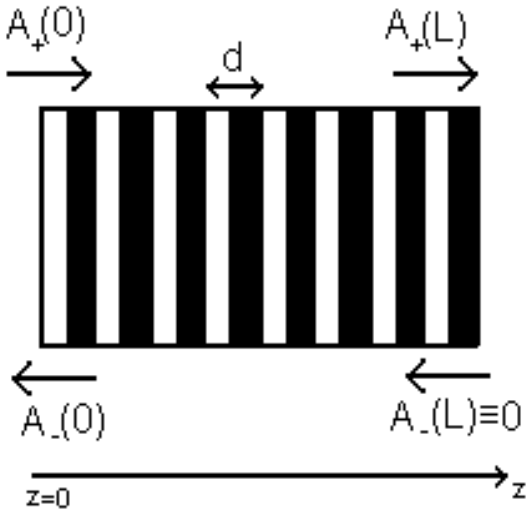

Figure 3.1 A schematic of a 1D Bragg structure of length L and showing the boundary conditions used to define the reflection and transmission coefficients of the incident and reflected waves.

The application of the one-dimensional (1D) Bragg structures which can act as narrow band reflectors in vacuum electronics in comparison with conventional mirrors which can have an extremely broad reflection band have one major advantage due to the fact that the trajectory of the electron beam will not be interrupted by the structures. The main limitation of the 1D Bragg structure is that the selectivity of the mirrors is reduced as the transverse dimension of the device increases due to the relative proximity of the reflection bands which become closer together with increasing diameter of the waveguide i.e. 1D Bragg structures can only maintain mode selectivity when the transverse size of the system, for example the diameter D, is of the order of a few wavelengths $D \approx (2-4)\lambda$. As the transverse diameter scales above this value the 1D Bragg structures can no longer be used to prevent excitation of more than one mode inside the interaction space i.e. the multimode excitation results in mode competition in the interaction region and as a result a loss of stable single mode operation. This restriction on the diameter of a system also serves to restrict the output power of such a device as the electron beam current density and microwave power density become limiting factors as beam power increases.

3.1.1.1 1D Bragg Frequency

Taking into account that the 1D Bragg structure studied has periodic perturbations occurring only along the z-coordinate it is possible to rewrite the Bragg condition.

$$\boldsymbol{k} = \boldsymbol{k}_{+} - \boldsymbol{k}_{-} \tag{3.16}$$

where k_+ and k_- are the longitudinal components of the incident and scattered waves respectively. The sign in the above equation has changed as in this case the scattered wave k_{zs} is propagating in the backward direction. By considering the dispersion relation equation below (3.4) in a waveguide with cylindrical geometry it is possible to manipulate the above expression to yield an equation which relates the transverse wave - vector of specific interacting modes to the Bragg resonant frequency of the interaction i.e. the Bragg frequency.

$$\frac{\omega^2}{c^2} = \boldsymbol{k}_z^2 + \boldsymbol{k}_t^2 \tag{3.17}$$

By substituting the above dispersion relation into equation (3.16) and taking into account the expression and the conservation of energy it is possible to resolve an equation to determine the Bragg frequency as follows:

$$k = \frac{\sqrt{2\boldsymbol{k}^2\left(\boldsymbol{k}_{ti}^2 + \boldsymbol{k}_{ts}^2\right) + \boldsymbol{k}_{ti}^4 + \boldsymbol{k}_{ts}^4 - 2\boldsymbol{k}_{ti}^2\boldsymbol{k}_{ts}^2 + \boldsymbol{k}^4}}{2\boldsymbol{k}} \tag{3.18}$$

where k_{ti} and k_{ts} are the transverse wave - vectors of the incident and scattered waves. This yields the following equation for the central frequency of the Bragg interaction:

$$f_{bragg} = c\frac{\sqrt{2\boldsymbol{k}^2\left(\boldsymbol{k}_{ti}^2 + \boldsymbol{k}_{ts}^2\right) + \boldsymbol{k}_{ti}^4 + \boldsymbol{k}_{ts}^4 - 2\boldsymbol{k}_{ti}^2\boldsymbol{k}_{ts}^2 + \boldsymbol{k}^4}}{4\pi\boldsymbol{k}} \tag{3.19}$$

which in the event of the incident and scattered wave being a TEM wave i.e. $\mathbf{k}_{ti} = \mathbf{k}_{ts} = 0$ equation (3.19) reduces to:

$$f_{bragg} = \frac{c\boldsymbol{k}}{4\pi} = c\frac{1}{2d} \tag{3.20}$$

where d is the period of the Bragg structure.

3.1.1.2 Coupled Wave Equation Model

To study theoretically the transmission and reflection profiles associated with the Bragg scattering, analysis of Maxwell's equations taking into account boundary conditions is required to understand propagation of the waves inside the waveguide structure [3.4, 3.5, 3.9-3.13]. Consider a

waveguide with circular geometry, a 1D Bragg structure can be obtained by machining a 1D corrugation on the surface of a conductor and can be described by:

$$l(z, \varphi, r) = r_0 + \Delta r \sin(\boldsymbol{k}z) \tag{3.21}$$

where Δr is the corrugation amplitude and r_0 is the mean radius of the waveguide. It can also be achieved by lining a dielectric material with a periodical dielectric permittivity such as shown by expression (3.22), below:

$$\varepsilon = \tilde{\varepsilon} + \varepsilon_1 \sin(\boldsymbol{k}z) \tag{3.22}$$

where ε is the permittivity of the dielectric medium, $\tilde{\varepsilon}$ is the unperturbed permittivity of the dielectric and ε_1 is the amplitude of the perturbations. Let us consider the second case where if the variation of the corrugation i.e. ε_1 is much less than the unperturbed value of $\tilde{\varepsilon}$ then the corrugation can be assumed to be low contrast and will not affect the transverse structure of the eigenwaves of the waveguide. By considering a potential oscillating in a hollow cylindrical waveguide, the following equation can be obtained from Maxwell's equations:

$$\nabla^2 \psi = \frac{1}{c^2} \frac{\partial^2 \psi}{\partial t^2} \tag{3.23}$$

Where $\nabla^2 = \left(\frac{\partial}{\partial x^2} + \frac{\partial}{\partial y^2} + \frac{\partial}{\partial z^2}\right)$ is the Laplacian vector operator, ψ is an oscillating field amplitude$\psi = \psi_0(r, \varphi)\exp(i(\omega t - kz))$, μ is the permeability of the medium of the waveguide and ω is the angular frequency. By substituting equation (3.22) into equation (3.23) a pair of equations are obtained, which describe the electromagnetic field amplitudes inside a waveguide with a Bragg structure. Then by taking into account the Bragg condition and by neglecting fast oscillating terms i.e. adopting the approximation of the slow variation of the amplitude envelope; it is possible to describe the wave scattering in the vicinity of the Bragg resonance. The amplitudes of the forward and backward propagating axial waves are given by the following pair of equations [3.9, 3.11]:

$$\frac{dA_+}{dz} = -i(\Delta + i\sigma)A_+ + i\alpha A_- \tag{3.24}$$

$$\frac{dA_-}{dz} = i(\Delta + i\sigma)A_- - i\alpha A_+ \tag{3.25}$$

where A_+ is the amplitude of the forward propagating electromagnetic wave, A_- is the amplitude of the backward propagating electromagnetic wave, Δ is the Bragg mismatch $\Delta = \frac{1}{2}(\boldsymbol{k} - \boldsymbol{k}_{+z} - \boldsymbol{k}_{-z})$ where k_{+z} is the propagation wave - vector in the positive axial direction, k_{-z} is the propagation wave - vector in the negative axial direction, σ is in this case the ohmic losses to the waveguide walls and α is the coupling coefficient. To define a simple meaning of the coupling coefficient one can assume that if $\Delta = 0$ and $\sigma = 0$ the set of equations (3.23 – 3.24) can be simplified to:

$$\frac{dA_+}{dz} = i\alpha A_- \tag{3.26}$$

$$\frac{dA_-}{dz} = -i\alpha A_+ \tag{3.27}$$

From equations (3.26 – 3.27) it is clear that α is the coupling coefficient determining the magnitude of the scattering of waves i.e. the larger the coupling coefficient the greater the interaction with the Bragg structure. The coupling coefficient as it will be shown also determines the amplitude of the reflected wave and defines the parameters of the reflection and transmission zones.

3.1.1.3 Coupling Coefficient

The RF field inside the 1D Bragg structure can be presented as a superposition of partial waves i.e.

$$E = \exp(i\omega t)\sum_{s=1}^{2} A_s E_s(\xi,\eta)\exp(-i\boldsymbol{k}_{z,s}z) \tag{3.28}$$

$$H = \exp(i\omega t)\sum_{s=1}^{2} A_s H_s(\xi,\eta)\exp(-i\boldsymbol{k}_{\boldsymbol{z},\boldsymbol{s}}z) \tag{3.29}$$

where A_s describes the amplitude of the signal, $E_s(\xi,\eta)$ and $H_s(\xi,\eta)$ describes the waves transverse structure. By assuming that the depth of the corrugation machined on the surfaces of the conductors to be much smaller than the wavelength of the incident wave it can be assumed that the transverse structures of the partial waves inside the 1D Bragg structure can be considered to coincide with the transverse structures of the unperturbed waveguide eigenmodes. Considering for simplicity that the perturbation is sinusoidal and has no azimuthal variation, as shown in equation (3.21), which

describes the longitudinal field distribution inside the structure, where a is the radius of the waveguide:

$$\frac{dA_z}{dz} = -\frac{1}{N_s}\oint i_j^m \, H_{-s} d\sigma_j \tag{3.30}$$

where i_j^m is the fictitious magnetic current induced on the surface *s* of the corrugated conductor denoted by the suffix j and N_s is the wave-norm given by the expression below;

$$N_s = \frac{c}{2\pi}\int E_s(\xi,\eta)\, H_{-s}(\xi,\eta) ds_j \tag{3.31}$$

where the integral is evaluated across the cross sectional area s_j of the unperturbed waveguide. Considering only the slowly oscillating terms on the right hand side of equation (3.30) i.e. when the Bragg conditions $\boldsymbol{k} + k_s - k_{s'} = 0$ are satisfied and the integral on the right hand side of equation (3.30) is nonzero:

$$\frac{dA_s}{dz} = -\frac{i\omega A_{s'} a_j}{8\pi N_s}\oint (E_{s'n} E_{-sn} + H_{s'\tau} H_{-s\tau})\, d\varsigma \tag{3.32}$$

where a_j is the corrugation depth on conductor *j*, where ς denotes the contour of the integral around the conductor surface and n and τ indicate the normal and tangential field components respectively. By manipulation of equation (3.17) and equation (3.19), an expression for the coupling coefficient can be found:

$$\alpha_s = \frac{\omega a_j}{8\pi N_s}\oint (E_{s'n} E_{-sn} + H_{s'\tau} H_{-s\tau})\, d\varsigma \tag{3.33}$$

It is clear that the coupling coefficient depends upon the geometrical parameters of the structure and the modes coupled by the corrugation and is proportional to the corrugation depth $\alpha \sim a_j$ within the constraints of the slow wave envelope approximation.

3.1.1.4 Reflection and Transmission

Taking into account energy conservation the relation between transmission T and reflection R coefficients can be found:

$$R^2 + T^2 + \Omega^2 = 1 \tag{3.34}$$

where Ω is the losses in the system, for example ohmic losses to the walls. By considering the slow varying field amplitudes along the Bragg structure the solution to equations (3.24 – 3.25) can be presented as:

$$A_+ = C_1 e^{-i\Gamma z} + C_2 e^{i\Gamma z} \tag{3.35}$$

$$A_- = C_3 e^{-i\Gamma z} + C_4 e^{i\Gamma z} \tag{3.36}$$

where C_n is the constant relating to the amplitude of the field component, Γ is an eigenvalue parameter and z is the axial co-ordinate. By substituting expressions (3.36) into the coupled wave equations (3.24 – 3.25) the following system of equations could be obtained:

$$(-i\Gamma C_1 + (i\Delta + \sigma)C_1 + i\alpha C_3) = 0 \tag{3.37}$$

$$(-i\Gamma C_2 + (i\Delta + \sigma)C_2 + i\alpha C_4) = 0 \tag{3.38}$$

$$(-i\Gamma C_3 + (i\Delta - \sigma)C_3 - i\alpha C_1) = 0 \tag{3.39}$$

$$(-i\Gamma C_4 + (i\Delta - \sigma)C_4 - i\alpha C_2) = 0 \tag{3.40}$$

This enabled the eigenvalue of Γ to be determined as: $\Gamma^2 = \alpha^2 + (\sigma + i\Delta)^2$. To determine the reflection profile produced by a 1D Bragg structure the coupled wave equations could then be solved for the complex field amplitudes in equation (3.33), by assuming that the field amplitudes only vary in the longitudinal dimension having no transverse propagation and by applying the following boundary conditions:

$$A_-(L) \equiv 0 \tag{3.41}$$

$$A_+(0) \equiv 1 \tag{3.42}$$

The reflection and transmission produced by the 1D Bragg structure can be given by:

$$R = \frac{A_-(0)}{A_+(0)} \tag{3.43}$$

$$T = \frac{A_+(L)}{A_+(0)} \tag{2.44}$$

It is possible to evaluate the above expressions and observe the relationship between the R and T coefficients (as shown in the equation (3.45)) and Δ the detuning from the central Bragg frequency, α the coupling coefficient of the interaction, L the length of the structure and Γ is the eigenvalue parameter discussed previously.

$$R = \frac{i\alpha sinh\Gamma L}{\Gamma cosh\Gamma L + (i\Delta - \sigma)sinh\Gamma L} \tag{3.45}$$

with σ is the ohmic losses due to the finite conductivity of the walls. The transmission coefficient can be found simply from equation (3.34): $T^2 = 1 - R^2 - \Omega^2$. 2D Bragg structures

3.1.2 2D Bragg Structures

3.1.2.1 2D Periodic Structures

In order to obtain spatially coherent radiation from the oversized electron beam and improve mode control, the use of two-dimensional feedback has been successfully implemented [3.11, 3.8, 3.10]. This type of feedback can be realised by introducing a shallow, periodic double corrugation to the waveguide wall, and can be written as:

$$r = r_0 + \Delta r cos(k_z z + m\varphi) \tag{3.46}$$

where r_0 is the radius of the unperturbed waveguide, Δr is the amplitude of the corrugation, $k_z = 2\pi/d_z$, d is the period of the corrugation along the z direction and m is the corrugation azimuthal index.

This type of lattice offers indirect coupling of nearby waves via near cut off waves of the waveguide structure, where the coupling occurs due to Bragg scattering of waves propagating through the structure. Only waves satisfying the Bragg resonance condition will couple to the corrugation. 2D Periodic structures consist of a corrugation that is periodic in two dimensions i.e. on the surface of a waveguide having variation along two coordinates as shown in figure 3.2.

Figure 3.2: Postive aluminium former of a 2D periodic corrugation for electro-chemical deposition of copper with the aluminium former dissolved away resulting in an interaction region for mode coupling between an incident volume wave and a scattered backward wave.

With the 2D periodic structure mutual scattering of the electromagnetic energy fluxes propagating in the longitudinal and transverse directions takes place. The additional transverse electromagnetic energy fluxes synchronize the radiation across the transverse dimension of a large size electron beam. With the scattering of the electromagnetic fluxes occurring in two dimensions the conditions which should be met to observe the scattering are more stringent, as a result the 2D periodic structure has greater mode selectivity than a 1D Bragg structure in large oversized systems. Using a 2D periodic structure to provide feedback it is possible to increase the total beam power and, correspondingly, the microwave power while still keeping the current and radiation density per unit transverse size constant which acts to reduce the probability of RF breakdown in the interaction region, via increase of the transverse dimension of the interaction space without excitation of multiple modes. The 2D periodic structures may be used to provide feedback for Free Eletron Devices with a large transverse dimension of either a planar or annular beam or for a cavity region based on the Cyclotron or Cherenkov instability.

3.1.2.2 Coupled Wave Theory Model

Two-dimensional periodic structures can be obtained by providing a corrugation on the surface of a waveguide wall. It can be used as a distributed feedback mirror to provide frequency selective feedback for a cavity or as a filter in integrated optics or microwave electronics [3.17]. As discussed previously these structures meet the Bragg condition, equation (3.8) at each point in the feedback cycle and due to the more rigorous conditions, which must be met to provide feedback greater mode selectivity is observed. To numerically simulate the transmission and reflection profiles of specific mode interactions as a result of the Bragg scattering in a 2D periodic structure analysis of Maxwell's equations within a waveguide is required to understand the effect on the eigenmodes of waves scattered by the perturbation of the 2D periodic structure.

$$r = r_0 + \Delta r cos(\boldsymbol{k}_z z + m\varphi) \tag{3.47}$$

where Δr is the corrugation depth, $k_z = 2\pi/d_z$, d_z is the period of the corrugation over the z - coordinate and m is the number of variations of the corrugation over the azimuthal coordinate. The dispersion equation for the oscillating potentials of the waveguide can be reduced to the following form:

$$\boldsymbol{k}^2 = \frac{\omega^2}{c^2} \cong \boldsymbol{k}_z^2 + \boldsymbol{k}_t^2 \tag{3.48}$$

where ω is the wave frequency, c is the speed of light, k_z is the longitudinal wavenumber, $\mathbf{k}_t$ is the transverse wave - vector given by: $\boldsymbol{k}_t^2 = \boldsymbol{k}_r^2 + \boldsymbol{k}_\varphi^2$, where k_φ the azimuthal wave - vector is given by: $\boldsymbol{k}_\varphi = m/a$, where m is the number of azimuthal variations, $\mathbf{k}_r$ is the radial wave - vector $k_r = p\pi/\Delta a$ is the radial wavenumber and m and p are the azimuthal and radial variation indices respectively. The field inside the 2D Bragg structure can be presented in the form of four coupled waves [3.16-3.20]: $A_\pm$ propagating in the $\pm z$ and $B_\pm$ are transversely propagating in the $\pm x$ directions close to cut-off

$$\begin{aligned}\boldsymbol{E} = Re\{\big(E^0(r)(B_+(x,z)e^{-i\boldsymbol{k}_x x} + B_-(x,z)e^{i\boldsymbol{k}'_x x}\big) + E^0(r)(A_+(x,z)e^{-i\boldsymbol{k}_z z} \\ + A_-(x,z)e^{i\boldsymbol{k}'_z z}))e^{i\omega t}\}\end{aligned} \tag{3.49}$$

Here $A_{\pm}(x,z), B_{\pm}(x,z)$ are the slowly varying envelope functions of the fields in the x and z coordinates, $\boldsymbol{k}_x, \boldsymbol{k}'_x$ and $\boldsymbol{k}_z, \boldsymbol{k}'_z$ are the azimuthal and longitudinal wave numbers of the partial waves B_+, B_- and A_+, A_- respectively, $E^0(r)$ is the function that describes the spatial wave profile along the r – coordinate. Due to the circular geometry of the cylindrical system the wave amplitudes should satisfy the cyclic boundary conditions:

$$B_{\pm}\left(x + l_{x,}z\right) = B_{\pm}(x,z), \qquad A_{\pm}(x + l_x, z) = A_{\pm}(x,z) \tag{3.50}$$

Where $l_x = 2\pi r_0$ is the cavity mean circumference. These conditions allow the partial wave amplitudes $A_{\pm}(x,z), B_{\pm}(x,z)$ to be represented in the Fourier series:

$$A_{\pm}(x,z) = \sum_{m=-\infty}^{\infty} A_{\pm}^{m}(z)e^{imsx}, \quad B_{\pm}(x,z) = \sum_{m=-\infty}^{\infty} B_{\pm}^{m}(z)e^{imsx} \tag{3.51}$$

where $s = 2\pi/l_0$. The lattice eigenvectors can be presented as $\boldsymbol{k}_{\pm} = \boldsymbol{k}_x\hat{x}_0 \pm \boldsymbol{k}_z\hat{z}_0$ where $\hat{x}_0$ and $\hat{z}_0$ are the unit vectors along the x and z coordinates and $\boldsymbol{k}_x$, $\boldsymbol{k}_z$ are the amplitudes of the projections of the lattice eigenvectors $\boldsymbol{k}_{\pm}$ on the axes x and z. The partial wave A_+ propagating in the $+z$ direction is scattered into waves $B_{\pm}$ propagating in the transverse $\pm x$ directions and scattering into waves $A_{\pm}$, which ensures that the two dimensional feedback loop $A_{\pm} \leftrightarrow B \leftrightarrow A \leftrightarrow B_{\pm} \leftrightarrow A_+$ is complete. To obtain an efficient coupling of the partial waves $A_{\pm} \leftrightarrow B_{\pm}$ the following Bragg resonance conditions should be satisfied for each pair of coupled waves:

$$\boldsymbol{k}_z - \boldsymbol{k}_x = \boldsymbol{k}_-; \quad \boldsymbol{k}'_z - \boldsymbol{k}'_x = -\boldsymbol{k}_- \tag{3.52}$$

$$\boldsymbol{k}_z - \boldsymbol{k}'_x = \boldsymbol{k}_+; \quad \boldsymbol{k}'_z - \boldsymbol{k}_x = -\boldsymbol{k}_+ \tag{3.53}$$

Taking into account that the 2D - feedback loop can only be obtained when conditions (3.52 – 3.53) are fulfilled simultaneously the four partial waves undergo the coupling on the 2D structure if:

$$\boldsymbol{k}_z = \boldsymbol{k}'_z \cong \boldsymbol{k}_z, \qquad \boldsymbol{k}_x = \boldsymbol{k}'_x \cong \boldsymbol{k}_x \quad |\boldsymbol{m}| = |M| \; and \; |\boldsymbol{k}_z| = |\boldsymbol{k}'_t| \tag{3.54}$$

where k'_t is the transverse wavenumber of the partial waves $B_{\pm}$. The last condition in equation (3.54) does not follow from equations (3.52 – 3.53) but from the condition that the waves $B_{\pm}$ should be near

cut-off of the waveguide. From equation (3.54) the resonant frequency of the Bragg interaction ω_0 can be found in the same manner as described for 1D Bragg structures. The field scattering on the corrugation, when equation (3.54) are satisfied, can be described by the set of coupled wave equations for the dimensionless amplitudes $A_{\pm}$, $B_{\pm}$:

$$\pm\frac{\partial A_{\pm}}{\partial z} + i\delta A_{\pm} + \sigma A_{\pm} + i\alpha(B_{+} + B_{-}) = 0 \tag{3.55}$$

$$\pm\frac{\partial B_{\pm}}{\partial x} + i\delta B_{\pm} + \sigma B_{\pm} + i\alpha(A + A_{+}) = 0 \tag{3.56}$$

Where $\delta = (\omega - \omega_0)/c$ is the small frequency detuning from the Bragg resonance, $\omega_0 = c\sqrt{k^2 + k_r^2}$ is the Bragg frequency, σ is the distributed power losses, α is the wave coupling coefficient [3.11].

3.1.2.3 Reflection and Transmission

The reflection and transmission coefficients from such a structure can be found by taking into account the following boundary conditions:

$$A_{+}^{m}(z = 0) = A_{0}^{m}, \quad A_{-}^{m}(z = l_z) = 0 \tag{3.57}$$

Where l_z is the length of the 2D structure. The analytic expressions for the reflection R_m and the transmission T_m coefficients can be obtained as functions of the azimuthal index m and frequency detuning δ_0 of the incident wave, where $\delta = (\omega - \omega_0)/c$ and ω_0 is the Bragg frequency. Let us note that δ_0 is real, in contrast to $\tilde{\delta}$ which is complex.

$$R_m = \frac{\boldsymbol{\lambda}_m^2 - p_m^2}{q_m\left(p_m - \boldsymbol{\lambda}_m ctg(\boldsymbol{\lambda}_m l_z)\right)} \tag{3.58}$$

$$T_m = \frac{-i\boldsymbol{\lambda}_m}{\sin(\boldsymbol{\lambda}_m l_z)\left(p_m - i\boldsymbol{\lambda}_m ctg(\boldsymbol{\lambda}_m l_z)\right)} \tag{3.59}$$

Where

$$q_m = \frac{2\alpha^2\tilde{\delta}}{s^2m^2 + \tilde{\delta}^2}, \qquad p_m = \frac{2\alpha^2\tilde{\delta}}{s^2m^2 + \tilde{\delta}^2} + \tilde{\delta}, \qquad \tilde{\delta} = i\tilde{\delta}_0 + \sigma \tag{3.60}$$

And

$$\boldsymbol{\lambda}_m = -i\,\delta\sqrt{\frac{4\alpha^2}{\delta^2 + s^2 m^2} + 1} \tag{3.61}$$

where σ is associated with the RF power losses. It should be noted that for each mode with index *m* such a structure provides an effective reflection zone (forbidden band gap), inside a frequency interval defined by the condition $Re(\boldsymbol{\lambda}_m^2) \leq 0$. The coupling coefficient for the 2D Bragg structure α is proportional to the corrugation depth b_1 and was calculated using the same method for the coupling coefficient of the 1D Bragg using the expression (3.33) to evaluate the coupling coefficient for the normal and tangential components of the electric and magnetic fields on the unperturbed waveguide surface.

3.1.2.4 2D PSL Dispersion

The dispersion diagram for the 2D PSL was derived by using the coupling of the surface field of the $TE_{m,1}$ mode with the volume field of the $TM_{0,n}$ mode. A coupling coefficient for $TE_{5,1}$ and $TM_{0,2}$, of 0.55 was derived by Dr. Liang Zhang of the ABP group, department of physics, University of Strathclyde using perturbation theory. The W-band PSL (obtained via 3D printing) was incorporated in the experiment ($r_0 = 4$ mm, d_z =1.6 mm, $\Delta m = 3.5mm$ and $\Delta r = 1.6$ mm). The frequency versus axial wavenumber dispersion for the two modes was calculated using the MATLAB program listed in appendix A and is plotted in figure 3.3 along with four electron beam dispersions for an acceleration voltage 80 kV, γ =1.156, axial guide magnetic field of 1.8T and a beam alpha v_{par}/v_{per} of 0.4 (v_{para} ~0.46c and v_{per} ~0.19c).The beam parameters were obtained from CST Particle Studio simulations of the electron gun used in the experiment, section 6.4.8.

1) Backward Wave Oscillator (blue dotted line) electron beam dispersion

$$\omega = k_z v_z \pm \frac{\omega_b}{\gamma^{\frac{3}{2}}} \tag{3.62}$$

2) Fundamental electron cyclotron beam (light blue solid line) dispersion

$$\omega = k_z v_z + \frac{eB}{\gamma m_0} \tag{3.63}$$

3) Second harmonic electron cyclotron beam (black dotted line) dispersion

$$\omega = k_z v_z + \frac{2eB}{\gamma m_0} \tag{3.64}$$

4) Surface modulated electron beam dispersion (solid orange line)

$$\omega = k_z v_z \pm \frac{2\pi}{d_z} v_z \tag{3.65}$$

where ω is the angular frequency, v_z is the axial velocity, d_z is the period of the corrugation, e is the charge of the electron, B is the axial magnetic field, $m\gamma_0$ is the relativistic mass of the electron and ω_b is the beam plasma frequency given by

$$\omega_b = \left(\frac{|\rho_0|e^2}{\varepsilon_0 m\gamma_0}\right)^{\frac{1}{2}} \tag{3.66}$$

The *ω/k* dispersion diagram for the 2D PSL constructed and described in section 6.6.2 for coupling between the $TM_{0,2}$ volume mode and the $TE_{5,1}$ surface mode is shown in figure 3.3

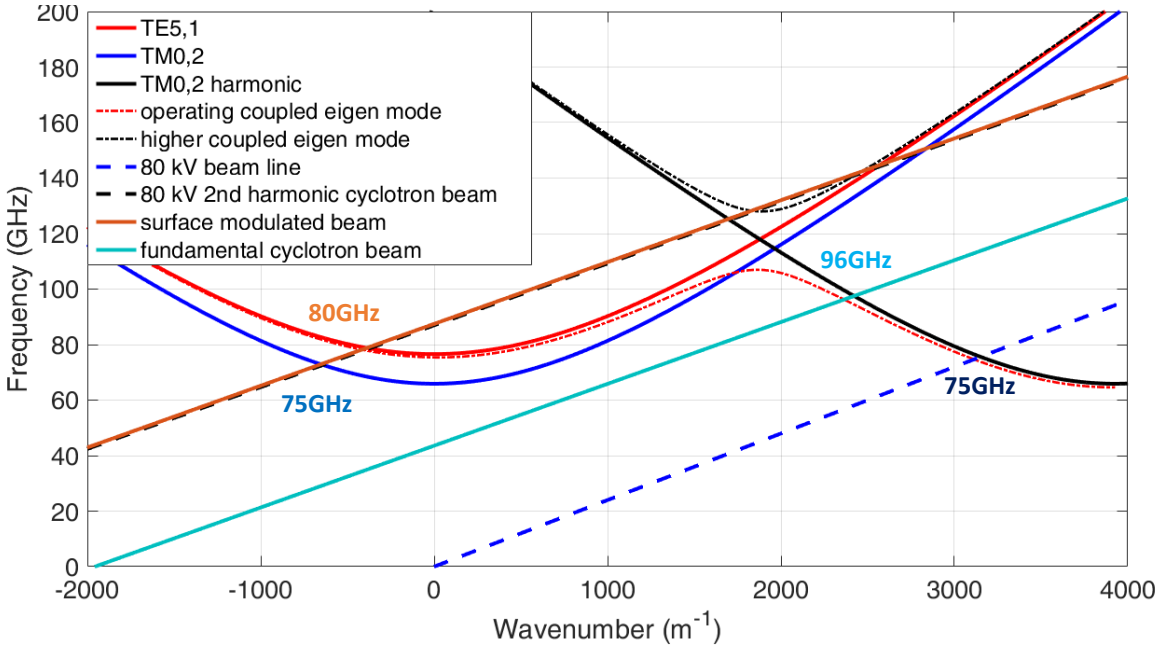

Figure 3.3 Frequency as a function of axial wavenumber of the $TM_{0,2}$ mode and the surface $TE_{5,1}$ wave for a 2nd harmonic gyrotron BWO interaction (black dotted line) The orange line represents the electron beam–electromagnetic wave interaction with the synchronous harmonic of the cavity eigenmode's partial surface field at the lattice interface. The light blue line represents the fundamental gyrotron BWO interaction for a cavity magnetic field of 1.8 T. The straight blue dotted line represents the negative energy space charge wave of a beam of axial velocity 0.46c with a beam plasma frequency of ~3 GHz (appendix C) indicating a grazing with the backward wave at the first spatial harmonic on the $TM_{0,2}$ mode..

The parameters of the 2D PSL constructed and described in chapter 6 were as follows

Parameter	Symbol	Value
Longitudinal Period	dz	1.6 mm
Azimuthal Period	Δm	3.5 mm
Number of Longitudinal Periods	n	16
Amplitude	dr	0.8 mm
Amplitude (Peak-to-Peak)	dr (pk-pk)	1.6 mm
Inner Radius of input and output waveguide	r	4 mm
Minimum radius of perturbation (ID)	r_{min}	3.6 mm
Mean radius of perturbations	r_0	4.4 mm
Maximum radius of perturbation (OD)	r_{max}	5.2 mm

Table 3.1 The parameters of the 2D PSL used in the electron beam experiment

For a beam energy of 80kV, γ ~1.156, v_{para}~ 0.46c, and v_{per}~ 0.19c and a 2D PSL of period dz = 1.6 mm, equation (3.65) indicates that the surface mode will cross the y-axis (x=0) on the ω/k dispersion diagram at ~85 GHz.

For strong coupling between the electron beam and the electromagnetic fields the number azimuthal variations is given by

$$\frac{2\pi r_0}{\gamma \lambda_0} \tag{3.67}$$

For the parameters of the 2D PSL as detailed in Table 3.1 and used in the experiment described in chapter 6 where an electron beam of energy 80keV was used this condition [3.15] indicates that the number of azimuthal variations of the surface wave will ~ 5.

$$\frac{2\pi r_0}{\gamma \lambda_0} \sim 5 \tag{3.68}$$

The other main condition that needs to be satisfied to observe a beam wave interaction is that the volume field must be able to exists within the interaction region. For the dispersion shown in Figure 3.3 the cut-off frequency of the $TM_{0.2}$ mode in the 2D PSL was calculated using

$$k = \frac{J_i}{R_{min}} \tag{3.69}$$

Where k is the axial wavemunber, J_i is the root of the Bessel function and R_{min} (3.5mm) is the minimum radius of the waveguide. For the parameters of the 2D PSL shown in Table 3.1, the cut-off frequency of the $TM_{0.2}$ mode was calculated to be 75 GHz. It is important to note that for a high contrast periodic surface lattice (corrugation depth of 1.6 mm is greater than λ/4) the electron beam can interact with propagating wave moving in either forward or backward direction as described in chapter 4.

4

Numerical Design, Construction and Measurement of 2D Periodic Surface Lattice

4 Numerical Methods, Computational Software

4.1 Introduction

In this chapter the electromagnetic equations solved using the numerical simulation software CST Microwave Studio and Magic 3D as well as the mathematical principles behind their operation are discussed. The manufacture of a serpentine mode converter used to measure the transmission and reflection properties of the 2D PSL compatible with a 75 GHz to 110 GHz and 140 GHz to 220 GHz VNA is presented. The relatively new technique of making the 2D PSL based on 3D printing of a wax model which is then used to cast a silver chromium structure and the alternative technique of electrochemical deposition of copper on an aluminium former with the subsequent dissolving of the aluminium former to leave a copper structure are also introduced.

4.2.1 Maxwell's Equations

The transportation of electromagnetic waves obey four fundamental laws that are collectively known as Maxwell's Equations:

Gauss's Law	$\nabla \circ \boldsymbol{E} = \frac{\rho}{\varepsilon_0}$	(4.1)
Gauss's Law For Magnetism	$\nabla \circ \boldsymbol{B} = 0$	(4.2)
Maxwell-Faraday Law	$\nabla \, x \, \boldsymbol{E} = -\frac{\partial \boldsymbol{B}}{\partial t}$	(4.3)
Maxwell-Ampere Law	$\nabla \, x \, \boldsymbol{B} = \mu_0 \left(\boldsymbol{J} + \varepsilon_0 \frac{\partial \boldsymbol{E}}{\partial t} \right)$	(4.4)

Table 4.1: Maxwell's equations in differential form for free space (with no term relating to the relative permittivity or permeability of a particular medium).

Gauss's Law (Integral form)	$\oint_{\boldsymbol{S}} \boldsymbol{E} \circ \hat{n} \, da = \frac{q_{enc}}{\varepsilon_0}$	(4.5)
Gauss's Law For Magnetism (Integral form)	$\oint_{\boldsymbol{S}} \boldsymbol{B} \circ \hat{n} \, da = 0$	(4.6)
Maxwell-Faraday Law (Integral form)	$\oint_{\boldsymbol{C}} \boldsymbol{E} \circ d\boldsymbol{l} = -\frac{d}{dt} \int_S \boldsymbol{B} \circ \hat{n} \, da$	(4.7)
Maxwell-Ampere Law (Integral form)	$\oint_{\boldsymbol{C}} \boldsymbol{B} \circ d\boldsymbol{l} = \mu_0 \left(I_{enc} + \varepsilon_0 \frac{d}{dt} \int_S \boldsymbol{E} \circ \hat{n} \, da \right)$	(4.8)

Table 4.2: Maxwell's equations in integral form, again for free space. These equations explain the relationship between charge and its associated electric and magnetic field but in integral form they are demonstrated relative to particular geometric areas or loops.

These equations are the basis for classical electromagnetism and have been proven both numerically and experimentally many times since their discovery in the late 19th century [4.1]. For any non-zero solution, initial conditions must be set that will define the boundary beyond which the solution may no longer be valid. Often these 'boundary conditions' involve encapsulating the electromagnetic field in an enclosed system, outside of which, the components of **E** or **B** may equal 0. Periodic boundaries restrict the space and time for electromagnetic propagation within a particular volume which can then represent systems vastly larger in scale. This 'unit cell' approach has the advantage that calculation time can be greatly reduced. Even with the many approaches that are available, analytical solutions can still be problematic and with the advent of more and more complex computational techniques and exponentially increasing computing power, numerical analysis offer a solution to electromagnetic problems that continue to increase in accuracy.

4.2.2 Numerical Methods

4.2.2.1 Finite Element Method (FEM)

The principle behind the Finite Element Method (FEM) is that large complex systems can be broken down and approximated by smaller more easily managed structures or 'elements' [4.2,4.3]. This idea has been seen in computational systems for many years, for example the digitisation of analogue signals into their digital equivalent involves the approximation of those analogue values whose accuracy can increase with CPU processing power. This is visualised below in figure 4.1:

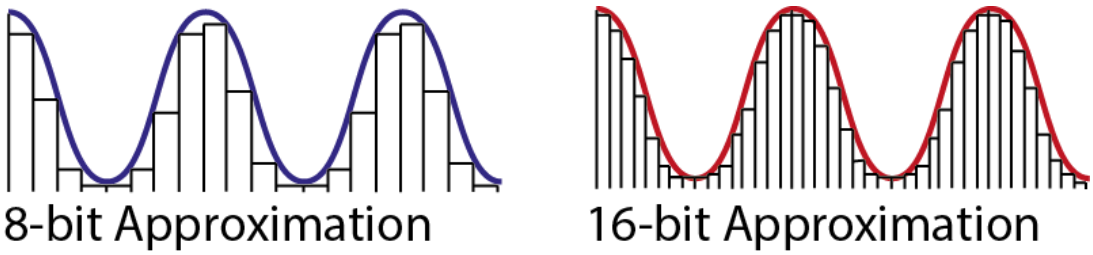

Figure 4.1: A visual representation of an analogue signal converted into its digital equivalent with higher sampling rates offering increased accuracy. Although these images are not to scale they clearly demonstrate how analogue to digital conversion works and how a higher sampling rate can offer a more accurate representation of the original signal.

Finite element analysis has the advantage that it can accurately represent complex geometry and include different physical properties, such as, thermal conductivity and permittivity in each finite element. However, the smaller the finite element and the more complex the physical parameters, the higher the accuracy of the solution but at the cost of an increased calculation time. In 3D systems the approximation takes the form of a grid or mesh where each individual unit is a separate analysis domain so that the interaction between electric and magnetic fields, geometric boundaries and particles can be analysed in a sequential manner.

There are many different numerical techniques used for solving the Maxwell equations although common to all numerical approaches is the act of separating the desired space into sub-domains, where solutions can be found more easily. To solve the full problem, all single-entity solutions are summed up in a usually large system of equations, which need to be solved in one way or another. When discussing the properties of the different methods, it is necessary to classify them where the major point of difference is the domain in which they are operating. This is either the time domain or the frequency domain. On the time domain side we have the Finite Integration Technique (FIT) and the Finite Difference Time Domain (FDTD). The frequency domain is represented by the Finite Element (FE) method, the FIT and the Method of Moments solvers. All of these methods are volume discretization methods, except for the Moment of Methods (MoM), which is a surface discretization method.

For the purposes of this research, both FDTD and FI solver based codes were used. The FDTD code used was Magic©, which solves the partial differential form of the Maxwell equations which are discretized using the central-difference approximation to the space and time partial derivatives. The Finite Integration based modeller used was CST Microwave Studio, where the FI technique solves the integral form of Maxwell's equations. The use of these two different types of solver allows for consistency checks to be carried out.

4.2.2.2 Finite Difference Time Domain (FDTD)

If the definition of a derivative is: $\partial_x f = \frac{f(x+dx)-f(x)}{dx}$ for $dx \to 0$ then the same equation can be used to represent a finite difference where $dx \nrightarrow 0$ but becomes very close to zero. This is then an approximation of the original derivative with the accuracy dependent on how close to zero dx becomes. Since dx does not = 0 the formula can be numerically solved since there would be no division by zero. A smaller value of dx will result in increased accuracy but will take longer to compute. This idea is the basis for the Finite Difference Time Domain (FDTD) method [4.4] where the time–dependent Maxwell's equations are used in their differential form and the discretisation of the entire simulation into space and time partial derivatives results in a set of finite-difference equations that can be solved sequentially from one point in space and time to the next. The electric field vector is solved in the first instance in time and in the next the magnetic field is solved. As in the FEM method, each discretised unit can have varying properties for permittivity, permeability and conductivity. Also, as the **E** and **H** fields are calculated at each point in space and time, data processing can occur at any point and the simulation can be paused and resumed should further

analysis be required. However, FDTD requires the entire simulation domain to be initially discretised with a mesh fine enough so that the smallest electromagnetic wavelength and smallest geometrical components can be accurately modelled. This can increase both simulation time and required memory.

The internal mathematical processes that occur within the FDTD calculation domain involve what is called the 'Yee Cell' formulation [4.5]. The basic principle behind this idea is that the full-grid and half-grid locations of field elements results in perfect $\nabla x \nabla f = 0$ and $\nabla . \nabla x f = 0$ in the finite difference representation. This is illustrated below in figure 4.2:

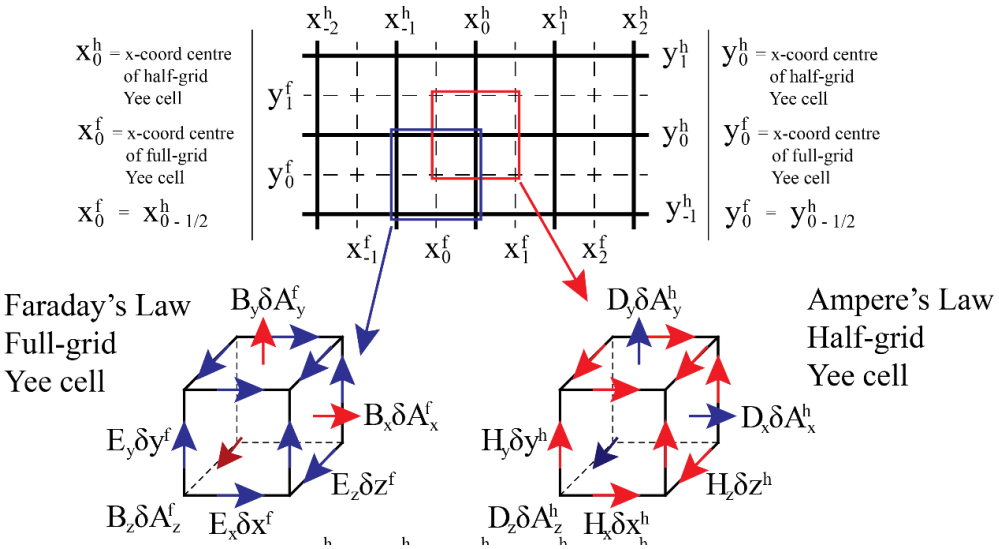

Figure 4.2: A visual representation of the 'Yee Cell' used in FDTD numerical analysis to calculate electric and magnetic field propagation as well as charged particle dynamics. The coordinate system shown is Cartesian although any coordinate system can be used although the mathematical equations change accordingly.

Vector difference equations have identical properties to vector differential equations, this results in the possibility that they can be solved numerically and be a realistic approximation of the analytical theory. The **E** and **B** fields are solved sequentially w.r.t time with the **E** field component being solved at integer time steps and the **B** field component being solved on integer plus half time steps. The actual process that is used is as follows:

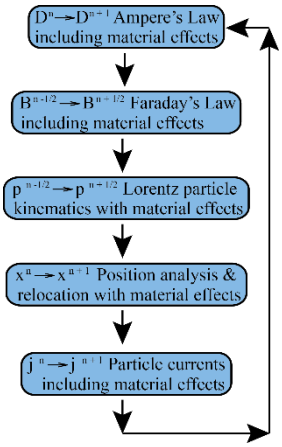

Figure 4.3: The actual process that FDTD analysis software uses to calculate the position and momentum of the charged particles and electric and magnetic fields within the simulation domain. Each section is processed for a particular Yee cell and then the simulation is moved forward by one time step. The time step itself must be small enough that the particles and fields do not move beyond the calculation space of that particular Yee cell until ready to do so.

4.2.2.3 Finite Integration Technique (FIT)

Where the FDTD method is a time domain method, the Finite Integration Technique (FIT) [4.6] is both a time and frequency domain solver that numerically solves a spatially and temporarily discretised simulation. Maxwell's equations are applied in integral form and the fields are calculated in a staggered fashion, **E** then **H** over space and time. The meshing of the simulation geometry utilises tetrahedral elements to achieve a high degree of geometrical accuracy while attempting to keep the required memory and simulation time at a minimum. In CST Microwave Studio (CST MWS) this technique utilises the Perfect Boundary Approximation (PBA) [4.7] where rather than hexahedral cube-like shapes, the surface of the structure is mapped out using a series of triangular cells, much like the way 3D objects are digitally modelled with software packages today. Once this process is complete, the internal volume is then meshed using the surface mapping as the spatial foundation, for this reason tetrahedral meshing can include curved meshing.

4.2.2.4 Particle in Cell (PiC)

The Particle in Cell (PiC) [4.8] approach uses a discretised spatial grid, similar to the previous methods but where the various physical properties of individual particles are calculated. The software is based on the Finite Difference Time Domain Technique (MAGIC) or the finite integration technique (CST Particle Studio) and the particle in cell algorithm for 3D analysis of charged particle dynamics in electromagnetic fields. It is able to self-consistently solve the full set of time dependent Maxwell's equations and the complete Lorentz force equations through the use of PIC code. The PIC method as the name suggests defines macro particles inside a physical domain discretized by a mesh. The macro particles can be viewed as a cluster for particles with the same charge mass ratio. The idea is to solve the fields in the entire physical domain with appropriate intial and boundary conditions and interpolate the force exerted by these fields on all particles that lie inside the corresponding mesh cell. Once the force on each particle is known, the equations of motion given are solved to get the new particle positions and velocities. The charge carried by each macro particle is then assigned to the cell nodes in which it lies. The above procedure is repeated in each time step. The general PIC computational cycle for the interaction between electrons and electromagnetic fields is shown in Figure 4.4.

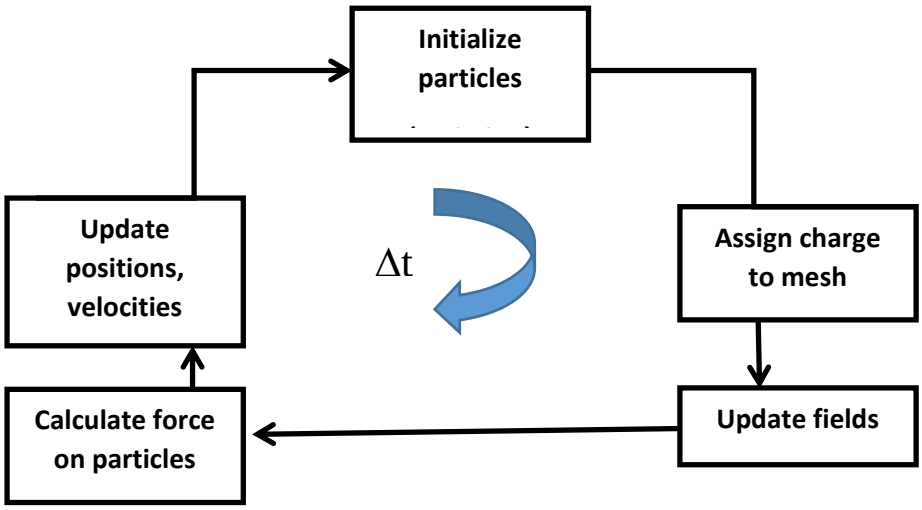

Figure 4.4. Particle in cell computational cycle

4.2.3 Numerical Software Packages

4.2.3.1 CST Microwave Studio

High frequency and charged particles can be simulated in CST Studio suite with the particle trajectory solver. The software is based on the finite integration technique (FIT) and particle in cell (PIC) algorithm for a 3D analysis of charge particle dynamics of electromangeitc fields using methods already mentioned in this chapter. CST Microwave Studio is a package that offers a number of different solvers to calculate electromagnetic propagation within the simulation domain. The transient solver offers both time domain analysis and broadband frequency domain results in the form of S-Parameters and field visualisation through active field monitors that can analyse and animate the electromagnetic field components within the system. The frequency domain solver employs the tetrahedral meshing system by default and uses CST's Perfect Boundary Approximation (PBA) as well as other techniques to analyse the various parameters within the simulation. This solver is similar to the transient solver in that it offers the same frequency domain options of S-Parameters and field component calculations. CST MWS studio is known to be memory intensive especially when using PBA, however, memory efficiency can be improved by use of 'sub-gridding' in both the transient and frequency domain solvers.

4.2.3.2 ATK Magic 3D

ATK's Magic is a charged particle and EM evolution software package that primarily uses the FDTD and PiC numerical methods. Initially it was used for magnetron design; it naturally evolved to accommodate a variety of charged particle physical problems. With increasing computer processing power Magic is now capable of analysing some very complex electromagnetic and particle problems. As with many numerical codes Magic starts from an initially defined state and simulates the physical process as it evolves in time. The electromagnetic fields are determined by solving Maxwell's equations in their time dependent form and particle dynamics are similarly defined using the Lorentz force equation taking into account the relativistic state of the particles should it be required. A number of algorithmic options are available to construct potentially any complex geometry, simulate material properties or mimic different forms of particle emission processes. Magic offers both 2D and 3D analysis.

4.3 Numerical Modelling

4.3.1 Electromagnetic Field Evolution

4.3.1.1 The Serpentine Mode Convertor

An S-Type cylindrical serpentine waveguide mode converter was used for conversion between the fundamental $TE_{1,1}$ and azimuthally symmetric $TM_{0,1}$ modes within the system leading up to the PSL cavity structure. The design is shown below in figure 4.5:

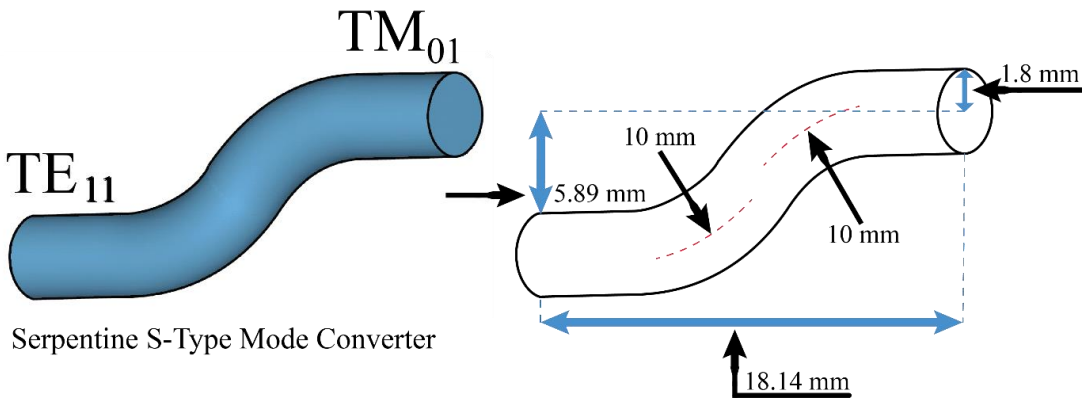

Figure 4.5: The serpentine mode converter that induces the conversion of the fundamental $TE_{1,1}$ mode into the azimuthally symmetric $TM_{0,1}$ mode for coulping into the coaxial horn. This conversion ensures that the electric field is of equal magnitude around the azimuth of the entrance to the horn so that a stable field enters the PSL cavity. The radius is chosen to accommodate maximum conversion effiency with single mode operation at a frequency of approximately 80 to 90 GHz.

The radius of curvature of the centre line of the waveguide is 10 mm and the entire structure rotates anti-clockwise by 45° and then rotates back by 45° in the opposing direction. The inner radius of the waveguide itself is 1.8 mm which was determined for W-band from the following relationship given below in table 4.3:

TE_{11}	$f_{cut-off}(GHz)\ x\ a_1(cm) = 11.4743$	(4.9)
TM_{01}	$f_{cut-off}(GHz)\ x\ a_1(cm) = 18.2824$	(4.10)
	$\frac{18.2824}{80(GHz)} \leq a_1(cm) \leq \frac{18.2824}{100(GHz)}$	(4.11)
	$0.229 \leq a_1(cm) \leq 0.182$	(4.12)

Table 4.3: The equations that determine the inner radius of the S-Type serpentine mode convertor. It can be seen that the value to be used for the radius is dependent on the mode in question and the cut-off frequency for that mode.

Two serpentine mode converters were designed and constructed one operating in the frequency range of ~80 to 100 GHz and a smaller dimensioned one operating in the 140 GHz to 220 GHz frequency range. For the 80 GHz to 100 GHz serpentine mode converter an inner radius of 1.8 mm was selected. Numerical simulation of serpentine mode converter of the parameters given above using CST MWS enabled the signal transmission as a function of frequency to be calculated, figure 4.6.

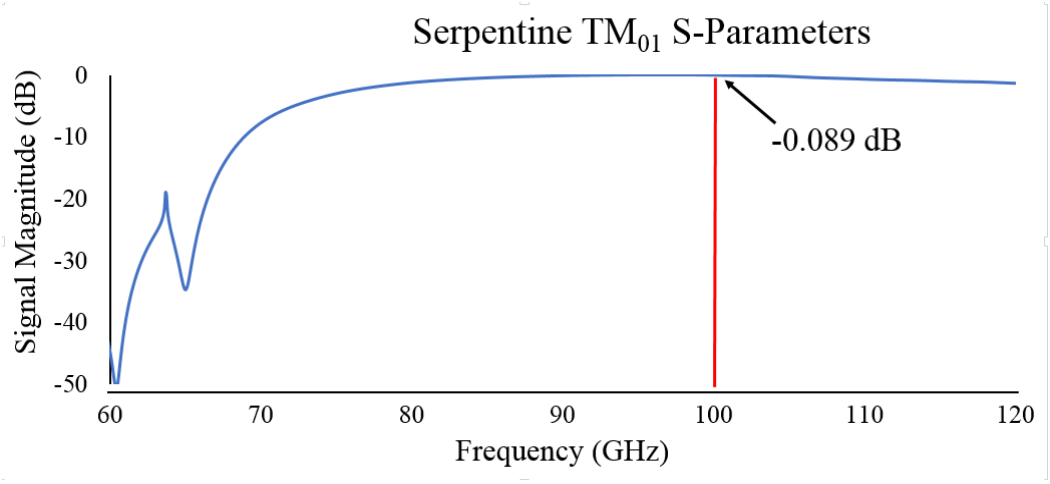

Figure 4.6: The S-parameters for the serpentine S-Type mode converter. An output signal of -0.089 dB represents a loss of only about 1 %, this means that 99 % of the input signal reaches the output port in the form of the $TM_{0,1}$ mode. Manufacturing tolerances of less than ± 50 microns would allow for further conversion of the last 1 % but for the manufacture of the system there will always be loss, the ideal system seen in CST MWS would not be replicated in the actual experiemnt but a 99 % conversion ratio is sufficent for the cold test measurements to demonstarte the PSL cavity eigenmode formation process.

With approximately 99 % conversion at the output port from the input $TE_{1,1}$ mode to the $TM_{0,1}$ mode at 90 GHz, the serpentine waveguide distributes the electric field such that it can be coupled into the coaxial horn in an azimuthally symmetric manner. Figure 4.6 shows that the input wave begins to experience a 110dB drop in transmission at ~70 GHz and reaches a maxima of conversion at around 94 GHz. The actual mode conversion can be visualised by CST MWS. Below in figure 4.7, the E_z component can be seen morphing from its original $TE_{1,1}$ form into the $TM_{0,1}$ form at the output, the redistribution of the field from (1) to (2) occurs due to modification of the E-field vector as it comes into contact with the inner wall of the waveguide structure.

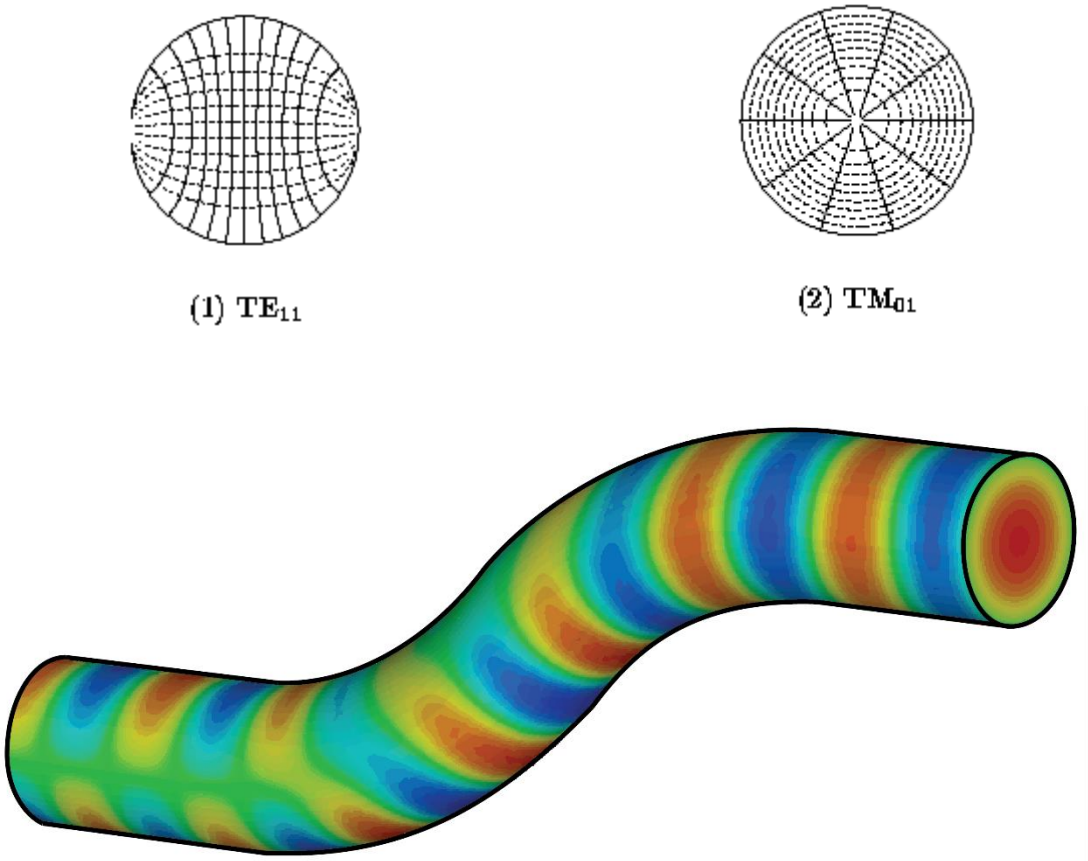

Figure 4.7: CST interpretation of the z component of the electric field vector as it moves through the waveguide. Conversion begins as soon as there is contact with the axially evolving inner wall and the electric field redistributes itself into the next available mode on the Bessel root ladder.

The $TE_{1,1}$ mode is the fundamental mode for a circular waveguide and can be seen at the left port (1) with the $TM_{0,1}$ mode seen at the right (2). The field has now been optimised for coupling into the coaxial horn.

4.4 Millimetre Wave Measurements

Computational analysis allows us to visualise physical outcomes to theoretical simulations before going ahead and building the system. As computer power increases exponentially the accuracy and complexity of the analysis also experiences a corresponding increase, culminating in results that can be very close to what is seen in experiments. It should not be said however that a numerical result should replace its corresponding experimental verification, in actual fact it serves only as a guide to creating the experiment. With this in mind an experimental analysis was conducted to investigate electromagnetic wave formation in the PSL structure. Two serpentine mode converters one operating in W-band to measure the transmission through copper 2D PSLs and the other operating in G-band to measure the propagation of millimetre waves through a silver 2D PSL were designed and constructed.

4.4.1 Component Design and Manufacturing

4.4.1.1 Autodesk Inventor Visualisation of the Physical Model

Since the process of creating a 3D interpretation of the manufactured 2D PSL differs in CST MWS or Magic 3D when compared to an actual component to be constructed such as CST MWS concentrating more on the vacuum space within the structure rather than the structure itself, the CAD package Autodesk Inventor 2015 was used to design a manufacturing model that could be fabricated. When using this program it is beneficial to concentrate more on how each component will join to the next as well as the minimum and maximum manufacturing limits rather than how the wave will travel through the structure as modelled using CST MWS. The full aluminium mode conversion system was built, separately from the PSLs, as two separate pieces that were split in the x-y plane assuming that the wave propagates in z.

Previous PSL designs at lower frequencies [4.10], such as Ka band allowed the manufacture of the each isolated piece to occur separately and then all pieces were joined together to form the whole. This was not ideal at W band and G-band since at higher frequencies, the join between two parts could become a point of internal reflection or result in increased losses that could adversely affect system performance. For this reason the full mode conversion system (minus the PSL itself) was designed as a single piece with respect to the longitudinal propagation of the wave. An example of which is shown below in figure 4.8:

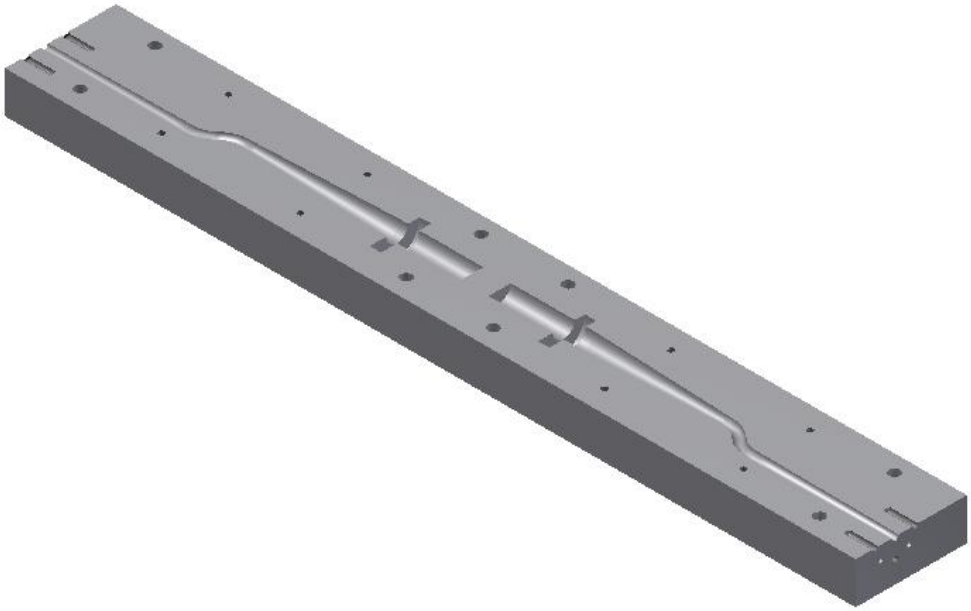

Figure 4.8: An example of an Autodesk Inventor drawing of a mode conversion system showing two halves of the serpentine mode converter. This one is slightly different from the one used in the cold test experiment in that the last taper is replaced by a straight cylindrical section.

This drawing was then saved in a 3D CAD format such as an IGES or STL file of high resolution and using the CNC milling software, OneCNC to plot the tool paths; the milling script was created that allowed the automated HAAS TM-1CE milling machine to create the part. This process is seen below in figure 4.9:

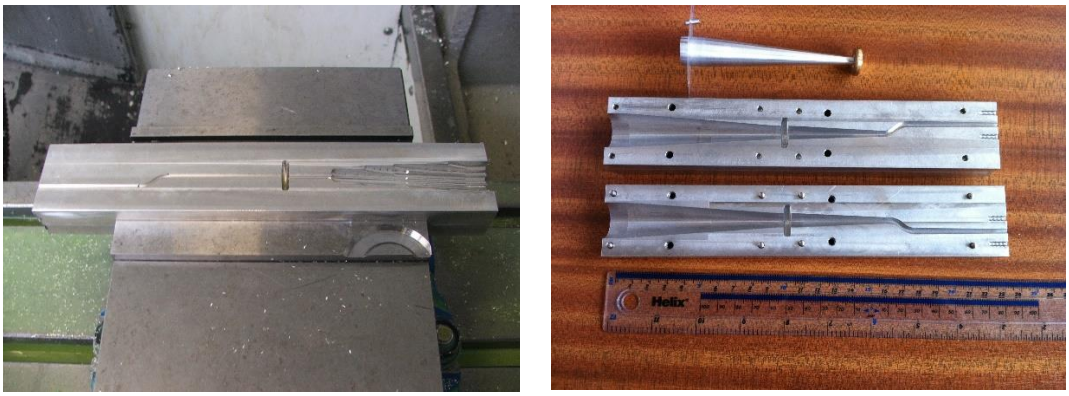

Figure 4.9: The fabrication process for the mode conversion system with the image on the left showing the structure during the milling process. The image on the right shows the complete setup with the two halves of the system and the inner conductor. The brass component on the inner rod connects to the inner conductor via a Mylar window, holding in place the inner conductor of the co-axial horn.

A similar serpentine mode converter and taper conical horn in the 140 GHz to 220 GHz frequency range was designed and constructed and used to measure the millmetre wave transmission of the silver 2D periodic surface lattice.

4.4.1.3 High Resolution Synthetic Polymer 3D Printing With Silver Injection Moulding

The PSL to be used in the 'hot' experiment was constructed using a high resolution 3D printing process that included the injection moulding of a silver chromium alloy. 3D printing, originally developed in the mid 1980's [4.11], offers the possibility of producing objects that have resolutions on the 10's of microns scale. 3D printing is an additive process by which consecutive layers in the x-z plane are deposited sequentially in the +ve y direction (upwards), resulting in a high resolution (approximately ± 15 microns) mould that is then used in a casting process that ultimately results in the silver alloy 2D PSL, seen in the image below. The printing process follows the pattern in a given CAD input file, usually in the STL (Stereolithograph) file format where every face is built from a series of interconnected triangles represented by 3 separate 32-bit floating-point Cartesian coordinates. More often now the new X3D file format is implemented which incorporates the XML programming interface and further enhancements over its predecessors [4.12]. The design is sliced into digital layers so that that a curve is 'approximated' by many square sided slices, with the thickness of each layer representing the resolution of that particular 3D printing process. Figure 4.10 demonstrates the result of the 3D printing process with a complete 2D PSL made from a silver alloy of Ag = 92.5 % and Cr = 7.5 %.

Figure 4.10: The finished Silver PSL, created using a high resolution 3D printing process that was quicker and cheaper than the normal milling on a positive aluminium former followed by a copper electro-deposition process. Although the injection moulding process results in a manufacturing tolerance of (± 125 microns) more than double that of the milling process (± 50 microns) the results seen in the next section prove that the process is effective for use as a PSL at W-band frequencies.

4.4.2 Surface field excitation by incident waves in copper 2D PSLs

4.4.2.1 Investigation of corrugation amplitude on wave coupling

A larger diameter (20 mm) 2D PSL structure of period 3 mm was studied for interaction with a high voltage up to 300 kV electron beam but it was later decided for the first experiments to use an electron beam with a lower energy of ~80 keV. It was decided to reduce the electron beam accelerating voltage from 300 kV to 80 kV for the first expermients as it enabled a single stacked inverting cable Blumlein generator to be used as compared to a more complex and hence higher risk doubled stacked cable Blumlein high voltage generator. Reducing the electron accelerating potential from 300kV to 80kV required the lattice period to be adjusted from 3 mm to 1.6 mm as detailed in reference [3.15] and section 4.4.4. Nevertheless the larger diameter 20 mm 2D PSL structure was studied using the vector network analyser to investigate the coupling between the surface and volume field as a function of corrugation amplitude.

Several cylindrical 2D Periodic Surface Lattices (PSL) as shown in figure 4.11 were created by machining sinusoidal radial variations onto an aluminium former. Copper was electroformed onto the surface of the formers and once machined to the required radius the aluminium was removed by dissolving it in a strong alkaline solution. This leaves the copper structure with the perturbations on the inside wall

$$r = r_0 + \Delta r cos(\boldsymbol{k}_z z)\cos(m\varphi) \tag{4.13}$$

here, r_0 = 10 mm is the unperturbed radius of the cylindrical waveguide, Δr is the corrugation amplitude, $\boldsymbol{k}_z = 2\pi/d_z$, d_z = 3 mm is the period of the perturbations in the z - direction and m =20 is the number of azimuthal variations. Individual aluminium formers of varying perturbation amplitude [Δr = 0.25 mm; 0.3 mm; 0.5 mm; 0.8 mm] were constructed, in order to investigate the effect of the amplitude of the perturbations on the coupling of the surface and volume fields.

Figure 4.11 Photograph of the 2D PSL machined on the inner surface of a copper cylinder and having: mean radius r_0=1 cm; amplitude of corrugations Δr =0.25, 0.3, 0.5, 0.6, 0.8 mm ; number of azimuthal periods 20 and longitudinal period 3 mm.

In figure 4.11 the photograph of the structure with Δr =0.5 mm is shown. All lattices were machined to have 7 full longitudinal periods (d_z) each with a 5 mm section of smooth cylindrical waveguide before and after the corrugation to ensure good connection between the lattice and the experimental set up.. The large diameter of the structure allows a high current (low current density) electron beam transportation, while avoiding RF breakdown disrupting the beam while preventing parasitic mode generation and for long pulse or high repetiion rate operation the large surface area enables the structure to be efficiently cooled preventing overheating. To study such a structure using a wave-beam consisting of a single mode, an apparatus described in section 4.4.1.1 made from a single block of aluminium was designed and constructed. It was developed to excite surface fields on the inner surface of the cylindrical periodic structure. This configuration allows irradiation of the cylindrical lattice at a range of angles between the wave vector and the axis of the cylinder from approximately 90 degrees (a nearly cut-off wave) to approximately zero degrees (a propagating wave having transverse wavenumber much smaller than the longitudinal wavenumber, i.e. a 'near-grazing' wave).

Numerical modelling of the electromagnetic field evolution and eigenmode excitation has been conducted using the 3D code MAGIC to improve understanding of the experimental measurements. The 3D modelling of such structures is a challenge due to the large variation of the geometrical parameters (dimensions) and the oversized nature of the lattice structure. To optimise the use of the computer memory and the computer performance a square wave approximation was applied in the case of the low contrast model, while a sinusoidal corrugation has been used to simulate the high contrast lattices. To compare the profiles of the lattices in figures a and b the *r-z* cross-sections of the high and low contrast structures (left and right columns respectively) are shown. The inserts in these figures show the typical contour plots of the azimuthal magnetic component B_φ of the eigenfield,

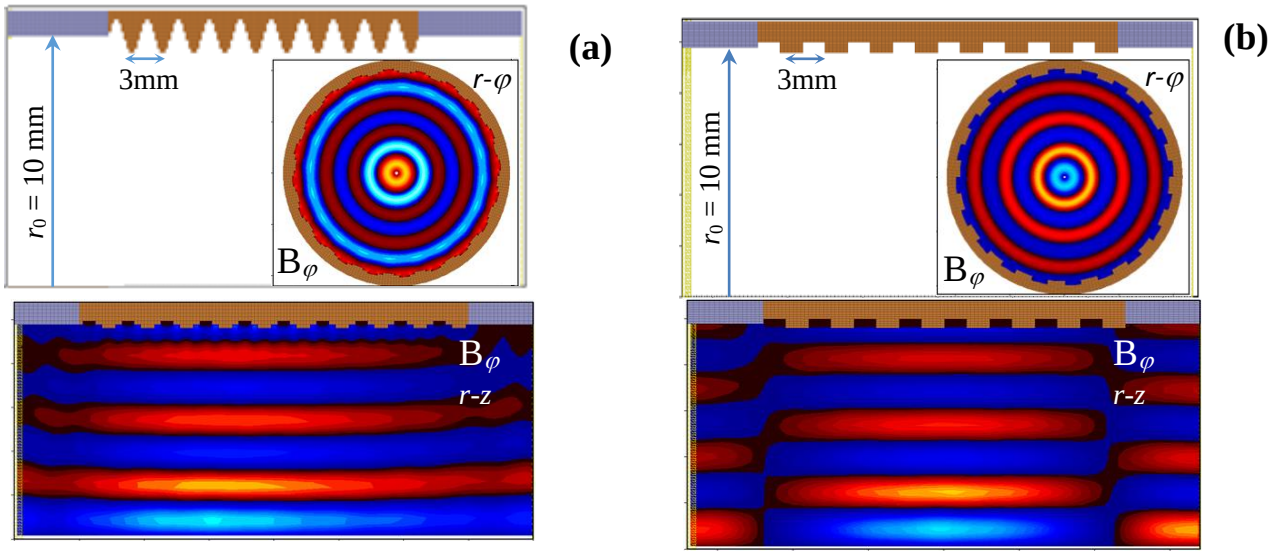

Figure 4.12 Numerical models of the (a) high and (b) low contrast 2D PSLs showing r-z cross-sections of the structures and contour plots of the eigenmodes' azimuthal magnetic field component excited, in r-φ (insert to the first figure) and r-z (second figure) cross-sections.

The contour plots shown in figures 4.12 (a) and (b) were observed by launching an amplitude-modulated microwave pulse in the TM_{01} mode, having a flat frequency spectrum in the frequency range from 80 GHz to 110 GHz. The lattice response spectra were studied using wave beams formed by TEM and TM_{01} modes and measuring the decaying field spectra after the electromagnetic pulse fully propagated through the structure. Later the spectra of eigenmodes excited inside high/low contrast structures (left/right rows) using TEM (solid line) and TM_{01} (dotted line) modes with the measured spectra were compared. As will be discussed below by changing the radial index of the waveguide modes which form the input pulse the radiation angle with respect to the lattice can be effectively controlled.

To measure the properties of the lattice the electromagnetic wave was formed using the mode converter described in section 4.4.1 where the fundamental $TE_{1,1}$ mode of a cylindrical waveguide into either the $TM_{0,1}$ mode of a cylindrical waveguide, or the TEM mode of a coaxial waveguide. The wave was then launched via either a co-axial line termination plane launcher (such that the lattice is irradiated at all possible angles simultaneously) or via a directly irradiating structure with the $TM_{0,1}$ wave-beam (oblique irradiation of the lattice at a small grazing angle). The termination of the coaxial line mediates the excitation of the azimuthally symmetric TM_{on} modes with a finite set of transverse wavenumbers (defined by the radial index n). At the maximum value of n ($n=N$), the near cut-off wave is observed and the structure is similar to that shown in figures 4.12 (a) and (b). The measurements of the PSLs were conducted in the far field zone (27 cm from the output aperture) and millimeter-wave absorbent material was used to reduce parasitic reflections. A millimeter-wave Anritsu Vector Network Analyser was used for the measurements. In the first set of experiments the structures were excited using a co-axial line termination plane launcher. The results of the measurements are shown in figures 4.13 (a) and (b). As expected the PSL eigenmode excitation was observed in both cases i.e. for both the high and the low contrast PSLs. In figures 4.13 (a) the comparison of the results is shown for the low contrast lattices (corrugation amplitudes of 0.25 mm, 0.3 mm and 0.5 mm) excited by the co-axial launcher.

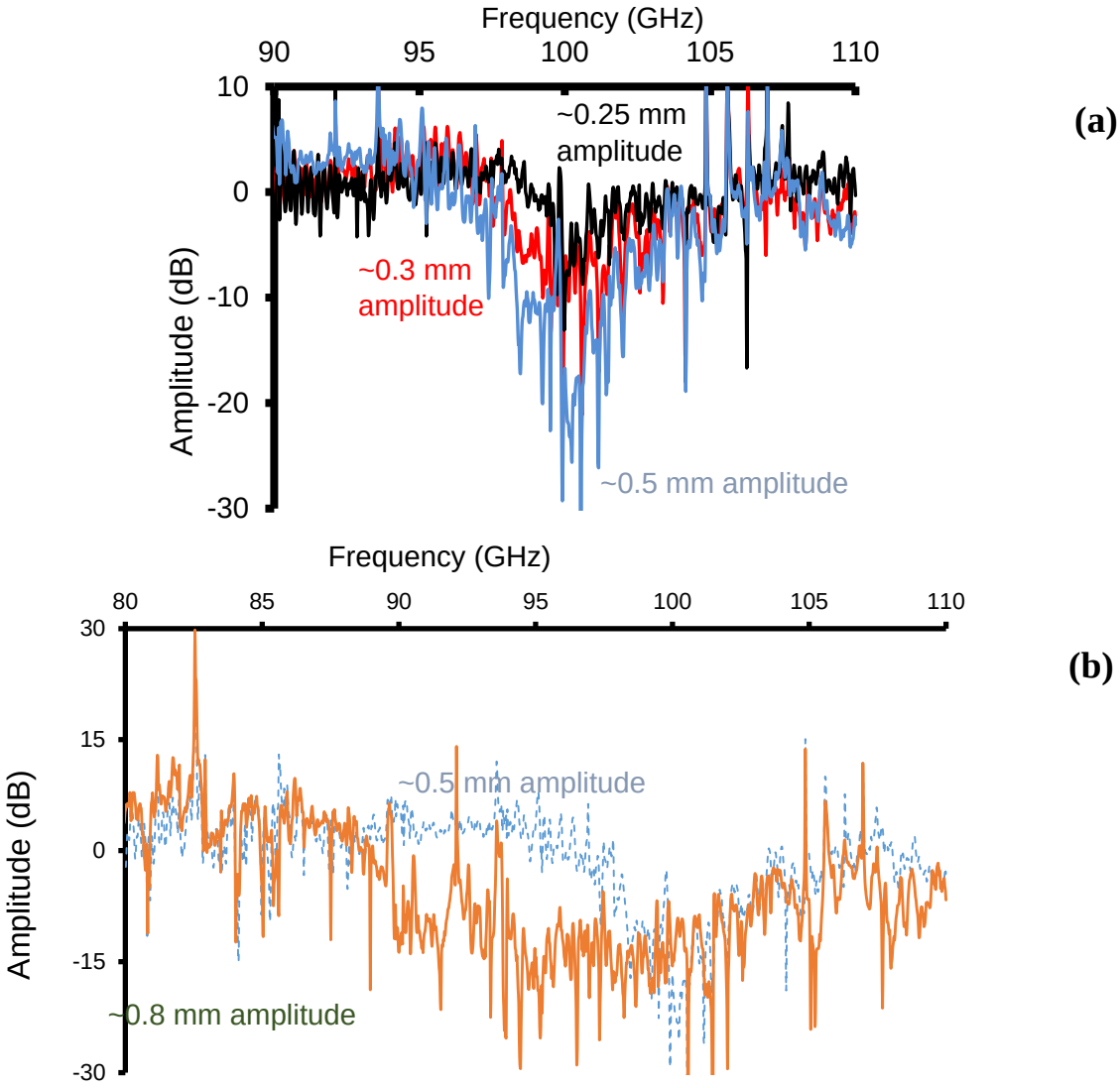

Figure 4.13 Results of measurements of the electromagnetic signal transmission versus frequency (2D PSL spectral response) through **(a)** low (amplitude of corrugations 0.25mm, 0.3mm and 0.5mm) and **(b)** high (amplitude of corrugation 0.8mm) contrast structures, if the structure is radiated using co-axial launcher based on terminated co-axial line. Scattering of near cut-off (normal incidence to the surface) wave on the lattice takes place. In figure (b) the spectral responses of the high (solid line) and the low (broken line) contrast structures are also compared.

It is clear that the responses observed are similar and the dependence on the amplitude of the corrugation is as expected i.e. with increase of the amplitude of the corrugation the amplitude and the width of the minima measured grows but the centers are located at the same frequency, indicating the coupling of the same modes. In this case the eigenmode having 8 radial variations (formed with the partial $TM_{0,8}$ mode) and having minima around 100 GHz was excited. However, when the PSL with 0.8 mm corrugation amplitude was measured a different behavior was observed (4.13(b)). The minimum of the transmission became very broad while its amplitude stayed the same, or became smaller. Also it looks like few modes are coupled and the minima are merged together resulting in a "red-shift" of the center of the gap. Let us note that far from the resonance frequencies the measurements coincide well at high and low frequencies. However when the co-axial launcher was substituted with the direct launcher the excitation of only the high-contrast structure was observed. In figure 4.14, the results of the measurements of the structures with 0.5 mm and 0.8 mm corrugation amplitude are shown.

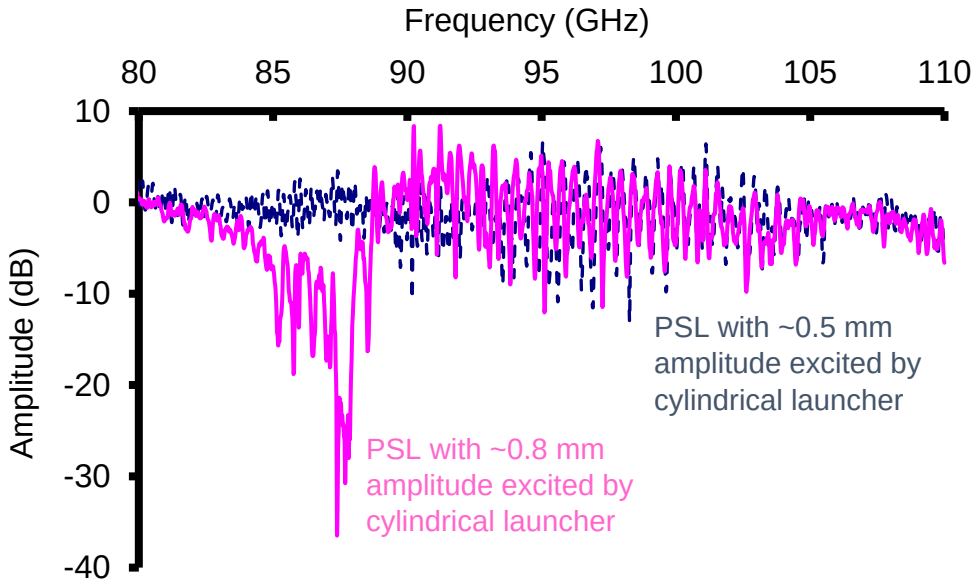

Figure 4.14 Results of measurements of the electromagnetic signal transmissions versus frequency (2D PSL spectral response) through low (broken line) and high (solid line) contrast 2D PSL. The structures are irradiated by an oblique (near-grazing) incident wave-beam formed by the TM_{01} mode of the cylindrical waveguide.

To observe the data the PSLs were excited using a TM_{01} wave (figure 4.12). It is interesting to note that no excitation of the low contrast structure was observed in spite of the indications from the numerical predictions. This can be explained by low coupling (which is proportional to the amplitude of the corrugation) between the lattice and the fields and relatively high losses. Comparing with the previous data we see that the position of the minima observed for the high contrast lattice is associated with the eigenmode having 7 radial variations (formed with the partial TM_{07} mode) and having

downshifted minima around 85 GHz. In figure 4.15 a comparison of the spectra observed from numerical modelling and experimental measurements are shown. The minima in the measured spectra correspond to excitation of structure eigenmodes which are composed from surface fields and near cut-off fields i.e. the EM energy remains and dissipates inside the lattice. The good agreement can be clearly seen from the figures, while small deviations can be attributed to the tolerances in the lattice manufacturing as a variation of the lattice mean radius Δr_0 ~0.1 mm will result in the measured frequency shift.

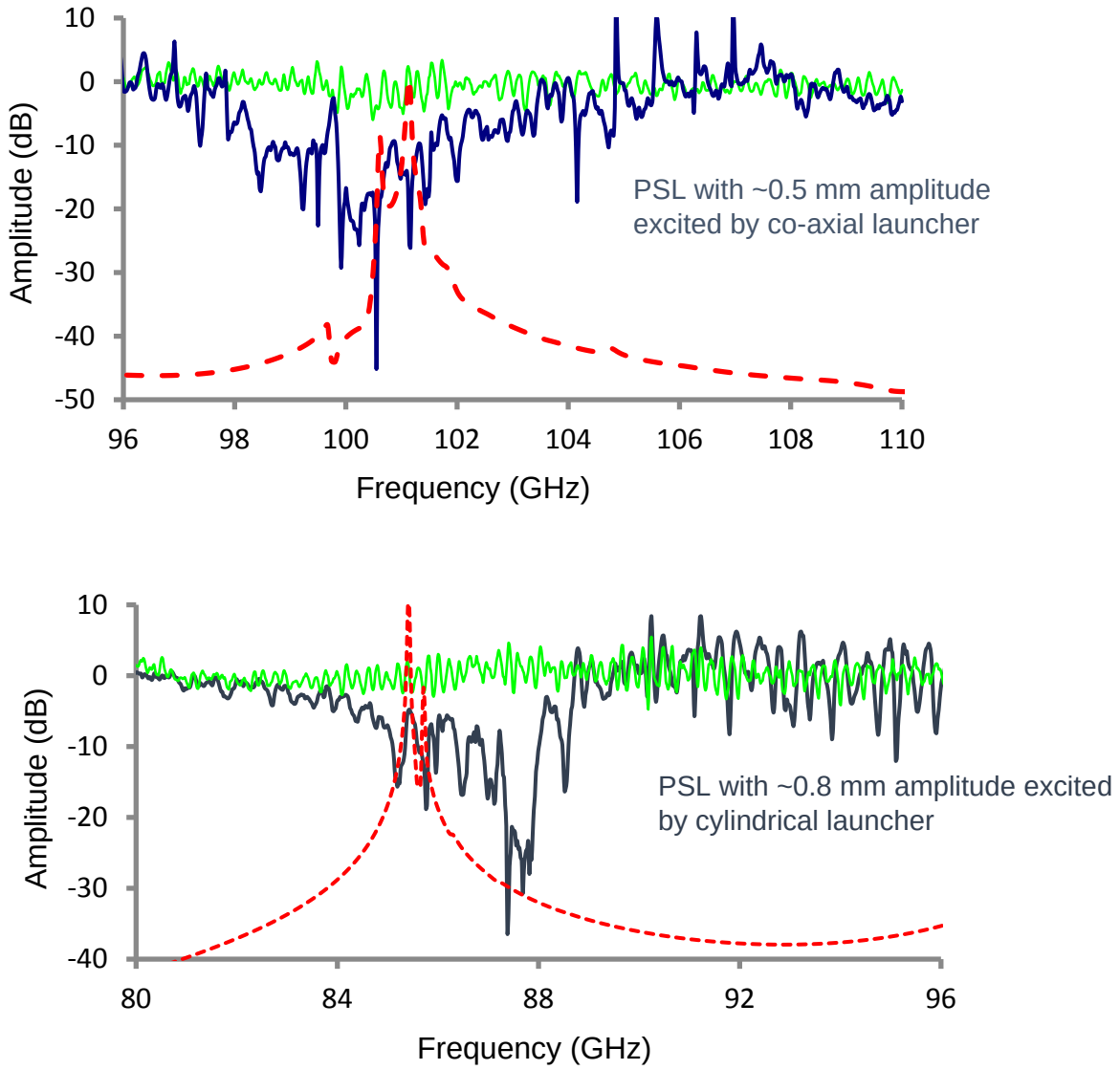

Figure 4.15. Comparison of the experimental data (solid bold line) showing spectral gaps in the signal transmissions and theoretical predictions (dashed line) of 2D PSLs' eigenmodes excitation for (a) low and (b) high contrast 2D PSLs. In both figures the thin lines show the measured lattice responses if the amplitude of the corrugations is zero.

4.4.2.2 Far – field Description

At the aperture of a section of cylindrical waveguide, the electric field of the escaping radiation expands into free space. At a sufficient distance from the aperture, the field behaves in a particular manner, according to the mode in which it is polarised. Once in this 'far – field' regime, the angular distribution of the field no longer changes as a function of distance. To ensure radiation has reached its far - field limit, the Fraunhofer distance, R_{Fraun}, can be calculated. This is the minimum distance required to be within the far - field regime, and is given by equation (4.14). Here, D is the diameter of the aperture, and λ is the free-space wavelength of the radiation.

$$R_{Fraun} = \frac{2D^2}{\lambda} \tag{4.14}$$

Figure 4.16 below depicts important parameters within the far - field regime. Here, the x and y axes are aligned with the plane of the output aperture, while the measurement point P is located a distance R from the aperture, and makes an angle of θ with respect to the z-axis, and φ with respect to the x-axis.

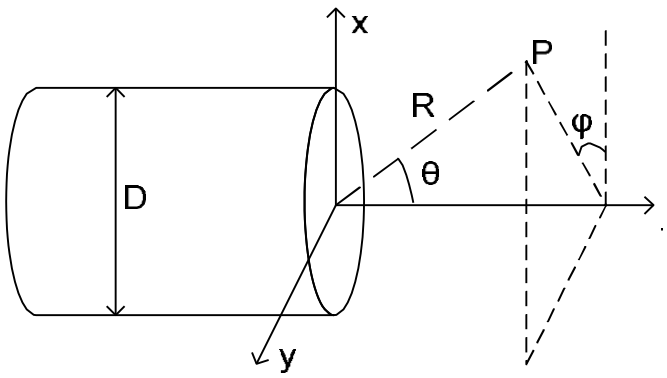

Figure 4.16 – Far - field position measured from the centre of a cylindrical waveguide.

Working from Huygen's principle and in the general case of emitted radiation from an open – ended waveguide, the E_θ and E_φ components detected at position P can be given by equations (4.15) and (4.16), respectively.

$$E_\theta = jk\frac{\exp(-jkr)}{2\pi r}c_\theta f_y(\theta,\phi)sin\phi \tag{4.15}$$

$$E_\phi = jk\frac{\exp(-jkr)}{2\pi r}c_\theta f_y(\theta,\phi)cos\phi \tag{4.16}$$

Where $f_y(\theta,\phi)$ is the Fourier transform of the E_y component at the aperture and $c_\theta = \frac{1+cos\theta}{2}$ is the 'obliquity factor'.

4.4.3 Silver & Copper 2D PSL Results

Upon exiting the output aperture of the system, the electromagnetic field diverges to form a distribution determined by its wavevector. If the wavevector of the VF is parallel to the z-axis upon entering the interaction region, the wavevector of the cavity eigenmode deviates away from the z-axis due to diffraction at the perturbations and at the output, resulting in a transverse component that is not negligible. The resulting far-field pattern, measured at a distance of $2D^2/\lambda$ from the exit aperture, where D is the aperture diameter, takes the following form:

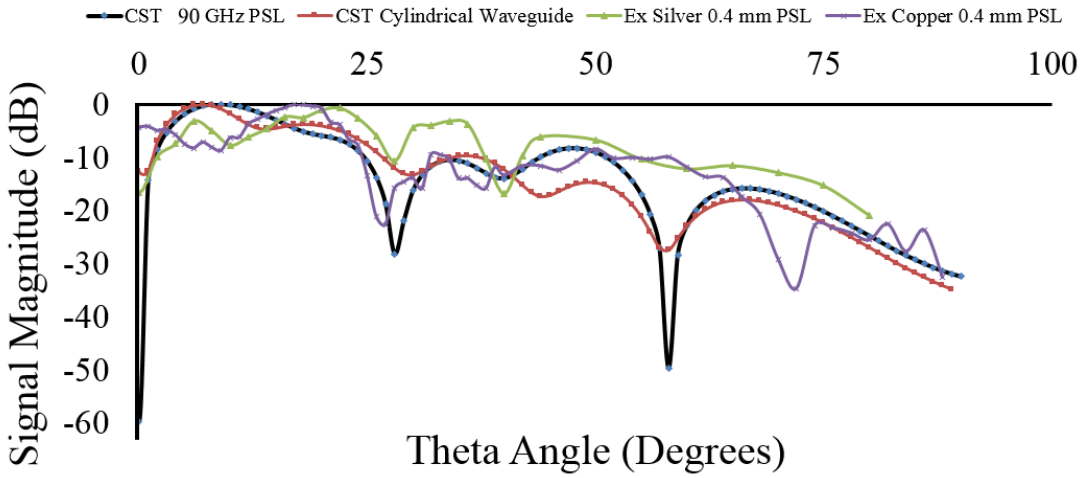

Figure 4.17: The farfield mode scan of the W-band PSL with the 0.4 mm perturbations (0.4 mm represents the perturbation amplitude as opposed to the peak to peak distance which would be 0.8mm) . The numerical and experimental results approximately agree up to around 50°, there is a little deviation in the experimental results which will be due to noise and losses in the experimental setup.

The far-field mode pattern seen in figure 4.17 above demonstrates the 'directivity' of the field as it moves beyond the exit aperture. The formation of frequency dependent 'side lobes' occurs due to the diffraction of the wavevector at the perturbations and the output with the signal magnitude being directly proportional to the field superposition at a particular distance from the output. There is a central singularity at theta and phi = 0, i.e. on the z-axis because of the diffraction that the wavevector experiences. The idea that the mode pattern should be symmetrical about zero holds only on the assumption that the internal structural dimensions of the PSL are consistent at all points within the PSL. This is easily achieved in numerical simulations but difficult in experiments where manufacturing tolerances of +/- 50 microns can have a significant and detrimental effect on the observed mode pattern. This idea then explains the difference in signal magnitude relative to scan angle for opposing sides of $\theta = 0$ °.

This data can also be displayed in a 360 º radar plot which allows, by imagining the device with its exit aperture positioned at the centre point of the plot, the visualisation of a more practical view of the electric field distribution as it exits the output aperture. This is shown below in figure 4.18:

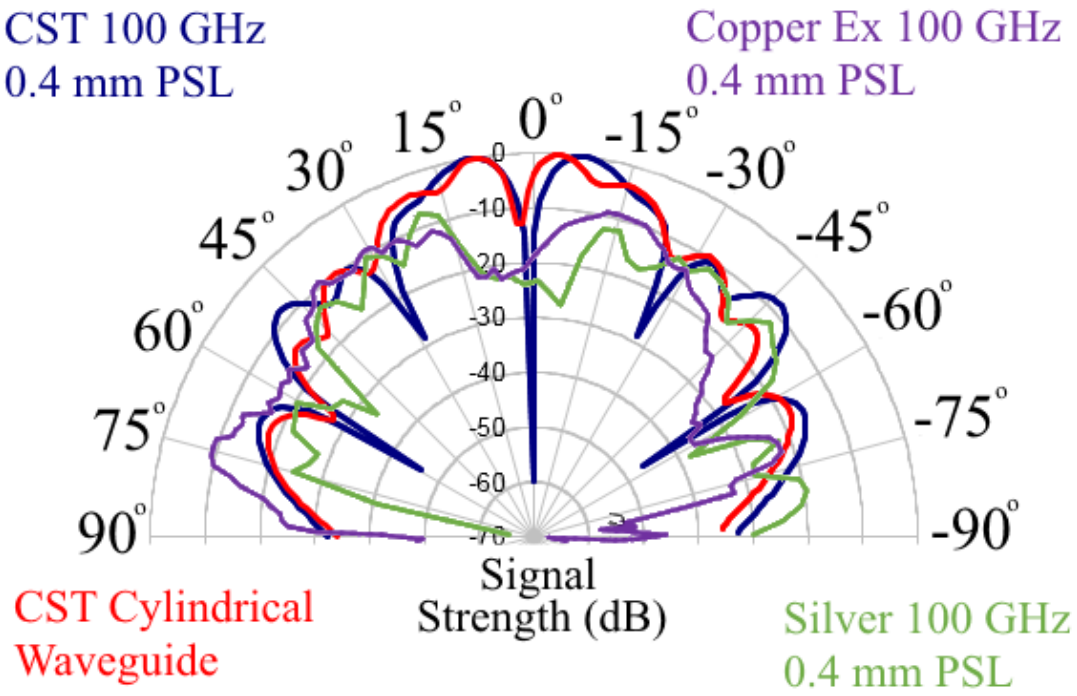

Figure 4.18: The electric field distribution at the farfield position as seen both numerically (red and blue lines) and experimentally (green and purple lines). Since the experimental data suffers from reflections, losses, measurement errors and PSL structural inequalities it is to be expected that it will not be exactly what CST predicts. The important points are the singularity at 0 degrees and the magnitude and position of the side lobes.

5

Numerical Analysis and Optimisation

5.1 From 1D to 2D

The question has been asked: “What advantage does the 2D PSL structure give over the 1D structure?” The answer is of course mode control. For both structures the operating mode is dependent on the unperturbed inner radius of the interaction region and by selecting a particular value then a specific mode will be ‘near cut-off’ and a cavity will form during the interaction. However for a 1D structure the perturbation which does not vary azimuthally acts in a way similar to a decrease in the inner radius and serves to cut-off the desired mode at the high frequency where you want the structure to operate. For a 2D structure the variation around the azimuth means that the desired mode is not cut-off and can exist at all points within the interaction region. What this means for the interaction is that for a 1D structure the cavity will either not form at all or will form a lower order mode at a lower frequency as compared to the mode formed in a 2D structure. This is visualised below from two separate Magic simulations that have the same physical properties of electron beam and PSL physical dimensions but with one and only one distinct difference. The image on the left is a 2D structure and the image on the right is a 1D structure.

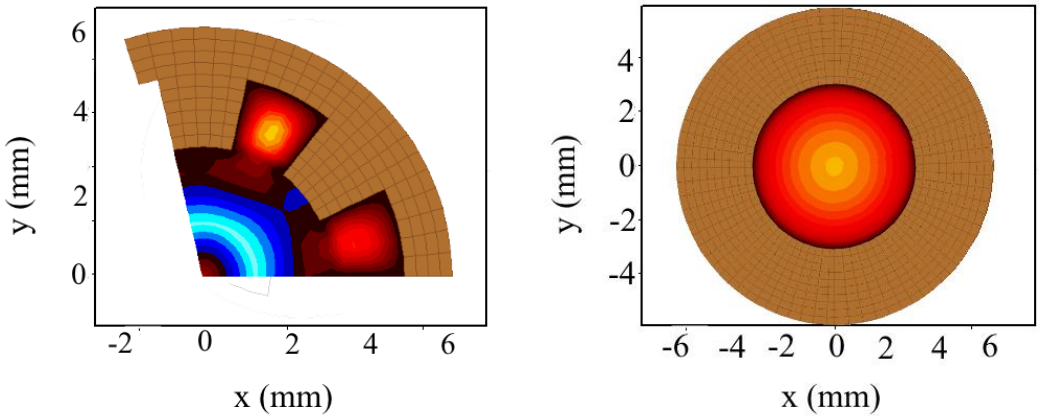

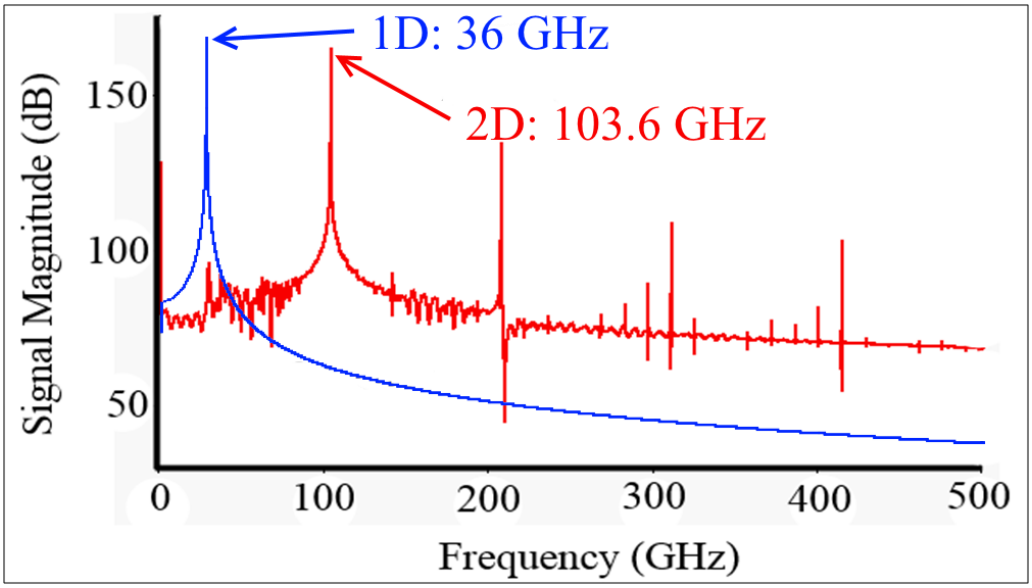

Figure 5.1: The image on the top left is the E_z mode pattern for the 2D Structure showing the formation of the $TM_{0,3}$ mode. The image on the top right is the E_z pattern for the 1D structure showing the formation of a $TM_{0,1}$ mode and the image on the bottom shows the operating frequencies of both devices.

It can be seen from the simulation results shown in the images above, in figure 5.1, that the beam-wave interaction seen in both systems operate at different frequencies utilising different operating modes. The 2D structure operates with a higher order $TM_{0,3}$ mode due to coupling with the transverse surface wave at a frequency of 103.6 GHz. Whereas the 1D structure preferred mode of operation is with the $TM_{0,1}$ mode at a frequency of 36 GHz. This demonstrates that although a successful beam-wave interaction can occur with the 1D structure we have far more control with the 2D structure with the ability to operate with a higher order mode at a higher frequency as compared to a 1D structure..

To increase the power available to a beam wave interaction either the energy of the beam may be increased (this is often undesirable because of the voltages involved) or the current flowing in the beam. Electron beam density cannot be arbitrarily increased however as at some point the internal space charge forces on the beam, and the influence of the surrounding environment contrive to impose limits on the beam stability and propagation. In addition, the increased RF power density can result in breakdown and the effect known as pulse shortening. To avoid these issues, it is necessary to consider the possibility of increasing the transverse size of the beam and therefore, in general, of the microwave circuit itself, if a further increase of power is to be achieved. Unfortunately, increasing the transverse size of the microwave circuit beyond a ratio of $D/\lambda \sim 2$ to 4 (where D is the transverse size of the microwave circuit and λ is the radiation wavelength) results in a drop in efficiency and spectral purity as the source loses mode selectivity. To tackle this problem, the use of a 2D periodic surface lattice results in the coupling of 4 waves (a forward and backward longitudinal wave and a clockwise and anti-clockwise azimuthal wave) to control the transverse modes which can interact with the electron beam in an oversized interaction space. This enables high efficiency even when the transverse size of the electron beam exceeds the radiation wavelength by more than 2 to 3 orders of magnitude.

5.2 Cathode Design in ATK Magic 3D & CST Microwave Studio

5.2.1 Explosive Emission

Once the physical parameters of the solenoid are known, the cathode can then be designed around these values. Having selected the 1.8 T water-cooled solenoid due to the availability of all necessary components, the critical parameter of the solenoid Inner Diameter (ID) was set at 18 mm.

To minimise the transverse velocity of the electrons from the cathode numerical studies were carried out to investigate if it would be possible to insert the cathode in the strong axial magnetic field region of the solenoid. To achieve emersion of the cathode in the strong axial magnetic field region an anode can of outer diameter of 14 mm needed to be used. The cathode dimensions were then calculated to fit within the 12 mm inner diameter of the anode can, these can be seen in table 5.1 below:

Cathode Radius	2.0 mm
Cathode – Anode Gap	8.0 mm
Emitter Thickness	0.25 mm
Emitter Radii	1.4 mm – 1.9 mm
Anode Outer Radius	6.95 mm
Anode Inner Radius	5.98 mm
Anode Length	4.49 mm

Table 5.1: The physical parameters of the cathode design implementing explosive emission.

Table 5.1 above displays the various physical parameters that were used to create the simulation geometry in Magic 3D. It should be noted that once the components are manufactured for use in the electron beam experiment they cannot be changed without remaking the part, however, this fact does not include the cathode – anode gap which can be changed in order to investigate the optimum anode cathode gap separation to optimise beam parameters. The following images present the final result of the Magic 3D simulations and the explosive emission cathode design:

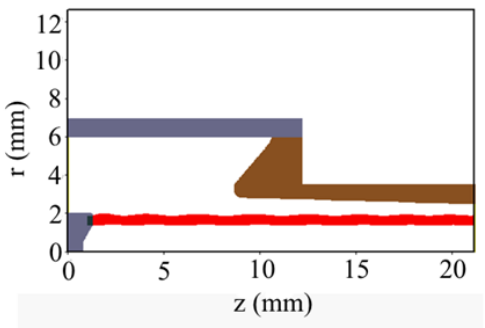

Figure 5.2: The beam trajectory for the high field cathode simulated in Magic 3D with a beam thickness of 0.5 mm, a 1.8 T magnetic 'guide' field, 100 kV accelerating voltage resulting in an output current of approximately 290 A after a 'rise time' of 600 ps.

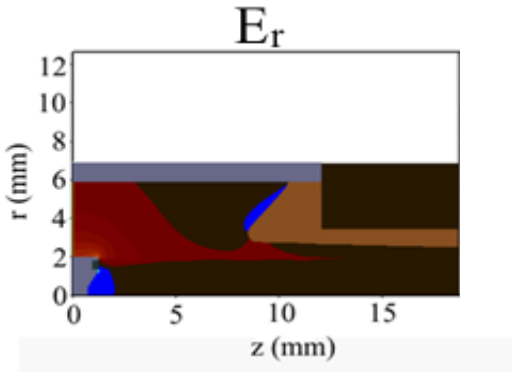

Figure 5.3: The E_{rho} component of the electric field within the cathode – anode region displaying a maximum approximately 100 MVm^{-1} at the upper tip of the cathode surface.

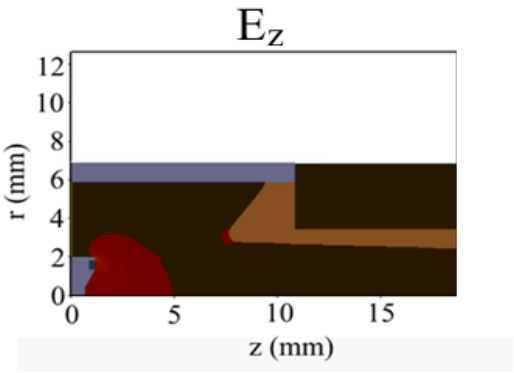

Figure 5.4: The E_z component of the electric field for the beam emitted at the cathode surface. The maximum value for this field component was approximately 110 MVm^{-1}.

The electric field calculated at the emitter surface of the cathode in the anode region reached a maximum of ~ 11 x 10^7 Vm^{-1}, which is well above the threshold value required for electrical breakdown as measured in previous experimental studies [4.2]. Because of the small diameter of the anode can as compared to the cathode diameter electrical breakdown between the cathode and the side wall of the anode was a concern. To mitigate the possibility of electrical breakdown in the electron gun it was decided to investigate the insertion of a dielectric layer between the cathode and anode along the entire length of the cathode on the inner wall of anode with only the tip of the cathode in the strong electric field region of the diode. CST MWS Magnetostatic simulation results demonstrate a reduced field of ~ 1 x 10^6 Vm^{-1} was possible with the use of the dielectric layer indicating sufficient E - field magnitude to induce a high current electron beam with possibility that the dielectric layer may prevent electrical breakdown of the cathode to the side walls of the anode. The following images from CST MWS confirm the presence of a dielectric layer results in the creation of an accelerating electrostatic field that is of the required magnitude.

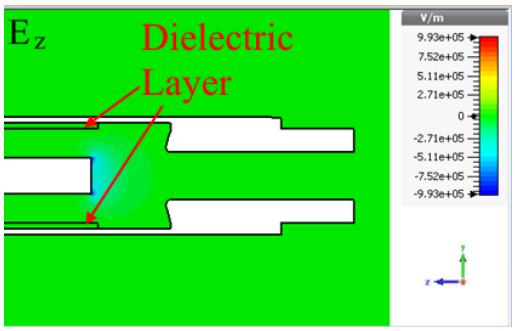

Figure 5.5: The E_z component within the cathode – anode region showing that with the presence of the dielectric layer the field reduces to less than 1 MVm^{-1} and so electrical breakdown may be avoided.

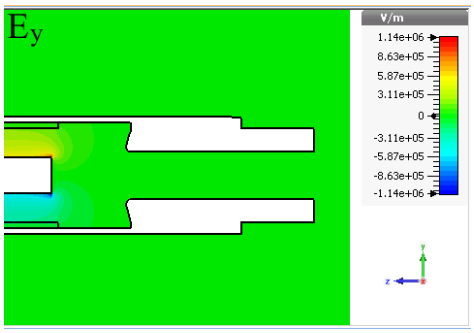

Figure 5.6: The E_y component within the cathode – anode region at the reduced value of 1.14 MVm^{-1} due to the presence of the dielectric layer.

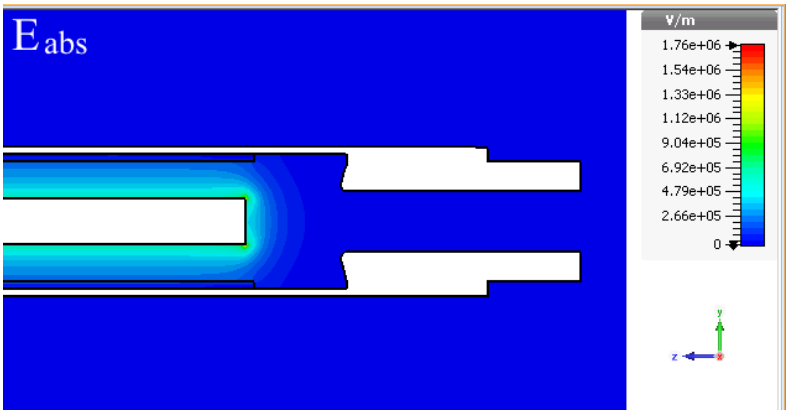

Figure 5.7: The absolute value of the electric field within the cathode – anode region demonstrates that the highest value of the total electric field reaches only 1.76 MVm^{-1} in the presence of a dielectric layer and so the possibility of breakdown is reduced while maintaining a high enough field to generate an electron beam with the majority of its velocity in the axial direction.

The ω - k dispersion diagram for the axial electron beam simulated is shown in figure 5.8

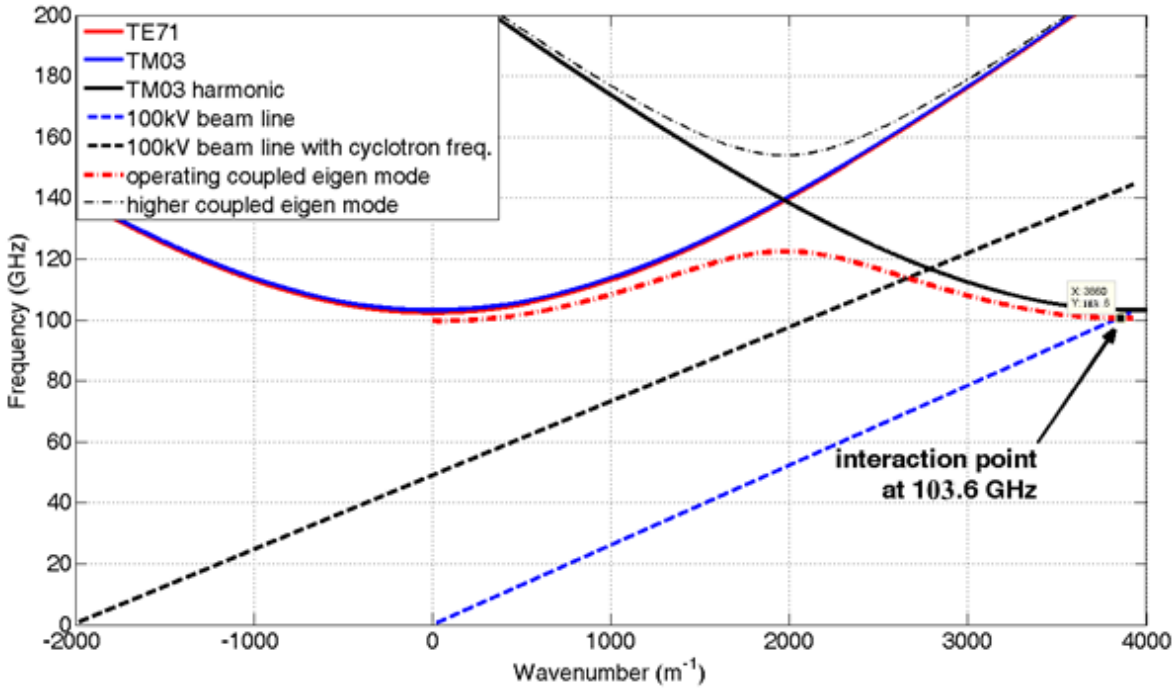

Figure 5.8: The dispersion relation diagram for a coupled $TE_{7,1}$ and $TM_{0,3}$ modes and a 100 kV Cherenkov Electron beam.

5.3 CST Particle Studio

5.3.1 Pierce Type Emission

As a precautionary measure in case the failure during experiments of the dielectric layer on the inner wall of the anode preventing electrical breakdown in the diode terminating the generation of the electron beam, a second electron gun which used a Pierce type velvet cathode was designed and simulated using CST Particle Studio (CST PS). In this case the anode can sat outside the inner bore of the 1.8 T guide magnet with the electron beam compressed as it entered the main cavity solenoid magnetic field. The electron beam was then focussed down through the main cavity solenoid magnetic field however this resulted in an electron beam that has both axial and transverse velocity ratio of ~0.4. This was demonstrated in CST particle tracking solver simulations of the Pierce type electron gun that takes into account space charge effects. The image below shows the final design of the cathode and anode that sits outside the main cavity solenoid that produces a compressed beam as seen in CST PS:

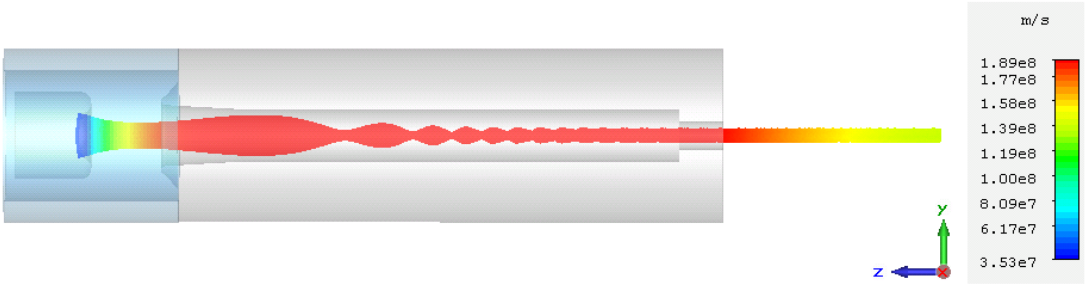

Figure 5.9: The beam profile from the particle tracking solver in CST PS. Notice that by the time the beam reaches the Bragg (section of smaller inner radius) the scalloping has subsided and the beam is stable with a vpara~ 0.46c, and vper~ 0.19c.

The beam profile seen in the image 5.9 represents the final design of the Pierce type emission source. A cathode radius of approximately 7.5 mm, cathode anode gap of 20 mm and an accelerating voltage of 80 kV results in a beam current of 20A and a beam waist diameter of approximately 5 mm in the Bragg section where the lower perturbation peak to peak diameter of approximately 7.2 mm, this should ensure that the beam interacts with the surface field within the interaction region. The magnetic field profile is such that at the cathode there is a B_z component of approximately 0.06 T at the cathode that reaches 0.13 T at the anode and then rises quickly to its flat top value of approximately 1.8 T. This field profile can be adjusted and its effect on the transverse velocity of the electrons studied at the maximum magnetic field of 1.8T and a beam alpha $\alpha = 0.4$ calculated.

5.4 Magic Simulations of the Beam-Wave Interaction

The optimisation of the physical design of the beam-wave interaction region for an electron beam with most of its velocity in the axial direction was carried out through numerical simulation taking into account the setup determined by boundary conditions that are set by the physical dimensions of the magnet that was used in the experiment, of which more detail will be given in chapter 7. The magnet chosen for this experimental analysis has an inner diameter of 18 mm which means that we will have a minimum inner diameter for the 2D PSL structure of 7.2 mm or 3.6 mm unperturbed inner radius. Due to restrictions in space there was little room for increasing or decreasing this value should the simulations show that it is necessary to do so.

The next step is to determine what azimuthally symmetric $TM_{0,n}$ mode is near-cutoff and at what exact frequency for that particular value of inner radius. Using the equation for the cut-off frequency for a mode in a cylindrical waveguide it was found that the $TM_{0,3}$ mode is cut-off at approximately 103.2 GHz in a structure of inner radius of 3.6 mm. Using the analytical equations found in reference [3.15] it was determined that using a longitudinal period, d_z = 1.6 mm the device that the $TM_{0,3}$ type mode would operate at approximately 103.6 GHz, we had found our operating mode and our longitudinal period. It was also found that, again using the equations from reference [3.15] that for a high energy beam (300keV) the number of azimuthal periods, m, should be equal to or greater than 7.

The next step is to demonstrate this interaction in Magic 3D using those specific physical parameters. First of all is confirmation of the magnitude of the longitudinal period dz by demonstrating how changes in this value affects the operating frequency of the device. Figure 5.10 below shows this relationship:

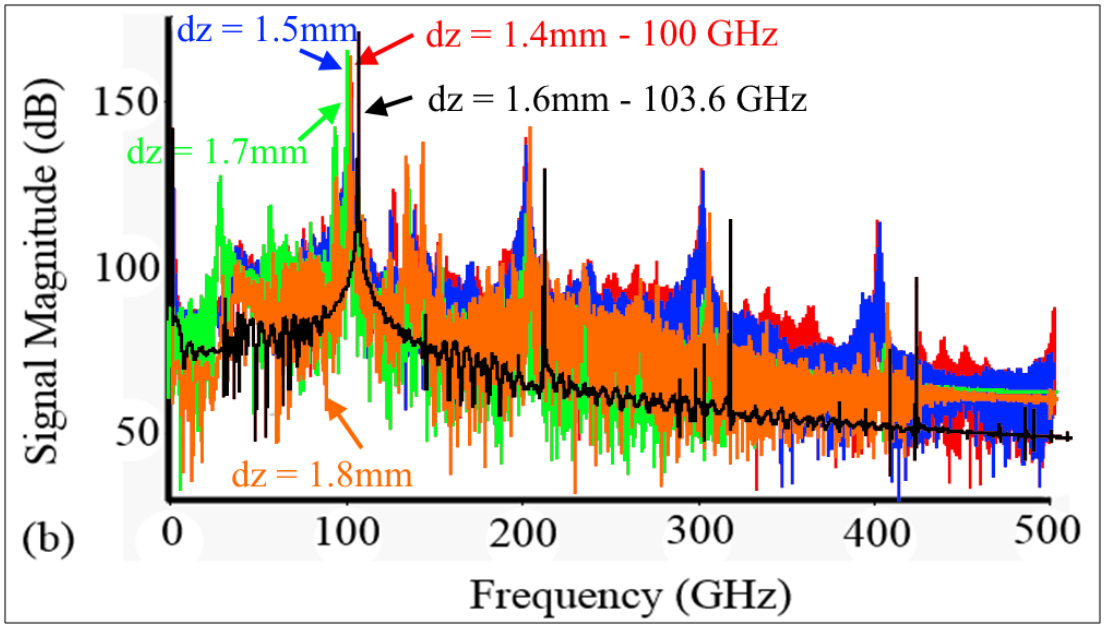

Figure 5.10: The relationship between longitudinal period dz and the operating frequency of the device.

The analytical theory predicted that a dz of 1.6 mm and coupling between the $TE_{7,1}$ mode and the $TM_{0,3}$ mode will result in an operating frequency of 103.6 GHz and this is demonstrated in the figure above by the black line. The other lines (red, blue, green and orange) represent longitudinal periods of 1.4, 1.5, 1.7 and 1.8 mm respectively taking into account that the 2D PSL constructed by 3D printing had a manufacturing tolerance of +- 0.125mm. There were a number of other values simulated but this selection shows that the 1.6 mm longitudinal period structure operated at a frequency of 103.6GHz. The value of dz = 1.6 mm is therefore confirmed and optimised, next we must investigate the same relationship between the azimuthal period and the operating frequency.

Using the same method it can be shown that the relationship between azimuthal period and operating frequency is similar to the relationship between longitudinal period and frequency and so can be optimised in the same way. Shown below in figure 5.11 is this relationship:

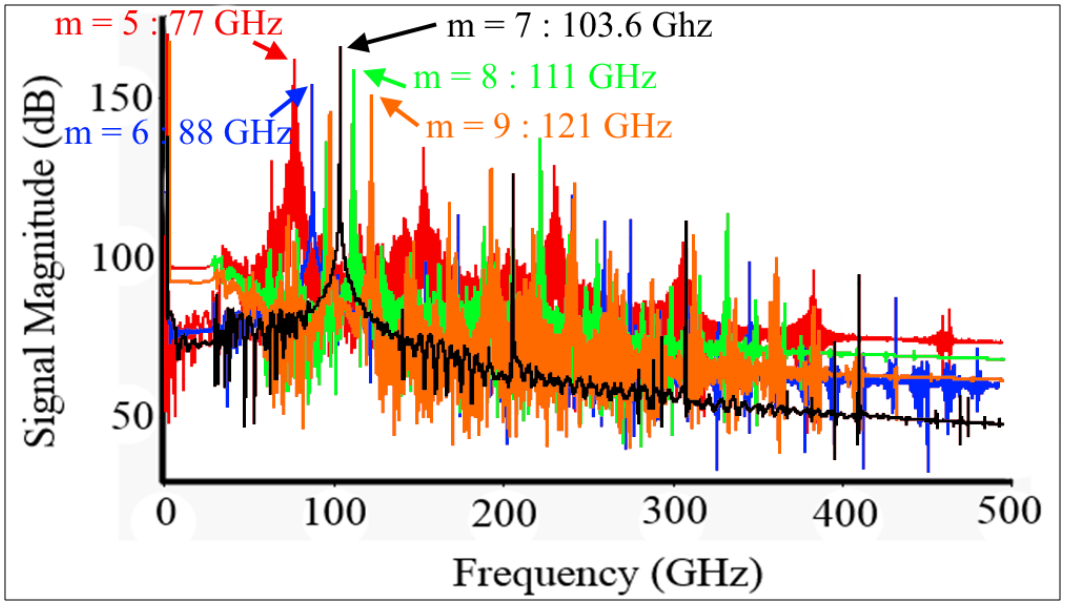

Figure 5.11: The relationship between the azimuthal period and the operating frequency.

It can be seen from figure 5.11 above that an operating frequency of 103.6GHz is achieved for a wave of azimuthal index 7 and an operating frequency of just below 80GHz is achieved for a wave of azimuthal index of 5. The Magic simulations have therefore confirmed that the optimised cavity design incorporates an azimuthal index of seven at 103.6GHz with a azimuthal index of five at 77GHz as predicted by analytical theory. It is now necessary to analyse and optimise the perturbation amplitude and understand its effect on output power.

The dependence of the reflection zone on perturbation amplitude was carried out. Several simulations of differing perturbation amplitudes dr [(peak to peak)/2] were tested ranging from 0.0 to 1.6 mm (peak to peak) amplitudes in steps of 0.05 mm. A selection of these simulations is shown below in figure 5.12:

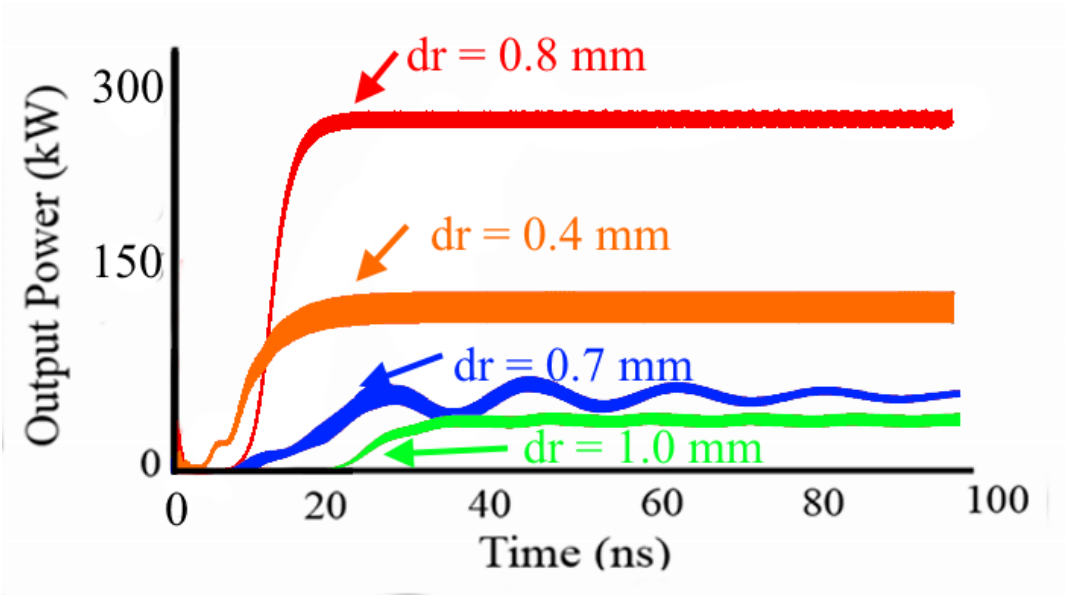

Figure 5.12: The relationship between perturbation amplitude and output power.

From figure 5.12 we see that for the interaction at 103.6GHz using explosive emission filed immersed cathode the optimal size for the perturbation amplitude was found to be 0.8 mm with values above and below this producing a reduced output power although it should be noted that a beam-wave interaction does still occur in each case. It is therefore noted that the effect of changing the perturbation amplitude results in a change in the strength of the interaction. The numerical simulations therefore predicted for an electron beam with most of its velocity in the axial direction the optimal perturbation amplitude [(peak to peak)/2] of the device was 0.8 mm in order to maximise the output power generated.

The next physical parameter that was optimised was the number of longitudinal periods of the device. This value will be important for maximising the output power since if it is too long the electrons will start taking energy back from the wave and if it is too short then the energy passed to the wave from the electrons will not be maximised. The image below shows the relationship between the number of longitudinal periods and the output power. A number of simulations were conducted ranging from 5 periods to 45 and a selection is shown in figure 5.13:

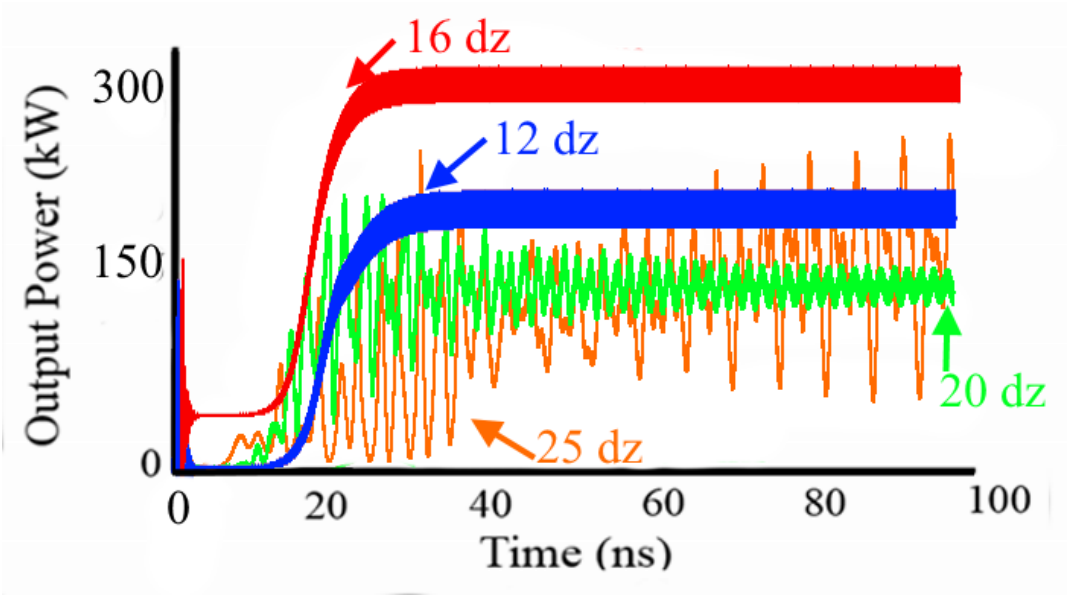

Figure 5.13: The relationship between the number of longitudinal periods and the output power of the device.

The graph above demonstrates that there is indeed a certain number of longitudinal periods where the beam – wave interaction is optimised and the energy transmitted from the electrons to the microwaves is maximum for 16 longitudinal periods. Values below this number produce an output that is similar to the output for 16 dz in that it is clean and stable but that the maximum steady state value is lower than that of 16 dz. Values above 16 produce an output that is unstable and noisy as the electrons both give and take energy to and from the wave. These graphs also have a mean value that is less than that of the 16 dz output. For maximum output the Magic simulations therefore confirm that 16 longitudinal periods should be used in the electron beam experiment. The system described above produces a beam – wave interaction that utilises a cavity eigenmode that is formed from the coupling between a $TM_{0,3}$ and a $TE_{7,1}$ mode. This is visualised in the figure below:

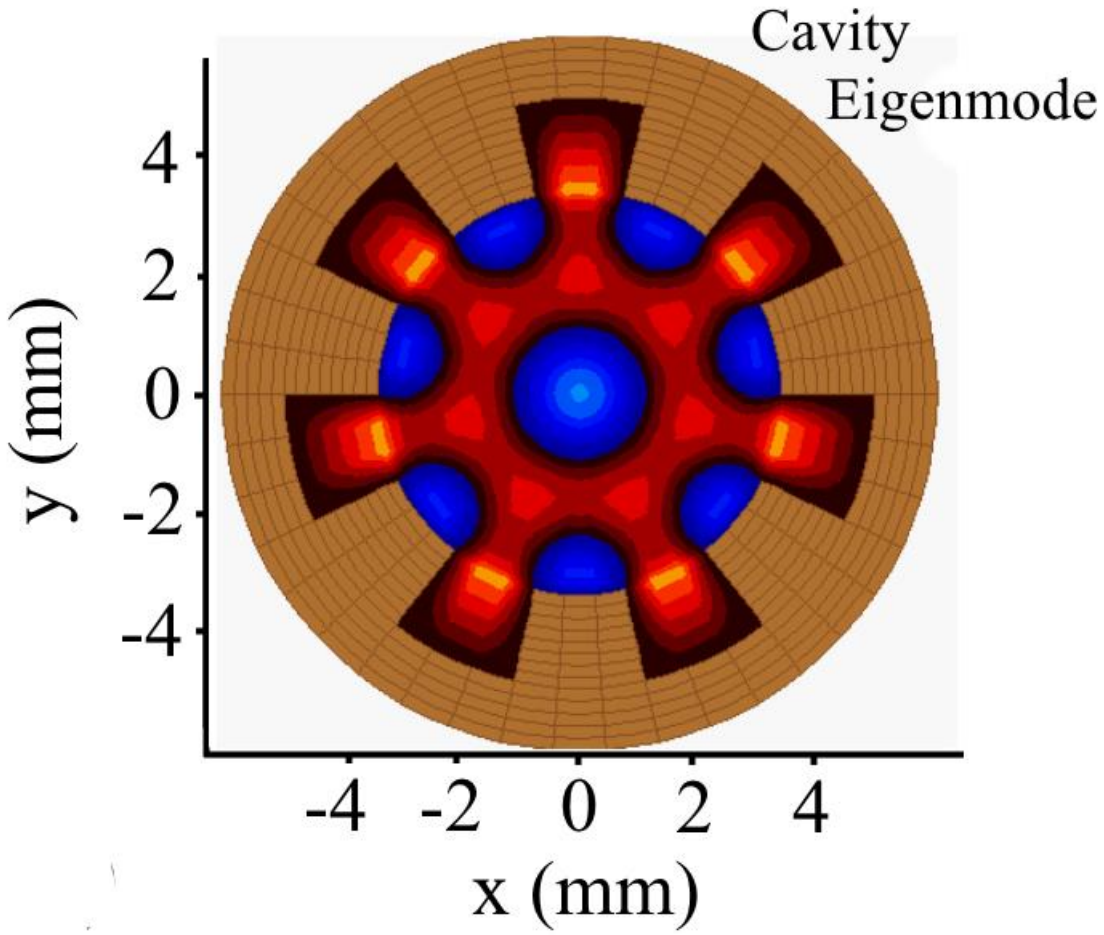

Figure 5.14: The cavity eigenmode seen in the optimised beam –wave interaction.

Figure 5.14 above demonstrates the cavity eigenmode that will be present within the interaction cavity. The important point here is that the surface field seen at the perturbations is equal in each instance. This is a direct result of the azimuthal symmetry of the $TM_{0,3}$ volume field and it is the reason that this volume mode is selected through the physical design of the cavity structure. This means that the beam will feel the same field at each perturbation which will result in better coherence in the output.

The above system is designed with explosive electron emission field immersed cathode, if in the event of electrical breakdown from the cathode to the side walls of the anode prevents beam formation or some other problem, the second Pierce type emission cathode will need to be used in its place. Magic simulations of this second type of Pierce type cathode resulted in a successful beam wave interaction but with much less power and at a lower frequency. Below is the frequency and power results of a system that utilises Pierce type emission and an explanation of the different processes that produced this result.

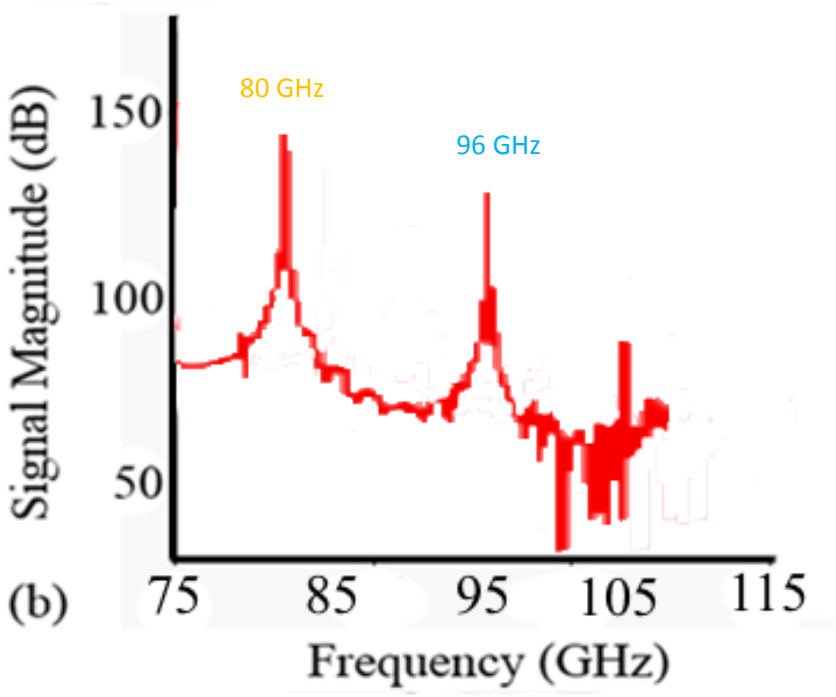

Figure 5.15: The output frequencies seen at the output port in the Magic 3D simulation of ~80 GHz and ~96 GHz

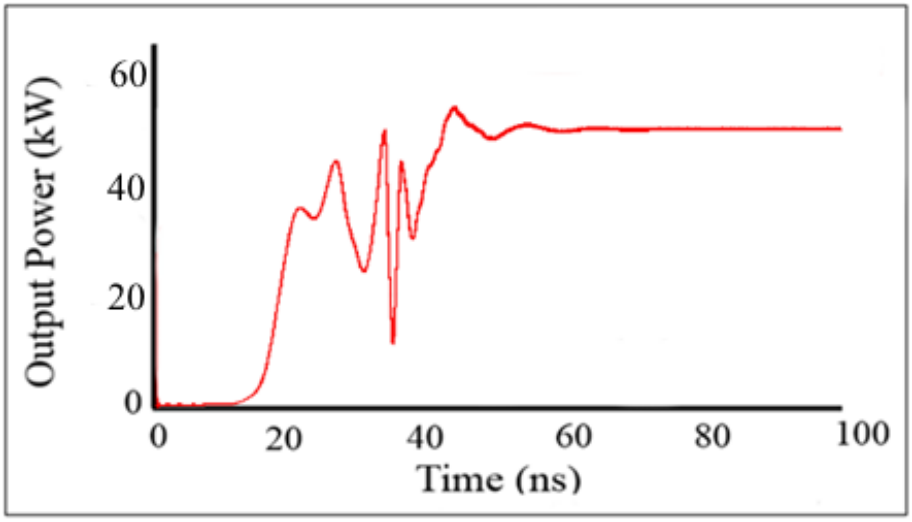

Figure 5.16: The output power of the device once the Pierce type gun is implemented..

By utilising a Pierce type emission setup an electron beam with a non-negligible transverse component to the electron velocity $v_\perp$ was generated. This meant that there may possibly be an interaction between this new velocity component and the transverse electric component of the cavity eigenmode. Since a deep corrugation of above $\lambda/4$ or greater results in the presence of a transverse electric component of the cavity eigenmode that is of sufficient magnitude to be involved in a gyro interaction it is therefore possible or even likely that a gyro interaction may be present in our system.

When we combine the above result with the dispersion diagram seen in figure 5.8 we must allow for the possibility that the use of a Pierce type cathode will promote a dominant gyro interaction.

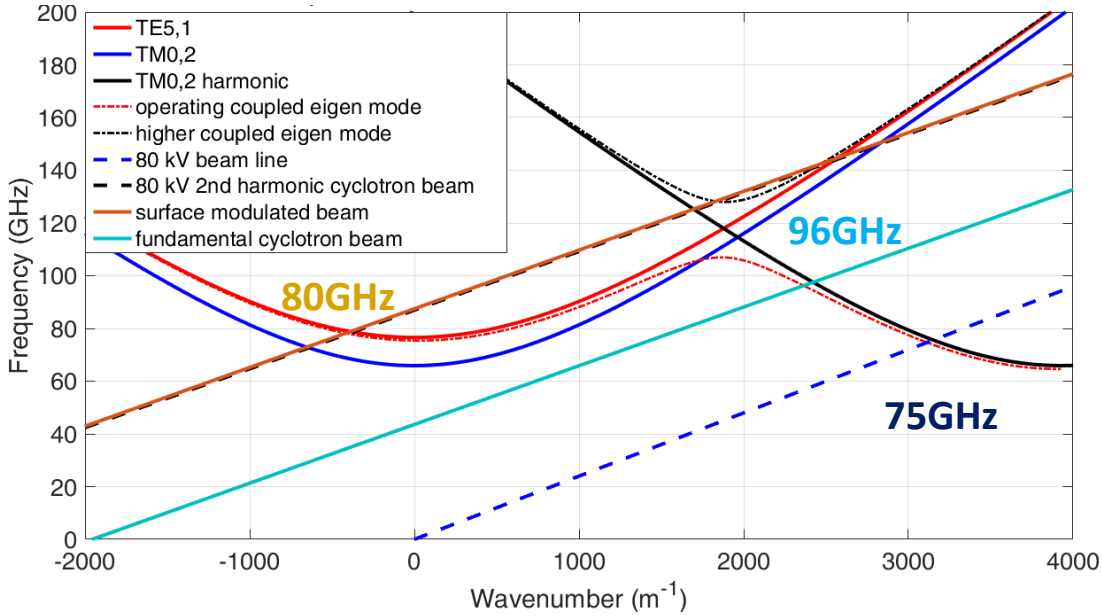

Figure 5.17: The dispersion plot for the new interaction utilising the pierce type cathode.

The mode pattern seen in this interaction is shown below in figure 5.18 and 5.19:

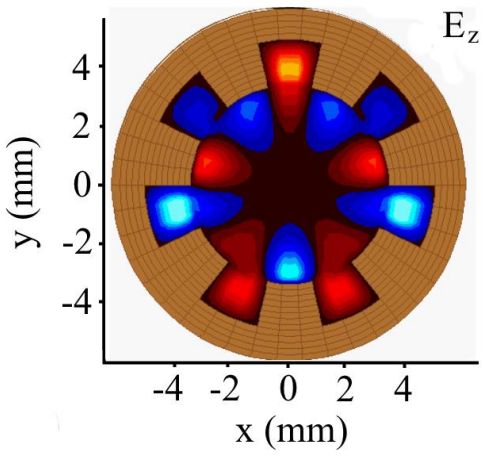

Figure 5.18: The Ez component of the gyro interaction

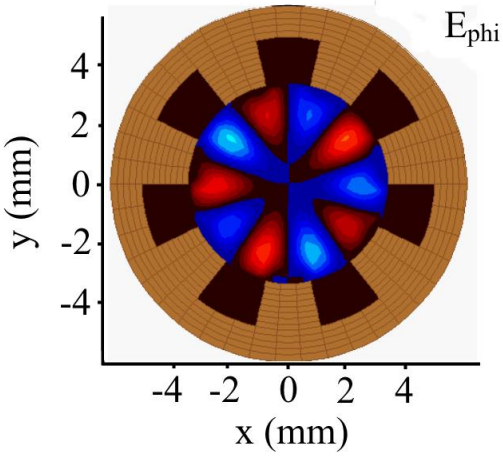

Figure 5.19: The Ephi component of the gyro interaction.

The mode patterns above demonstrates the fact that the surface field is not equal at each instance. The $TE_{5,1}$ based cavity eigenmode would therefore not produce an optimised output when excited by an electron beam that has a large fraction of its velocity in the transverse direction as compared to the TM_{03} mode coupling to the $TE_{7,1}$ mode with an electron beam with most of its velocity in the axial direction generating a frequency of 103.6GHz.

6

Experimental Design and Construction

6 Numerical Analysis: Beam – Wave Interaction

6.1 Particle in Cell (PiC) Method

Since this method was discussed in the previous chapter, this section shall be a short summary that serves to simply reiterate the main points but will not be a full overview of the Particle in Cell method. As with other methods, the particle in cell approach breaks the simulation domain down into spatially and temporally finite elements that are small enough to safely accommodate the smallest spatial and temporal portions of the physical model. This grid is then operated in a leap frog manner, with particle position and momentum determined at the beginning and end points of each grid unit and then repeating the process in the next cell. Electromagnetic field calculations are performed within each grid cell and for each time step and applied to each particle using the relevant vector operations.

6.2 Software Packages

6.2.1 CST Particle Studio

Charged particle dynamics immersed in 3D electromagnetic fields can be modelled using CST Particle Studio accurately and efficiently. The particle tracking solver can model the behaviour of particles through static fields that might arise from the electron gun emission processes. The Particle in Cell (PiC) solver works in the time domain and can accurately simulate particle-wave interactions in complex geometries. The stationary particle tracking solver tracks particles based on the Lorentz Force equation in pre-calculated electromagnetic fields. These fields can be either static electric fields, static magnetic fields or eigenmodes. The space charge effect on the electric field can be taken into account by the Gun Iteration option. Several emission models including fixed, space charge limited, thermionic and field emission are available. Furthermore, secondary electron emissions can be simulated. Both CST MWS & PS can model dispersive and lossy materials but also offer the theoretical Perfect Electrical Conductor (PEC) and a multitude of post processing options are available for analysis and to present the simulation results in various formats. GPU hardware acceleration, multithreading and distributed computing offer means to increase performance and decrease simulation times.

6.3 Electron Gun Design

Initial Design Considerations

The design of the electron gun and the 2D PSL interaction region was dependent on the bore diameter of the magnetic solenoid that was to be used in the experiment. Selecting the solenoid determined the rest of the setup and there were three possible options to choose from.

Option	Solenoid Design
1	Superconducting solenoid – up to 9 T field, flat top portion of magnetic field of 90 mm and cavity inner diameter of 50 mm
2	Water cooled DC solenoid – up to 2.1 T field, max cavity length of 100 mm and max cavity diameter of 18 mm
3	Low field (0.4 T) larger bore 50 mm solenoid

Table 6.1: The available solenoid designs.

The ideal option would have been to use the 9 T superconducting (SC) solenoid to enable the cathode to be positioned in the flat top portion of the 9 T magnetic field with a carbon cathode that could generate a thin annular electron beam close to the inner diameter of the 2D PSL inserted in a stainless steel anode can of inner diameter of 46 mm to be inserted in the bore of the SC magnet. This electron gun configuration would result in the generation of an electron beam with most of its velocity in the axial direction with the cathode anode gap spacing sufficient to mitigate breakdown in the radial direction. As indicated in simulations using such an electron beam would result in an efficient beam – wave interaction and hence the generation of the high power microwaves. However at the time of undertakng the experiment it proved difficult to guarantee the delivery of the liquid Helium required to cool the superconducting magnet. The low field solenoid, although of large physical size, the magnitude of the magnetic field was not sufficient to confine the electron beam. The option which could be achieved experimentally using the equipment and resources available in the laboratory was to use the water cooled continuous wave solenoid as it was capable of generating a magnetic field of up to 2.1 T and although the small bore size dictated that the cathode had to be placed outside the solenoid with the magnetic compression resulting in the production of an electron beam that had both axial as well as transverse velocity. As the 2.1 T DC water cooled solenoid did not require liquid Helium it was decided that this solenoid be used in the 2D PSL experiment.

As before, once the physical parameters of the solenoid are known, the cathode can then be designed around these values. The parameters of the solenoid to be used in the experiments are shown in table 6.2

Magnetic Field Range	1.65 - 2.1 T
Layers	14
Turns/layer	103
Average Diameter	5.68 cm
Wire size	2.2 x 2.2 mm
Length of wire required	285.25 m

Table 6.2: Gives the properties of the cavity solenoid important for e-gun design consideration.

6.4 Electron Beam Dynamics

In all vacuum electronic devices, the kinetic energy of an injected electron beam is converted into electromagnetic radiation through some process. The performance of the device can greatly depend on the properties of the electron beam, particularly on its quality. Therefore, given the crucial role which electron beams play within vacuum devices, it is useful to discuss the generation, propagation and characteristics of such beams.

6.4.1 Electron Emission Regimes

The emission of electrons from the surface of a solid plays an important role in the field of vacuum electronics. As such, it is appropriate to briefly discuss a couple of the main electron emission processes typically utilised by electron guns.

6.4.2 Thermionic Emission

For temperatures greater than absolute zero, a number of electrons within a solid will have enough energy to escape from its surface. By increasing the temperature, the number of electrons which have the potential to escape will also increase. However, the nature of the surface of the solid also plays a role in the rate at which electrons can escape. The act of heating the surface of a solid to cause electron emission is known as thermionic emission. The thermionic emission process can be understood by examination of the classical energy level diagram shown in Figure 6.1, below. Here, the interface between electrons at the surface of a metal and vacuum is depicted, with the parabolic curves representing electron energy levels. The upper occupied energy levels merge in a metal to form

a conduction band – also known as the 'Fermi sea' – indicated by the shaded area in the diagram. The difference in energy between the top of the conduction band within the solid and the free electrons in the vacuum is known as the work function energy, $e\varphi_{work}$, measured in eV. Here, φ_{work} is the potential difference between the electrons at the top of the Fermi sea and the free vacuum electrons. Only those electrons with sufficient momentum can overcome the potential barrier of the work function energy, and escape from the solid to vacuum.

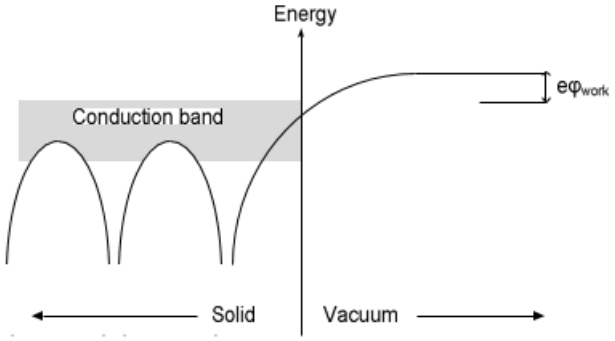

Figure 6.1: Energy level diagram for electrons close to a metal surface.

The thermionic current density, J, can be given by the Richardson-Dushman equation [6.1], shown by equation (6.1) below, where A_0 is an emission constant of 1.20 x 10^6 A m^{-2} K^{-2}. The exponential term can be seen to dominate the equation, with small changes in either the work function or temperature greatly affecting the current density for a cathode operating in the thermionic emission regime.

$$J = A_0 T^2 exp\left(\frac{-e\varphi_{work}}{k_B T}\right) \tag{6.1}$$

6.4.3 High Field Emission Theory

High field emission, also known as Fowler – Nordheim emission, is the process by which surface electrons are emitted from a particular material in the presence of and due to the application of a high magnitude external electric field. When the electric field that is applied to the surface of a cathode reaches beyond 1 x 10^9 V/m, it has been shown [6.2] that the resultant electron emission increases exponentially and is seen to be independent of cathode temperature, allowing for efficient 'cold cathode' design. This process is produced by a quantum mechanical effect and is an important mechanism for thin barriers as those found in semiconductor junctions and at the surface boundary of metals. The current density J can be found by:

$$J_{fn} = a|\boldsymbol{E}|^2 \exp(-b/|\boldsymbol{E}|) \tag{6.2}$$

Where a and b are constants defined by the physical properties of the material which reflect the material's work function and surface shape.

6.4.4 Pierce Type Emission

The type of electron gun in most common use is that involving a convergent cylindrical symmetric flow [6.3]. This gun illustrated below in figure 6.2 is frequently employed to initiate a focussed electron beam for use in a high – power klystron or TWT.

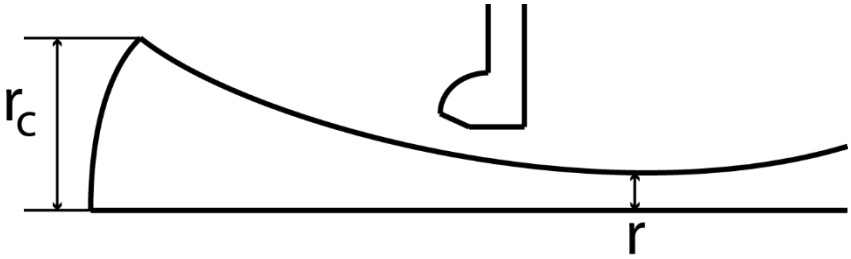

Figure 6.2: The Pierec type gun where the beam waist is dependent on the radius of the cathode.

The electron flow in this gun is in the form of a truncated cone; the cathode being the other and the anode being the inner, spherical surface. A hole in the inner, spherical – shaped anode permits the flow of electrons to leave the gun. This type of electron gun is based on flow between segments of concentric spheres. The theory of such flow has been determined by Pierce to yield the following relation for the current in a complete sphere;

$$I = \frac{16\varepsilon_0 V^{3/2}}{9\alpha^2}\left[\frac{2e}{m}\right]^{1/2} \tag{6.3}$$

Where

$$\alpha = \gamma - 0.3\gamma^2 + 0.075\gamma^3 - 0.001432\gamma^4 + 0.002161\gamma^5 - 0.0002679\gamma^6 \tag{6.4}$$

6.4.5 Space Charge Effects

Once electron emission has started, the presence of the negative charge will reduce the potential that was present in its absence [6.4]. In the region close to the surface of an emitting cathode, where many electrons are present, the reduction has a significant effect on the emission process. The initial potential in the electron gun increases linearly from cathode to anode. However the presence of an electron beam, this potential profile is depressed, the depression growing deeper as the emission is increased. The equilibrium, or space charge limit occurs when the electron beam is sufficiently dense

so as to reduce the electric field at the cathode surface to zero (were the potential to become negative, the electrons would be forced back toward the cathode). Should the field deviate in either the positive or negative direction, more or less electrons will flow from the cathode, re-establishing the equilibrium. Once the space charge limit has been reached, parameters such as cathode temperature or surface quality have no effect on electron transmission. This property proves highly useful as it eliminates the necessity for extreme uniformity in cathode temperature or smoothness of the cathode surface. Should the diode voltage be increased, the potential at all points is raised and additional current will flow to suppress the cathode surface potential to zero. Diode current in this regime is, therefore, dependent only on diode voltage. In the case of a parallel plane diode it is again rather straightforward to derive the following expression for current density in the space charge limited regime:

$$J = \frac{4}{9}\varepsilon_0 \left(\frac{2e}{m}\right)^{\frac{1}{2}} \frac{V^{\frac{3}{2}}}{x^2} \tag{6.5}$$

This is the Child-Langmuir law for the flow of electrons in a parallel plane, space charge limited diode and is commonly written in the simplified form:

$$J = 2.33x10^{-6} \frac{V^{\frac{3}{2}}}{x^2} \tag{6.6}$$

Where I=JA, with A being the area of the cathode. P is known as the diode perveance and for a parallel diode is given by:

$$I = PV^{\frac{3}{2}} \tag{6.7}$$

Importantly, perveance is only a function of diode geometry. Whilst the perveance varies from one geometry to the next, all geometries obey the above equation. The phase velocity is the velocity at which the phase of the wave propagates down the waveguide. This is always greater than the speed of light in a smooth walled waveguide as the TE wave is a superposition of the two plane waves. When the wave-front moves down a waveguide filled with vacuum at speed c the point A moves to the right at a speed greater than c, this is the phase velocity.

6.4.6 Beam Spreading and Focussing

In a real situation, as a beam travels through a system, it will spread out in the radial direction, since the electrons will have some transverse velocity component. In addition, space-charge repulsion between the particles serves to increase the beam radius. In order to prevent beam expansion, a confinement system of some description is required, in order to keep the beam travelling along the axis of propagation, giving a constant or slowing varying beam radius. This confinement is often attained through either a continuous or periodic magnetic field [6.5]. The trajectory of a particle, or number of particles, is determined entirely by the fields to which the particle encounters, and the particles momentum at a given point. On knowing these, the orbits of the particles can be calculated through equations of motion, in terms of a force acting on a particle of known charge. Given the nature of electron beams' role in vacuum electronic devices, the motion of particles must be considered in the presence of self-generated and external electric and magnetic fields. In order to accomplish this, the equation of motion depicted by the Lorentz force – shown in equation (6.8) below – is integrated in the given fields.

$$\frac{d\boldsymbol{p}}{dt} = e(\boldsymbol{E} + \boldsymbol{v}\ x\ \boldsymbol{B}) \tag{6.8}$$

6.4.7 Magnetic Focussing

One of the first assumptions when considering a focussing problem is to assume that there is no magnetic flux through the cathode. Therefore, the first magnetic flux experienced by an electron beam would be from a solenoid or permanent magnet at some point downstream of the cathode [6.6]. If it is assumed that a solenoid is used, then as the electron beam enters the solenoid, it will encounter radially directed magnetic flux lines, as shown in Figure 6.3, below. An electron above the beam axis, would experience a component of magnetic flux directed downward, resulting in a magnetic force directed into the page. Conversely, for an electron below the axis, the magnetic flux is directed upward, causing the magnetic force to be directed out of the page. The net effect of this means that the electron beam rotates in a clockwise direction as it enters the solenoid.

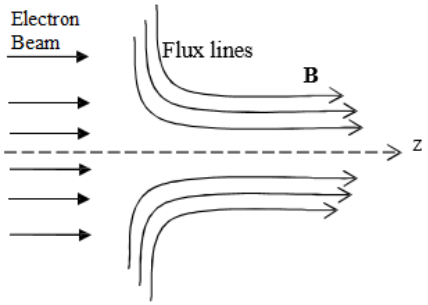

Figure 6.3: Schematic of the magnetic flux lines at the entrance of a solenoid.

As the electrons continue to propagate into the magnetic field, they encounter a stronger axial magnetic flux component. The interaction of the B_z field with the rotating beam is responsible for providing the magnetic focussing force. At such a point, an electron above the beam axis will have a velocity component which is directed out of the paper. Through the cross – product of the Lorentz force, **v** x **B**, it can be shown that the resultant force is directed away from the axis. As a result, it can be seen that individual electrons undergo a helical trajectory about the axis of the solenoid. This can be visualised, as seen in Figure 6.4 below, for a single electron.

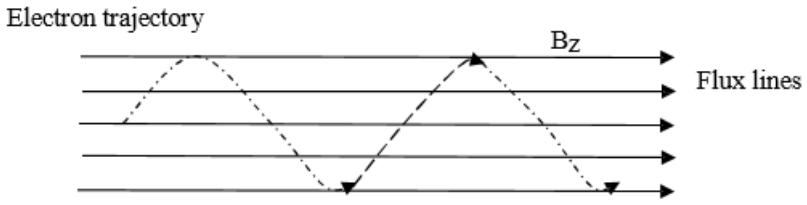

Figure 6.4, Schematic of helical electron trajectory in magnetic flux lines.

If the space charge forces acting within the beam are exactly balanced by the magnetic forces from the solenoid, then, assuming the electrons entered the region of the solenoid with no radial velocity, the diameter of the beam will remain constant as the beam rotates through the field region. If there is no flux through the cathode, and the space charge forces can be balanced, the required magnetic flux from the solenoid is known as the Brillouin field, B_B, with the motion of the electrons within such a field being referred to as Brillouin flow. The equilibrium radius, r_{equil}, of a beam in Brillouin flow can be expressed as shown by equation (6.9), where B_z is the axial flux density, I_{beam} is the beam current and v_z is the axial velocity of the beam.

$$r_{equil} = \frac{1}{B_z}\sqrt{\frac{2m_0 I_{beam}}{\pi e \varepsilon_0 v_z}} \tag{6.9}$$

A solenoid is simply a multiple layers of continuously looped wire, which generates axis - symmetric, static radial and axial magnetic fields due to a current, I_{soln}, being passed along it. The magnitude of the magnetic field produced can be determined using equation (6.10), below, where *n* is the number of turns per unit length, μ is the permeability of free space and I_{soln} is the current flowing through the solenoid

$$B_z = \mu n I_{soln} \tag{6.10}$$

6.4.8 Electron beam profile predicted with CST Microwave studio

A Pierce type cathode that used a velvet emitter modelled using CST MS is now presented. The particle tracking solver as described in chapter 4 utilising the gun iteration technique therefore ensuring that space charge effects are considered was used to analyse the properties of the beam produced by the electron gun. Initial design considerations put certain restrictions on the dimensions used such that the beam must fit radially into the anode can while maintaining a sufficient anode cathode gap so that a stable relativistic beam of the required dimensions is produced at the entrance to the 2D PSL interaction region. The image below shows the final design of the pierce cathode and anode that produces the desired beam as seen in CST PS:

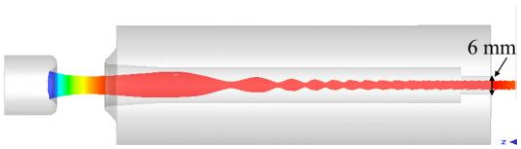

Figure 6.5: The beam trajectories as seen in CST PS. The pierce type electrodes focus the beam when it leaves the cathode producing a beam of outer diameter of 4 mm and inner diameter of 2 mm

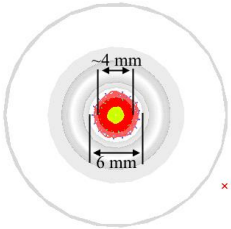

Figure 6.6: Beam image on the x – y pane. The yellow middle section shows that there are fewer electrons in this region and that they have less energy than those in on the outside portion of the beam.

The images from CST Particle Studio show that the structure of the beam is annular using the cathode shape, cathode – anode gap distance, accelerating voltage (80 kV) and cavity magnetic field (1.8 T) as used in the experiment. The beam outer diameter from the right image is 4 mm and the beam width is ~2mm mm. The Pierce type cathode produced a beam with a current of 20 A predicted in the simulation. The current generated by the electron gun was dictated by the Child-Langmuir law for space charge limited emission in the diode region.

The beam profile seen in the image 6.6 represents the design of the Pierce type emission source. A cathode radius which in the experiment was in the form of a velvet disk was 7.5 mm, the cathode anode gap was 20 mm and an accelerating voltage was 80 kV. The simulations predict a beam current of 20 A and a beam waist diameter of approximately ~5 mm in the 2D PSL section where the lower perturbation peak to peak diameter (minimum diameter) was 7.2 mm, this should ensure that the beam interacts with the surface field within the interaction region. The magnetic field profile is such that at the cathode there is a B_z component of approximately 0.06 T at the cathode that increases at the anode to 0.13 T and then rises quickly to its flat top value of approximately 1.8 T. This field profile can be adjusted and its effect on the transverse velocity of the electrons studied but with a maximum magnitude of 1.8 T a beam α of 0.4 was predicted. The beam alpha predicted by CST PS was 0.4

found from v_z of 0.46 c and a v_{perp} of 0.19 c. The B-field parameters were taken from the values measured using a Hall probe (Chapter 7). From the simulations the explosive emission cathode predicted an annular beam with the following parameters

Beam Voltage	80 kV
Beam Current	20 A
Beam Radius	~3 mm
Beam Velocity v_z	0.46 c
Beam Velocity v_{perp}	0.19 c
Beam alpha: v_{perp} /v_z	0.4

Table 6.3: Parameters of the 80 kV beam seen in CST PS.

6.4.9 The Electron Gun

6.4.9.1 Plasma Flare Field Emission Cathode

A field emission cathode gets its name from the fact that the electric field at the surface of the cathode is high enough that the potential barrier that the electrons have to overcome in order to escape from the solid into vacuum is sufficiently narrow to enable quantum mechanical tunnelling of the electrons through the barrier [6.7]. The cathode used for the experiments was a flat velvet disk of diameter of 14.95 mm. Velvet was used as the cathode material to ensure that when voltage was applied to the diode field enhancement at the velvet tips resulted in a high enough electric field to enable quantum mechanical tunnelling of the electrons through the potential barrier. Initially the current from each tip is small but the cross section of each velvet tip is also small and hence the current density can be high. Therefore field emission near the tips results in a small electron current which causes local heating and vaporisation of the material due to the small cross sectional area involved. This process creates surface plasma with an effective work function of zero at the surface of the velvet. The electron beam is then formed from a plasma at the surface of the velvet which can dynamically expand in the anode-cathode gap hence the name plasma flare emission cathode. The velvet was glued onto a copper disk which was then attached to a stainless steel cathode stock manufactured for the experiment. The velvet cathode is also known as a ‘cold’ cathode because it does not implement any form of external heating to induce thermionic emission. A voltage pulse with a 100 ns duration flat top profile of magnitude 80 kV was generated across the anode cathode gap using a stacked inverting cable pulser Blumlein generator. A plasma flare cathode can generate currents, typically $\geq$ 50 A and $\geq$ 1 kA for different cathode materials such as velvet and carbon and applied electric fields often givng more beam current in experiments than is predicted in simulations.

The electron beam pulse duration generated by the plasma flare cold cathode is governed by the gap-closure time which is the time for the plasma to travel across the cathode - anode gap, effectively shortening the accelerating voltage. As it is only relativistic electrons which may transfer energy to the beam-wave instability, these low voltage electrons whose velocity may be further reduced by space charge effects will play no part in the beam-wave interaction process. Due to these phenomena the high field emission source results in a short pulsed beam whose duration is dictated by the time it takes for the plasma to travel from the cathode and reach the anode which for an anode-cathode gap distance of 2 cm is typically of the order of ~1 to 2 μs. The advantages of this emission source are that it requires only 10^{-6} mbar for a vacuum, no external heating and it produces a reliable relativistic beam of current of ~100 A for a 1 cm^2 disk of velvet and up to 1 kA for a carbon cathode. The pulsed operation might not be suitable for some applications where continuous wave operation is required but it is an excellent cathode for proof of concept experiments.

6.4.9.2 Velvet Cathode

The cathode structure itself was constructed from copper with a small solid disk of velvet material glued onto copper as the emitting surface. Velvet can produce approximately 100 Acm^{-2} at ~100 kV for an anode - cathode gap distance of ~ 2 cm which will increase proportionally with surface area and accelerating voltage [6.8, 6.9]. The copper component of the velvet cathode was initially designed in Autodesk Inventor 2015 and is shown below with a small velvet emitter in the next image:

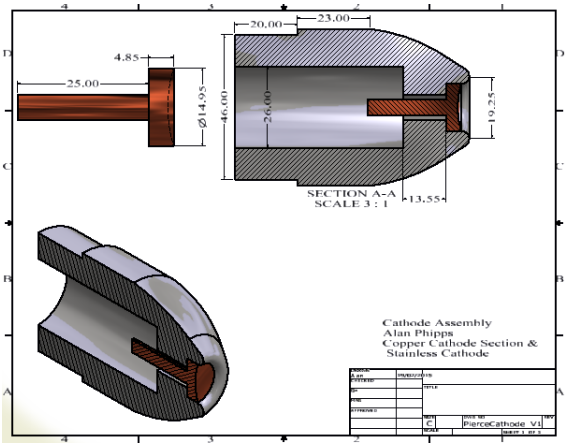

Figure 6.7: The copper section of the velvet cathode showing the concaved surface on the front end where the velvet will be affixed. The full structure is based on the Pierce cathode design but optimised for our physical parameters

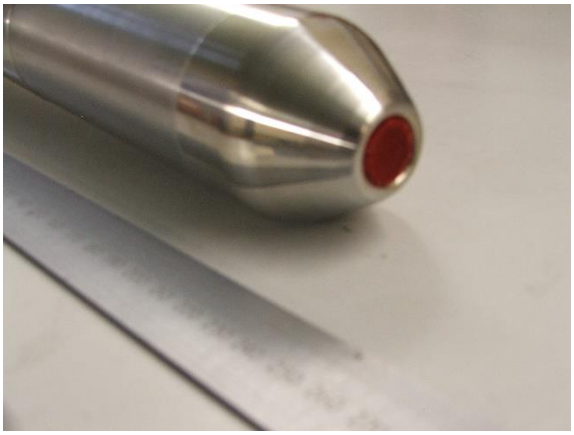

Figure 6.8: A photograph of the cathodes showing the copper holder and the velvet emitting surfaces.

Once electron emission has started, the presence of the negative charge will reduce the potential that was present in its absence. In the region close to the surface of the velvet cathode,

where many electrons are present, the reduction has a significant effect on the emission process. The initial potential in the electron gun increases linearly from cathode to anode. However, in the presence of an electron beam, this potential profile is depressed, the depression growing deeper as the emission is increased.

6.4.10 Pierce Gun

The electron gun used in almost all linear-beam devices is called the Pierce Gun named after J.R. Pierce. A circular or annular emitting surface is used, in conjunction with focusing electrodes, known as Pierce electrodes and designed through a method set out by J.R. Pierce [6.10]. The electrodes are used to shape the equi-potentials that are distorted by the presence of the electron beam for focusing the beam. Without the beam present, these equi-potentials would be straight and equally spaced. When the electron beam is emitted, the electrons repel each other and cause the beam to diverge outwards changing the equi-potentials. If the electrodes are shaped such that the equi-potentials stayed straight with the beam present, then the beam would no longer diverge and a high quality beam could be obtained. The electrodes can be rotated towards the anode which straightens the equi-potentials when there is a beam. The angle between the electrode and the beam edge can be adjusted. When that angle reaches 67.5 degrees, this straightens the equi-potentials for a space-charge limed beam. Electrodes operated at this angle are called Pierce electrodes.

6.5 High Voltage Blumlein Cable Pulser

The operating characteristics of the inverting stacked Blumlein HT pulse generator may be explained by considering the simplest form of cable generator where a DC charged signal has its output cable transferred to a load via a suitable switch. The magnitude of the resultant output pulse is determined by the ratio of the load to the generator impedance Z_L/Z_0 with a matched system ($Z_L = Z_0$) delivering V_{Charge} / 2 to the load and a voltage approaching the charging voltage for a high impedance load. As the nominal output voltage of the system can never exceed the charging voltage, it is difficult to generate large voltages without reverting to very expensive and bulky high-voltage cable. An alternative method which produces higher output voltages without overstressing the cable is the Blumlein technique. With this arrangement a voltage gain of 2 is possible by charging two transmission lines in parallel and by connecting them in series to produce the output. In principle, with both cables charged to V, switch S is closed and this launches a negative voltage pulse down the cable. When the pulse front appears at the load it doubles (assuming $Z_L >> Z_2$) and produces a voltage of magnitude 2 V. The nominal voltage output is given by:

$$V_L = \frac{2VZ_L}{Z_1 + Z_2 + Z_L} \tag{6.11}$$

This voltage gain is achieved by folding the cable back on itself with the length of the centre cable being such that its transit time equals the duration of the voltage pulse, in this case 100 ns. The cable braid is removed from two sections of the cable which essentially creates three transmission lines. The minimum length of cable braid removed is dependent upon the surface flashover length required for twice the operating voltage. With the cables fully charged to V, the Blumlein generator is fired by closing switch S which consisted of a pressured spark gap. This results in a voltage of 2 V being produced between both cable ends. This inverting stacked Blumlein HT pulse generator was constructed from 50 ohm coaxial cable resulting in a total impedance of 200 ohms. With each cable having a DC rating 40 kV a nominal output of 160 kV is possible. However the output voltage which was produced from the inverting stacked Blumlein HT pulse generator was also dependent on the load impedance and the inherent operating efficiency of the supply. Due to the transmission line properties of the inverting stacked Blumlein generator this HT pulse power supply was capable of producing an 100 kV output voltage pulse which had a characteristic envelope shape comprising of a 10 ns rise-time, a 100 ns ‘flat top’ and a 10 ns fall - time.

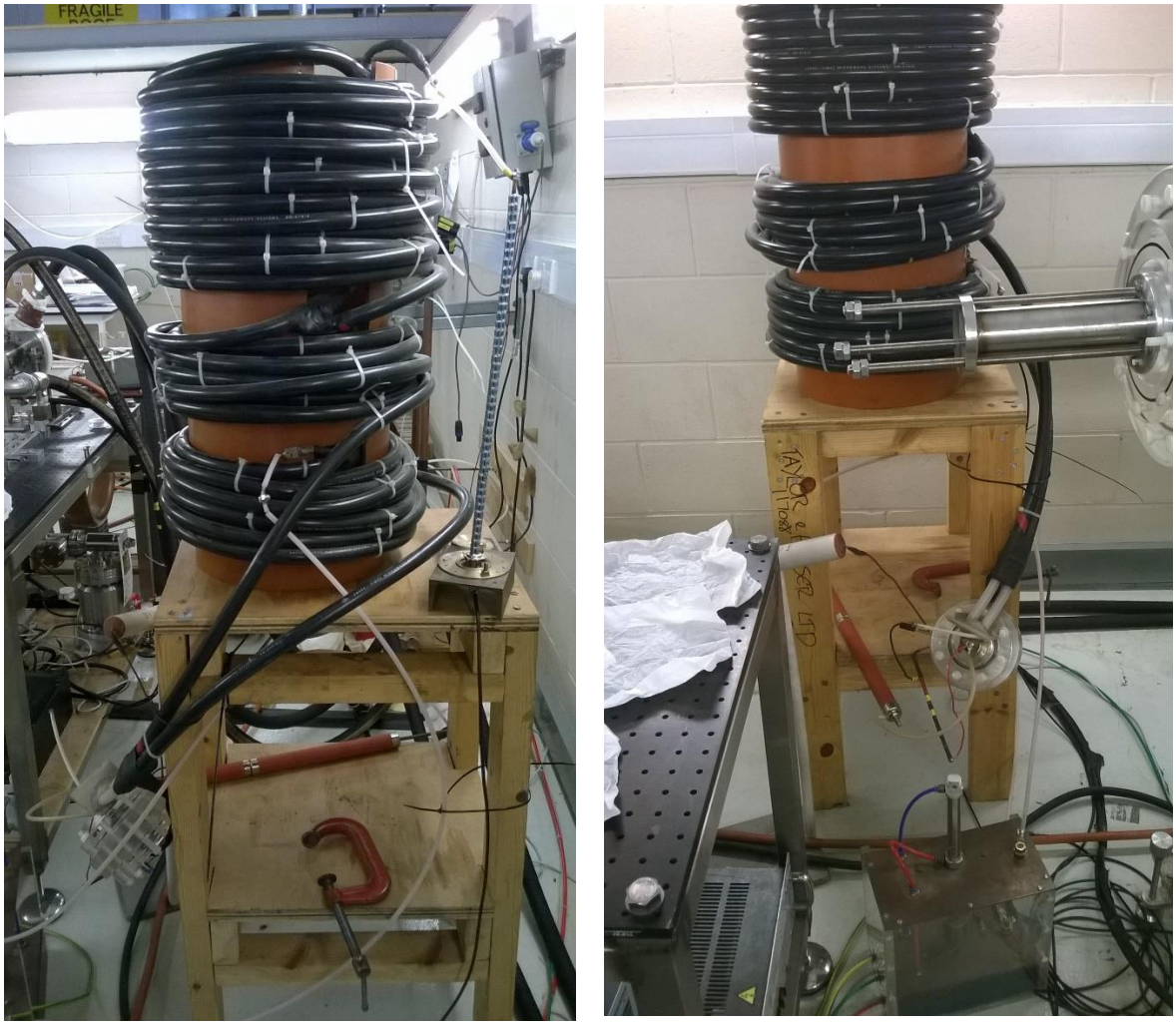

Figure 6.9: The Blumlein pulse generator that was used to power the system. The system uses a coaxial line whose length corresponds to the pulse duration of the voltage pulse seen at the cathode. In both images you can see the spark gap at the end of the black cables that is the switch for the system. Initially this switch is open and no current pulse is passed to the cathode but once the trigger button is pushed the Thyratron closes the switch and the systems fires.

6.6 The Magnetic Guide Field

6.6.1 2 Tesla Water Cooled Solenoid

The solenoid design that was chosen for this experiment was the 2 T water cooled solenoid that was constructed and tested in – house and that can produce the required 1.8 T magnetic field. The actual solenoid itself has a number of design characteristics that must be kept in mind when building the rest of the system around it. Firstly, the design of the solenoid has to take into consideration the cooling of the wires by allowing a large volume of water to pass through the wires within the setup. This is required due to the large amount of heat produced in such a small volume. Secondly, the

addition of an insulating varnish coating on the surface of the 2.2 mm by 2.2 mm square copper solenoid wire is necessary so that no breakdown will occur between the layers of the coils. A Matlab script was used to calculate the B – field profile, shown in chapter 6, using the physical parameters of the setup such as the length of the wire, the radius of each turn and the number of layers and turns. The script also takes into consideration the thickness of the wire and the thickness of the fishing wire that sits between the layers to allow the water to channel between them. The length of the wire, L, is found to be 285 m. After this the resistance of the wire was found through:

$$R = \frac{L\rho}{A} \tag{6.12}$$

Where ρ is electrical resistivity of the wire and A is cross-sectional area of wire. The current required to produce a B - Field for the solenoid can then be found from Amperes law:

$$I \approx \frac{B}{\mu_0 N} \tag{6.13}$$

Where N is the turn density or turns per metre and the voltage can be found from Ohm's Law: V = IR and Power from $P = I^2R$. The results of these calculations show that the electrical power needed by the solenoid to produce a magnetic field of 2.1 T was 62.3 kW thus high pressure water is required to cool the solenoid. Other values can be seen in the table below

	B_0 = 1.65 T	B_0 = 1.8 T	B_0 = 2.1 T
Resistance (Ohms)	0.99	0.99	0.99
Current (A)	211.4	228.8	262.6
Voltage (V)	209	226	260
Power (kW)	44.3	51.9	68.3

Table 6.4: The various current, voltage and power values for given magnetic field magnitudes.

Water channels of 0.4 mm are placed between each layer of the copper wire and these channels are kept from closing through high strength nylon wire that is tied along the gaps axially. The number of nylon wires required increases but the distance between each wire is kept at around 10 mm in order to keep a uniform cooling channel around the circumference of the solenoid. Matlab simulations show that the cavity coil requires 14 layers of 2.2 mm wire, 103 turns is required to provide the desired magnetic field profile. Also, a shim coil is added at each end of the solenoid of 2 layers and 15 turns per layer in order to increase the length of the flat top region of the magnetic field so that the length of the solenoid can be reduced hence lowered the overall electric power. To insulate the wire from the metal former a 4 mm thick polycarbonate mesh was used at both ends of the solenoid and channels were formed for water passing through the mesh. The finished solenoid is shown in the image below:

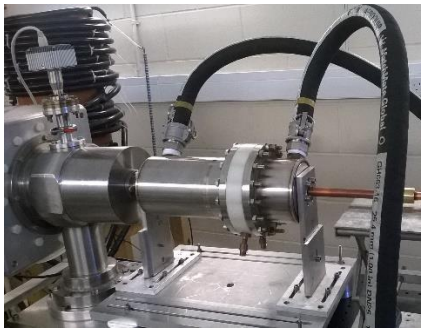

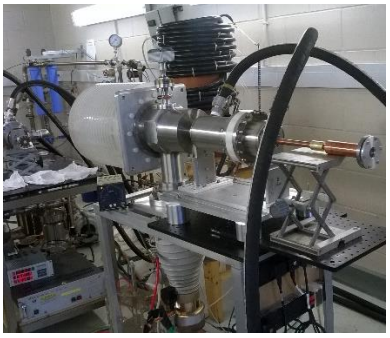

Figure 6.10: The copper coils of the water cooled solenoid showing the main coils all along the length of the device and the shim coils at each end.

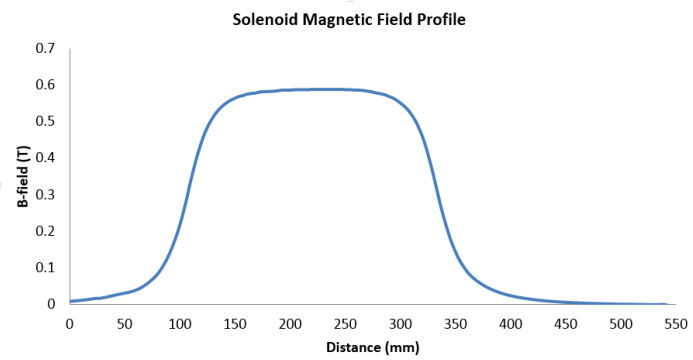

Figure 6.11: The B – field profile produced by the Matlab script running with the same physical parameters as used in the solenoid described above.

6.7 The Vacuum Subsystem

6.7.1 The Rotary Pump

The Edwards oil sealed rotary vane pump is the first step on our way to acquiring our desired vacuum pressure of 1 x 10^{-6} mbar. This pump has a pump throughput ranging from 3 to 12 m^3hr^{-1}, a noise level of approximately 48 dB at 50 Hz (1500 rpm) and an ultimate pressure of 3 x 10^{-2} mbar, operating at 450 W. The inlet vale is connected to a series of components that each serve a specific purpose in helping to achieve and sustain the required vacuum pressure, the first component is the foreline trap that captures and prevents oil from the diffusion pump returning to the rotary pump and contaminating its inner workings. The second device is a magnetic switch that when powered remains open and in the event of a power cut blocks the backward path to the rotary pump, therefore maintaining the vacuum and protecting the rotary. Next are a series of valves that allow control of the operation of the vacuum system by allowing or preventing the suction force within the system, also offering different paths for the air to flow out so that the diffusion pump can be isolated from the process.

6.7.2 Diffusion Pump

The Edwards Diffstack Vapour Diffusion Pump Model B346322978 is the second pump that is used to obtain our required vacuum pressure of 1 x 10^{-6} mbar. The pump body is water – cooled and made of stainless steel and so can be safely used in a high B – field environment. Pump fluid, commonly known as Santovac 5, is heated in the boiler at the base of the system to produce a vapour which passes up through the interior of the assembly and emerges as a high – velocity vapour stream. The vapour stream 'grabs' air molecules and as it cools falls back into the pump assembly and condenses on the assembly walls, returning to the base where it is heated again and the process repeats. The Diffstack has a pumping speed of 700 ls^{-1} for nitrogen and heating power of 1.4 kW.

6.7.3 The Vacuum Diode

A specifically designed vacuum diode was implemented in the system that allowed for acceleration of electrons in the anode-cathode region and the formation of an electron beam in the cavity. The high voltage HT pulse power supply was connected to the cathode stalk. The cathode and anode were separated by a Perspex insulator. The cathode position with respect to the anode was able to be moved forwards and backwards allowing alteration of the anode – cathode gap. The vacuum was sealed at the cathode stalk and stainless steel anode was achieved by using O rings as shown – below:

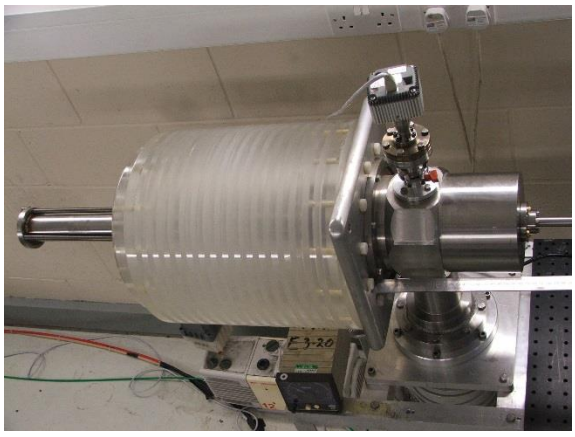

Figure 6.12: The vacuum diode that houses the stainless steel cathode stock, insulator made from Perspex and stainless steel plate and anode can. A pressure of 1 x 10^{-6} mbar pressure was achieved by using a diffstack backed by a rotary pump.

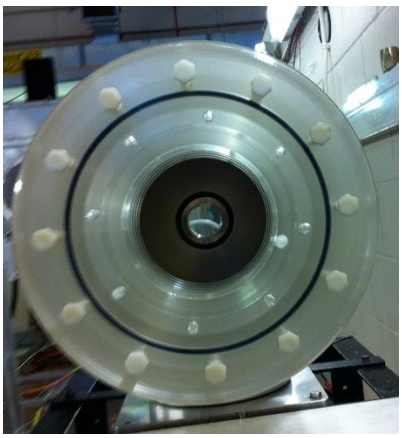

Figure 6.13: The front end view of the vacuum diode showing one of the O – ring seals.

6.8 The Output System

Upon leaving the beam – wave interaction region the microwaves have to be launched into free space with the electrons removed from the system by impacting on the walls of the vacuum system. An output horn and a window consisting of a 0.127 mm thick Mylar sheet are shown in the drawing below:

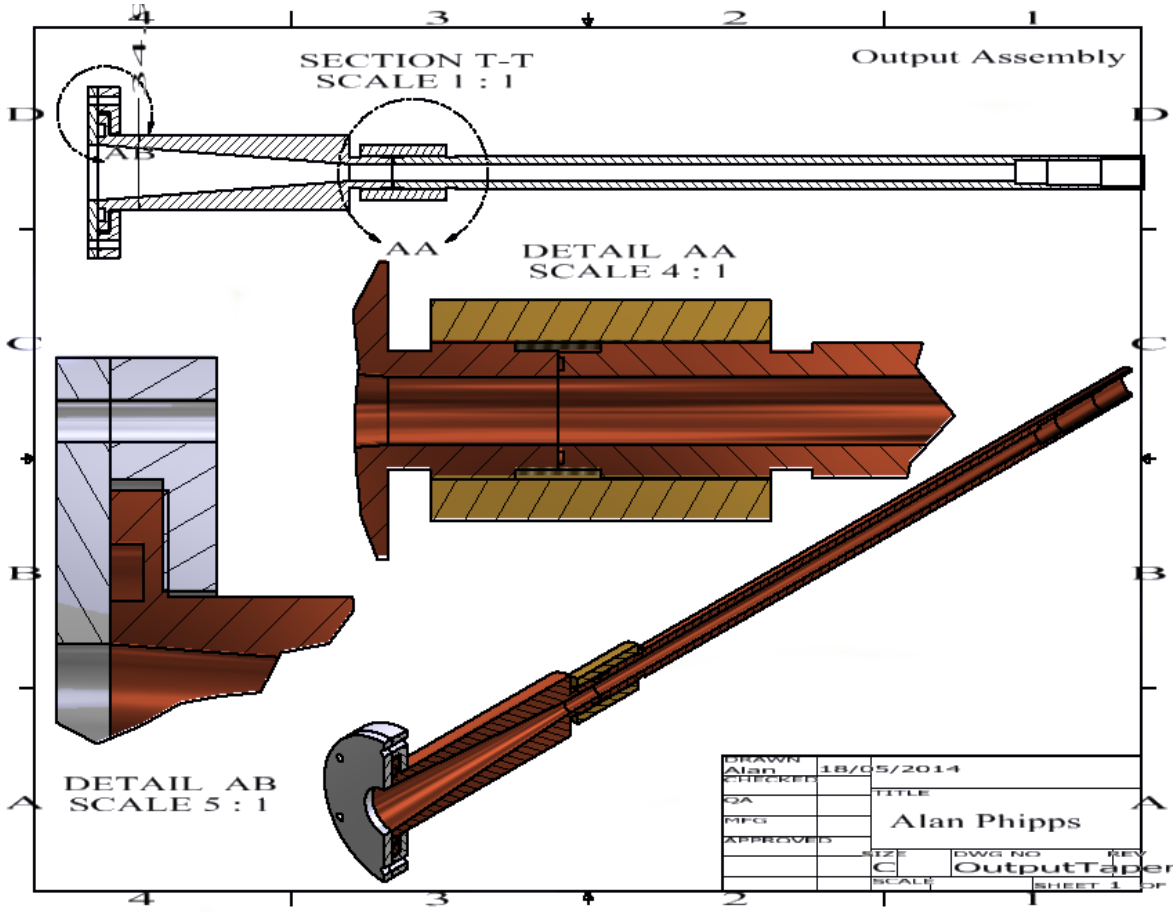

Figure 6.14: The full output system showing how each section fits together. The cylindrical waveguide and horn sections are sealed with an O – ring seal and held together with a brass piece. An O – ring seal is also used at the output end with a stainless clamp structure holding the Mylar window in place.

6.9 Output Horn

The output section consists of two main parts, firstly, a long piece of cylindrical waveguide that allows the microwaves and the electrons to move away from the PSL region while maintaining the vacuum. Secondly the tapered horn and window both sections are shown below:

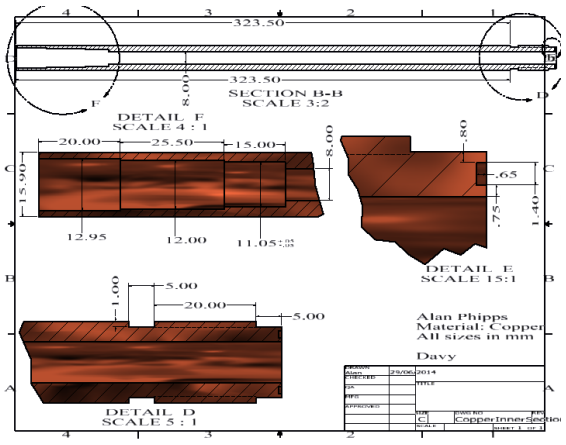

Figure 6.15: The cylindrical waveguide section that contained the PSL and is connected to the output horn and window.

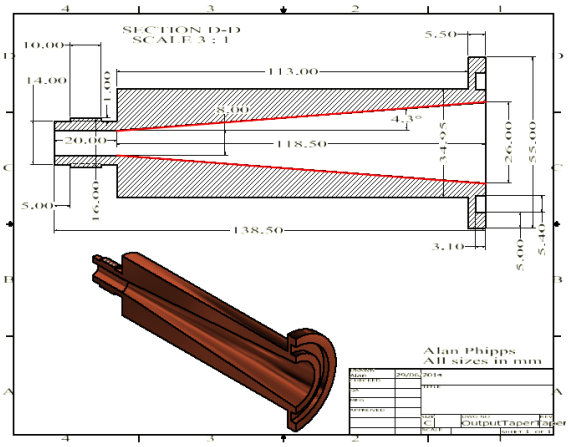

Figure 6.16: The output horn showing O-ring seal for Mylar window that allows the microwaves to leave the vacuum system and enter free space.

The length of the cylindrical section was chosen so as to be able to dismantle the system by moving the solenoid in the longitudinal direction to insert the PSL structure in the centre of the solenoid. The output horn was required so that the wave impedance of the waveguide can be matched to the wave impedance of the room so as to minimise reflection at the output.

6.9.1 Mylar Window

As the output window separates the vacuum from the outside world, the material has to be mechanically strong to withstand atmospheric pressure while at the same time minimising the reflection at the output of the device. This window consisted of 0.127 mm Mylar sheet stretched over the end of the output horn and sealed with a 4 mm cross section O – ring and fixed with Araldite epoxy resin. The Mylar window will be sufficient to maintain the required 1 x 10^{-6} mbar vacuum. A disadvantage of the Mylar window is that it will be restricted to low duty cycle (one pulse per second) since the Mylar will experience heating problems with any increase in the pulse repetition rate.

6.10 The Complete System

This section is designed simply to visualise the full system as seen in Autodesk Inventor 2015, it includes all the components that were manufactured specifically for this system and that were designed by the author. The following image shows all the components that were fabricated and assembled:

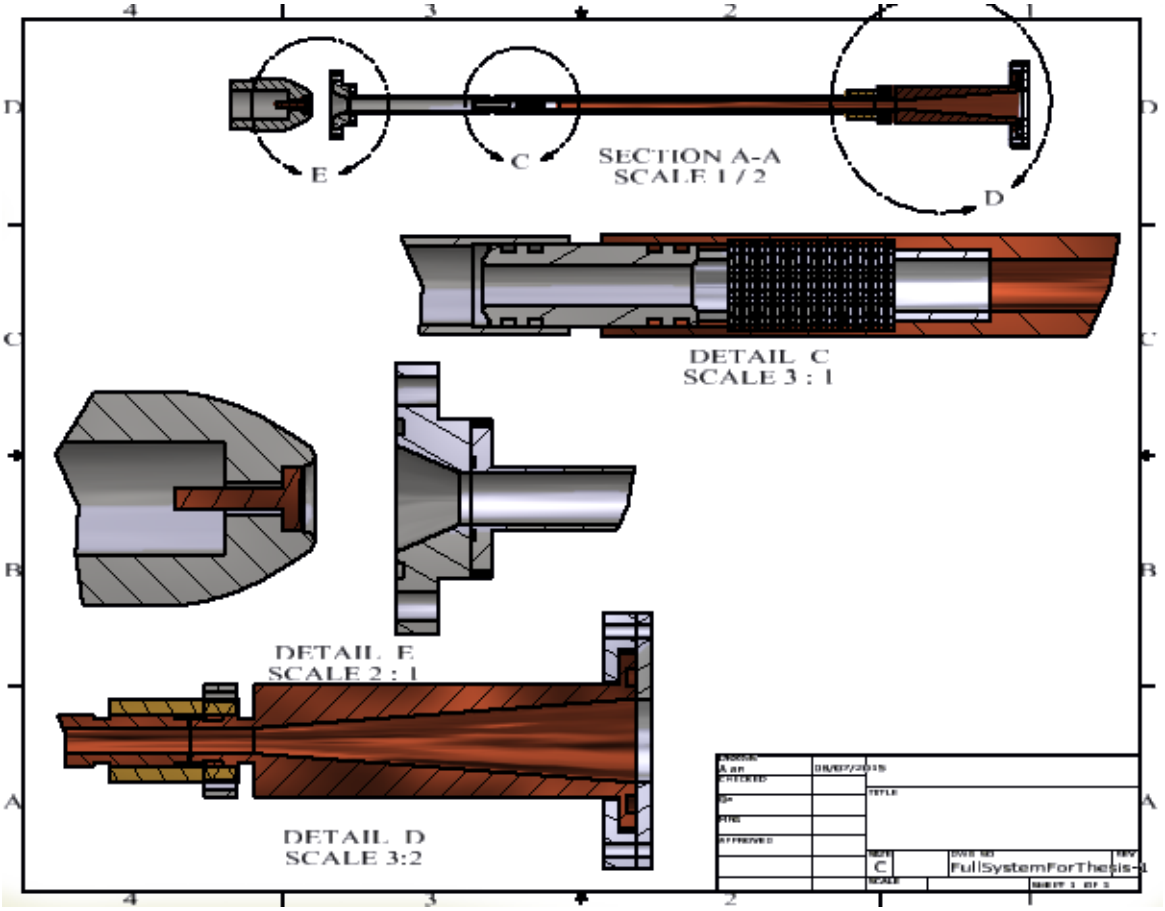

Figure 6.17: The complete system. Many revisions and changes have been made to get to this point, some for practical reasons and some to accommodate the physics involved. All components were designed with the inner diameter of the solenoid (16 mm) as the starting point, meaning that all sizes had to be selected as to fit within an 8 mm radius of the solenoid while still maintaining component strength, the vacuum seal and the ability to accommodate the high electric fields present within the structure.

Figure 6.17 above displays the complete design for the ‘electron beam’ experiment, all components have been designed and simulated and have proven to be suitable for their particular requirement. The particular point in the design process involves many revisions and changes that were implemented in order to accommodate the physical requirements of the experiment with the most important changes being the use of a Pierce type electron source and the use of the 2 T solenoid since these changes involved the biggest changes to the physical setup. A cross sectional schematic diagram of the 2D PSL beam wave interaction region is shown in figure 6.18.

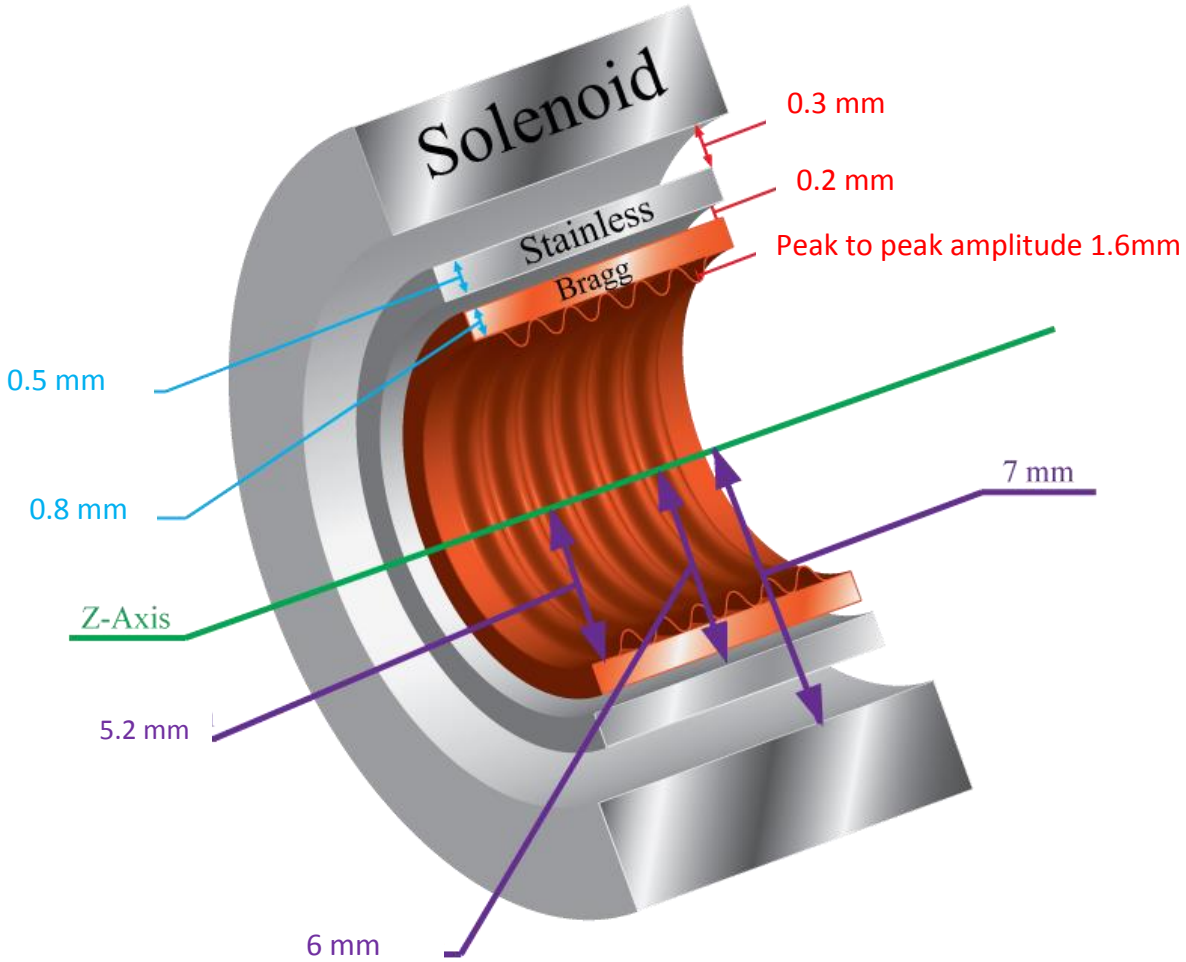

Figure 6.18. Schematic diagram showing the clearance between the 2D PSL (only 1D corrugations shown n schematic), the vacuum jacket and the solenoid

7

Diagnostics, Magnetic Field Profile, Electron Beam and Millimetre Wave Measurements

7.1 System Diagnostics

7.1.1 Electron Beam Diagnostics

The electron beam properties of interest are the electron energy, the profile of the electron beam and current. The measurement of these electron beam parameters are presented in chapter 7 along with measurements of the magnetic field profile used to form and guide the electron beam. Measurement of the frequency of the millimetre wave radiation generated, the output power and mode pattern are also presented.

7.1.1.1 Faraday Cup

A faraday cup is a metal cup or cylinder with a small orifice used to collect the current of the electrons in the beam. The impacting electrons hit the wall transferring a current onto a tap off resistor where the voltage drop across the tap off resistor can be measured using a digital storage oscilloscope. The design of the Faraday cup is relatively simple, a drawing of which can be seen in the figure 7.1. The design has to minimise the number of secondary electrons emitted which can increase errors in the measurement of current. A way of reducing secondary electrons is to specially shape the cup. Due to the current induced in the faraday cup this has to be separated from the other parts of the experiment with an insulator to ensure the current flows through the current measuring resistor. There are two 100 ohm resistors that connect the faraday cup to the beam tube of the experiment which is grounded with a 10 ohm tap off resistor at the bottom connected to a digital oscilloscope. Any current measured by the Faraday cup will then pass through the resistor to earth while the oscilloscope connected to the bottom resistor measures the voltage across it which is futher attenuated with the insertion of 30dB in line attenuator. The impedance of he oscilloscope is 50Ω and hence by measureing the voltage on the oscilloscope the current ca be measured. The cup section of the device was therefore electrically separate from the rest of the experiment and the nylon piece that surrounded the cup section ensured no electrical breakdown. A schematic of the design which is specific to this experimental setup is shown in figure 7.1, as well as a photograph of the Faraday cup diagnostic used in the experiment.

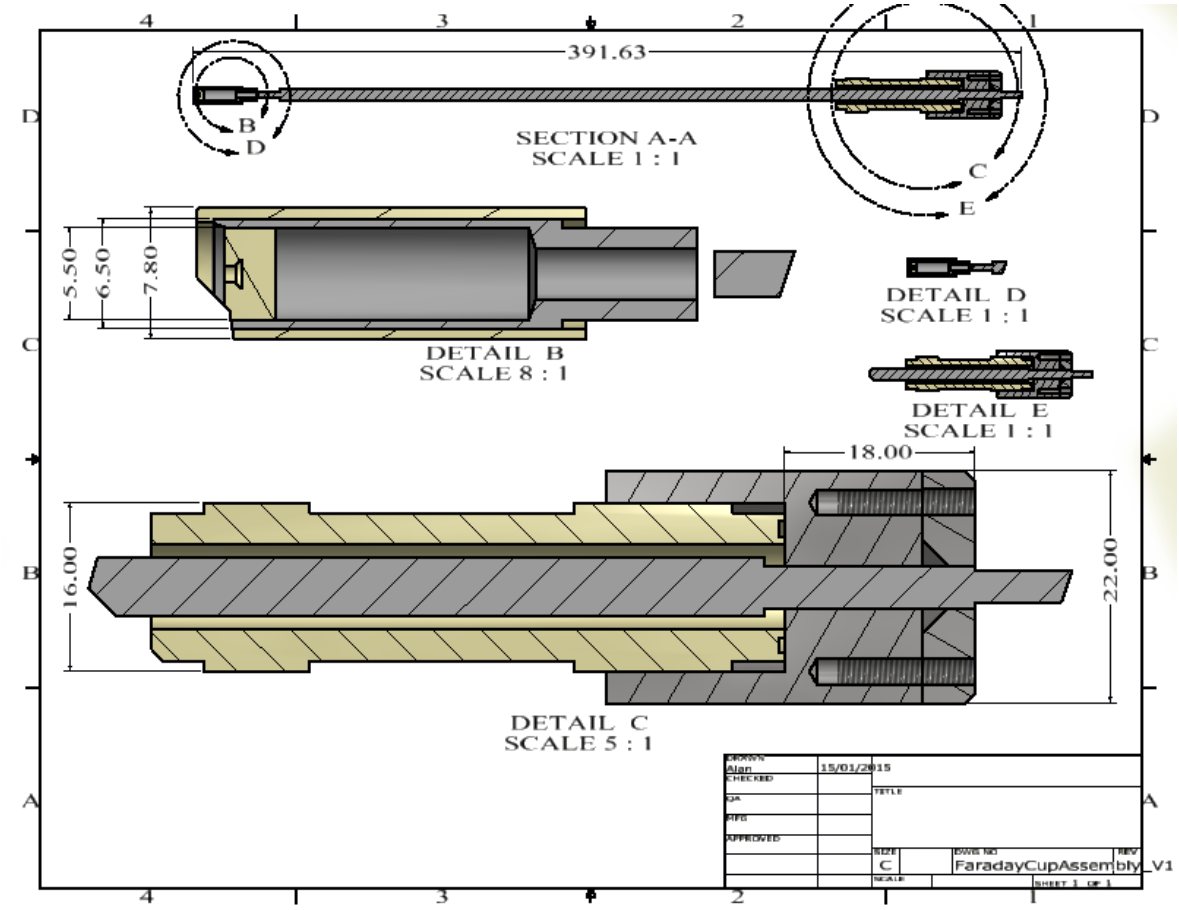

Figure 7.1: The current probe setup as seen in Autodesk Inventor 2015. The overall length of the Faraday cup was 400 mm which results in the cup section sitting within the flat top part of the B – field profile. The main Faraday cup is made from stainless steel and the insulating sections are made from nylon

Figure 7.2: The complete Faraday cup that was built for the experiment. At 400 mm long the cup section was placed within the flat top part of the B – field close to the interaction region. This was used to measure the beam current and to collect information on the tranverse profile of the beam by attaching a thin sheet of electron sensitive material to the front of the Faraday cup which changed colour from yellow to red when struck by electrons.

7.1.1.2 Electron Pulse Profile Diagnostic

The measurement of the size, shape and profile of the electron beam is most commonly performed through a witness plate technique. Using the witness plate technique, a thin sheet of

material is placed directly in the path of the electron beam perpendicular to the direction of propagation enabling the beam size, shape and profile to be measured. For this experiment, the material used was viniprose which changed colour from yellow to red when energetic electrons were incident upon it and which retained its colour when the beam was not intercepted. The viniprose was fixed to the end of the Faraday cup using Araldite glue and was placed in the path of the electron beam in the same position as the PSL structure as well as the location of the Faraday cup when the beam current was measured. A phtotograph of the viniprose after one electron beam pulse impact can be seen in the image below:

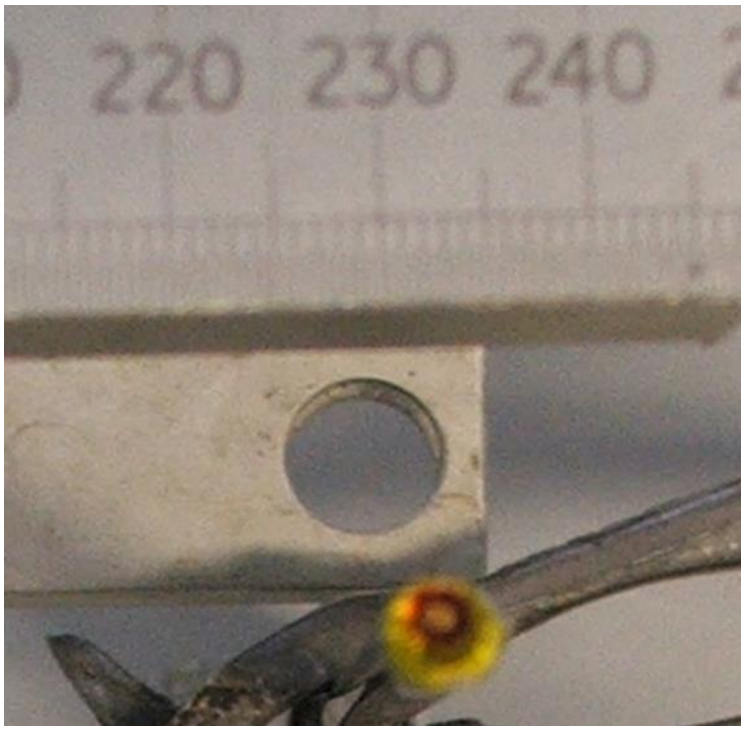

Figure 7.3: The viniprose witness plate displaying the beam shape and profile. The viniprose had a diameter of 6mm with the outer beam diameter of ~4 mm.

The viniprose was placed within the flat top portion of the B – field so as to obtain the beam structure as it would be during the beam - wave interaction, from this pattern the electron beam cross sectional shape was measured. The viniprose had a diameter of 6mm with the outer beam diameter of the beam measured to be ~4 mm.

7.1.1.3 Voltage Pulse Diagnostics

The voltage pulse generated by the Blumlein power supply was measured using a voltage divider, this was necessary since the voltage used in the experiment was far too high to be measured directly. The basic principle of such a diagnostic component is to split the total applied voltage in the ratio of two resistors, thus permitting the magnitude of a large voltage pulse to be evaluated through

the measurement of a considerably smaller signal. The governing equation for the diagnostic may be derived through the dependence of voltage on the resistor ratio governed by.

$$V_{out} = \frac{R_2}{R_1 + R_2} V_{in} \tag{7.1}$$

where V_{in} is the input voltage, V_{out} is the output voltage and the values R_1 and R_2 are the series resistances.

The voltage divider was made up of a series of metal resistors. When constructing such a voltage probe, particular care must be taken to ensure a smooth finish at the joints for the purposes of field relief. A circuit diagram for the diagnostic is shown in Figure 7.4.

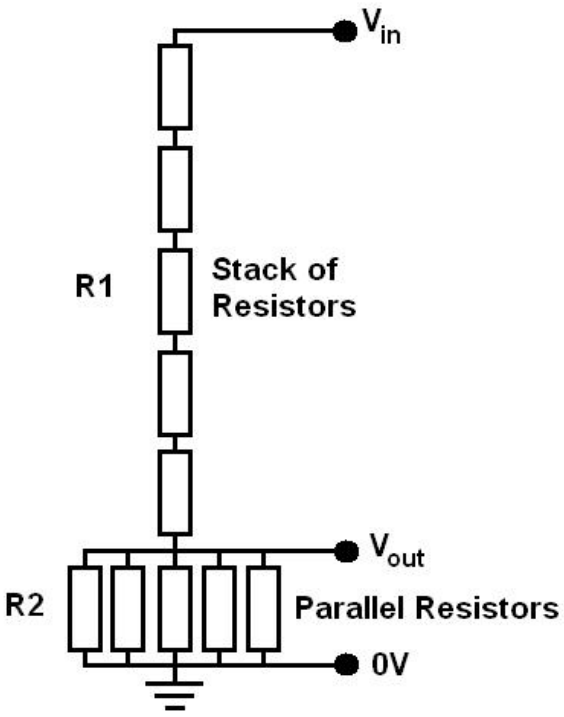

Figure 7.4: Circuit diagram for the resistive voltage probe. Experimentally, the stack consisted of around 225 resistors and the parallel set of about 5 tap off resistors at the bottom of the stack.

The diagnostic was calibrated against a commercially produced probe each operating at voltages up to a maximum of 15 kV. The voltage divider used in this experiment had a stage 1 resistance of 2.8 kOhm with a tap off resistance of 3.3 Ohm. The voltage divider located next to the cable Blumlein generator can be seen in the image below:

Figure 7.5: The voltage divider (red box) can be seen on the right of the Blumlein cable pulser. It consisted of a 2.8 kOhm first stage and a 3.3 Ohm tap of resistor second stage.

7.2 Microwave Radiation Diagnostics

The mm – wave measurements were made using a W – band microwave receiver system that was screened in a metal box. A W – band horn was placed at a point where it could receive radiation through a hole in the box and the entire setup was manually placed at a point of expected high field according to numerical analysis of the farfield mode pattern.

The experiments were operated in single-pulse mode and the microwave receiver system, screened in a metal box, was composed of a small microwave receiving horn followed by attenuators and a Flann microwave detector. Power levels were measured by the W-band Flann rectifying crystal detector, which essentially rectified the millimetre wave signal to produce a DC voltage output. There is a limit to the range of power that can be safely measured using a crystal detector. As a general rule, a crystal should not be exposed to more than a 300 mV signal. The millimetre wave signal was kept to an acceptable level by attenuating the signal using a Flann Microwave FMI2711 Rotary Vane Attenuator (RVA) in front of the rectifying crystal detector.

The detector signals were sent through to a screened control room through low-loss cables where they were observed on scopes and downloaded to a computer. The frequency output was analysed using a series of high pass cut-off filters.

7.3 Electron beam and High Power Millimetre Wave Measurements

7.3.1 Introduction

The culmination of the previous six chapters enabled electron beam and high power millimetre wave experiments to be conducted. Measurement of the magnetic field profile, electron beam accelerating potential, beam current and electron beam profile were carried out using the electron beam diagnostics described in section 7.1. In section 7.3 the measured electron beam is compared to the results of numerical simulation. The millimetre wave radiation generated is also presented. The millimetre wave radiation was measured using a rectified crystal detector with the output mode pattern recorded by scanning the crystal detector across the output window and plotting the magnitude of the millimetre wave pulse as a function of angle. The frequency of the experiment was measured using a series of high pass cut-off filters in combination with the millimetre wave crystal detector with the mode pattern measured in the far field. The measured millimetre wave signal is plotted on the predicted beam- wave dispersion and the beam –wave interaction mechanism anlaysed.

7.3.2 Magnetic Field Profile Measurement

The magnetic field profile created by the solenoid is an important factor in determining the formation of the electron beam. This profile has been predicted numerically in chapter 6 however it is important that the profile is measured to verify the numerical predictions of the magnetic profile. Measurement of the magnetic field was carried out using a Hall probe, which is a device that implements the Hall Effect, where the magnetic field applied to a semi-conductor produces a voltage difference across the semi-conductor and the magnitude of this voltage is proportional to the magnitude of the magnetic field. Using the Hall probe the magnetic field profile was measured as shown in figure 7.6.

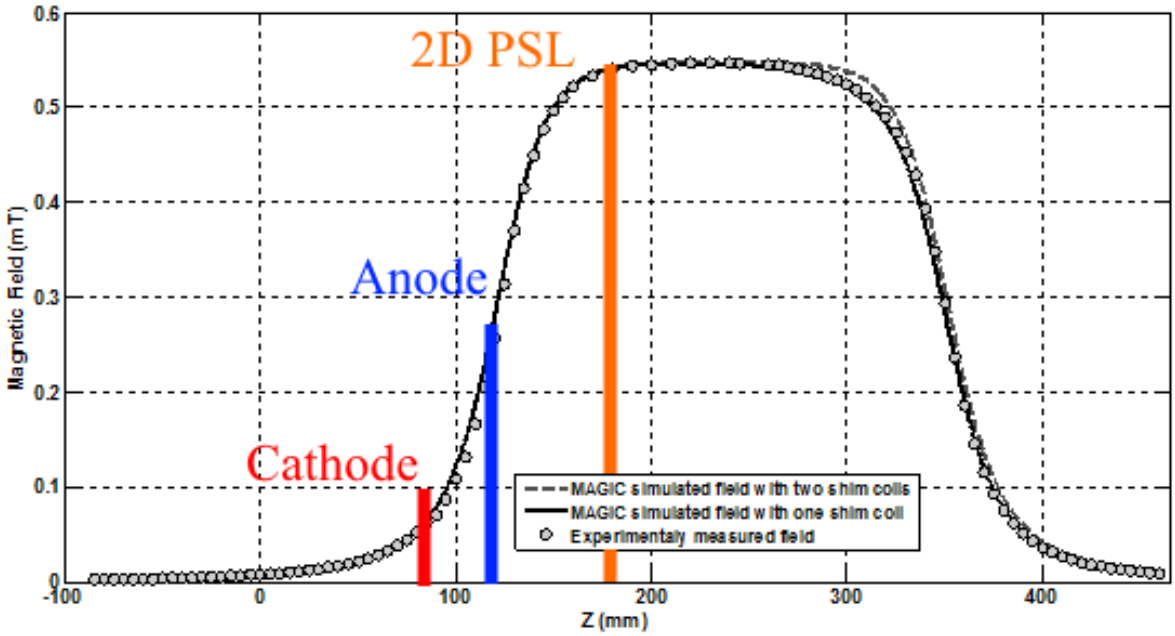

Figure 7.6: Comparison between the numerical and experimental profiles for the magnetic field produced by the solenoid. The units of mT are present since a much smaller current was in use during the testing phase. When running during the experiment a much higher current was used. The shape of the curve will remain the same.

These measurements allowed the correct positioning of the solenoid with respect to the cathode and to ensure the correct beam parameters were obtained within the interaction region. As shown in the simulations it was important that the PSL beam-wave interaction region is positioned as close as possible to the flat top profile of the B-field. The centre of the PSL structure and cathode locations corresponded to position 180 mm and 80 mm respectively as shown on figure 7.6.

7.3.3 Electron Beam Voltage

The voltage pulse produced by the Blumlein cable pulser applied to the diode was measured using the voltage probe described in section 7.1.1.3. The voltage measurements below are a typical example of the pulse produced by the Blumlein cable pulser:

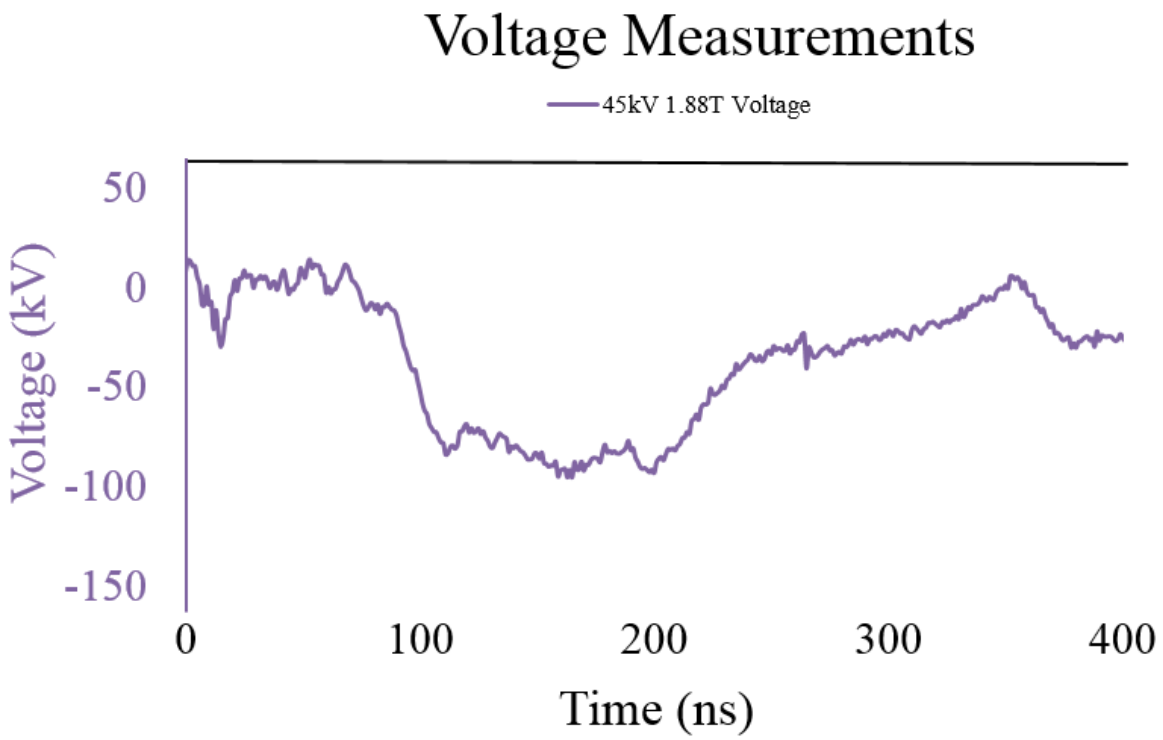

Figure 7.7: The voltage pulse applied to the diode. The voltage in the legend corresponds to the charging voltage.

The voltage pulse produced by the Blumlein cable pulser was approximately 80 kV in the 85 ns flat top portion of the pulse wih a fall and rise time of 20 ns.

7.3.4 Beam Current Measurements

The electron beam current passing through the 2D PSL produced from the velvet cathode and confined by the magnetic field was measured using the Faraday cup beam diagnostics as described in section 7.1.1.1 The experimental results (Figure 7.8) show a steady current of up to 100 A incident on the Faraday cup:

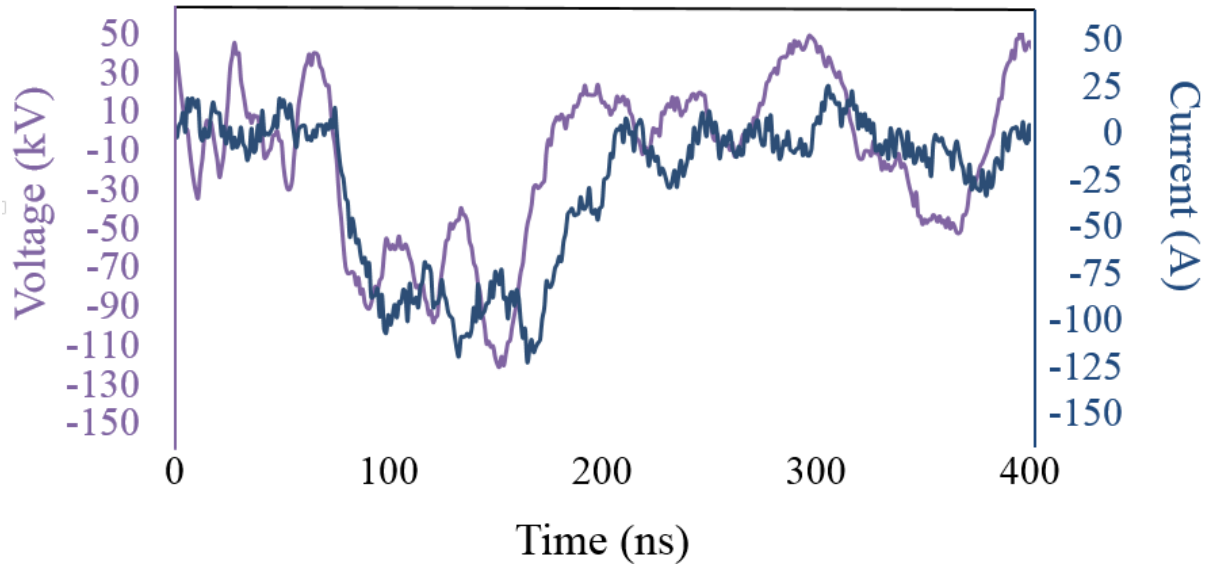

Figure 7.8: The beam current and accelerating voltage seen at the cathode. A value of 80 kV produced a current of approximately 100 A.

The magneitude of the measured beam current was greater than that predicted by numerical simulation. This can be explained in the experiment by a larger area of the cathode such as the surrounding stainless steel electrodes producing current as well as the velvet emitting disk. From simulations the duration of the beam current was sufficient to build-up and feedback microwave radiation in the 2D PSL cavity resulting in the generation of millimetre wave radiation. The current measurements seen at the collection point of the Faraday cup are shown in figure 7.8.

7.3.5 Beam Structure

The position, electron density and cross-sectional geometry of the electron beam were measured through the use of a witness plate. A solid velvet cathode was used in the experiments. To analyse the beam structure a witness plate made from electron sensitive film was inserted at the output of the 2D PSL cavity perpendicular to the direction of the propagating beam. This was achieved by attaching the film to the end of the Faraday cup using Araldite glue. A typical electron beam pulse profile that was recorded is shown in figure 7.9: for one pulse and one cavity B-field configuration at a time. The beam profile produced by the velvet cathode measured by the witness plate is shown in the image displayed in figure 7.9:

Figure 7.9: The electron sensitive witness plate shows the shape of the electron beam after one pulse has passed through the 2D PSL interaction region. The yellow film turns red when high energy electrons impact on the film. It can be clearly seen on the 6 mm diameter witness plate that the electron beam has a circular shape with an outer diameter 4 mm and an inner diameter of 2 mm.

The electron sensitive film itself has an outer diameter of 6 mm. The outer diameter of the electron beam is 4 mm in diameter this would put its outer edge close to 1.2 mm away from the inner diameter of the perturbation. The proximity of the beam to the pertubation greatly affects the millimetre wave output since a more efficient beam – wave interaction would occur the closer the electron beam is located to the perturbations.

Magic 3D simulations were performed with the beam at a distance of 0.5 mm from the perturbation giving a strong coupling between the beam and the wave. This means that in the experiment the beam is more than twice the distance away from the perturbations than the case for the 3D Magic simulations which predicted strong beam-wave interaction. In chapter 8 there will be a discussion on the effect the proximity of the annular electron beam to the perturbations has on the millimetre wave output.

7.3.6 Comparison of Experimental Results with Magic 3D Simulations Incorporating an Idealised Beam

To show how the electron beam cross section measured in the experiment compares to the idealised beam used for the Magic 3D simulations of the beam – wave interaction please refer to figure (7.10) which shows the measured inner and outer diameter of the annular electron beam in the x-y plane superimposed on the idealised beam shape used in Magic 3D represented by the red ring.

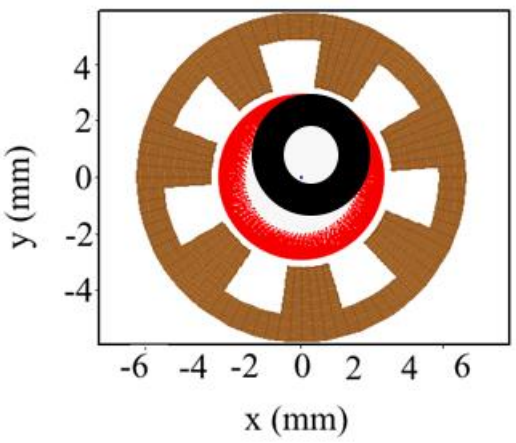

Figure 7.10: The beam spatial profile in the x – y plane as seen in Magic 3D, in a numerical analysis the beam is idealised and hence is perfectly positioned and shaped exactly to ensure strong coupling between the surface wave and the volume wave. The idealised beam in red is 2.7 mm in radius (5.4 mm in diameter) to the beam mid-point, which is to say, half way between inner and outer radii, the beam is also 1 mm thick. The beam in red is 0.5 mm away from the perturbation edge placing it in a region of the strong surface field. The inner and outer black circle represents the position and size of the beam as observed in the experiment using the witness plate diagnostic..

The red image above shows the idealised situation where a perfect beam for this experiment was defined within the 2D PSL interaction region (red cylinder) super-imposed with the beam produced in the experiment (represented by black cylinder the inner and outer diameter). As shown in figure 7.10 the idealised beam sits at exactly 0.5 mm away from the perturbations at all points azimuthally and the beam is uniformly 1 mm thick. The experimentally measured beam is smaller in diameter (4 mm) it is 2 mm thick and is also slightly misaligned, as shown in figure 7.10. In the experiment it was not possible to offset the position of the anode can with respect to the solenoid to ensure the beam propagated down the centre of the 2D PSL due to the outer wall of the vacuum vessel being a tight fit inside the solenoid. The mis-alignment in the experiment is thought to be due to factors such as the cathode support being at a slight angle to the solenoid which was not included in the CST Particle Studio simulations.

7.3.7 Summary of electron beam measurements

The important aspects of the electron diagnostics are the energy of the electrons, the beam shape and current of the electron beam within the 2D PSL cavity region since it is these parameters that dictate the beam dispersion that interacts with the wave that is coupled on the 2D PSL as well as the overall efficiency of the device. It is therefore these aspects that determine the strength and nature of the interaction and the mm – waves produced. Using a 80 kV pulse with a flat-top output of 80 ns in duration produced by the Blumlein cable pulser the Faraday cup measured a beam of duration similar to that of the voltage pulse with beam current of magnitude up to 100 A. The velvet emitter used in the experiment was of a solid velvet cathode. The beam was also found to be reproducible over many shots. The measured beam cross section had an outer diameter of 4 mm and an inner diameter of 2 mm and was similar to that as predicted by CST PS simulations although it was found to be off centre in the experiment. The electron gun design was confirmed by measurement of the

electron beam at the output of the 2D PSL and found to be sufficient for use in the next step of the experiment namely the generation of millimetre wave radiation.

7.4 Millimetre Wave Measurements

To measure the amplitude of the output radiation field from the experiment, a W-band (75 to 110 GHz) Flann rectifying crystal detector with a rotary vane W - band attenuator and Flann 15 dB horn (figure 7.11) were used located at a distance of 0.6 m from the output window.

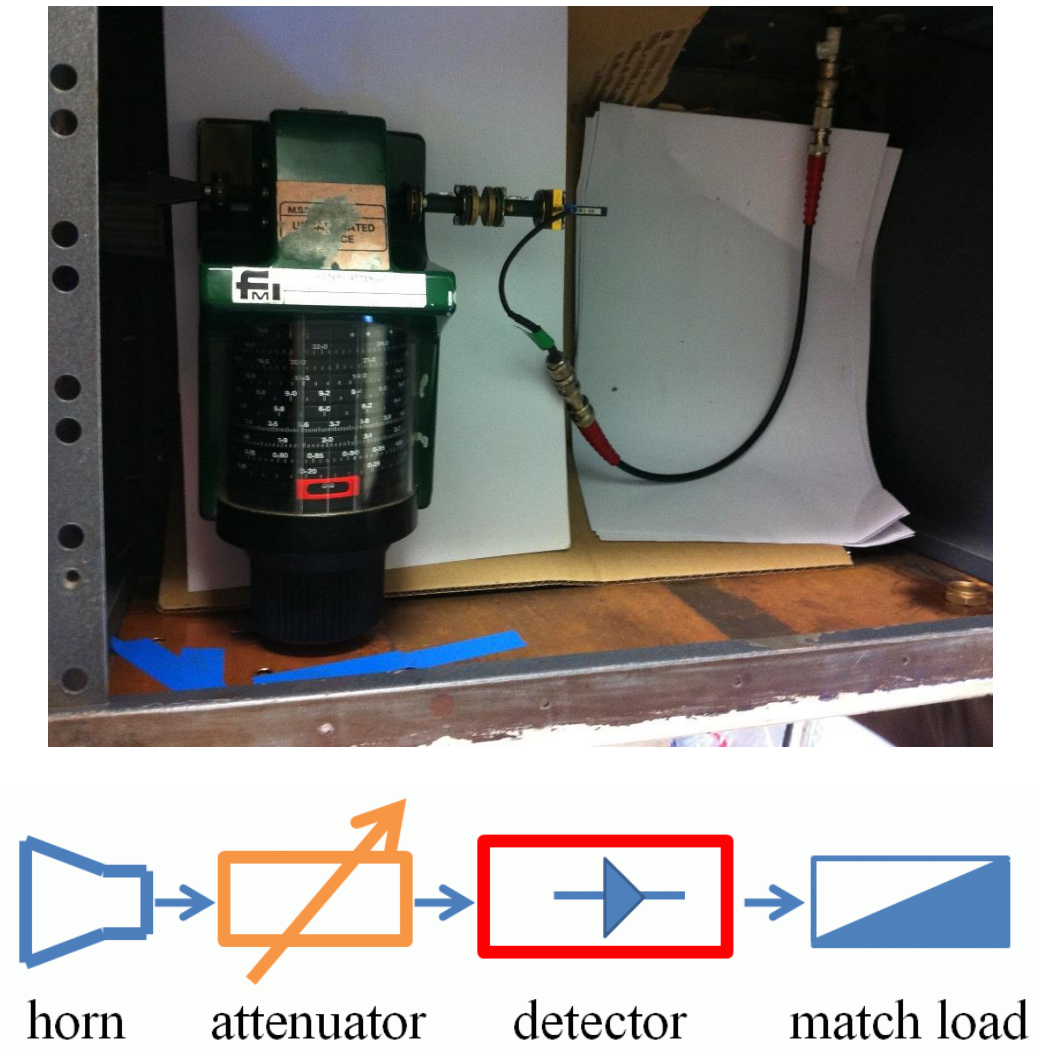

Fig 7.11: The setup of the microwave detector.

The millimetre wave detector consists of a rectangular horn to collect the generated millimetre wave signal, an attenuator to reduce the strength of the signal, a crystal detector to convert the millimetre wave signal into a voltage signal. The millimetre wave signal in mVs was recorded using a digital storage oscilloscope as shown in figure 7.11 after passing through a series of high pass cut-off filters and when there was not cut-off filter, with only the 75 GHz to 110 GHz W-band rectangular waveguide section present which had a cut-off frequency of 60 GHz. The mode pattern was measured

and the power and efficiency calculated. This section ends with a comparison of the measured parameters of the experiment with the Magic 3D simulations and the possible beam-wave interaction points shown on the ω/k dispersion diagram.

7.4.1 Cut-off filters

The high pass cut-off filters provided frequency information about the millimetre wave output when used in conjunction with a Flann W-band millimetre wave detector and W-band attenuator. Cut-off filters were in the form of different diameter hollow cylindrical waveguides situated between the receiving horn and the detector as shown in Figure 7.12. Each cut off filter had a different frequency band of propagation, which will be greatly attenuated as the frequency approached (from the high frequency side) the cut-off frequency.

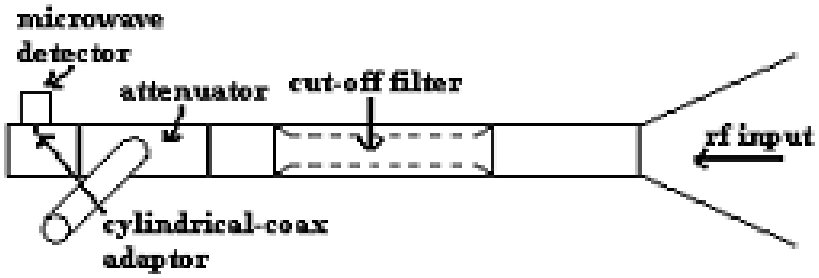

Figure 7.12: Detector apparatus for measuring output millimetre wave radiation generated including input horn, cut off filter, attenuator and detector

Each cut-off filter was placed in the above apparatus during operation of the experiment in order to determine the frequency band of operation. The millimetre wave pulse was measured by the Flann rectified crystal detector with the output recorded on a digital storage oscilloscope with the rectified mV output from crystal detector plotted as a function of time.

7.5 mm-wave Oscillator experiment

Using the analysis from chapter 3, this thesis will concentrate on a device that implements a 1.6 mm longitudinal period periodic surface lattice that has a peak to peak amplitude of 1.6 mm (parameters as shown in the table 7.1 below) interacting with an electron beam.

Parameter	Symbol	Value
Longitudinal Period	dz	1.7 mm
Azimuthal Period	Δm	3.5mm

Number of Longitudinal Periods	n	16
Amplitude	dr	0.8 mm
Amplitude (Peak-to-Peak)	dr (pk-pk)	1.6mm
Inner Radius of input and output waveguide	r	4 mm
Minimum radius of perturbation (ID)	r_{min}	3.6 mm
Mean radius	r_0	4.4 mm
Maximum radius of perturbation (OD)	r_{max}	5.2 mm

Table 7.1: The physical parameters of the 2D PSL structure that is used in the 'hot' experiment

The periodic surface lattice (PSL) was designed with a beam – wave interaction in mind as well as being able to accommodate the physical parameters of the structure in the guide magnetic field. Having selected a 16 mm bore water cooled solenoid to generate the 1.8 T axial magnetic field and having successfully modelled the design numerically, the next phase was to build the PSL that will be used in the electron beam experiment.

7.6 Fabrication Process

7.6.1 High Speed Milling

Previous experiments (chapter 4) using PSLs that were manufactured using a high speed milling process that begins by producing an aluminium former that represents the shape of the vacuum space within the 2D PSL structure, as seen in CST (see chapter 4). This aluminium former is then sent to Waveform Electroforming Ltd which grew the copper onto the surface of the aluminium using an electrolyte solution. More copper than is needed is grown onto the mandrel and the component is then machined to the correct size using a lathe. The entire component is then returned to Waveform to have the aluminium dissolved out using an alkaline solution, the complete piece is then ready use.

7.6.2 High Resolution 3D Printing and Injection Moulding

The 3D printing process is a two stage process [7.1]. The first stage involves creating a wax former to the 10's of microns scale and then using this former to create a mould for the component where the silver – chromium molten alloy is deposited, with the resulting part having a resolution of ±

125 microns. Although this resolution is not as high as the previous milling process, it does have the advantage of taking a lot less time to reach the finished part and so in conjunction with the cheaper cost, the 3D printing process is more efficient overall. A new 2D PSL was created for use in the electron beam experiment, manufactured to a different set of physical parameters when compared to the previous 3D printed PSL. The parameters are the same as those used in the numerical analysis and can be seen in table 7.1. Below are images of the silver 2D PSL:

Figure 7.13: The 3D printed 2D PSL for use in the electron beam experiment. The structure was made with an oversized outer radius and then turned in a lathe by our ABP technician to the required outer diameter of 13.5 mm.

Figure 7.14: Here the 3D printed 2D PSL seen end on, showing the perturbations on the inner wall of the structure. The square nature of the perturbations can be seen both azimuthally and longitudinally.

Figure 7.15: The length of the PSL is 16 x 1.6 (25.6) mm longitudinal periods with two straight sections aat either end.

7.7 Vector Network Analyser measurements in G-band of the 2D PSL used in the 2nd harmonic gyrotron BWO experiment

The 2D PSL that was used in the beam – wave interaction experiment was manufactured using the 3D printing method with a modest D/λ of 2.1 to ensure it fitted within the 16 mm bore of the 1.8T solenoid coil. The corrugation amplitude of 0.8 mm (peak to peak amplitude of 1.6 mm) was chosen to investigate the interaction of the electron beam with a propagating electromagnetic wave.

Using the serpentine co-axial mode converter similar to the one described in chapter 4 but operating in G-band 140 GHz to 220 GHzz a $TM_{0.n}$ wave was launched into the high contrast (1.6 mm deep corrugation) 2D PSL with the transmission measured over the G-band (140GHz to 220GHz) frequency range using an Anritsu ME7808B Broadband Lightening Vector Network Analyzer VNA with two transmit and receive SM5952 140-220 GHz OML extender heads as shown in figure 7.16

Figure 7.16: Anritsu ME7808B Broadband Lightening Vector Network Analyser with SM5952 140-220 GHz OML heads

The launching of the $TM_{0.n}$ mode in the 2D PSL was achieved with the setup shown in figure 7.17

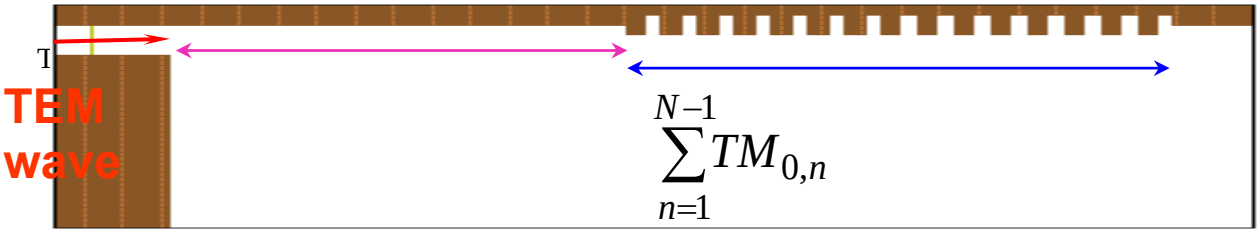

Figure 7.17: Shows the launching of a $TM_{0,1}$ mode from circular serpentine mode converter to a TEM mode in the co-axial conical horn to a $TM_{0,n}$ in the cylindrical silver 2D PSL

When testing the structure using the VNA the interaction produces an electromagnetic wave that is interacting with the 1.6 mm longitudinal period giving a response in G-band resulting in a resonance at 187.7GHz as shown in figure 7.18 showing the millimetre wave transmission as a function of frequency.

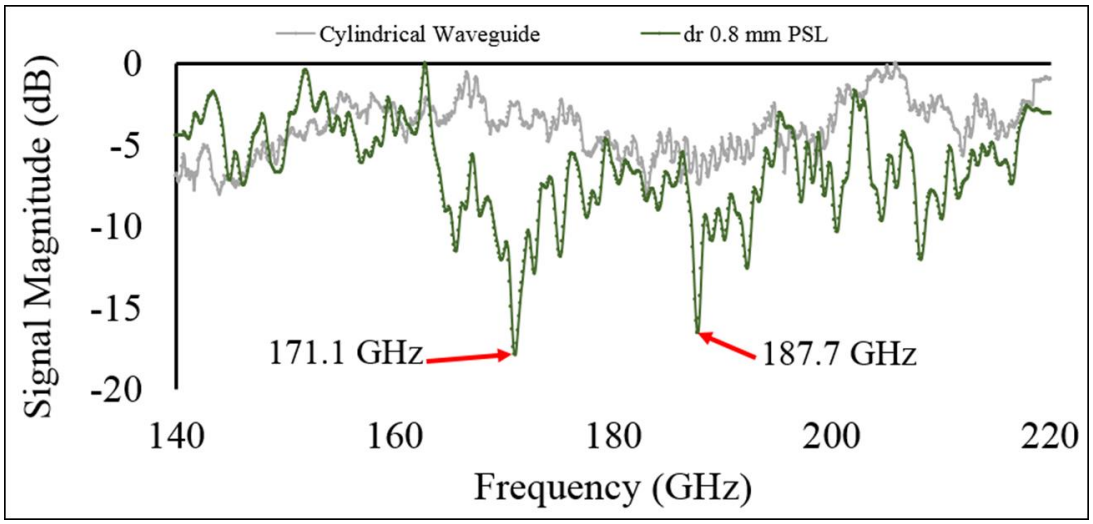

Figure 7.18: The measured transmission as a function of frequency of the 2D PSL over the 140 GHz to 220 GHz frequency range

For an electron beam with an accelerating potential of 80 kV, γ= 1.156, a beam alpha of 0.4, v_z of 0.46c, v_{perp} of 0.19c and dz= 1.6 mm, equation 3.51 indicates the localized surface wave will cross the y-axis on the ω / *k* dispersion diagram at ~ 85 GHz

$$\omega = \mathbf{k}_z v_z \pm \frac{2\pi}{d_z} v_z \sim 85 \text{ GHz} \tag{7.2}$$

The electromagnetic wave when interacting with the 3.5 mm azimuthal period will give a fundamental resonance in W-band at ~85 GHz and a resonance at the 1st harmonic at 171.1 GHz in G-band (this is what gives the 171.1 GHz resonance shown in the VNA measurement). At zero axial wavenumbers from equation (3.65) with a longitudinal period of 1.6 mm and with the magnitude of the longitudinal electron beam velocity 0.46c [corresponding to an accelerating potential of ~80 kV] the electron beam will excite the longitudinal 1.6mm period at a frequency of ~ 85 GHz.

$$\begin{aligned} \omega &= \frac{2\pi}{d_z} v_z \\ f &\sim \frac{v_z}{d_z} \\ f &\sim 85 \text{ GHz} \end{aligned} \tag{7.3}$$

The electron beam driven 2D PSL can be regarded as a W-band structure from the point of view of the frequency of the output of the radiation source. It is because the electron beam is travelling in this case at about half the speed of light and it is the electron beam that is exciting of the longitudinal structure in "W-band".

7.8 Millimetre wave measurements from 2nd harmonic Gyrotron BWO

7.8.1 Frequency Measurements

Figure 7.19 below displays the power output as measured in mV from the crystal detector in relation to the particular cut – off filter that was in place during a particular shot, note that a number of shots were taken for each filter and these are simply representative of the power achieved over successive shots. Figure 7.19 demonstrates that the millimetre wave output lies between ~80 GHz and 85 GHz. Although the magnitude of the power varies a little when different filters were used it is clear that the mm wave output is produced at a frequency of interaction of the 2D PSL surface and volume field at ~80 GHz.

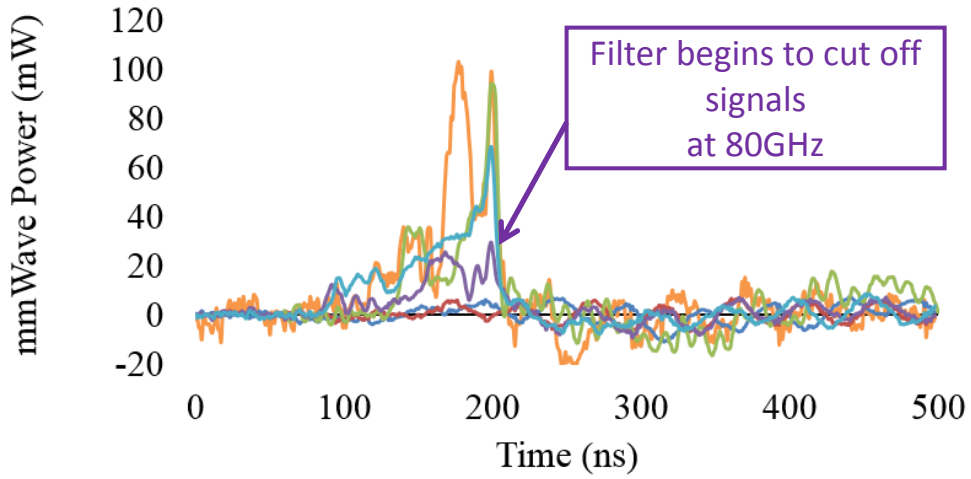

Figure 7.19: The power produced in the presence of a particular cut – off filter. Light blue line 70 GHz, Green line – 75 GHz, Purple line 80 GHz, red line 85 GHz dark blue line 95 GHz. It is noted that using a 85 GHz cut – off filter results in no mm wave output at all with output measured for cut-off filters above 80 GHz indicating that the signal lies below 85 GHz.

7.8.2 Mode Structure Analysis

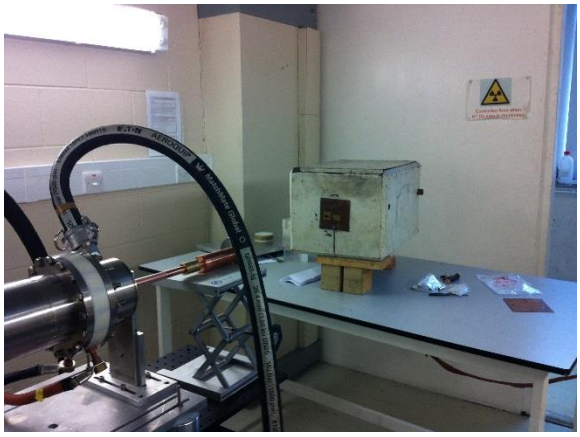

Figure 7.20: The mode scan setup with the detector housed within the white box and positioned approximately 60 cm away from the output horn.

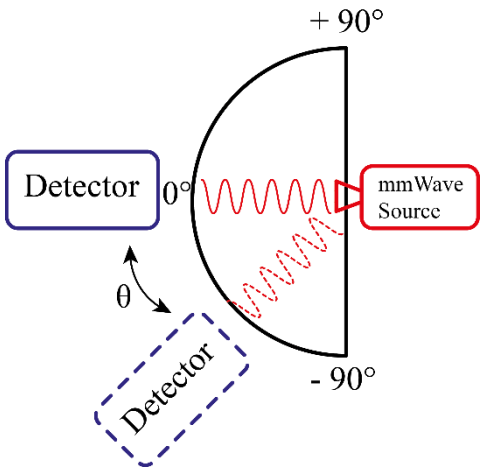

Figure 7.21: A schematic of the mode scan setup demonstrating how the detector was scanned across the output window.

In order to understand the mode generated, a farfield analysis was performed on the output mode launched through the horn and Mylar window. This was performed using the experimental setup shown in Figure 7.20 and 7.21. Here, a sector plate marked in single degree intervals, θ, was used, with the output horn and window located at the centre of the semi-circular plate and a rectangular waveguide receiving antenna mounted above the plate at the other end of the semi-circle. The apertures of the 2D PSL output horn and the detector receiving horn were separated by a distance, 0.6 m. The receiving antenna was positioned on a moveable rail, allowing measurements that could be taken at values of θ between -90° and 90°, as shown in Figure 7.21. In order to ensure accuracy with the measurements, the output aperture of the experiment was placed directly above the pivoting point of the semi-circular plate.

Upon exiting the output horn the electric field distribution of the wavefront changes and expands continually as the wave propagates forward. This process reaches a final state at a distance referred to as the far – field distance. Mathematically determined by the equation $2D^2/\lambda$ where D is the aperture diameter and λ is the operating wavelength, this distance is the point at which a measurement can be taken showing a mode pattern that will be distinct from other modes, meaning that the waveguide mode that was seen inside the vacuum system determines the distribution of the far – field so that no two modes have exactly the same far – field pattern. This can be used to help identify which operating mode interacts with the beam inside the 2D PSL structure. The mode scan results are shown in figure 7.22:

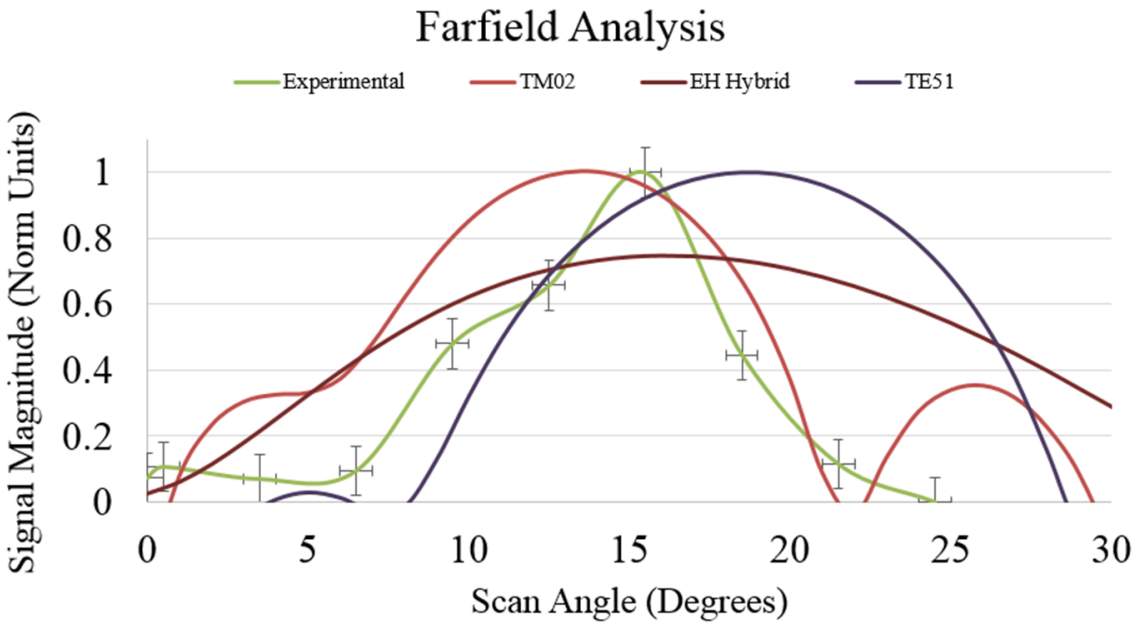

Figure 7.22: From the mode scan results measurements the peak of the green curve corresponds best due to a combination of the $TM_{0,2}$ mode and the $TE_{5,1}$ mode, the EH hybrid ($TE_{5,1}$ / $TM_{0,2}$) mode only exists in the cavity which then mode converts and is represented by the brown line. Although it is difficult to make a perfect match the mode pattern measurements indicates that the more likely mode pattern is a combination of the $TM_{0,2}$ volume and $TE_{5,1}$ surface mode.

The frequency as measured using the cut-off filters and the mode pattern analysis combined suggest that it is plausible that the interacting mode is a combination of the $TM_{0,2}$ volume mode and the $TE_{5,1}$ surface wave due to a 2nd harmonic gyrotron interaction via analysis of the dispersion curve plotted in chapter 3. The four main candidates for electron oscillation are 1) a 2nd harmonic gyrotron backward wave interaction at 80 GHz with the operating eigenwave due to the coupling of the $TM_{0,2}$ volume mode with the $TE_{5,1}$ surface wave, 2) a 2nd harmonic gyrotron backward wave oscillator interaction with a pure $TE_{5,1}$ mode (80 GHz) although it is important to note the gyro-BWO with a deep corrugation the preferred mode of interacton is with a hybrid EH type wave, 3) a 2nd harmonic gyrotron Backward Wave Oscillator with a pure $TM_{0,2}$ mode (75 GHz) and 4) a BWO interaction operating with the first spatial harmonic of the $TM_{0,2}$ volume mode (75 GHz).

The ω/k dispersion diagram for the 2D PSL constructed and described in chapter 3 for coupling between the $TM_{0,2}$ volume mode and the $TE_{5,1}$ surface mode is shown in figure 7.23

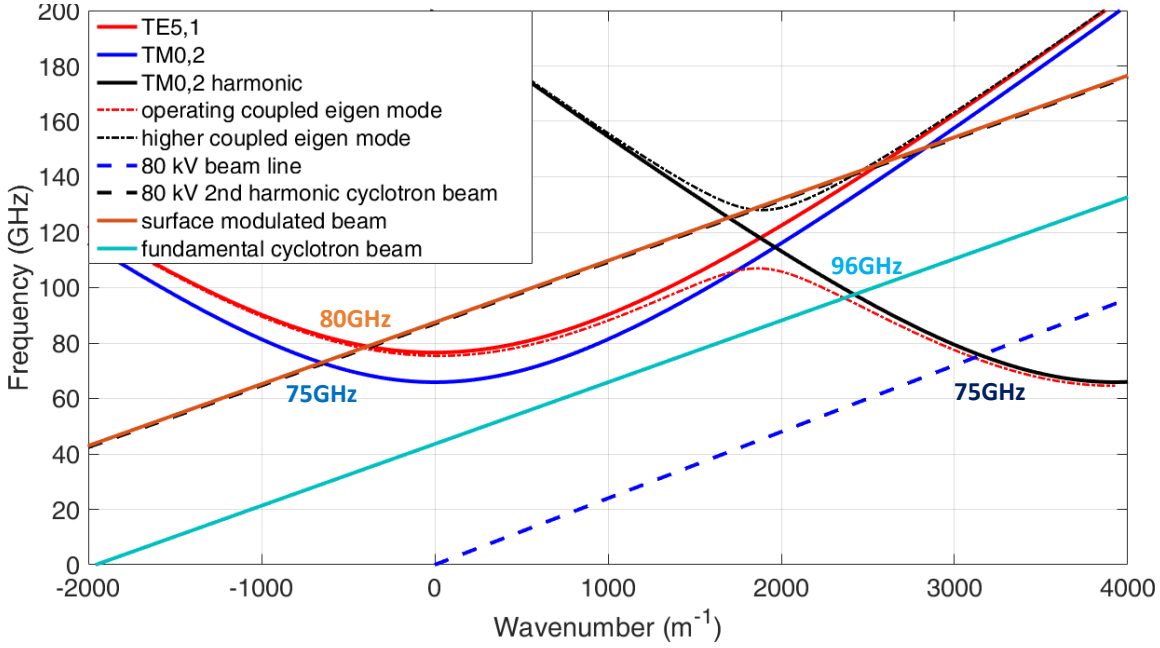

Figure 7.23 Frequency as a function of axial wavenumber of the $TM_{0,2}$ mode and the surface $TE_{5,1}$ wave for a 2nd harmonic gyrotron BWO interaction (black dotted line). The orange line represents the electron beam–electromagnetic wave interaction with the synchronous harmonic of the cavity eigenmode's partial surface field at the lattice interface. The light blue solid line represents the fundamental gyrotron BWO interaction for a cavity magnetic field of 1.8 T. The straight dark blue dotted line represents the negative energy space charge wave of a beam of axial velocity 0.46c with a beam plasma frequency of 3 GHz (appendix C) indicating a grazing with the backward and the first spatial harmonic of the $TM_{0,2}$ mode.

The peak of the measured mode pattern indicate the interaction could be a 2nd harmonic gyrotron backward wave interaction at 80 GHz with the operating eigenwave due to the coupling of the $TM_{0,2}$ volume mode with the $TE_{5,1}$ surface wave, although to conclusively experimentally prove which interaction is dominating a more accurate 1) frequency measurement using a heterodyne frequency diagnostic and 2) mode pattern measurement are required which will be part of the future work.

7.8.3 Power & Efficiency Calculation

Each measurement seen on the oscilloscope has a corresponding power value assigned to it determined by the calibration curve of the detector. The overall power of the entire output signal can be calculated once a mode scan has been performed. By summing all the measured signal magnitudes then by multiplying by the average distance between the values on the x – axis and then by multiplying by 2π and lastly by dividing by the area of the receiving horn aperture the total power output can be approximated. The output power is an important factor when attempting to calculate the efficiency of the device and ultimately serves as a standard for future optimisation. The overall efficiency of the device is a standard by which the beam – wave interaction can be judged, this value represents the number of electrons that contribute to the output power, what proportion of their kinetic

energy they pass to the wave and how much energy is lost in the entire process. Generally for a 2nd harmonic gyrotron BWO device an efficiency of 20 % would be considered a very good achievement. The efficiency calculation is the total millimetre wave output wave power divided by the electron beam power (P = IV).

Using the previously mentioned process the total output power seen in the experiment was calculated to be 134 ± 20 kW. The process by which this value was calculated only takes into account the main lobe of the output since beyond this the measurement was indistinguishable from noise, the signal was also subject to losses at many points in the process that may not be included in a simulation. The movement of the detector at three degree intervals may not have included the point of largest field in the theta or phi axes and the conversion from millivolts to milliwatts is also a source of error from the analysis of the calibration curve of the detector. By taking all these factors into account it can then be seen that the reduction of the output power from what was seen in the Magic simulation to what was measured in the experiment is realistic. From an input power (P = IV) of 100 A x 80 kV = 8 MW and a output power of 134 kW, the efficiency of the device was estimated to be ~1.7 %. This efficiency is quite low and represents a weak beam – wave interaction. The cause of this, other than the errors mentioned above is the fact that the beam is not close to the perturbations as well as being mis-aligned. Because of this the beam does not interact with the surface field as efficiently as it could which will affect the output frequency, mode pattern and power measured and ultimately result in the low efficiency of 1.7%. It cannot be stressed enough the importance of having the 80 kV electron beam close to the wall and to have the PSL structure in good alignment to the electron beam. At W – band frequencies this is difficult to achieve in the experiment. In a future experiment a superconducting magnet will be used with its bore diameter of 50 mm as compared to the 16 mm of the solenoid used in the first experiments making it easier to align the cathode to be radially central to the PSL and to have a cathode structure immersed in a strong magnetic field to produce a thin annular electron beam with most of the velocity of the electrons in the axial direction with a radius close to the surface of the PSL structure [6.2].

7.9 Summary of Experimental Measurements

Experiments have been carried out demonstrating a beam – wave interaction within a 2D PSL structure. A 100 A mildly relativistic electron beam produced by 80 kV Pierce type electron gun driven by a Blumlein generator and confined by a 1.8 T solenoid was used. Cut-off filter frequency measurements ascertained that the frequency was ~80 GHz. The frequency measurements combined with mode pattern analysis indicate evidence of a 2nd harmonic gyrotron BWO beam-wave interaction with a cavity eigenmode produced by the coupling of a $TM_{0,2}$ volume field and a $TE_{5,1}$ surface field coupling within the interaction region of a 2D SWS.

An 80 kV Pierce type electron gun and a 1.8 T magnetic field guided a 100 A electron beam through the 2D PSL cavity generating approximately 134 ± 20 kW of millimetre wave power resulting in a relatively weak beam – wave interaction of ~1.7 % efficiency. This experiment does demonstrate that the 2D PSL can be used to promote the successful beam – wave interaction for high power mm wave generation. It is important to note however that as a direct consequence of the beam not being as close to the perturbations as desired which in this case was 1.8 mm radially from the wall, and also beam mis-alignment there existed the possibility of a pure 2^{nd} harmonic gyrotron BWO interaction. For for a high contrast periodic surface lattice (corrugation depth of 1.6 mm is greater than $\lambda/4$) a hybrid EH type mode can be excited. The mode pattern measurement along with the cut-off filter measurements gives some evidence of an interaction with a cavity eigenmode produced by the coupling of a $TM_{0,2}$ volume field and a $TE_{5,1}$ surface field within the 2D SWS. To conclusively experimentally prove the dominant interaction a more accurate 1) frequency measurement using a heterodyne frequency diagnostic and 2) a higher resolution mode pattern measurement is required which will be part of future work

8

Conclusions and Future Work

8.1 Conclusions and Future Work

8.1.1 Introduction

The work presented in this thesis describes the theoretical, numerical and analytical design, simulation and experiments of a 2nd harmonic W-band gyrotron BWO based on a 2D periodic surface lattice. The numerical design of the 2nd harmonic gyrotron BWO is described. This was followed by numerical simulation of the 2D PSL and the construction of the structure. The construction details of the experiment and finally the experimental results of the electron beam generated and observation of millimetre wave radiation from the W-band 2nd harmonic gyrotron BWO possibly due to the coupling of a $TM_{0,2}$ volume field and a $TE_{5,1}$ surface field on the 2D PSL are summarised

Chapter 8 combines the results and conclusions from the various chapters and explains the results gained and comparison, where appropriate, between the results achieved via theory/simulation and experiment. This chapter will also introduce the future work of the research which will build on the successful 2D PSL structure developed during this thesis.

8.1.1 Summary of high contrast 2D PSL structure

A high contrast 2D PSL structure was designed for a W-band 2nd harmonic gyrotron Backward Wave Oscillator. A novel 3D printing technique was used to manufacture in silver a 7.2 mm inner diameter 2D periodic surface lattice. A Vector Network Analyser was used to measure the transmission through the 2D PSL. It was observed in experiments that coupling between a 'near grazing', obliquely incident wave and a surface field is possible if a high-contrast structure (having the corrugation amplitude larger than a quarter of the operating wavelength) is used. The millimetre wave transmission through the 2D PSL was measured with good agreement between theory and measurement achieved.

8.1.2 Summary W-band Backward Wave Oscillator Experiments

An electron gun based on a velvet cathode was designed and constructed. Experiments were conducted using the electron gun with the electron accelerating voltage produced by a cable Blumlein generator and the electron beam formed and transported through the 7.2 mm inner diameter silver 2D PSL beam-wave interaction region using a 1.8.T guide magnetic field. An 80 kV, 100 A electron beam of diameter of 4mm was measured. Propagating the electron beam through the 2D PSL 2nd harmonic gyrotron BWO produced millimetre wave radiation at a frequency of ~80 GHz at an output power of 134 ± 20 kW corresponding to an operating efficiency of ~1.7 %. Using the electron beam parameters measured in the experiment as the input beam parameters for a Magic particle-in-cell code

simulation, good agreement between experimental measurements and numerical simulation was achieved.

Evidence has been observed of mildly relativistic electron beam excitation of a 2nd harmonic gyrotron BWO with a specifically tailored cavity eigenmode consisting of the superposition between a $TM_{0,2}$ incident Volume Field (VF) and a structurally induced $TE_{5,1}$ Surface Field (SF) on the high contrast 2D PSL structure. The peak of the electric field of the measured mode pattern gives evidence that the output millimetre wave radiation generated is a combination of the $TE_{5.1}$ surface wave and the $TM_{0.2}$ volume mode. To conclusively experimentally prove the dominant interaction a more accurate frequency measurement in the form of a heterodyne frequency diagnostic and mode patter measurement will be required as detailed in the future work section.

8.2.2 Future work

8.2.2.1 Improved Heterodyne frequency diagnostic

A W-band 100 GHz heterodyne frequency diagnostic will be used to achieve a more accurate measurement of the frequency of oscillation. An in-band fundamental mixer (Millitech MXP-10-R) and a local oscillator signal produced from a 95 GHz Gunn diode (Millitech GDM-10-1013IR) would be used and the resultant intermediate frequency (IF) signal recorded on a 20 GHz, deep memory digitising oscilloscope (Agilent DSX-X 92004A). By applying a fast Fourier transform (FFT) to the IF signal recorded on the fast digitizing oscilloscope, it would be possible to determine the frequency of oscillation more accurately as compared to the use of high pass cut-off filters.

8.2.2.1 Improved mode scan measurement

An imporved mode scan can be achieved by automating the measurement with the use of a stepper motor to physcailly move the detector in 0.5 degree intervals across the output window with the system computer controlled enabling the amplitude of the millimetre wave signal to be recorded in smaller degree steps on a pulse to pulse basis.

8.2.2.2 Upgrade experimental equipment

8.2.2.2.1 Optimisation of high voltage power supply

Future work would be to use a high current accelerator as shown in figure 8.1 where (I) is a Marx bank power supply (V_{max} =1.5MV), (II) 10Ω coaxial transmission line filled with deionised water (15MΩ/cm), (III) is an output switch, (IV) plasma flare emission annular electron gun, (V) magnetic field system with the 2D PSL interaction region located at the centre of the solenoid.

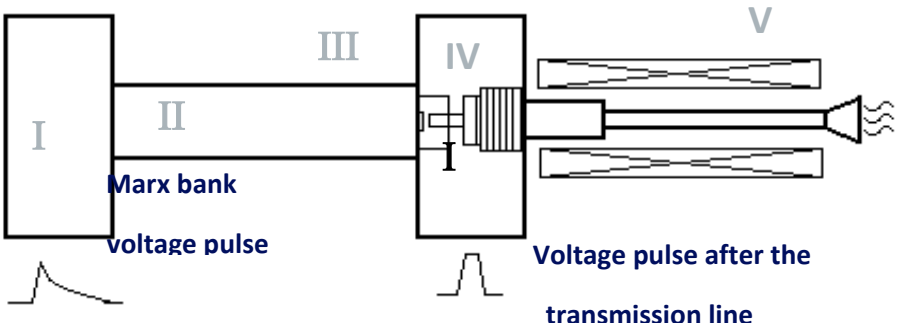

Figure 8.1 Deionized water filled transmission line.

The High Current Accelerator (HCA) has been built and tested. The output voltage of the Marx bank (fig.8.2a) and the transmission line (fig.8.2b) were measured using an aqueous copper sulphate voltage probe. The transmission line was connected to the HCA and the output voltage from the transmission line can be used for generation and acceleration of the electron beam when applied to the annular carbon cathode of the explosive emission electron gun.

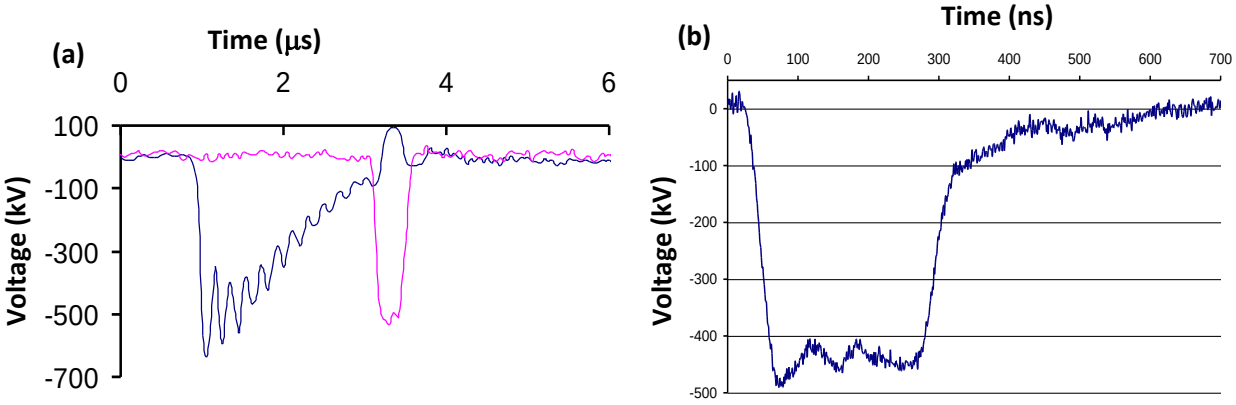

Fig. 8.2 Pulse waveforms of (a) Marx bank (blue line) and transmission line (magenta line) and (b) output voltage from transmission line (blue line)

8.2.2.2.2 Use a thin annular carbon cathode confined in the 50 mm bore of a magnetic field (6 T) produced by a superconducting magnet

Carbon, or more specifically, Graphite in a 50 mm anode can placed within the bore of a 0 to 9 T superconducting magnet would be used to generate a thin annular beam close to the wall of the 2D PSL structure. The design of the cathode is similar to that of velvet glued onto copper, the only difference being that the carbon cathode incorporates a knife edge emitting surface. A carbon cathode design was created in Autodesk Inventor 2015 and was fabricated by Erodex UK Ltd, this design is shown below with the actual cathode shown in the right image:

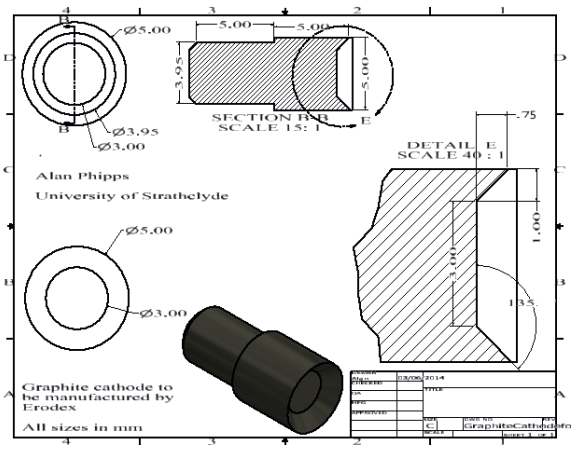

Figure 8.3: The carbon cathode to be manufactured by Erodex showing the knife edge surface from which the annular electron beam will be produced.

Figure 8.4: The carbon cathode, created by Erodex UK Ltd. Here we can see the knife edge that will emit the electrons when a high enough electric field is applied to the sharpened carbon knife edge .

The annular electron beam would be confined in the strong magnetic field produce by a superconducting magnet capable of generating a magnetic field of up to 9 T as shown in figure (8.5).

Figure 8.5 Oxford Instruments superconducting magnet

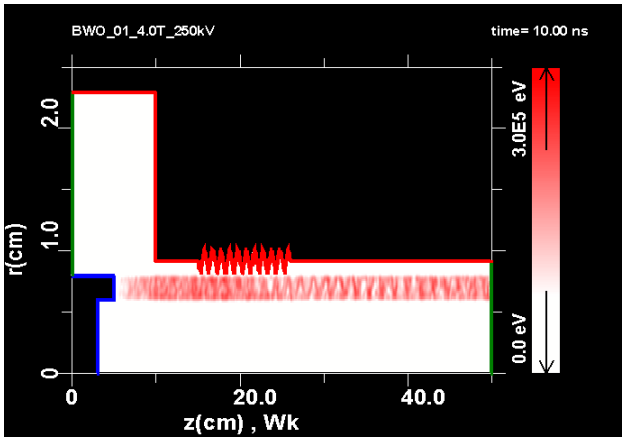

Figure 8.6 KARAT particle in cell simulation of the generation of annular electron beam produce by a sharpened carbon knife edge cathode

8.2.2.3 Numerical simulations of a 20 mm diameter 2D PSL

Numerical simulations of the electron beam produced by the carbon cathode was carried out using the particle in cell code KARAT, figure 8.6. An electron beam of current 1.6 kA, voltage of 300 kV, of outer radius of 9 mm and inner radius of 8 mm was modelled

The use of the superconducting magnet and the carbon cathode immersed in the strong axial magnetic field of 6 T would enable a 1 mm thick electron beam of inner radius of 8 mm and outer radius of 9 mm to propagate close to the wall of the 2D PSL allowing selectivity of the structure while operating at a frequency of 97 GHz when D/λ is equal to ~7. The structure of parameters detailed in table 8.1 and ref [8.1] would be used

Parameter	Symbol	Value
Longitudinal Period	dz	3 mm
Azimuthal Variations	m	16
Number of Longitudinal Periods	n	20
Amplitude	dr	0.5 mm
Amplitude (Peak-to-Peak)	dr (pk-pk)	1mm
Minimum radius of perturbation (ID)	r_{min}	9.5 mm
Mean radius of perturbations	r_0	10 mm
Maximum radius of perturbation (OD)	r_{max}	10.5 mm

Table 8.1: The parameters for the next step in the process

In the model (r_0 = 10 mm, r1 = 0.5 mm, $\overline{m}$ =16) the volume wave has the structure of a $TM_{0,6}$ mode of the cylindrical waveguide, while the surface wave is associated with the surface $HE_{16,1}$ wave. The structure's parameters were chosen to operate at 97 GHz with the field evolution inside the cavity modelled using the 3D software package MAGIC. The eigen mode formation predicted by Magic is shown in figure 8.7

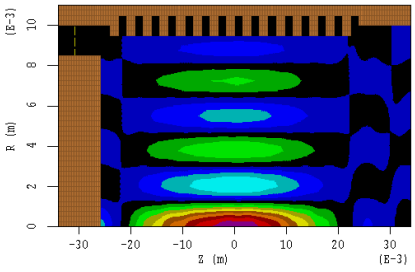

Figure 8.7 2D contour plot of the Ez field component associated with "volume" field of the cavity eigenmode having 6 radial variations.

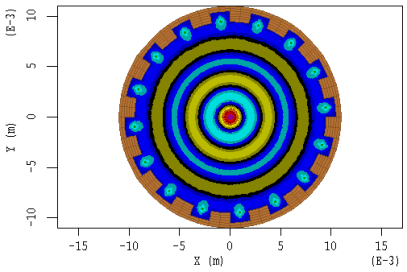

Figure 8.8 The contour plots of the longitudinal electric (Ez) component of the field inside the cavity observed using the 3D code MAGIC

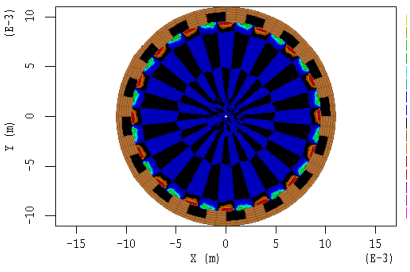

Figure 8.9 The contour plots of the magnetic (Bz) component of the field inside the cavity observed using the 3D code MAGIC

The 2D PSL cavity can be driven by a relativistic (300 kV), high current (1.6 kA) electron beam of annular (mean radius - 8 mm, wall thickness – 1 mm) geometry. The electrons propagating in the vicinity of the lattice behaved as a set of oscillating dipoles having a frequency of

$$\Omega_{eff} = 2\pi \frac{v_z}{d_z} \tag{8.1}$$

(v_z is the axial velocity of the electron, d_z is the corrugation period). These dipoles excite an EH mode inside the lattice, the superposition of which results in a surface field having an azimuthal variation number equal to the number of lattice azimuthal variations. To observe a resonant interaction between the electron beam and the EM fields the synchronism condition.

$$\omega - k_z v_z = n\Omega_{eff} \tag{8.2}$$

has to be met, where ω is the angular frequency of the EM wave and k_z is the axial wavenumber. The interaction occurs with the surface waves ($HE_{16.1}$) are excited and couple with the $TM_{0,6}$ wave. The superposition of both fields forms the cavity eigenmode and ensures effective energy accumulation. The lasing takes place due to diffraction of the $TM_{0,6}$ wave while the $HE_{16,1}$ wave interacts with electrons and synchronizes the energy extraction from the different parts of the beam. Figure 8.10, generated by the 3D code MAGIC, shows the electron beam trajectory inside the interaction region indicating a dependence of the wave-beam coupling on the distance between the beam and the structure (see the insert). An interaction between the electron beam and the Ez component of the EM field manifests itself in the formation of the electron density wave which as expected increases along the interaction region. In fig8.11 the spectrum of the output radiation is shown and a single mode operation at a single frequency of 97 GHz is demonstrated. The dependence of the output power on the guide magnetic field strength was also studied and the variation of the efficiency versus guide magnetic field is presented in figure 8.12. To observe an efficiency of 30 % the guide field needs to be ~6 T.

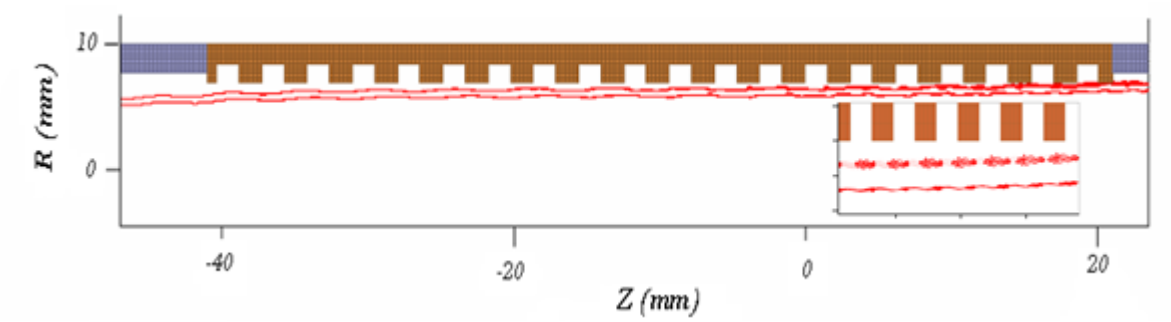

Figure 8.10 Results of numerical studies showing the relativistic electron beam trajectories inside the cavity with strong interaction between the electrons and surface wave manifesting itself in electron density wave formation (inserts) i.e. electron bunch formation

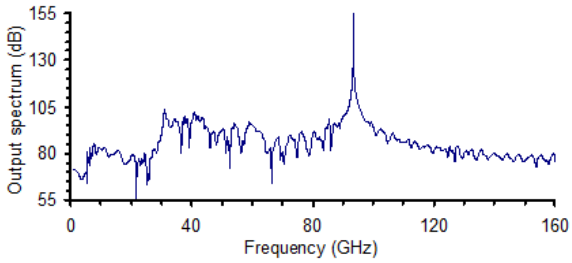

Figure 8.11 The output spectrum showing operation at ~97 GHz;

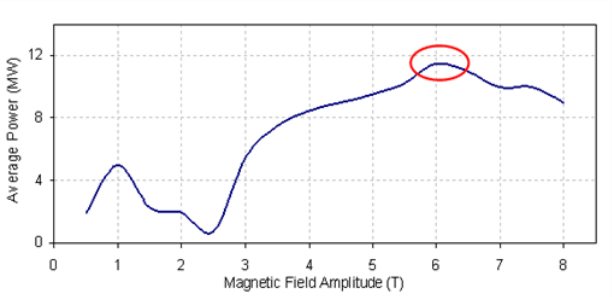

Figure 8.12 The variation in average output power with magnetic field amplitude.

From figure 8.10 we can see bunching of the electron beam occurring close to the structure, with the operating frequency 97 GHz and having an average output power of approximately 10 MW(x16). Note that this study is only performed for one sector of the entire structure due to the extensive run time (>50 hrs), the corresponding power value should therefore be multiplied by 16, giving a value ~160 MW

In the simulations an axial magnetic field of 6 T was used to guide a 1.6 kA, 300 kV annular electron beam with a mean radius of 8.5 mm and beam thickness of 1 mm through the 2D PSL where the beam was located 0.5 mm away from the inner diameter of the 2D PSL. Numerical simulations predict excitation of the 2D PSL by this electron beam will generate 160 MW of power at an operating frequency of 97 GHz corresponding to an electronic efficiency of 30 %.

Future work will involve using the carbon cathode, superconducting magnet and larger diameter (20 mm) 2D PSL structure to experimentally verify the predictions from the Magic simulations.

References

[1.1] B. I. Cohen, R. H. Cohen, W. M. Nevins, T. D. Rognlien, "*Theory of free-electron laser heating and current drive in magnetized plasmas*", Rev. Mod. Phys. **63**. 1991.

[1.2] V. L. Granatstein, W. Lawson, "*Gyro-Amplifiers as Candidate RF Drivers for TeV Linear colliders*", IEEE Trans. Plasma Sci., **24**, 1996.

[1.3] W. P. Leemans, C. G. R. Geddes, J. Faure, Cs. Tóth, J. van Tilborg, C. B. Schroeder, E. Esarey, G. Fubiani, D. Auerbach, B. Marcelis, M. A. Carnahan, R. A. Kaindl, J. Byrd, and M. C. Martin, Phys. Rev. Lett. **91**, 074802, 2003.

[1.4] P. Weightman, in Proceedings of the 32nd International Conference on Infrared and Millimetre Waves and 15th International Conference on Terahertz Electronics, pp.1-3, v.1. September 2-7, 2007.

[1.5] I. Evgenya, I. Smirnova, Amit S. Kesar, Ivan Mastovsky, Michael A. Shapiro, and Richard J. Temkin, Phys. Rev. Lett. **95**, 074801 (2005).

[1.6] J. R. Sirigiri, M. A. Shapiro, and R. J. Temkin, Phys. Rev. Lett. **90**, 258302 (2003).

[1.7] N. S. Ginzburg, A. A. Kaminsky, A. K. Kaminsky, N. Yu. Peskov, S. N. Sedykh, A. P. Sergeev, and A. S. Sergeev, Phys. Rev. Lett. **84** 3574 (2000).

[1.8] N. S. Ginzburg, N. Yu. Peskov, A. S. Sergeev, Opt. Commun., **96**, p.254, 1993.

[1.9] I. V. Konoplev, A. W. Cross, P. MacInnes, W. He, C. G. Whyte, A. D. R. Phelps, C. W. Robertson, K. Ronald, A. R. Young, Appl. Phys. Lett., **89**, 171503, 2006

[1.10] C. C. Cutler, J. Appl. Phys., 27(9), p.1028, 1956; H. F. Webster, J. Appl. Phys., 28(12), p.1388, 1957; H. F. Webster, Phys. of Plasmas, **7**, p.94, 2000.

[1.11] N. S. Ginzburg, N. Yu. Peskov, and A. S. Sergeev, Opt. Commun. **112**, 151 (1994).

[1.12] I. V. Konoplev, A. W. Cross, A. D. R. Phelps, K. Ronald, Phys. Rev. E, 68, 066613, 2003.

[1.13] A. W. Cross, I. V. Konoplev, K. Ronald, A. D. R. Phelps, W. He, C. G. Whyte, N. S. Ginzburg, N. Yu. Peskov, and A. S. Sergeev, Appl. Phys. Lett., **80**, 1517, 2002.

[1.14] N. S. Ginzburg, A. S. Sergeev, N. Yu. Peskov, G. R. M. Robb, A. D. R. Phelps, IEEE Trans. Plasma Sci. **24**, p.770, 1996.

[1.15] N. S. Ginzburg, N. Yu. Peskov, A. S. Sergeev, I. V. Konoplev, A. W. Cross, A. D. R. Phelps, G. R. M. Robb, K. Ronald, W. He, C. G. Whyte, J. Appl. Phys. **92**, p.1619, 2002.

[1.16] A. W. Cross, I. V. Konoplev , A. D. R. Phelps, K. Ronald, J. Appl. Phys., **93**, p.2208, 2003.

[1.17]. N.S. Ginzburg, A.S. Sergeev, N.Yu Peskov, I.V. Konoplev, G.R.M. Robb, A.D.R. Phelps, "Mode competition and control in free electron lasers with one and two dimensional Bragg

resonators”, Nuclear Instruments & Methods in Physics Research Section a: Accelerators, Spectrometers and associated equipment, **375**, pp202-206, 1996.

[1.18] I.V. Konoplev, “Free Electron Maser with two-dimensional distributed feedback”, PhD Thesis, University of Strathclyde Physics Dept. ABP Group, 2001.

[1.19] P. MacInnes, PhD Thesis, “The experimental investigation of a free-electron maser defined by a co-axial 2D-1D Bragg lasing cavity” University of Strathclyde Physics Dept. ABP Group, 2005.

[1.20] I.V. Konoplev, A.W. Cross, P. MacInnes, W. He, A.D.R. Phelps, C.G. Whyte, K. Ronald, and C.W. Robertson, "*Free-electron maser based on a cavity with two- and one-dimensional distributed feedback*," *Appl. Phys. Lett*. **92**, 211502, 2008.

[1.21] I.V. Konoplev, L. Fisher, A.W. Cross, A.D.R. Phelps, K. Ronald, and M. Thumm, "*Excitation of surface field cavity and coherence of electromagnetic field scattering on two-dimensional cylindrical lattice*," *Appl. Phys. Lett.* **97**, 261102, 2010.

[1.22] I.V. Konoplev, L. Fisher, K. Ronald, A.W. Cross, A.D.R. Phelps, C.W. Robertson, C.W. Robertson, and M. Thumm, "*Surface-field cavity based on a two-dimensional cylindrical lattice*," *Appl. Phy. Lett*. **96**, 231111, 2010.

[1.23] I.V. Konoplev, L. Fisher, A.W. Cross, A.D.R. Phelps, K. Ronald, and C.W. Robertson, "*Surface wave Cherenkov maser based on a periodic lattice*" *Appl. Phys. Lett*. **96**, 261101, 2010.

[1.24] L. Fisher, “Novel cavity design for high power microwave applications”. PhD Thesis, University of Strathclyde Physics Dept. ABP Group, 2010.

[1.25] A. R. Phipps, et al, “Periodic Structure towards the Terahertz Region Manufactured

Using High Resolution 3D Printing”, *8th UK-Europe-China Workshop on mm-waves and THz Technologies, 2015, Cardiff, UK.*

[1.26] A.R. Phipps, et al, “Electron Beam Excitation of Coherent Sub-Terahertz Radiation in Periodic Structures Manufactured by 3D Printing*” Nuclear Instruments and Methods in Physics Research B, accepted for publication, (2017)*

[1.27] E. Mazzucato, “*Localized measurement of turbulent fluctuations in tokamaks with coherent scattering of electromagnetic waves*”, Physics of Plasmas, **10**, 3, March 2003.

[1.28] V. Erckmann, U. Gasparino, “*Electron cyclotron resonance heating and current drive in toroidal fusion plasmas*”, IoP Plasma Physics and Controlled Fusion, **36**, 12, 1994.

[1.29] J. M. Watson, "*Status of the Los Alamos FEL*", Nuclear Instrumentation Methods, A250, p1, 1986.

[1.30] M. A. Agafonov et al. "*Generation of hundred joule pulses at 4mm wavelength by FEM with a sheet electron beam*", IEEE Trans. Plasma Science, **26**(3), p531, 1998.

[1.31] S. Nakamura and G. Fasol, "*The Blue Laser Diode*", Springer, Berlin 1997.

[1.32] G. G. Denisov and M. G. Resnikov, Izvest. Vyssh. Ucheb. Zaved. Radiofizkika, **25**, 5, 1982.

[1.33] H. Kogelink and C. V. Shank, "*Coupled Wave Theory of Distributed Feedback Dye- lasers*", J. App. Phys., **43** 1972, 2382.

[1.34] I. V. Konoplev, A. W. Cross, A. D. R. Phelps, W. He, K. Ronald, C. G. Whyte, C. W. Robertson, P. MacInnes, N. S. Ginzburg, N. Yu. Peskov, A. S. Sergeev, V. Yu. Zaslavsky, and M. Thumm, "*Experimental and theoretical studies of a coaxial free-electron maser based on two-dimensional distributed feedback*", Phys. Rev. E **76**, 056406 (2007).

[1.35] I. V. Konoplev, A. W. Cross, W. He, A. D. R. Phelps, K. Ronald, G. R. M. Robb, C. G. Whyte, N. S. Ginzburg, N. Yu. Peskov and A. S. Sergeev, "*Progress of the Strathclyde Free Electron Maser experiment using a 2D Bragg structure*", Nuclear Instruments and Methods in Physics Research Section A: Accelerators, Spectrometers, Detectors and Associated Equipment, Volume **445**, Issues 1-3, 1 May 2000, Pages 236-240

[1.36] I. V. Konoplev, A. W. Cross, A. D. R.Phelps, K. Ronald, M. Thumm, "*Coaxial 2D Bragg structures for microwave electronics*", 36th European Microwave Conference, 2006, p1366 – 1369.

[1.37] P. MacInnes, I. V. Konoplev, A. W. Cross, W. He, A. D. R. Phelps, C. G. Whyte, K. Ronald, C. Robertson, M. Thumm, "*Coaxial 2D-1D two-mirror cavity free-electron maser experiment*", IEEE 35th International Conference on Plasma Science, 2008.

[1.38] I. V. Konoplev, P. MacInnes, A. W. Cross, W. He, A. D. R. Phelps, K. Ronald, C. G. Whyte, C. W. Robertson, "*2D and 1D surface photonic band gap structures for accelerator applications*", Proceedings of EPAC 2006, Edinburgh, Scotland.

[1.39] N. S. Ginzburg, N. Y. Peskov, A. S Sergeev, A. D. R. Phelps, I. V. Konoplev, G. R. Robb, A. W. Cross, A. V. Arzhannikov, S. L. Sinitsky, "*Theory and design of a free-electron maser with two-dimensional feedback driven by a sheet electron beam*", Phys Rev E Stat Phys Plasmas Fluids Relat. Interdiscip. Topics, 1999, **60**(1):935-45.

[1.40] N. S. Ginzburg, V. Yu. Zaslavskii, A. M. Malkin, N. Yu. Peskov and A. S. Sergeev, "*Frequency stabilization in free-electron masers with 2D and 1D distributed feedback*", Volume **54**, Number 9, 1384-1388, Short Communications, Technical Physics.

[1.41] N. S. Ginzburg, V. Yu. Zaslavskii, A. M. Malkin, N. Yu. Peskov, A. S. Sergeev and M. Tumm, "*Azimuthal selection of modes in free-electron masers with coaxial Bragg resonators*", Journal of Communications Technology and Electronics Volume **54**, Number 9, 1015-1026, Microwave Electronics.

[1.42] A. W. Cross, W. He, I. V. Konoplev, A. D. R. Phelps, K. Ronald, G. R. M. Robb, C. G. Whyte, N. S. Ginzburg, N. Y. Peskov, A. S. Sergeev, "*Experimental and theoretical study of 2D Bragg structures for a coaxial free electron maser*", Nuclear Instrum. Methods Phys. Res., A 475, 1-3 (2001) 164-172.

[1.43] A. W. Cross, N. S. Ginzburg, W. He, I. V. Konoplev, N. Y. Peskov, A. D. R. Phelps, G. R. Robb, K. Ronald, A. S. Sergeev and C. G. Whyte, 2000, "*Experimental and theoretical study of a high-power co-axial FEM with 2-D distributed feedback*", International FEL Conference, Duke Free electron Laser laboratory (USA).

[1.44] S. E. Tsimring, "*Electron Beams and Microwave Vacuum Electronics*", 2007, Wiley Interscience.

[1.45] N. S. Ginzburg, N. Yu. Peskov, and A. S. Sergeev, I. V. Konoplev, A W. Cross, A. D. R. Phelps, G. R. M. Robb, K. Ronald, W. He, and C. G. Whyte, J. Appl. Phys., Vol. **92**, No. 3, 1 August 2002.

[1.46] I. V. Konoplev, P. McGrane, W. He, A. W. Cross, A. D. R. Phelps, C. G. Whyte, K. Ronald, and C. W. Robertson, Phys. Rev. Lett. **96**, 035002 (2006).

[1.47] I. V. Konoplev, P. McGrane, K. Ronald, A. W. Cross, W. He, C. G. Whyte, A. D. R. Phelps, C. W. Robertson, D. C. Speirs, N. S. Ginzburg, N. Yu. Peskov, A. S. Sergeev and M. Thumm, "*Free Electron Lasers and Synchrotron Radiation*", Joint 30th Int. Conf. on Infrared and Millimeter Waver & 13th Intl. Conf. on Teraherthz Electronics, 2005.

[1.48] I. V. Konoplev, A. W. Cross, W. He, A. D. R. Phelps, K. Ronald, G. R. M. Robb, C. G. Whyte, N. S. Ginzburg, N. Yu. Peskov, and A. S. Sergeev, Nuclear Instruments and Methods in Physics Research, A, **445** (2000) p236-240.

[1.49] I. V. Konoplev, A. D. R. Phelps, A. W. Cross, K. Ronald, P. McGrane, W. He, C. G. Whyte, N. S. Ginzburg, N. Yu. Peskov, A. S. Sergeev and M. Thumm, Nuclear Instruments and Methods in Physics Research, A, **528** (2004) p101-105

[1.50] I.V. Konoplev, A.W. Cross, P. MacInnes, W. He, A.D.R. Phelps, C.G. Whyte, K. Ronald, and C.W. Robertson, "*Free-electron maser based on a cavity with two- and one-dimensional distributed feedback,*" *Appl. Phys. Lett*. **92**, 211502, 2008.

[1.51] L. Fisher, 2010 "*Novel cavity design for high power microwave applications*", PhD thesis, University of Strathclyde.

[2.1] D. Constable, PhD Thesis, "*The Numerical and Experimental Investigation of Gyro-Multiplier Configurationsd*", Strathclyde University, 2013.

[2.2] Pozar D.M., 2004, "*Microwave Engineering*.", New York: Wiley.

[2.3] Lorrain, Corson, Lorrain, 1987, "*Electromagnetic Fields and Waves"*, W. H. Freeman and Company, New York.

[2.4] J. Vanderlinde, "*Classical Electromagnetic Theory*", Kluwer Academic Publishers, 2005.

[2.5] V. L. Granatstein and I. Alexeff, "*High Power Microwave Sources*", Artech House, Boston and London, 1987.

[2.6] S. H. Gold and G. S. Nusinovich, American Institute of Physics, Rev. Sci. Instrum., **68** (11) Nov. 1997.

[2.7] K. R. Chu, "*Review of Modern Physics*", Vol. **76**, April 2004.

[2.8] V. A. Flyagin, A. V. Gaponov, M. I. Petelin, and V. K. Yulpatov, IEEE Trans. on Microwave Theory and Tech., Vol. MTT-25, No. 6, June 1977.

[2.9] S. C. Zhang and M. Thumm, Appl. Phys. Lett. **88**, 033514 (2006).

[2.10] A. Grudiev and K. Schunemann, IEEE Trans. Plasma Sci. Vol. **30**, No. 3, June 2002.

[2.11] K. K. Chow, and R. H. Pantell, Proceedings of the IRE, Vol. **48**, Issue 11, p 1865-1870, Nov. 1960.

[2.12] Astaykin A. I.,"Microwave Devices and Applications", RFNC-VNIIF, ISBN 5-85165-400-7, pp 152-162, 2012.

[3.1] J.M. Watson, "*Status of the Los Alamos FEL*", Nuclear Instrumentation Methods, A250, p1, (1986).

[3.2] M.A. Agafonov et al. "*Generation of hundred joules pulses at 4mm wavelength by FEM with a sheet electron beam*", IEEE transaction on plasma science, **26**(3), p531. (1998).

[3.3] S. Nakamura and G.Fasol, "*The Blue Laser Diode*", (Springer, Berlin, 1997).

[3.4] G.G. Denisov and M.G. Resnikov, Izvest. Vyssh. Ucheb. Zaved. Radiofizkika, **25**, (5), (1982), 407-413

[3.5] H. Kogelnik and C. V. Shank, "*Coupled wave theory of distributed feedback dye lasers*", J. Appl. Phys., **43**, (1972) 2382.

[3.6] P. McGrane, PhD Thesis, "*Computational and Experimental studies of distributed Bragg feedback for use in a high-power Free-Electron Maser*", Strathclyde University, 2006.

[3.7] S. E. Tsimring, "*Electron Beams and Microwave Vacuum Electronics*", Wiley Interscience, 2007.

[3.8] Landmarks of science microform; Sir William Henry Bragg and William Laurence Bragg: "*X-rays and Crystal Microstructure*" G. Bell and Sons, (1915).

[3.9] W.H. Bragg and W.L Bragg, Proceedings of the Royal Society (London) **88**, p428, (1913).

[3.20] W.H. Bragg and W.L Bragg, Proceedings of the Royal Society (London) **89**, p246, (1913).

[3.11] A. Valle, L. Pasquera, Appl. Phys. Lett., 2001, "*Turn-off transients in current-modulated multitransverse-mode vertical-cavity surface-emitting lasers*", **79**, 24, pp3914-3916, (2001).

[3.12] A. Andre, M. D. Lukin, "*Manipulating Light Pulses via Dynamically Controlled Photonic Band gap*", Phys. Rev. Lett., **89**, 143602, (2002).

[3.13] B. Z. Katsenelenbaum, "*Theory of non-regular waveguides with slow variable parameters*", Academy of Science USSR, Moscow, 1961

[3.14] N.S. Ginzburg et al. "*High-Efficiency single mode Free-electron maser oscillator based on a Bragg resonator with step of phase corrugation*", Phys. Rev. Letters, **84**(16), p.3574, (2000).

[3.15] A.W. Cross, W.He, I.V. Konoplev, A.D.R. Phelps, K. Ronald, G.R.M. Robb, C.G. Whyte, N.S. Ginzburg, N. Yu Peskov and A.S. Sergeev, "*Experimental and theoretical study of 2D Bragg structures for a coaxial free electron maser*", Nuclear Instruments and Methods, A475, pp164-172.

[3.16] J.D. Jackson "*Classical Electrodynamics*", New York Wiley, (1999) Section 7.2.

[3.17] I. V. Konoplev, A. J. MacLachlan, C. W. Robertson, A. W. Cross, and A. D. R. Phelps, "Cylindrical periodic surface lattice as a metadielectric: Concept of a surface-field Cherenkov source of coherent radiation", Physical Review E, **84**, 013836, (2011).

[3.18] Konoplev, I. V.; Cross, A. W.; He, W.; Phelps, A. D. R.; Ronald, K.; Robb, G. R. M.; Whyte, C. G.; Ginzburg, N. S.; Peskov, N. Y.; Sergeev, A. S. "*Progress of the Strathclyde Free Electron Maser experiment using a 2D Bragg structure*", Nuclear Instruments and Methods in Physics Research Section A, Volume **445**, Issue 1-3, p. 236-240.

[3.19] A.W. Cross, I.V. Konoplev, A.D.R. Phelps and K.Ronald, "*Studies of surface two-dimensional photonic band gap structures*", Journal of Applied Physics, **93**, no.4, pp-2208-2218, (2003).

[3.20] A.W. Cross, I.V. Konoplev, K. Ronald, A.D.R. Phelps, W. He, C.G. Whyte, N.S. Ginzburg, N.Yu Peskov and A.S. Sergeev, "*Experimental studies of two-dimensional coaxial Bragg structure for a high power free-electron maser*", Applied Physics Letters, **80**, no.9 pp1517-1519, (2002).

[4.1] J. C. Maxwell, "*A Treatise On Electricity and Magnetism*", Oxford Clarendon Press, 1873.

[4.2] P. Monk, "*A Finite Element Method For Approximating The Time-Harmonic Maxwell's Equations**", Numer. Math. **63**, 243-261 1992.

[4.3] P. Monk. "*An Analysis of Nedelec's Method for the Spatial Discretization of Maxwell's Equations**", J. Comput. Appl.Maths, **47**, 101-121, 1993.

[4.4] G. G. O'Brien, M. A Hyman, and S. Kaplan. "*A study of the numerical solution of partial differential equations*". J. Math. Phys. **29**, 223–251, 1950.

[4.5] Kane Yee, "*Numerical solution of initial boundary value problems involving Maxwell's equations in isotropic media*". IEEE Trans. Antennas Propag, **14**, 302–307, 1966.

[4.6] T. Weiland, "*A Discretization Method for the Solution of Maxwell's Equations for Six-Component Fields"*, Electronics and Communications AEUE, **31**, 3, pp. 116–120, 1977.

[4.7] B. Krietenstein. *et al*, "*The Perfect Boundary Approximation Technique Facing The Big Challenge Of High Precision Field Computation*", Proceedings of the 19th LINAC Conference, Chicago, August 1998.

[4.8] J. M. Dawson, "*Particle simulation of plasmas*", Rev. Mod. Phys., 55, 403, 1983.

[4.9] T. J. M. Boyd, J. J. Sanderson, "*The Physics of Plasmas*", Cambridge University Press, 2003.

[4.10] L. Fisher, I. V. Konoplev, "*Surface-field cavity based on a two-dimensional cylindrical lattice*", Appl. Phys. Lett., **96**, 231111, 2010.

[4.11] C. W. Hull, "*Apparatus for Production of Three-Dimensional Objects by Stereolithography*", U.S. Patent 4,575,330.

[4.12] "*Extensible 3D (X3D)*", ISO/IEC 19775:2004, Web 3D Consortium.

[6.1] V. L. Granatstein and I. Alexeff, "*High Power Microwave Sources*", Artech House, Boston and London, 1987.

[6.2] R.H Fowler, L. Nordheim, "*Electron Emission In Intense Electric Fields*", Proc. Royal. Soc. London, Vol. **119**, No. 781, pp 173-181, May 1928.

[6.3] D. E. Radley, "*The Theory of the Pierce Type Electron Gun*", **4**, 2, pp 125-148, 1958

[6.4] P. T. Kirstein, G. S. Kino, W. E. Waters, "*Space-charge flow*", 1967, McGraw-Hill

[6.5] Humphries S., 1986, "*Principles of charged particle acceleration*". New York: John Wiley & Sons Ltd.

[6.6] Gilmour A.S., 1986, "*Microwave Tubes*": Artech House.

[6.7] E.L. Murphy, R.H. Good. Jr, "*Thermionic Emission, Field Emission, and the Transition Region*", Phys. Rev. **102**, 1464, (1956).

[6.8] R. Amitava, R. Menon, K. V. Nagesh, D. P. Chakravarthy, "*High-current density electron beam generation from a polymer velvet cathode*", J. Phys. D: Appl. Phys, **43**, 365202, (2010).

[6.9] Limin Li, Lie Liu, Lei Chong, Hong Wan, Jianchun Wwen, Yonggui Liu, "*Characteristics of polymer velvet as field emitters under high-current pulsed discharge*", Appl. Surf. Sci, **255**, pp 4563-4568, (2009).

[6.10] J. R. Pierce, "Rectilinear Flow in Beams", J. Appl. Phys, **11**, 548, (1940).

[7.1] A.R. Phipps, A.J. MacLachlan, C.W. Robertson, I.V. Konoplev, A.D.R. Phelps, A.W. Cross, "*Numerical analysis and experimental design of a 103 GHz Cherenkov maser*," *Infrared, Millimeter, and Terahertz waves (IRMMW-THz), 2014 39th International Conference on* , vol., no., pp.1,2, 14-19 Sept. (2014).

[7.2] N.S. Ginzburg, et al, "*Generation of powerful subnanosecond microwave pulses by intense electron bunches moving in a periodic backward wave structure in the superradiative regime*", Phys. Rev. E **60**, 3297, 1999.

[8.1] Fisher, L.; et al, "Surface wave Cherenkov maser based on a periodic lattice", Applied Physics Letters , Vol.**96**(26), p.261101, 2010.

Appendix A: Matlab Dispersion Analysis Code

The following code demonstrates the dispersion relations for the $TM_{0,2}$ and $TM_{0,3}$ VF modes with the $TE_{5,1}$ SF mode within the 2D PSL structure:

```
% dispersion calculation
clear all;
clc;

% the experiment frequency range is between r=1.1 (79.9GHz), r=1.045
% (84.06GHz)
c = 3.0E8;

d = 1.6E-3; % the period of the PSL
kb = 2 * pi / d;

kz_max = kb * 1; %
kz =  -kz_max : 1 : kz_max;



Fc_TE71 = 102.31E9; % Hz
Fc_TE51 = 84.3E9; % Hz
Fc_TM03 = 105.1E9;  % actually it is TM02
Fc_TM02 = 77.19E9; % Hz
%Fc_TM03 = 28.68; % Hz

Kc_TE71 = 2 * pi * Fc_TE71 / c;
Kc_TE51 = 2 * pi * Fc_TE51 / c;
Kc_TM02 = 2 * pi * Fc_TM02 / c;
Kc_TM03 = 2 * pi * Fc_TM03 / c;

Freq_TE71 = (Kc_TE71.^2 + kz.^2).^0.5 * c ./ ( 2 * pi * 1E9);
Freq_TE51 = (Kc_TE51.^2 + kz.^2).^0.5 * c ./ ( 2 * pi * 1E9);
Freq_TM02 = (Kc_TM02.^2 + kz.^2).^0.5 * c ./ ( 2 * pi * 1E9);
Freq_TM03 = (Kc_TM03.^2 + kz.^2).^0.5 * c ./ ( 2 * pi * 1E9);
kz_TM02_harm = kz + kb;
```

```
kz_TM03_harm = kz + kb;

figure('color','w')
set(gca,'fontsize', 18)
plot(kz, Freq_TE51,'r','LineWidth',3);
hold on
grid on
%plot(kz, Freq_TM02,'b','LineWidth',3);
plot(kz_TM02_harm, Freq_TM02,'k','LineWidth',3);
plot(kz_TM03_harm, Freq_TM03,'g','LineWidth',3);
plot(kz, Freq_TE71,'b','LineWidth',3);
xlabel('Wavenumber (m^{-1})')
ylabel('Frequency (GHz)')

% plot the beam line
gamma = 1 + 100/511;
beta = (1- gamma^(-2)).^0.5;
vz = beta  * c;
beamline = kz * vz / (2 * pi * 1E9) + 0;
plot(kz, beamline, '-.b','Linewidth',3)



% add the clycrotron frequency, not this one
%alpha = 0.4;
%Vz2 = vz / ((1 + alpha^2) ^ 0.5);
%omega = 28 * 1.75; % 1.75 Tesla
%beamline2 =  kz * Vz2 / (2 * pi * 1E9) + omega;
%plot(kz, beamline2, '--k','Linewidth',3)

% add the 2nd harmonic cyclotron frequency, not this one
alpha = 0.4;
Vz3 = vz / ((1 + alpha^2) ^ 0.5);
omega = 42 * 1.75; % 1.75 Tesla
beamline3 =  kz * Vz3 / (2 * pi * 1E9) + omega;
plot(kz, beamline3, '-.g','Linewidth',3)
```

```
% then work out the dispersion curve
% use the equation from L. Zhang MTT, 2012
% read the intersection point from the plot (1762, 132.8)

kz_TE71_inters = 1661; %%% need change when using different modes
kz_TE51_inters = 1832; %%% need change when using different modes
kz_TE71TM03_inters = 1795;
kz_TM03_inters = kb - kz_TE71TM03_inters;
kz_TM02_inters = kb - kz_TE71_inters;
kz_TM02TE51_inters = kb - kz_TE51_inters;
kapa2 = 1;   % coupling coefficient
h_range = 0:10:kb;

A2 = Kc_TE71.^2 + h_range.^2;
C2 = Kc_TE51.^2 + h_range.^2;
B2 = Kc_TM02.^2 + (kb - h_range).^2;
D2 = Kc_TM03.^2 + (kb - h_range).^2;
G2 = ( kz_TE71_inters * kz_TM02_inters * kapa2 ) ^ 2 * 0.55; % TM02: 0.55
H2 = ( kz_TE51_inters * kz_TM02TE51_inters * kapa2 ) ^ 2 * 0.55; % TM02: 0.55
I2 = ( kz_TE71TM03_inters * kz_TM03_inters * kapa2 ) ^ 2 * 0.55; % TM02: 0.55

% the euqation becomes :  (k^2 - kc1^2- h^2) * ( k^2 - kc2^2 - (kb - h)^2 ) = G^2
% and then to solve k with known h.
% then (k^2 - A^2) * ( k^2 - B^2 ) = G^2
% it becomes:
% k^4 - (A^2 + B^2) * k^2 + A^2 * B^2 - G^2 = 0

Kz_dis_Num = length(h_range);
Beta_fun_Order_4 = 1 .* ones(1,Kz_dis_Num);
Beta_fun_Order_3 = 0 .* ones(1,Kz_dis_Num);
Beta_fun_Order_2 = - ( A2 + B2 );
Beta_fun_Order_2a = - ( C2 + B2 );
Beta_fun_Order_2b = - ( A2 + D2 );
Beta_fun_Order_1 = 0 .* ones(1,Kz_dis_Num);
%Beta_fun_Order_0 =  A2 .* B2 - G2;
%Beta_fun_Order_0a =  C2 .* B2 - H2;
```

```
Beta_fun_Order_0 =  A2 .* B2 - G2/2;
Beta_fun_Order_0a =  C2 .* B2 - H2/2;
Beta_fun_Order_0b =  A2 .* D2 - I2/2;

Beta_fun_coef_Vector = [Beta_fun_Order_4' Beta_fun_Order_3' Beta_fun_Order_2'
Beta_fun_Order_1' Beta_fun_Order_0'];
Beta_fun_coef_Vector1 = [Beta_fun_Order_4' Beta_fun_Order_3' Beta_fun_Order_2a'
Beta_fun_Order_1' Beta_fun_Order_0a'];
Beta_fun_coef_Vector2 = [Beta_fun_Order_4' Beta_fun_Order_3' Beta_fun_Order_2b'
Beta_fun_Order_1' Beta_fun_Order_0b'];

% finally use root function to get the roots
Omega = [];
Omega1 = [];
Omega2 = [];
for ind = 1: length(Beta_fun_coef_Vector)
   Omega = [ Omega roots(Beta_fun_coef_Vector(ind,:))];
   Omega1 = [ Omega1 roots(Beta_fun_coef_Vector1(ind,:))];
   Omega2 = [ Omega2 roots(Beta_fun_coef_Vector2(ind,:))];
end
Omega = real(Omega');
Omega1 = real(Omega1');
Omega2 = real(Omega2');
Omega = Omega * c / ( 2 * pi ) / 1E9;
Omega1 = Omega1 * c / ( 2 * pi ) / 1E9;
Omega2 = Omega2 * c / ( 2 * pi ) / 1E9;

% it always has 4 roots.
% and we only need to get the first 2 higher result.
Omega_Sorted =(sort(Omega','descend'))';
Omega_Sorted1 =(sort(Omega1','descend'))';
Omega_Sorted2 =(sort(Omega2','descend'))';

freq_higher_Mode = Omega_Sorted(:,1);
freq_higher_Mode1 = Omega_Sorted1(:,1);
freq_higher_Mode2 = Omega_Sorted2(:,1);
```

```
freq_lower_Mode = Omega_Sorted(:,2);
freq_lower_Mode1 = Omega_Sorted1(:,2);
freq_lower_Mode2 = Omega_Sorted2(:,2);
plot(h_range, freq_lower_Mode, '-.b', 'LineWidth',2);
%plot(h_range, freq_lower_Mode1, '-.r', h_range, freq_higher_Mode1, '-.k', 'LineWidth',2);
plot(h_range, freq_lower_Mode1, '-.r', 'LineWidth',2);
plot(h_range, freq_lower_Mode2, '-.y', 'LineWidth',2);

% Create the Legend
legend('TE51','TM02 harmonic','TM03 harmonic','TE71','100kV beamline','100kV 2nd Harm Beamline','TE71-TM02 Eigenmode','TE51-TM02 Eigenmode','TE71-TM03 Eigenmode');
```

Appendix B: Magic 3D Beam – Wave Interaction Code

The following code is the Magic 3D code that was used to calculate the beam – wave interaction output parameters for the BWO experiment:

```
HEADER ORGANIZATION "Atoms, Beams & Plasmas" ;
HEADER Author "Alan Phipps" ;
HEADER DEVICE "2D PSL Cherenkov maser";

!*********************************************************************
! System Variables
!*********************************************************************

!GRAPHICS PAUSE ;
TERMINATE ERROR;
! (R,Phi,Z)
SYSTEM Polar ;

!*********************************************************************
! Constants
!*********************************************************************

Assign pi = 3.14159 ;
Assign Mu0 = 1.2566E-6 ;
Assign Eps0 = 8.8544E-12 ;

!*********************************************************************
! Simulation Variables
!*********************************************************************

Assign Frequency_Lo = 70 GHz;
Assign Frequency_Hi = 130 GHz;
parameter Frequency_Mid = 0.5*(Frequency_Lo + Frequency_hi) ;
Assign Frequency_Window_Lo = 0 GHz;
Assign Frequency_Window_Hi = 500 GHz;
Assign DesiredFrequency = 103.6 GHz;
Assign Wavelength = 1.C/DesiredFrequency ;
Real FrequencyDriver;
Assign zFrequency_Driver = 153.6 GHz;
Assign Runtime = 100 nanoseconds;
Assign Azimuthal_Variations = 7;
Assign Symmetry_Phi_Lo = 0;
!Assign Symmetry_Phi_Hi = 2pi / Azimuthal_Variations;
Assign Symmetry_Phi_Hi = 2pi;
Assign Symmetry_Phi_Mid = (Symmetry_Phi_Hi-Symmetry_Phi_Lo)/2;
Assign Frequency_Window_Mid =
0.5*(Frequency_Window_Lo+Frequency_Window_Hi);
Assign Time_Filter = 1/Frequency_Window_Mid;
Assign Frequency_Mid = (Frequency_hi+Frequency_Lo)/2;
Real Longitudinal_Period;
Assign Longitudinal_Period = 1.6 mm;
Real Number_Periods_z;
Assign Number_Periods_z = 16;
Assign PSL_Length = Longitudinal_Period * Number_Periods_z;
Assign Cyl_Section_Length = Longitudinal_Period*4;
Assign Simulation_Length_z = PSL_Length + (Cyl_Section_Length * 2);
Assign Perturbation_Amplitude = 0.85 mm;
Assign Perturbation_Amplitude_Eqn = Perturbation_Amplitude * 2;
Assign Azimuthal_Period = 2pi/Azimuthal_Variations;
!*********************************************************************
! Radius_Mid = Inner Radius of Simulation
!*********************************************************************
Assign Radius_Mid = 4.0 mm;
Assign Radius_Outer = Radius_Mid + Perturbation_Amplitude;
Assign Radius_Inner = Radius_Mid - Perturbation_Amplitude;
```

```
ASSIGN Shell_Radius = Radius_Outer + 1.0mm ;
Assign ZPos_Min = -Simulation_Length_z / 2 ;
Assign ZPos_Max = +Simulation_Length_z / 2 ;
Assign PSL_ZPos_Min = -0.5*PSL_Length ;
Assign PSL_ZPos_Max = +0.5*PSL_Length ;
Assign dz = Longitudinal_Period;
Assign dr = Perturbation_Amplitude;
Assign dPhi = Azimuthal_Period;
! dz & dr must be divisible by 2 so to have main grid lines on structrue
edges
! dphi must be divisible by 3 (360 / 3 or 6 or 9 = whole number)
! CHECK GRID AFTER CHANGING THESE VALUES, works better if major grid lines
lie on structure edges
Assign dz_factor = (Nint((1 / (1000 * (Longitudinal_Period / 10)) * 1)) -
2);
Assign dr_factor_Shell = (Nint((1 / (1000 * ((Shell_Radius - Radius_Outer)
/ 10)) * 1)) - 0);
Assign dr_factor_Perturbations = (Nint((1 / (1000 *
((Perturbation_Amplitude * 1) / 10)) * 2)) - 2);
Assign dr_factor_Void = (Nint((1 / (1000 * (Radius_Inner / 8)) * 1)) -
0.25);
Assign dr_factor_Port = (Nint((1 / (1000 * ((Shell_Radius) / 10)) * 4)) -
0);
;
Assign dPhi_factor = 12;
Assign PSL_ZPos_Min_Plus_6dz14 = ZPos_Min +(3*dz) ;
Assign ZPos_Max_Minus_2dz14 = ZPos_Max -dz;
Assign ZPos_Max_Minus_10dz14 = ZPos_Max -(5*dz);
! ZPos_Dump determines where the electrons will dump into wall, must be
recalculated if B-field magnitude is changed
Assign ZPos_Dump = PSL_ZPos_Max - (1 * Longitudinal_Period);
Assign Phi_Lo = dPhi;
Assign Phi_Hi = Symmetry_Phi_Hi - Phi_Lo;
Assign Nz = Simulation_Length_z /dz ;
Assign Nr = Radius_Inner /dr ;
Assign Nx = 2*Nr ;

Grid Origin x1 0;

!
**********************************************************************
*************
! PSL Functions
!
**********************************************************************
*************

Function PeriodzEqual2piRads(z) = Sin((2pi / Longitudinal_Period) * z);
Function PeriodPhiEqual2piRads(t) = Sin((Azimuthal_Variations * t) - (pi /
Azimuthal_Variations));
Function PSLFunction(r,t,z) = Radius_Mid + (0.5 *
Perturbation_Amplitude_Eqn * (Sign(PeriodzEqual2piRads(z) *
Sign(PeriodPhiEqual2piRads(t)))));
Function PSLVoidFunc(r,t,z) = (PSLFunction(r,t,z) - r);

!
**********************************************************************
*************
! Annular section for Right Side of PSL
!
**********************************************************************
*************

Point AnnularLeft.pt1 0, Symmetry_Phi_Lo, ZPos_Min;
Point AnnularLeft.pt2 0, Symmetry_Phi_Hi, PSL_ZPos_Min;

VOLUME AnnularLeft ANNULAR AnnularLeft.pt1, AnnularLeft.pt2, Radius_Mid,
Shell_Radius ;
```

```
MARK AnnularLeft X1 Min Max SIZE +dr/dr_factor_Shell ;
MARK AnnularLeft X2 Min Max SIZE +dPhi/dphi_factor;
MARK AnnularLeft X3 Min Max SIZE +dz/dz_factor ;

!
**********************************************************************
*************
! Confining Shell and Cylindrical Void Section
!
**********************************************************************
*************

POINT Shell.pt1 0, Symmetry_Phi_Lo, PSL_ZPos_Min ;
POINT Shell.pt2 0, Symmetry_Phi_Hi, PSL_ZPos_Max ;

VOLUME Shell CYLINDRICAL Shell.pt1, Shell.pt2, Shell_Radius ;
MARK Shell X1 SIZE +dr/dr_factor_Shell ;
MARK Shell X2 Min Max SIZE +dPhi/dphi_factor ;
MARK Shell X3 Min Max SIZE +dz/dz_factor ;

POINT ShellVoid.pt1 0, Symmetry_Phi_Lo, ZPos_Min ;
POINT ShellVoid.pt2 0, Symmetry_Phi_Hi, ZPos_Max ;

VOLUME ShellVoid CYLINDRICAL ShellVoid.pt1, ShellVoid.pt2, Radius_Inner ;

! Mark parts of shell that will remain after void at lo and hi z
Point ShellrhoHi_rho_0_ZMin, Shell_Radius, 0, ZPos_Min;
Mark ShellrhoHi_rho_0_ZMin X1 Size +dr/dr_factor_Shell ;
Point ShellrhoHi_rho_0_ZMax, Shell_Radius, 0, ZPos_Max;
Mark Shellrhohi_rho_0_ZMax X1 Size +dr/dr_factor_Shell ;

Point ShellrhoLo_rho_0_ZMin, Radius_Outer, 0, ZPos_Min;
Mark ShellrhoLo_rho_0_ZMin X1 Size +dr/dr_factor_Shell ;
Point ShellrhoLo_rho_0_ZMax, Radius_Outer, 0, ZPos_Max;
Mark ShellrhoLo_rho_0_ZMax X1 Size +dr/dr_factor_Shell ;

MARK ShellVoid X2 Min Max SIZE +dPhi/dphi_factor ;
MARK ShellVoid X3 Min Max SIZE +dz/dz_factor ;

!
**********************************************************************
*************
! Annular Section for Right Side of PSL
!
**********************************************************************
*************

Point AnnularRight.pt1 0, Symmetry_Phi_Lo, PSL_ZPos_Max;
point AnnularRight.pt2 0, Symmetry_Phi_Hi, ZPos_Max;

VOLUME AnnularRight ANNULAR AnnularRight.pt1, AnnularRight.pt2, Radius_Mid,
Shell_Radius ;

MARK AnnularRight X1 Min Max SIZE +dr/dr_factor_Shell ;
MARK AnnularRight X2 Min Max SIZE +dPhi/dphi_factor;
MARK AnnularRight X3 Min Max SIZE +dz/dz_factor ;

!
**********************************************************************
*************
! PSL Void USing Functional Volume (Cannot be Marked)
!
**********************************************************************
*************

VOLUME PSLVoid Functional PSLVoidFunc(r,t,z) Radius_Inner 0 PSL_ZPos_Min,
Radius_Outer 2pi PSL_ZPos_Max ;
```

```
!
*********************************************************************************
*************
! PSL & mark grid Points
!
*********************************************************************************
*************

! Mark non PSL section as before and PSL section with function

Assign zTmpVar_1 = Longitudinal_Period / 2;
Assign zTmpVar_2 = 2pi / (Azimuthal_Variations * 2);
Assign zTmpVar_3 = 2pi - zTmpVar_2;
Assign zTmpVar_4 = 0 + zTmpVar_2;
Assign Radius_Inner_Minus3Halfdr = Radius_Inner - (3 * (dr /
dr_factor_Perturbations));

! Create & Mark z axis
Point PSL_zAxis_PSLZPosMin 0, 0, PSL_ZPos_Min;
Mark PSL_zAxis_PSLZPosMin X3 Size +dz/dz_factor ;

Do zPoint = PSL_ZPos_Min, PSL_ZPos_Max, zTmpVar_1;

  Do phiPoint = zTmpVar_4, 2pi, zTmpVar_2;

    ! Mark rho from 0 to radius_shell using dr_factor you want for the
volume that starts at that point
    Point rhoOrigin_'phipoint'_'zpoint', 0, 'phiPoint', 'zPoint';
    Mark rhoOrigin_'phipoint'_'zpoint' X1 Size +dr/dr_factor_Void;

    Point rhoPertLo_'phipoint'_'zpoint', Radius_Inner_Minus3Halfdr,
'phiPoint', 'zPoint';
    Mark rhoPertLo_'phipoint'_'zpoint' X1 Size +dr/dr_factor_Shell;

    Point rhoPertHi_'phipoint'_'zpoint', Radius_Outer, 'phiPoint',
'zPoint';
    Mark rhoPertHi_'phipoint'_'zpoint' X1
       Size +dr/dr_factor_Perturbations ;

    Point rhoShell_'phipoint'_'zpoint', Shell_Radius, 'phiPoint', 'zPoint';
    Mark rhoShell_'phipoint'_'zpoint' X1 Size +dr/dr_factor_Shell ;

    Point phiRadHi_'phipoint'_'zpoint', Radius_Outer, 'phiPoint', 'zPoint';
    Mark phiRadHi_'phipoint'_'zpoint' X2 Size +dphi/dphi_factor ;

  EndDo ;

EndDo ;

!
*********************************************************************************
*************
! Diagnostic Volumes
!
*********************************************************************************
*************



!
*********************************************************************************
*************
! Diagnostic and Symmetry Areas
!
*********************************************************************************
*************
```

```
Area Diag_PHI_LOPLANE CONFORMAL 0 Symmetry_Phi_Lo ZPos_Min Radius_Outer
Symmetry_Phi_Lo ZPos_Max ;
Area Diag_PHI_HIPLANE CONFORMAL 0 Symmetry_Phi_Hi ZPos_Min Radius_Outer
Symmetry_Phi_Hi ZPos_Max;

!
**************************************************************************
*************
! Diagnostic Lines
!
**************************************************************************
*************

POINT DiagL_ZAxis.pt1 0, 0, 0 ;
POINT DiagL_ZAxis.pt2 0, 0, ZPos_Max ;

LINE DiagL_ZAxis CONFORMAL DiagL_ZAxis.pt1, DiagL_ZAxis.pt2 ;

Line DiagL_LPort_0 Conformal 0,0,-0.5*Simulation_Length_z,Radius_Inner,0,-
0.5*Simulation_Length_z ;
Line DiagL_Mid_0 Conformal 0,0,+0.0,Radius_Inner,0,+0.0 ;
Line DiagL_RPort_0 Conformal
0,0,+0.5*Simulation_Length_z,Radius_Inner,0,+0.5*Simulation_Length_z ;
Line DiagL_LPort_PhiMid Conformal 0,0.5*Symmetry_Phi_Mid,-
0.5*Simulation_Length_z,Radius_Inner,0.5*Symmetry_Phi_Mid,-
0.5*Simulation_Length_z ;
Line DiagL_Mid_PhiMid Conformal
0,0.5*Symmetry_Phi_Mid,+0.0*Simulation_Length_z,Radius_Inner,0.5*Symmetry_P
hi_Mid,+0.0*Simulation_Length_z ;
Line DiagL_RPort_PhiMid Conformal
0,0.5*Symmetry_Phi_Mid,+0.5*Simulation_Length_z,Radius_Inner,0.5*Symmetry_P
hi_Mid,+0.5*Simulation_Length_z ;

Assign Radius_Quarter = 0.25*Radius_Inner ;
Assign ZPos_Min_Plusdz =-0.5*Simulation_Length_z+dz ;
Assign ZPos_Centre = 0 ;
Assign ZPos_Max_Minusdz =+0.5*Simulation_Length_z-dz ;

Point QuartRadQuartPhidz14
Radius_Quarter,.25*Symmetry_Phi_Hi,ZPos_Min_Plusdz;
Point QuartRadQuartPhiz0 Radius_Quarter,.25*Symmetry_Phi_Hi,ZPos_Centre;
Point QuartRadQuartPhizMaxMinusdz14
Radius_Quarter,.25*Symmetry_Phi_Hi,ZPos_Max_Minusdz;

Line DiagL_QuRadQuPhiAllz Conformal
Radius_Quarter,.25*Symmetry_Phi_Hi,ZPos_Min_Plusdz
Radius_Quarter,.25*Symmetry_Phi_Hi,ZPos_Max_Minusdz ;
Line DiagL_QuRadQuPhidz14 Conformal 0,0.25*Symmetry_Phi_Hi,ZPos_Min_Plusdz
Radius_Quarter,0.25*Symmetry_Phi_Hi,ZPos_Min_Plusdz ;
Line DiagL_QuRadQuPhiMaxdz14 Conformal
0,0.25*Symmetry_Phi_Hi,ZPos_Max_Minusdz
Radius_Quarter,0.25*Symmetry_Phi_Hi,ZPos_Max_Minusdz ;

! Ivan's Line
Assign ZPosMaxMinusdz = ZPos_max - dz;
Assign QuarterRadius = Radius_Mid*025;
Line DiagL_QuartR_QuartPhi_Maxz Conformal
0,0.25*Symmetry_Phi_Hi,ZPosMaxMinusdz
QuarterRadius,0.25*Symmetry_Phi_Hi,ZPosMaxMinusdz ;

!
**************************************************************************
*************
! Ports
!
**************************************************************************
*************
```

```
Area LeftPort Conformal 0 Symmetry_Phi_Lo ZPos_Min,Radius_Mid
Symmetry_Phi_Hi ZPos_Min;
Mark LeftPort X1 Size +dr/dr_factor_Port ;
Mark LeftPort X2 Size +dphi/dphi_factor ;

Area RightPort Conformal
0,Symmetry_Phi_Lo,ZPos_Max,Radius_Outer,Symmetry_Phi_Hi,ZPos_Max;
Mark RightPort X1 Size +dr/dr_factor_Port ;
Mark RightPort X2 Size +dphi/dphi_factor ;

!
**************************************************************************
*************
! Construct Grid
!
**************************************************************************
*************

Grid Origin X1 0;

Assign Shell_Thickness = Shell_Radius - Radius_Outer;
Assign rStepVoid = dr / dr_factor_Void;
Assign rStepPerturbations = dr / dr_factor_Perturbations;
Assign rStepShell = dr / dr_factor_Shell;
Assign rStepPort = dr / dr_factor_Port;
Assign PertPeaktoPeak = Perturbation_Amplitude * 2;
Assign VoidRadius = Radius_Inner;

! Cylindrical void section then peak to peak perturbations then shell
Grid Uniform X1 Distance VoidRadius First rStepVoid;
Grid Uniform X1 Distance PertPeaktoPeak First rStepPerturbations;
Grid Uniform X1 Distance Shell_Thickness First rStepShell;


AUTOGRID X2 ;

Assign zStep = dz/dz_factor;
Assign zStepx2 = zStep * 2;
Assign Cyl_Sec_Len_Minus3HalfzStep = Cyl_Section_Length - (3 * zStep / 2);

GRID ORIGIN X3 ZPos_Min ;

! Left port then Left Annualar then PSL then Right Annular then right port
GRID Uniform X3 Distance zStepx2 First zStepx2;
GRID Uniform X3 Distance Cyl_Section_Length First zStep;
GRID Uniform X3 Distance PSL_Length First zStep;
GRID Uniform X3 Distance Cyl_Sec_Len_Minus3HalfzStep First zStep;

!
**************************************************************************
*************
! System Parameters
!
**************************************************************************
*************

Duration Runtime;
Maxwell High_Q ;

!
**************************************************************************
*************
! Define Materials
!
**************************************************************************
*************

Conductor AnnularLeft Material Copper;
```

```
Conductor Shell Material Copper;
Void PSLVoid;
Conductor AnnularRight Material Copper;
Void ShellVoid;

!
*********************************************************************************
*************
! Symmetry (Should be Done After AutoGrid)
!
*********************************************************************************
*************

Symmetry Periodic Diag_PHI_LOPLANE POSITIVE Diag_PHI_HIPLANE NEGATIVE ;

!
*********************************************************************************
*************
! Port RF Fields
!
*********************************************************************************
*************

! Normalise to 0 so Erho and EPhi are 0 in current source
FUNCTION ERHO(R,PHI,z) = 0;
FUNCTION EPHI(R,PHI,z) = 0;

Assign Period = 1 / zFrequency_Driver ;
Assign BetaPhase = 1 / SQRT(1 - (DesiredFrequency /
zFrequency_Driver)**2) ;
Assign Omega_Lo = 2PI * Frequency_Lo;
Assign Omega_Hi = 2PI * Frequency_hi;
Assign Omega_Mid = 0.5 * (Omega_Lo + Omega_Hi);
Assign TPulse = 10 nanoseconds;
Parameter Transit_time = 2 * (SYS$X1MX) / 1.c ;
Parameter TEND_SIGNAL = 15.001 nanoseconds;
Parameter Tstart_SIGNAL =0.001 nanoseconds;

! Input Frequency based input signal - RF modulated pulse with flat
spectrum - Avoid Division by Zero
Assign TPulse = 10 nanoseconds;
FUNCTION INPUT_SIG(T) = SMOOTH_RAMP(0.1*Frequency_Mid*T) *
SMOOTH_RAMP(0.1*Frequency_Mid*(TEnd_Signal-T)) * ( SIN(Omega_Lo*(T-TPulse))
- SIN(Omega_Hi*(T-TPulse)) )/ ( Omega_Mid*(T-TPulse) ) ;
Assign Tsignal_mid=0.5*(TEND_Signal+TStart_signal);
Assign Tsignal_lengt=TEND_Signal-TStart_signal;
Function signal_shape(T)=step(T,Tstart_signal)-step(T,Tend_signal);
Function input_signal(T)=signal_shape(T)*input_sig(T);

PORT RightPort NEGATIVE Phase_Velocity BetaPhase;

!
*********************************************************************************
*************
! eBeam Function
!
*********************************************************************************
*************

Assign Radius_Beam_Centre = 2.5 mm;
Assign Beam_Thickness = 1.0 mm;
Assign Delta_rp_Beam = Radius_Beam_Centre - (0.5 * Beam_Thickness);
Assign Delta_rn_Beam = Radius_Beam_Centre + (0.5 * Beam_Thickness);
Assign G_b_max = 1.1;
Assign G_b_min = 1.1;
Assign Voltage_Max = 150 kiloVolts;
Assign Beam_Current_Density = 1 ;
Assign BField_Magnitude = 4.0 Tesla;
```

```
Assign Beam_Current = 675 Amp / Azimuthal_Variations;

Function G(T) = G_b_min + (G_b_max - G_b_min)* T / Runtime;
Function beam_frame_x1(r,t,z) = Step(r,Delta_rp_Beam) -
step(r,Delta_rn_Beam);
Function beam_frame_x2(r,t,z) = -step(t,2*Phi_Hi) + Step(t,Phi_Lo);
Function beam_frame(r,t,z) = beam_frame_x1(r,t,z) * beam_frame_x2(r,t,z);
Function gaus(r,t,z) = exp(-((Radius_Beam_Centre - r)**2) / (2 *
Beam_Thickness));
Function beam_s(r,t,z) = Step(Delta_rn_Beam,r) * Step(r,Delta_rp_Beam);

CURRENT_SOURCE J1 INPUT_SIGNAL ERHO LEFTPORT ;
CURRENT_SOURCE J2 INPUT_SIGNAL EPHI LEFTPORT ;

Import LeftPort positive BEAM Beam_Current beam_s Voltage_Max
Radius_Beam_Centre BField_Magnitude LeftPort
   species Electron ;

!************************************************
! Magnetic Field
!************************************************

ASSIGN GuideField = BField_Magnitude;
ASSIGN DumpField = BField_Magnitude;

Function BGuide(x1,x2,x3) = GuideField * (1 - smooth_ramp((x3 - ZPos_Dump)
/ 0.02));

PRESET B3ST FUNCTION BGuide(x1,x2,x3) MODIFY REPLACE ;

Function BDump(x1,x2,x3) = DumpField * (0 + smooth_ramp((x3 - ZPos_Dump) /
0.005));

PRESET B1ST FUNCTION BDump(x1,x2,x3) MODIFY REPLACE ;

!
************************************************************************
*************
! Output Diagnostics
!
************************************************************************
*************

! Variables
ASSIGN timer_1nanosecond = 1 nanosecond ;
ASSIGN timer_10nanoseconds = 10 nanoseconds ;
ASSIGN timer_100picoseconds = 0.1 nanoseconds ;

! Timers
Timer pPlots_RT periodic Real 0nanoseconds runtime 1picosecond;
;
TIMER cPlots PERIODIC REAL timer_1nanosecond timer_10nanoseconds
timer_100picoseconds ;
Timer vPlots Periodic Real 0nanoseconds timer_1nanosecond 1picosecond;
Timer pPlots Periodic Real 0nanoseconds runtime timer_10nanoseconds;


! Magnetostatic Bz Field
RANGE FIELD B1ST DiagL_ZAxis TSYS$FIRST DUMP ;
RANGE FIELD B3ST DiagL_ZAxis TSYS$FIRST DUMP ;

! Beam Diagnostics
Observe Emitted LeftPort ALL Current ;
Observe Emitted LeftPort ALL Energy ;
Observe Emitted LeftPort ALL Power ;

Observe Collected All All Current;
Observe Collected All All Energy;
```

```
Observe Collected All All Power;

! Partical Motion
phasespace axes x3 x1 pPlots_RT nodump;
PHASESPACE AXES X2 X1 pPlots ;

! Frequency at Ivan's Line
OBSERVE FIELD E1 DiagL_RPort_PhiMid fft magnitude window
   frequency Frequency_Window_Lo Frequency_Window_Hi db_scale 6 dump;
OBSERVE FIELD E2 DiagL_RPort_PhiMid fft magnitude window
   frequency Frequency_Window_Lo Frequency_Window_Hi db_scale 6 dump;
OBSERVE FIELD E3 DiagL_RPort_PhiMid fft magnitude window
   frequency Frequency_Window_Lo Frequency_Window_Hi db_scale 6 dump;

! Power at Right Port
OBSERVE FIELD_POWER S.DA RightPort FILTER STEP PERIOD DUMP ;

! Mode plots
CONTOUR FIELD E1 RightPort cPlots SHADE ;
CONTOUR FIELD E2 RightPort cPlots SHADE ;
CONTOUR FIELD E3 RightPort cPlots SHADE ;

CONTOUR FIELD E1 OSYS$MIDPLANE1 cPlots SHADE ;
CONTOUR FIELD E2 OSYS$MIDPLANE1 cPlots SHADE ;
CONTOUR FIELD E3 OSYS$MIDPLANE1 cPlots SHADE ;

CONTOUR FIELD E1 OSYS$MIDPLANE2 cPlots SHADE ;
CONTOUR FIELD E2 OSYS$MIDPLANE2 cPlots SHADE ;
CONTOUR FIELD E3 OSYS$MIDPLANE2 cPlots SHADE ;

CONTOUR FIELD E1 OSYS$MIDPLANE3 cPlots SHADE ;
CONTOUR FIELD E2 OSYS$MIDPLANE3 cPlots SHADE ;
CONTOUR FIELD E3 OSYS$MIDPLANE3 cPlots SHADE ;

!
**************************************************************************
*************
! Go
!
**************************************************************************
*************

Display_3d ;

START ;
STOP ;
```

Appendix C: Beam Plasma Frequency Calculation

I = 100A, V = 90 kV, $r_1 = 4x10^{-3}$m, $r_2 = 1x10^{-3}$m

$$J = \frac{100\ A}{A_1 - A_2} = \frac{100\ A}{\pi(r_2^2 - r_1^2)} = \frac{100\ A}{\pi((2x10^{-3}m)^2 - (1x10^{-3}m)^2)} = 1.06x10^7 A,^{-2}$$

$$\gamma = \frac{1}{\sqrt{1 - \frac{v^2}{c^2}}} = 1 + \frac{eV}{m_0 c^2} = 1 + \frac{1.6\ x\ 10^{-19}C\ x\ 9x10^4 V}{9{,}1x10^{-31}kg\ x\ (3x10^8 ms^{-1})^2} = 1.176$$

$$\rho_0 = \frac{J}{\gamma ec} = \frac{1.06x10^7 Am^{-2}}{1.176x1.6x10^{-19}C\ x\ 3x10^8 ms^{-1}} = 1.88\ x\ 10^{17}$$

$$\omega_b = \left[\frac{\rho_0 e^2}{\varepsilon_0 m \gamma_0}\right]^{\frac{1}{2}} = \left[\frac{1.88x10^{17} x (1.6x10^{-19})^2}{8.85x10^{-12} x\ 9.1x10^{-31}kg\ x\ 1.176}\right]^{\frac{1}{2}} = 2.25\ x\ 10^{10} rads^{-1}$$

$$2\pi f = 2.25\ x\ 10^{10} rads^{-1} => f = 3.6\ GHz$$

Appendix D: List of Successful Conference Publications

A.R. Phipps, et al, "*Design of W-Band experimental set-up to form TEM mode in oversized coaxial waveguide*", Proceedings of NVEC 2011, Glasgow, Scotland.

A.R. Phipps, et al, "*Design of W-Band experimental set-up to form TEM mode in oversized coaxial waveguide*", Proceedings of 4th China-UK/Europe Workshop on Millimetre Waves and Terahertz Technologies, Glasgow, Scotland.

A.R. Phipps, et al, "*W-Band Cherenkov Maser Based on Periodic Surface Field Structure*", Proceedings of FEL 2012, Nara, Japan.

A.R. Phipps, et al, "*W-Band Cherenkov Maser Based on Periodic Surface Field Structure*", Proceedings of ICOPS 2012, Edinburgh, Scotland.

A.R. Phipps, et al, "*PiC Simulations and Experimental Design of a mm-Wave Source*", Proceedings of IET 2013, Glasgow, Scotland

A.R. Phipps, et al, "*PiC Simulations and Experimental Design of a mm-Wave Source*", Proceedings of IrMMTHz 2013, Mainz, Germany.

A.R. Phipps, et al, "*Numerical simulation and experimental design of a mm-wave BWO utilising a structurally-induced surface field*", Proceedings of NVEC 2013, QMUL London, UK.

A.R. Phipps, et al, "*Optimisation of Cavity Eigenmode for a W-Band Cherenkov Maser*", Proceedings of IrMMTHz 2014, Tucson, Arizona, USA.

A.R. Phipps, et al, "*Numerical Analysis and Experimental Design of a Cherenkov Maser based on a 2D Periodic Surface Lattice*", MURI 2014, Washington, USA.

Appendix E: Gyro BWO Theory

Nusinovich, and Drumbajs gave a general theory for gyro BWO devices in 1996 [1], where they state that a general formalism describing gyrodevices operating at traveling waves was recently presented in [2]. Without going into details of the derivations given in [2], let us point out that this formalism is valid for any gyro-TWT or gyro-BWO operating far enough from cut-off. To apply the equations derived in [2] for gyro-TWT's to our case of interaction with opposite waves it is enough to change the sign of the axial wavenumber k, whenever it is given in the equations. A corresponding self-consistent set of equations for an ideal electron beam (no spread in electron velocities and guiding centre) can be written as

$$\frac{du}{dz'} = \frac{1}{1+b(1-|u|^2)}\left\{F(u^*)^{s-1} - \frac{i}{s}u[\Delta - \mu(1-|u|^2)]\right\} \tag{1}$$

$$\frac{dF}{dz'} = I_0 \frac{1}{2\pi}\int_0^{2\pi} \frac{u^s}{1+b(1-|u|^2)}\, dv_0 \tag{2}$$

Here

$$u = \left[1 - \frac{2(1+h\beta_{z0})}{\beta_{\perp 0}^2}\frac{\gamma_0 - \gamma}{\gamma_0}\right]^{1/2} e^{iv/s} \tag{3}$$

is the complex variable describing slow changes in electron energy γ (γ is the electron energy normalized to the rest energy) and phase $\theta = s\Theta - (\omega t + k_z z)$ where Θ is the electron gyrophase; $z' = (1/\beta_{z0})(\omega z/c)$ is the normalized axial coordinate, $h = k_z c/\omega$ is the normalized axial wavenumber, and F is the normalized wave amplitude. Equations (1) and (2) contain four parameters: b, Δ, μ, and I_0, plus the normalized length of the interaction space

$$L' = \frac{\omega L}{\beta_{z0} c} \tag{4}$$

The parameter

$$b = \frac{h\beta_{\perp 0}^2}{2\beta_{z0}(1+h\beta_{z0})} \tag{5}$$

characterises changes in electron axial velocity during electron interaction with the wave. (We assume that electron axial momentum varies with changes in electron energy in accordance with the autoresonance integral. A small effect of violation of this integral for the wave with axially variable envelope has been analysed elsewhere [3].) The parameter

$$\mu = \frac{\beta_{\perp 0}^2(1-h^2)}{2(1+h\beta_{z0})} \tag{6}$$

is responsible for the disturbance of cyclotron resonance in the process of interaction. The cyclotron resonance mismatch is given by

$$\Delta = 1 + h\beta_{z0} - s\frac{\Omega_0}{\omega} \tag{7}$$

where Ω_0 is the unperturbed electron cyclotron frequency for electrons with $\gamma = \gamma_0$, and I_0 is the normalized beam current parameter. For an arbitrary waveguide

$$I_0 = \frac{2eI_b}{m_0c^3}\frac{c^2}{\omega kN}\frac{1+h\beta_{z0}}{\kappa\gamma_0}\left[\frac{1}{(s-1)!\,2^s}\left(\kappa\frac{s\beta_{\perp 0}}{1+h\beta_{z0}}\right)^{s-1}\right]^2 |L_s|^2 \tag{8}$$

where I_b is the beam current, N is the normalisation of the wave in a waveguide, $\kappa = k_\perp c/\omega$ is the normalised transverse wavenumber, and $|L_s|^2$ is the coupling impedance of electrons to the wave

$$L_s = \left[\frac{1}{k_\perp}\left(\frac{\partial}{\partial X} + i\frac{s}{|s|}\frac{\partial}{\partial Y}\right)\right]^{|s|}\psi(X,Y)$$

where X and Y are transverse coordinate of the electron guiding centres, and ψ is the membrane function describing the transverse structure of the wave. Note that the normalised wave amplitude F is also proportional to L_s: $F \sim AL_s$ where A is the amplitude of the wave (cf. [4]). Therefore, when electrons have spread in coordinates of guiding centres, the equation of motion (1) should be integrated for each beamlet with its specific F. Then, the equation for wave excitation (2) should be rewritten for A instead of F and the additional averaging over the beam cross section in its right-hand side has to be done (see [5] for details). Below we will restrict our consideration to a thin annular electron beam in a cylindrical waveguide. In such a case

$$I_0 = \frac{4eI_b}{m_0c^3}\frac{1+h\beta_{z0}}{\kappa\gamma_0}\frac{\kappa^2}{h}\left[\frac{1}{(s-1)!\,2^s}\left(\kappa\frac{s\beta_{\perp 0}}{1+h\beta_{z0}}\right)^{s-1}\right]^2\frac{J_{m\mp s}^2(k_\perp R_0)}{(\nu^2-m^2)J_m^2(\upsilon)} \tag{9}$$

Here, ν is the eigenvalue of the $TE_{m,p}$ wave, i.e., the pth root of the equation $J'_m(\nu) = 0$; R_0 is the guiding centre radius. The set of equations (1) and (2) must be accomplished with boundary conditions. For electrons unmodulated by any microwave field before a waveguide entrance $u(0) = e^{i\vartheta_0/s}$ where ϑ_0 is the initial phase homogeneously distributed between 0 and 2π. For the wave in a waveguide which is well matched at the output end, we can put the boundary condition $F(L') = 0$. This condition means the absence of opposite waves entering the exit of the interaction region from the output part of the tube. So, an opposite wave starts to be excited at the electron exit. Then, it propagates toward electrons in a waveguide where its amplitude grows in the process of interaction. At the electron entrance this wave can be extracted or reflected from the cutoff narrowing of the waveguide. In the latter case the reflected wave will again propagate through the waveguide. Now this is a forward nonsynchronous wave which travels through the waveguide without interaction with electrons and passes through the output cross section without reflection. The number of parameters in equations (1) and (2) can be reduced [6]-[8], [2]. We may either introduce new parameters

$$\begin{aligned} \zeta &= \sqrt{I_0}z' \\ F' &= F/\sqrt{I_0} \\ \mu' &= \mu/\sqrt{I_0} \\ \Delta' &= \Delta/\sqrt{I_0} \end{aligned} \qquad (10)$$

and exclude the parameter I_0, or use new variables

$$\begin{aligned} \zeta' &= \mu z' \\ F'' &= F/\mu \\ \Delta'' &= \Delta/\mu \\ I_0' &= I_0/\mu^2 \end{aligned} \qquad (11)$$

and exclude the parameter μ. In order to make our analysis consistent with the results given in [9], [6], and [2] we will use the normalisations given by (10). (The primes in (10) will be omitted below.) In these normalizations, equations (1) and (2) can be rewritten as

$$\frac{du}{d\zeta'} = \frac{1}{1 + b(1 - |u|^2)}\left\{F(u^*)^{s-1} - \frac{i}{s}u[\Delta - \mu(1 - |u|^2)]\right\} \qquad (12)$$

$$\frac{dF}{d\zeta'} = \frac{1}{2\pi}\int_0^{2\pi} \frac{u^s}{1+b(1-|u|^2)}\, d\vartheta_0 \qquad (13)$$

From (12) and (13) one can find that

$$\frac{d}{d\zeta'}\left\{|F|^2 - \frac{1}{2\pi}\int_0^{2\pi}|u|^2\, d\vartheta_0\right\} = 0 \qquad (14)$$

This equation leads us to the energy conservation law given elsewhere [6], [8], [2]. Taking into account the boundary conditions for the wave and electrons, one can express the electron orbital efficiency by using (14) in terms of the wave intensity at the entrance where F(0) = F_0

$$\eta_\perp = 1 - \frac{1}{2\pi}\int_0^{2\pi}|u(\zeta_{out})|^2 d\vartheta_0 = |F_0|^2 \qquad (15)$$

The total electron efficiency is

$$\begin{aligned}\eta &= \frac{\beta_{\perp 0}^2}{2(1-\gamma_0^{-1})(1+h\beta_{z0})}\eta_\perp \\ &= \frac{\beta_{\perp 0}^2}{2(1-\gamma_0^{-1})(1+h\beta_{z0})}|F_0|^2\end{aligned} \qquad (16)$$

Let us restrict our consideration to the case of a small tapering of the external magnetic field and/or waveguide radius. In such a case the tapering can be taken into account only in the cyclotron resonance mismatch Δ. This mismatch is small when the interaction length is large, therefore, even small changes in parameters defining Δ may cause significant change in Δ. Below we will consider only the case of linear tapering when Δ can be represented as

$$\Delta = \Delta_0 - \delta\zeta \qquad (17)$$

where A_0 is the mismatch at the waveguide entrance. Δ_0 was mentioned above, the smallness of the tapering also allows us to neglect the radial component of the magnetic field (this effect has been analysed elsewhere [10]). As follows from the definition of Δ, the mismatch Δ can depend on the axial coordinate when either the external magnetic field or the waveguide radius are tapered. In a general case, when both of them are linearly tapered

$$B = B_0\left(1+\delta B\frac{z}{L}\right), R = R_0 - ztg\varphi$$

the coefficient δ in (17) can be determined as

$$\delta = \frac{\beta_{z0}}{2\pi I_0}\frac{\lambda}{L}\left\{(1+h\beta_{z0})\delta B + \beta_{z0}\frac{tg\varphi}{2\pi}\frac{v^2\lambda L}{k_{z0}R_0^3}\right\} \qquad (18)$$

In (18), the second term has been derived under the assumption that the device operates far enough from the cutoff so that $(k_{z0}L)^2 \gg 2v^2 tg\varphi(L/R_0)^3$ and $h \simeq k_{z0}c/\omega$. As follows from (18), a small linear tapering of both the magnetic field and the resonator wall radius may lead to the same effect.

Refs

[1] G. S. Nusinovich, O. Drumbajs, "*Theory of Gyro-Backward Wave Oscillators with Tapered Magnetic Field and Waveguide Cross Section*", IEEE Trasn. Plas. Sci, **24**, 3, June 1996.

[2] G. S. Nusinovich and H. Li, "*Theory of gyro-travelling-wave tubes at cyclotron harmonics*," Int. J. Electron., vol. 72, pp. 895-907, 1992.

[3] V. L. Bratman, N. S. Ginzburg, G. S. Nusinovich, M. I. Petelin, and P. S. Strelkov, "*Relativistic gyrotrons and cyclotron autoresonance masers*," Int. J. Electron., vol. 51, pp. 541-567, 1981.

[4] G. S. Nusinovich and H. Li, "*Theory of gyro-travelling-wave tubes at cyclotron harmonics*," Int. J. Electron., vol. 72, pp. 895-907, 1992.

[5] G. S. Nusinovich, P. M. Malouf, and V. L. Granatstein, "*Theory of gyrotwystrons with mixed transverse geometry of various stages*," IEEE Trans. Plasma Sci., vol. 22, pp. 518-525, 1994.

[6] N. S. Ginzburg, I. G. Zamitsyna, and G. S. Nusinovich, "*Theory of relativistic cyclotron autoresonance maser with an opposite wave*," Radio Eng. Electron. Phys., vol. 24, no. 6, pp. 113-118, 1979.

[7] V. L. Bratman, N. S. Ginzburg, G. S. Nusinovich, M. I. Petelin, and P. S. Strelkov, "*Relativistic gyrotrons and cyclotron autoresonance masers*," Int. J. Electron., vol. 51, pp. 541-567, 1981.

[8] A. Flifet, "*Linear and nonlinear theory of the Doppler-shifted cyclotron resonance maser based on TE and TM waveguide modes*," Int. J. Electron., vol. 61, p. 1049, 1986. V. N. Glushenko, S. V. Koshevaya,

[9] V. K. Yulpatov, "*Nonlinear theory of interaction between curvilinear periodic electron beam and electromagnetic field*," Voprosy Radioelektvoniki, Ser 1. Elecktronika, no. 12. pp. 15-23, 1965 (in Russian).

[10] G. S . Nusinovich, "*Cyclotron resonance masers with inhomogeneous external magnetic fields*," Phys. Fluids B, vol. 4, pp. 1989-1997, 1992.

Appendix F: Published APL & NIMB Papers

Surface field excitation by an obliquely incident wave

I. V. Konoplev, , A. R. Phipps, , A. D. R. Phelps, , C. W. Robertson, , K. Ronald, and , and A. W. Cross

Citation: Appl. Phys. Lett. **102**, 141106 (2013); doi: 10.1063/1.4801759
View online: http://dx.doi.org/10.1063/1.4801759
View Table of Contents: http://aip.scitation.org/toc/apl/102/14
Published by the American Institute of Physics

Surface field excitation by an obliquely incident wave

I. V. Konoplev,[1] A. R. Phipps,[2] A. D. R. Phelps,[2] C. W. Robertson,[2] K. Ronald,[2] and A. W. Cross[2]
[1]*JAI, Department of Physics, University of Oxford, Oxford OX1 3RH, United Kingdom*
[2]*SUPA, Department of Physics, University of Strathclyde, Glasgow G4 0NG, United Kingdom*

(Received 28 February 2013; accepted 25 March 2013; published online 10 April 2013)

Observation of surface field excitation by an obliquely incident wave inside a cylindrical two-dimensional periodic surface lattice is a step forward toward THz Cherenkov amplifiers. Here we observe and discuss this phenomenon, investigating it using different approaches. The results are compared, and it is shown that an increase in the lattice contrast results in excitation of surface fields by an obliquely incident wave resulting in the eigenmode formation. Measurements were conducted by studying forward transmission of the signal, and it is shown that the measured gaps in the spectra are associated with the eigenmode formation rather than band gap establishment. © *2013 AIP Publishing LLC*. [http://dx.doi.org/10.1063/1.4801759]

Development of high-power amplifiers of coherent radiation capable of producing multi-watt output power in the sub-millimeter wavelength range is one of the challenging problems. Such devices are required for weather radar applications, for tracking nano-satellites and space debris, as well as for plasma diagnostics, volcano monitoring, and quality control of pharmaceutical products, and for the study of historical artefacts.[1–3] In recent work,[4–6] it has been suggested that periodic patterns machined on the inner surface of a cylindrical conductor exhibit properties of a thin dielectric layer allowing such phenomena as Cherenkov instabilities to be observed. In particular this is an attractive possibility for creating high-intensity sources of THz radiation driven by mildly relativistic electron beams, as such structures should allow very effective heat, stress, and electric charge management via their quick dissipation into the main body "sink" of the material. Conventionally the surface periodic structures previously considered[4–8] were low contrast (the corrugation amplitude is less than a quarter of the operating wavelength) and were used as distributed mirrors and high-Q cavities or low contrast interaction regions to mediate a Cherenkov instability.[7,8] Until now it has only been demonstrated that coupling between a wave at normal incidence and a surface field has been possible,[4] thus effectively denying the possibility of applying such structures to design an amplifier. In this paper we can now demonstrate that coupling between a "near grazing," obliquely incident wave and a surface field is possible if a high-contrast structure[6] (corrugation amplitude is larger than a quarter of the operating wavelength) is used. We are studying both low and high contrast Periodic Surface Lattice (PSLs), with the ultimate goal of designing a lattice exhibiting the properties that can enable it to support broadband amplification in the THz frequency range, demonstrating the possibility of tailoring artificial structures for a specific need. Indeed we are planning to exploit the main advantages of such an artificial structure to design an Amplifier of Coherent Radiation (ACR). One can define the structure built from a good conducting metal (like copper) showing dielectric properties on its surface as a "topological conductor" in contrast to the well-known "topological insulator." The 2D surface patterns improve mode stability while mediating coupling between the specific surface and propagating volume fields, thus bringing the possibility of maintaining the radiation coherence and observing the input signal amplification. In this paper we present the results of numerical and experimental studies of a cylindrical 2D PSL with a range of contrasts and designed as an initial "proof of principle" in the W-band (75 GHz-110 GHz) frequency range (Fig. 1(a)). We show that increase of the lattice contrast results in the appearance of coupling between the oblique (near-grazing) volume wave and the surface field resulting in excitation of an eigenmode of the PSL.

The cylindrical 2D PSL shown in Figure 1 has been created by machining sinusoidal radial variations onto an aluminium former

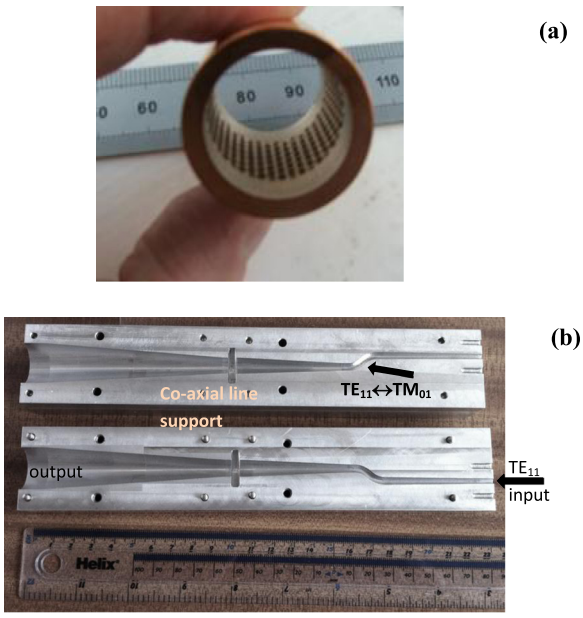

FIG. 1. (a) Photograph of the 2D PSL machined on the inner surface of a copper cylinder and having mean radius $r_0 = 1$ cm; amplitude of corrugations $\Delta r = 0.5$ mm; number of azimuthal periods 20; and longitudinal period 3 mm. (b) Photograph of the experimental setup designed to measure 2D PSLs as shown above.

$$r = r_0 + \Delta r \cos(\bar{k}_z z)\cos(\bar{m}\varphi). \quad (1)$$

Here $r_0 = 10$ mm is the unperturbed radius of the cylindrical waveguide, Δr is the corrugation amplitude, $\bar{k}_z = 2\pi/d_z$, $d_z = 3$ mm is the period of the perturbations in the z–direction, and $\bar{m} = 20$ is the number of azimuthal variations. Four individual aluminum formers of varying perturbation amplitude [$\Delta r = 0.25$ mm; 0.3 mm; 0.5 mm; 0.8 mm] were constructed, in order to investigate the effect of the amplitude of the perturbations on the coupling of the surface and volume fields. Copper was electroformed onto the surface of the formers, and once machined to the required radius the aluminum was removed by dissolving it in a strong alkaline solution. This leaves the copper structure with the perturbations on the inside wall. The structure with the highest amplitude of perturbations 0.8 mm is a high contrast case, as its peak-to-peak corrugation of 1.6 mm (from top to bottom of the grating) is larger than a quarter of the operating wavelength. In Figure 1(a) the photograph of the structure with $\Delta r = 0.5$ mm is shown. All lattices were machined to have 7 full longitudinal periods (d_z) each with a 5 mm section of smooth cylindrical waveguide at the ends to ensure good connection between the lattice and the experimental set up. Let us note that the parameters of the lattices studied are close to ones which are planned to be used to observe ACR based on a Cherenkov interaction. The large diameter of the structure will allow high current (low current density) electron beam transportation while avoiding RF breakdown, structure overheating, beam disruption, and parasitic mode generation. To study such a structure using a wave-beam consisting of a single mode, an apparatus made from a single block of aluminium was designed and constructed (Figure 1(b)). The apparatus is different, from the conventional set-ups such as Kretschmann-Raether and Otto configurations.[9] It was developed to excite surface fields (surface plasmons in optics) on the inner surface of the cylindrical periodic structure. This configuration allows irradiation of the cylindrical lattice at a range of angles between the wave vector and the axis of the cylinder from approximately 90° (a nearly cut-off wave) to approximately 0° (a propagating wave having transverse wavenumber much smaller than the longitudinal wavenumber, i.e., a "near-grazing" wave). It was also designed to be manufactured from a single block of aluminum (Fig. 1(b)) to reduce the number of connections, thus enabling us to avoid internal scattering and mode transformation via minimising the number of connections before the input of the PSL. The full length of the set-up after machining was 223.9 mm long with an input port of 2.6 mm diameter and a launching port of 20 mm diameter.

Numerical modelling of the electromagnetic field evolution and eigenmode excitation has been also conducted using the 3D code MAGIC to improve understanding of the experimental measurements. The 3D modelling of such structures is a challenge due to the large variation of the geometrical parameters (dimensions) and the oversized nature of the lattice structure. To optimise the use of the computer memory and the computer performance a square wave approximation was applied in the case of the low contrast model,[4] while a sinusoidal corrugation has been used to simulate the high contrast lattices. To compare the profiles of the lattices in Figures 2(a) and 2(b) the *r-z* cross-sections of the high and low contrast structures (left and right columns respectively) are shown. The insets in these figures show the typical contour plots of the azimuthal magnetic component B_φ of the eigenfield. The contour plots shown in Figures 2(a) and 2(b) were observed by launching an amplitude-modulated RF pulse in the TM_{01} mode, having a flat frequency spectrum in the frequency range from 80 GHz to 110 GHz. The lattice response spectra were studied using wave beams formed by TEM and TM_{01} modes and measuring the decaying field spectra after the electromagnetic pulse fully propagated through the structure. Later in this paper we compare the spectra of eigenmodes excited inside high/low contrast structures (left/right rows) using TEM (solid line) and TM_{01} (dotted line) modes with the measured spectra. As will be discussed below by changing the radial index of the waveguide modes which form the input pulse the radiation angle with respect to the lattice can be effectively controlled. We note that the field structure observed inside the high contrast structure is very similar to that observed inside the low contrast lattice leading us to conclude that the theory developed in Refs. 4–6 for low contrast structures can be extrapolated (to some extent) to a high contrast structures.

To measure the properties of the lattice the electromagnetic wave-beam was formed using the set up shown in Fig. 1(b) which is capable of converting the fundamental $TE_{1,1}$ mode of a cylindrical waveguide into either the $TM_{0,1}$ mode of a cylindrical waveguide or the TEM mode of a coaxial waveguide. The wave-beam was then launched via either a co-axial line termination plane launcher (such that the lattice

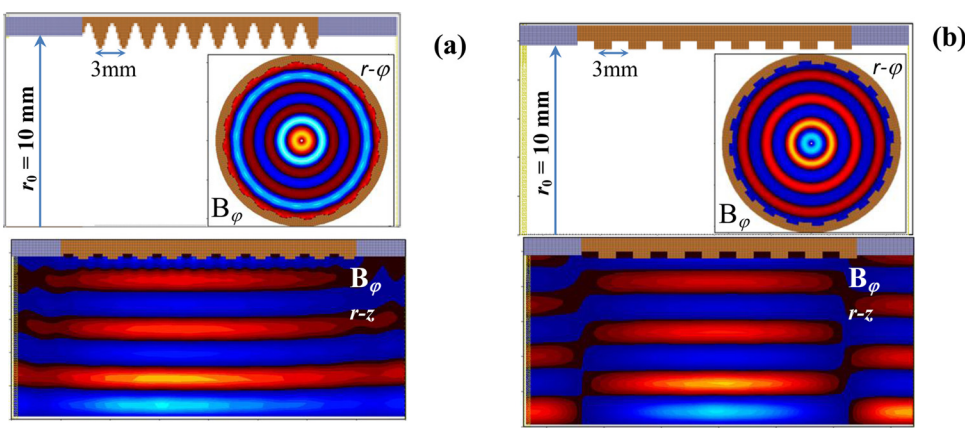

FIG. 2. Numerical models of the (a) high and (b) low contrast 2D PSLs showing *r-z* cross-sections of the structures and contour plots of the eigenmodes' azimuthal magnetic field component excited, in *r-φ* (inset to the first figure), and *r-z* (second figure) cross-sections.

is irradiated at all possible angles simultaneously) or via a directly irradiating structure with the $TM_{0,1}$ wave-beam (oblique irradiation of the lattice at a small grazing angle). The termination of the coaxial line mediates the excitation of the azimuthally symmetric TM_{on} modes with a finite set of transverse wavenumbers (defined by the radial index n). At the maximum value of n ($n = N$), the near cut-off wave is observed (wave vector at almost 90° to the axis of the cylinder), and the structure is similar to that shown in Figures 2(a) and 2(b). The measurements of the PSLs were conducted in the far field zone (27 cm from the output aperture), and millimeter-wave absorbent material was used to reduce parasitic reflections. A millimeter-wave Anritsu Vector Network Analyser (ME7808B) was used for the measurements. In the first set of experiments the structures were excited using a co-axial line termination plane launcher. The results of the measurements are shown in Figures 3(a) and 3(b). As expected the PSL eigenmode excitation was observed in both cases, i.e., for both the high and the low contrast PSLs. In Figure 3(a) the comparison of the results is shown for the low contrast lattices (corrugation amplitudes of 0.25 mm, 0.3 mm, and 0.5 mm) excited by the co-axial launcher. It is clear that the responses observed are similar, and the dependence on the amplitude of the corrugation is as expected, i.e., with increase of the amplitude of the corrugation the amplitude and the width of the minima measured grow but the centers are located at the same frequency, indicating the coupling of the same modes. In this, low contrast structure, case the eigenmode having 8 radial variations (formed with the partial TM_{08} mode) and having minima around 100 GHz was excited. However, when the PSL with 0.8 mm corrugation amplitude was measured a different behavior was observed (Fig. 3(b)). The minimum of the transmission became very broad while its amplitude stayed the same or became smaller. Also, it looks like few modes are coupled, and the minima are merged together resulting in a "red-shift" of the center of the gap. Let us note that far from the resonance frequencies the measurements coincide well at high and low frequencies. However when the co-axial launcher was substituted with the direct launcher the excitation of only the high-contrast structure was observed. In Figure 4 the results of the measurements of the structures with 0.5 mm and 0.8 mm corrugation amplitude are shown. To observe the data the PSLs were excited using a TM_{01} wave-beam (Fig. 2). It is interesting to note that no excitation of the low contrast structure was observed in spite of the indications from the numerical predictions. This can be explained by low coupling (which is proportional to the amplitude of the corrugation) between the lattice and the fields and relatively high losses.[10] Comparing with the previous data (low contrast case) we see that the position of the minima observed for the high contrast lattice is associated with the eigenmode having 7 radial variations (formed with the partial TM_{07} mode) and having downshifted minima around 87 GHz. We also note that the propagating mode is now coupled to the PSL eigenmode. In Figure 5 a comparison of the spectra observed from numerical modelling and experimental measurements are shown. The minima in the measured spectra correspond to excitation of structure eigenmodes which are composed of surface fields and near cut-off fields, i.e., the radiation losses are minimal and electromagnetic (EM) energy remains and dissipates inside the lattice. To study numerically the eigenfield excitation inside the PSL based structure the near cut-off partial field associated with eigenfield was monitored. The set of maxima of the spectra observed in the numerical models is associated with excitation of the near cut-off fields which have different radial indices and thus associated with different eigenmodes of the structure. The good agreement can be clearly seen from the figures, while small deviations can be attributed to the tolerances in the lattice manufacturing as a variation of the lattice mean radius $\Delta r_0 \sim 0.1$ mm will result in the measured frequency shift.

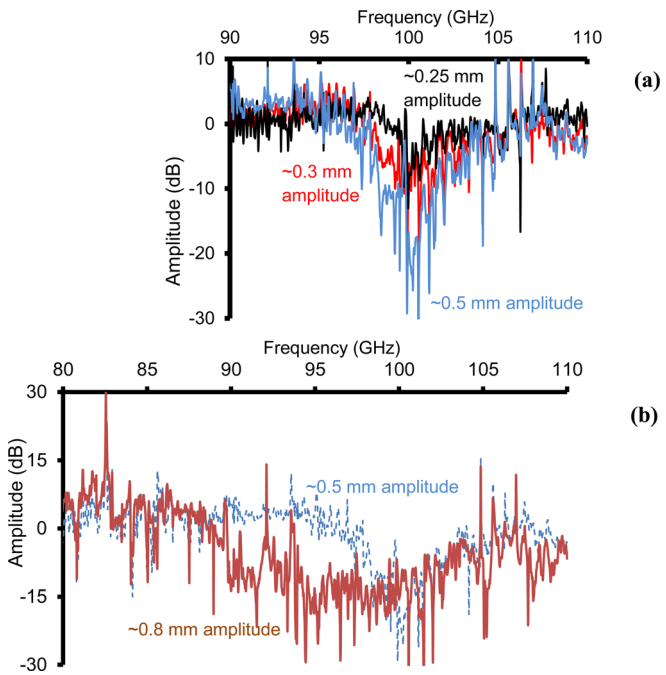

FIG. 3. Results of measurements of the electromagnetic signal transmission versus frequency (2D PSL spectral response) through (a) low (amplitude of corrugations 0.25 mm, 0.3 mm, and 0.5 mm) and (b) high (amplitude of corrugation 0.8 mm) contrast structures, if the structure is radiated using co-axial launcher based on terminated co-axial line. Scattering of near cut-off (normal incidence to the surface) wave on the lattice takes place. In (b) the spectral responses of the high (solid line) and the low (broken line) contrast structures are also compared.

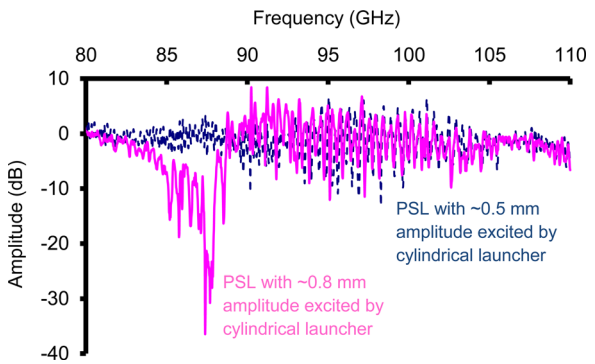

FIG. 4. Results of measurements of the electromagnetic signal transmissions versus frequency (2D PSL spectral response) through low (broken line) and high (solid line) contrast 2D PSL. The structures are irradiated by an oblique (near-grazing) incident wave-beam formed by the TM_{01} mode of the cylindrical waveguide.

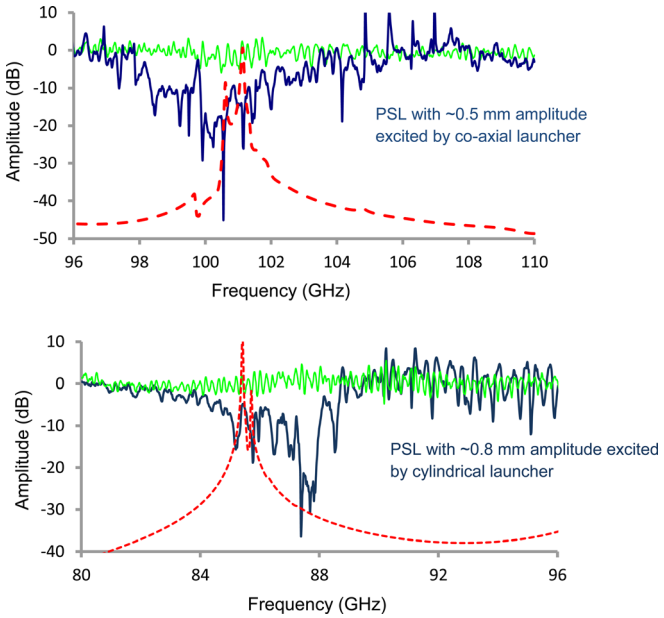

FIG. 5. Comparison of the experimental data (solid bold line) showing spectral gaps in the signal transmissions and theoretical predictions (dashed line) of 2D PSLs' eigenmodes excitation for (a) low and (b) high contrast 2D PSLs. In both figures the thin lines show the measured lattice responses if the amplitude of the corrugations is zero.

In this paper we presented numerical and experimental studies of low and high contrast two-dimensional surface periodic structures of cylindrical topology. We have shown that coupling between an oblique, near-grazing TM wave and a PSL is possible if the amplitude of the corrugation is large (high contrast structure). The coupling was not observed for low contrast structures in spite of the fact that the numerical modelling indicates the possibility of such a coupling. One of the possible explanations is that coupling is weak compared with the losses (diffraction and ohmic) inside the structure.[10] Also, such losses are more difficult to take into account in numerical studies, whereas they are always present in real experiments. We note that we demonstrated the coupling between a propagating mode and the eigenmode of the PSL via the scattering of near cut-off and surface partial fields leading to the possibility of radiation synchronisation from an oversized beam in devices such as slow-wave Cherenkov amplifiers, thus allowing such devices capable of amplifying a THz input signal to be designed and investigated. We also have studied the dependence of the PSL spectral response on the amplitude of the corrugations, and the results have been presented and discussed. Using the 3D code MAGIC we have illustrated that if no losses are considered the eigenmode structures inside the lattices, as well as the spectral response of the structures of different contrast to excitation with an electromagnetic pulse having a flat spectrum in the frequency range 80 GHz–110 GHz, are similar. The results of the experimental measurements have been presented and compared with the results from the numerical simulations, and a good agreement between the numerical models and the experimental measurements has been shown. We note that the structures studied were designed to develop THz amplifiers as the lack of such amplifiers significantly restricts the development of a number of applications in the medical and biological sciences and in the pharmaceutical and security industries.

[1]J. F. Federici, B. Schulkin, F. Huang, D. Gary, R. Barat, F. Oliveira, and D. Zimdars, Semicond. Sci. Technol. **20**, S266 (2005).
[2]E. Abraham, A. Younus, A. El Fatimy, J. C. Delagnes, E. Nguéma, and P. Mounaix, Opt. Commun. **282**, 3104 (2009); J. B. Jackson, J. Bowen, G. Walker, J. Labaune, G. Mourou, M. Menu, and K. Fukunaga, IEEE Trans. Terahertz Sci. **1**, 220 (2011).
[3]G. L. Carr, Nature (London) **420**, 153 (2002).
[4]I. V. Konoplev, L. Fisher, A. W. Cross, A. D. R. Phelps, K. Ronald, and C. W. Robertson, Appl. Phys. Lett. **97**, 261102 (2010); A. W. Cross, I. V. Konoplev, K. Ronald, A. D. R. Phelps, W. He, C. G. Whyte, N. S. Ginzburg, N. Yu. Peskov, and A. S. Sergeev, *ibid.* **80**, 1517 (2002); A. W. Cross, I. V. Konoplev, A. D. R. Phelps, and K. Ronald, J. Appl. Phys. **93**, 2208 (2003).
[5]J. B. Pendry, L. Martín-Moreno, and F. J. Garcia-Vidal, Science **305**, 847 (2004); I. V. Konoplev, L. Fisher, A. W. Cross, A. D. R. Phelps, K. Ronald, and C. W. Robertson, Appl. Phys. Lett. **96**, 261101 (2010); A. Pors, E. Moreno, L. Martin-Moreno, J. B. Pendry, F. J. Garcia-Vidal *et al.*, Phys. Rev. Lett. **108**, 223905 (2012).
[6]I. V. Konoplev, A. J. MacLachlan, C. W. Robertson, A. W. Cross, and A. D. R. Phelps, Phys. Rev. A **84**(1), 013826 (2011); Appl. Phys. Lett. **101**, 121111 (2012).
[7]T. S. Chu, F. V. Hartemann, B. G. Danly, and R. J. Temkin, Phys. Rev. Lett. **72**, 2391 (1994); N. S. Ginzburg, A. A. Kaminsky, A. K. Kaminsky, N. Yu. Peskov, S. N. Sedykh, A. P. Sergeev, and A. S. Sergeev, *ibid.* **84**, 3574 (2000); I. V. Konoplev, P. McGrane, W. He, A. W. Cross, A. D. R. Phelps, C. G. Whyte, K. Ronald, and C. W. Robertson, *ibid.* **96**, 035002 (2006).
[8]T. Tajima and M. Cavenago, Phys. Rev. Lett. **59**, 1440 (1987); K. Okamoto, T. Noma, A. Komoto, W. Kubo, M. Takahashi, A. Iida, and H. Miyata, *ibid.* **109**, 233907 (2012); A. Schilke, C. Zimmermann, P. W. Courteille, and W. Guerin, *ibid.* **106**, 223903 (2011); I. V. Konoplev, L. Fisher, K. Ronald, A. W. Cross, A. D. R. Phelps, C. W. Robertson, and M. Thumm, Appl. Phys. Lett. **96**, 231111 (2010).
[9]A. V. Zayats, I. I. Smolyaninov, and A. A. Maradudin, Phys. Rep. **408**, 131 (2005).
[10]I. V. Konoplev, A. W. Cross, A. D. R. Phelps, and K. Ronald, Phys. Rev. E **68**, 066613 (2003).

Nuclear Instruments and Methods in Physics Research B 402 (2017) 202–205

Contents lists available at ScienceDirect

Nuclear Instruments and Methods in Physics Research B

journal homepage: www.elsevier.com/locate/nimb

Electron beam excitation of coherent sub-terahertz radiation in periodic structures manufactured by 3D printing

A.R. Phipps [a], A.J. MacLachlan [a], C.W. Robertson [a], L. Zhang [a], I.V. Konoplev [b], A.W. Cross [a], A.D.R. Phelps [a,*]

[a] Department of Physics, SUPA, University of Strathclyde, Glasgow G4 0NG, UK
[b] John Adams Institute, Department of Physics, University of Oxford, Oxford OX1 3RH, UK

ARTICLE INFO

Article history:
Received 28 November 2016
Received in revised form 14 March 2017
Accepted 15 March 2017
Available online 5 April 2017

Keywords:
Periodic structures
Electron beam
Sub-terahertz radiation
3D printing

ABSTRACT

For the creation of novel coherent sub-THz sources excited by electron beams there is a requirement to manufacture intricate periodic structures to produce and radiate electromagnetic fields. The specification and the measured performance is reported of a periodic structure constructed by additive manufacturing and used successfully in an electron beam driven sub-THz radiation source. Additive manufacturing, or "3D printing", is promising to be quick and cost-effective for prototyping these periodic structures.

1. Introduction

Additive manufacturing [1], or "3D printing", is a quick and cost-effective method for prototyping periodic structures. In the present work the technical performance of a periodic structure manufactured by 3D printing is reported. The structure reported here has been used in an electron beam driven radiation source that has produced mm-wave output in the 80–90 GHz region. French and Shiffler [2] have reported successfully creating a powerful microwave source in the 4–5 GHz range using 3D printing. Such structures are of great interest because the application of smart electromagnetic designs is having a positive impact on research leading to improved high-power coherent microwave, mm-wave and sub-THz electron-beam-driven sources including both fast wave and slow wave interactions [3–12]. Macor et al. [13] have demonstrated the capability of constructing a variety of passive components for millimetre to terahertz electromagnetic waves, using metal-coated polymers shaped by 3D stereolithography, which uses essentially the same methodology as additive manufacturing, or 3D printing.

One of the motivations for our present research is to explore the range of source frequencies for which 3D printing manufacturing methods for active components can be usefully applied. The dimensional precision that 3D printing can achieve is tending to improve, which should lead to the widening of the frequency range for which this constructional method of producing complex microwave/mm-wave source structures can be applied.

2. Two dimensional (2D) periodic surface lattice (PSL)

The 2D PSLs [14] can be created by manufacturing shallow periodic perturbations on the inner surface of a hollow electrically conducting cylinder. The cylindrical PSL structures need to be compatible with vacuum conditions and the use of energetic electron beams, while also providing the required boundary conditions for the electromagnetic fields. Manufacturing the cylindrical PSLs out of a suitable metal usually provides a good vacuum envelope and the good electrical conductivity allows conduction away of any electrical charges impacting on the surfaces. A good thermal conductivity coefficient is another property that metals tend to possess and is helpful for PSLs intended for use in high power sources.

The interactions between charged particle beams and periodic structures, that can be one, two, or three dimensional provide a very fruitful research area [15,16]. Structures used to excite Smith-Purcell radiation share many of the same modeling [16], constructional and measurement challenges as the present work. Periodic structures that produce electromagnetic radiation can be used for several applications that exploit a variety of physical phenomena [17]. A dispersion relation describing the coupling of the volume and surface fields inside a 2D PSL of cylindrical topology was derived by Konoplev et al. [18]. Under certain conditions, when driven by a suitable electron beam this structure can support

* Corresponding author.
E-mail address: a.d.r.phelps@strath.ac.uk (A.D.R. Phelps).

http://dx.doi.org/10.1016/j.nimb.2017.03.093
0168-583X/

a Cherenkov instability that provides a coherent source of electromagnetic radiation [19].

The cylindrical 2D periodic structure can be described by Eq. (1)

$$r = r_0 + \Delta r \cos(kz + m\varphi) \quad (1)$$

where r_0 is the radius of the unperturbed waveguide, Δr is the corrugation depth, $k_z = 2\pi/d_z$, d_z is the period of the corrugation over the z – coordinate and m is the number of variations of the corrugation over the azimuthal coordinate.

3. 3D printing of cylindrical 2D PSL

Periodic structures in cylindrical geometry have been successfully prototyped using 3D printing to create a primary mould, which has then been used to cast successfully a metallic cylindrical PSL to form the interaction cavity for a novel sub-THz source.

The 3D printing process is a two stage process. The first stage involves creating a wax former to the 10's of microns scale and then using this former to create a mould for the component where the silver – chromium molten alloy is deposited, with the resulting part having a resolution of ±125 μm. The PSL to be used in the 'hot' experiment was constructed using a high resolution 3D printing process that included the injection moulding of a silver chromium alloy. 3D printing, originally developed in the mid 1980's, offers the possibility of producing objects that have resolutions on the 10's of microns scale. 3D printing is an additive process by which consecutive layers in the x-z plane are deposited sequentially in the positive y direction (upwards), resulting in a high resolution (approximately ± 15 μm) wax model that is then used in a casting process that ultimately results in the silver alloy (80–90) GHz 2D PSL, seen in the image below. The printing process follows the pattern in a given CAD input file, usually in the STL (Stereolithograph) file format where every face is built from a series of interconnected triangles represented by 3 separate 32-bit floating-point Cartesian coordinates. More often now the new X3D file format is implemented which incorporates the XML programming interface and further enhancements over its predecessors. The design is sliced into digital layers so that a curve is 'approximated' by many square sided slices, with the thickness of each layer representing the resolution of that particular 3D printing process.

Although this resolution is not at present as high as can be achieved with a precision milling process, it does have the advantage of taking a lot less time to achieve the finished structure and in conjunction with the lower cost, the 3D printing process is more efficient overall.

A 2D PSL structure with parameters as shown in Table 1 was manufactured for electromagnetic measurements using a VNA and for subsequent use in electron beam experiments. Images of the cylindrical 2D PSL made using 3D printing are shown in Fig. 2.

The 2D cylindrical PSL shown in Fig. 2 is made from a silver alloy of 92.5% silver and 7.5% chromium.

Table 1
The physical parameters of the 2D PSL structure.

Parameter	Symbol	Value
Longitudinal Period	dz	1.6 mm
Azimuthal Variations	m	7
Number of Longitudinal Periods	n	16
Amplitude	dr	0.8 mm
Amplitude (Peak-to-Peak)	dr (pk-pk)	1.6 mm
Inner Radius of input and output waveguide	r	4 mm
Minimum radius of perturbation (ID)	r_{min}	3.6 mm
Mean radius	r_0	4.4 mm
Maximum radius of perturbation (OD)	r_{max}	5.2 mm

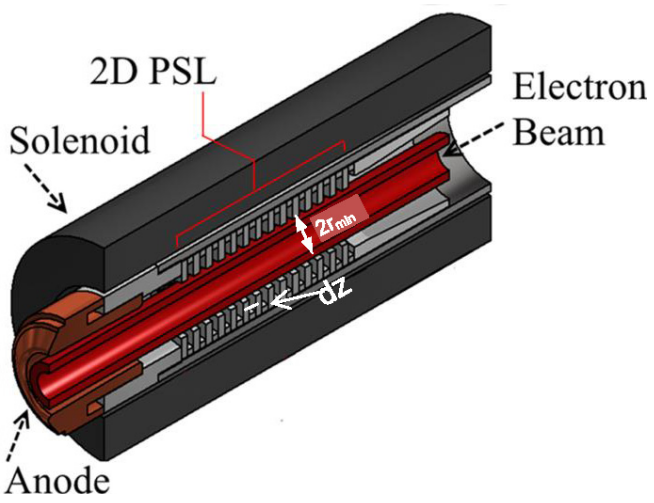

Fig. 1. Configuration of the cylindrical periodic surface lattice and annular electron beam guided by the solenoidal magnetic field.

Fig. 2. Cylindrical PSL manufactured using 3D printing.

4. Electromagnetic measurement of the cylindrical 2D PSL

Measurements, made using a vector network analyser, of the electromagnetic properties of the cylindrical PSL manufactured by these methods, are compared with simulations made using the software CST Microwave Studio.

Using a serpentine co-axial mode converter operating in G-band (140–220 GHz) a $TM_{0,n}$ wave was launched into the high contrast (1.6 mm deep corrugation) 2D PSL with the transmission measured over the 140–220 GHz frequency range using an Anritsu ME7808B Broadband Lightening Vector Network Analyzer VNA with two transmit and receive SM5952 140–220 GHz OML extender heads. The $TM_{0,1}$ mode from the circular serpentine mode converter becomes a TEM mode in the co-axial conical horn which then launches a $TM_{0,n}$ mode in the cylindrical 3D printed 2D PSL.

When testing the structure using the VNA the interaction produces an electromagnetic wave that interacts with the 1.6 mm longitudinal period giving a response in G-band resulting in a resonance at 187.7 GHz, as shown in Fig. 3 showing the millimetre wave transmission as a function of frequency. The electromagnetic wave when interacting with the 3.5 mm azimuthal period will give

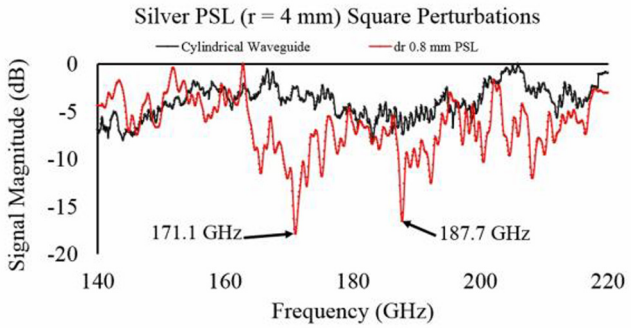

Fig. 3. The measured transmission as a function of frequency of the 2D PSL over the 140 GHz to 220 GHz frequency range.

a fundamental resonance at ~85 GHz and a resonance at the 1st harmonic in G-band. The latter is considered to give rise to the 171.1 GHz resonance in G-band shown in the VNA measurement.

5. Electron beam interaction with the cylindrical 2D PSL

For an electron beam with the parameters as shown in Table 2, having an accelerating potential of 80 kV, and $v_z = 0.46c$, interacting with the cylindrical 2D PSL structure for which dz = 1.6 mm, Eq. (2) indicates the electrons will interact with a localized surface field at a frequency of ~85 GHz

$$\omega = k_z v_z \pm \frac{2\pi}{d_z} v_z \sim 85 \text{ GHz} \quad (2)$$

This matches with the electromagnetic wave fundamental resonance in the azimuthal direction of ~85 GHz.

6. Electron beam experiments and mm-wave output measurements

The cylindrical 2D PSL was assembled with the electron gun and output waveguide and window. The cylindrical 2D PSL was located inside a water-cooled solenoidal electromagnet that was capable of providing a uniform axial magnetic field of up to 2 T over the axial extent of the 2D PSL, as shown in Fig. 1. An axial magnetic field of 1.8 T was used in the experiments reported here. A two stage vacuum pumping system was used to evacuate the integrated system to a pressure of $\sim 1 \times 10^{-6}$ mbar which was sufficient for short pulse (~100 ns) cold cathode electron beam production. The complete experimental assembly is shown in Fig. 4.

Measurements of the magnetic field profile, electron beam accelerating potential, beam current, electron beam profile and output millimetre wave radiation have been carried out. A pulsed power supply capable of providing up to 100 kV peak voltage pulses was applied to a vacuum diode and an electron beam was extracted from a cold cathode. A measurement of the accelerating potential and the electron beam current is shown in Fig. 5.

Table 2
The parameters of the electron beam.

Parameter	Symbol	Value
Accelerating potential	V	80 kV
Axial velocity	v_z	0.46c
Perpendicular velocity	v_{perp}	0.19c
Lorentz factor	γ	1.156
Maximum current	I_{max}	100A
Applied axial magnetic field	B	1.8T
Electron beam radius	R_{beam}	2.0 mm

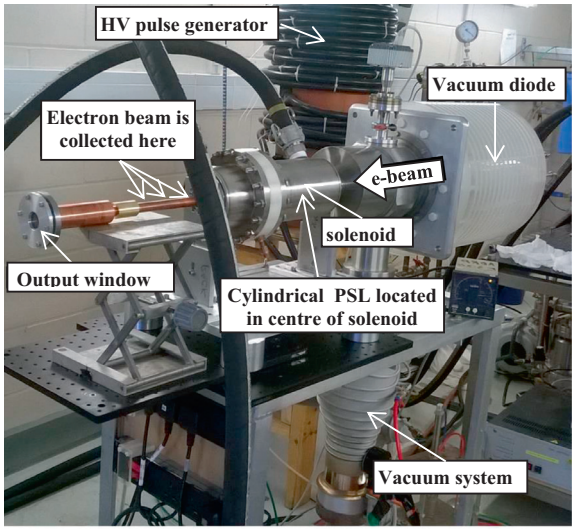

Fig. 4. Complete experimental assembly showing the vacuum diode source of the electron beam, the magnetic field solenoid surrounding the cylindrical 2D PSL and the output window.

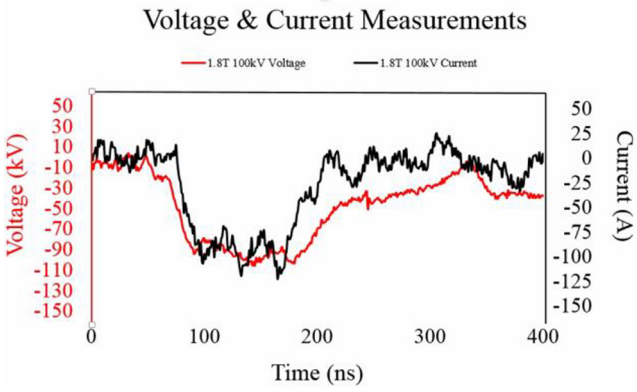

Fig. 5. The beam current and accelerating voltage seen at the cathode. A value of 80 kV produced a current of approximately 100 A.

A witness plate diagnostic was used to record the cross-sectional profile of the electron beam. The measured cross-sectional beam profile appears to be annular [20], which is ideal, although the optimum configuration would be for the beam to pass even closer to the surface of the 2D PSL The 80 kV, 100 A electron beam was measured to have a beam radius of 2.0 mm which was approximately 1.6 mm away from the inner surface of the 2D PSL corrugation. The pulse repetition frequency is very low and the experiment is effectively 'single shot'. No changes in the radiated sub-THz radiation and no changes in the properties of the PSL were observed during these experiments, indicating no significant damage of the PSL. It is planned to reduce the distance between the electron beam and the inner surface of the 2D PSL in a future series of experiments to further strengthen the electron beam 2D PSL interaction.

At the relatively low electron beam energies (<100 keV) used in these experiments the applied axial magnetic field of up to 2T is able to guide the electron trajectories. The alignment of the electron beam with the axis of the PSL depends both on good mechanical alignment and on alignment of the axis of the magnetic field. The radiation produced by the interaction of the electron beam with the PSL propagates within a conducting waveguide towards the output window. Radiation directivity effects produced by any misalignment of the electron beam and the PSL tend to be masked

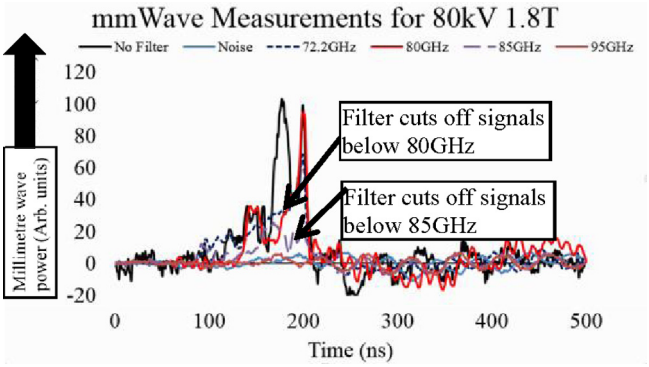

Fig. 6. Millimetre wave output and frequency diagnostic.

by the sub-THz radiation propagation through the conducting waveguide.

The millimetre wave radiation was measured using a rectifying crystal detector with the output mode pattern recorded by scanning the crystal detector across the output window and plotting the magnitude of the millimetre wave pulse as a function of angle. Initial measurements of the radiation pattern have been made. It is expected that the PSL should produce a coupling of a $TM_{0,2}$ field and a $TE_{5,1}$ field. The radiation pattern measurements are not inconsistent with this expectation but further measurements are needed before a firm identification is established."

The frequency of the millimetre wave radiation was measured using a series of high pass cut-off filters in combination with the millimetre wave crystal detector with the mode pattern measured in the far field. The use of the series of cut-off filters shows that millimetre wave output is being successfully generated as show in Fig. 6 and that this millimetre wave output lies between 80 GHz and 85 GHz. A more accurate frequency measurement in the form of a heterodyne frequency diagnostic will be used as part of our future work.

The measured peak power was estimated to be approximately 30 kW. The relatively low efficiency, of less than 1%, is considered to be a result of the electron beam not passing close enough to the PSL structure.

7. Conclusions

The magnetic field solenoid creates an applied, guiding axial magnetic field in these experiments, in the region where the electron beam is interacting with the electromagnetic fields of the PSL. This applied magnetic field then decreases by several orders of magnitude in the region just downstream of the PSL. The result of this is that the electrons follow the magnetic field lines and move out radially and are collected on the conducting wall of the vacuum vessel downstream of the PSL. The electron trajectories have also been numerically modelled and a negligible number of electrons are predicted to impact on the output window. The experimental observations are consistent with this. In practical applications to produce radiation using PSLs, bremsstrahlung production in the output window should not pose a significant risk.

The construction and operation of an electron beam driven millimetre wave source based on a cylindrical 2D PSL has been achieved and the millimetre wave output has been measured. A novel feature of this result is that the 2D PSL has been constructed using 3D printing. Sources in the microwave frequency range have only relatively rarely been constructed previously using 3D printing. As the wavelength decreases the need for higher precision increases and the results reported here have extended the applicability of 3D printing as a construction method into the millimetre wave range.

Acknowledgements

This project has received funding from the Leverhulme Trust, United Kingdom, through an International Network Grant IN-2015-012. The research effort has been supported by AFOSR, USA, through award number FA8655-13-1-2132. Alan Phipps and Amy MacLachlan thank the EPSRC, United Kingdom, for funding their PhD studentships.

References

[1] I. Gibson, D. Rosen, B. Stucker, Additive Manufacturing Technologies: 3D Printing, Rapid Prototyping, and Direct Digital Manufacturing, 2nd ed., Springer, New York, NY, USA, 2015.
[2] D.M. French, D. Shiffler, High power microwave source with a three dimensional printed metamaterial slow-wave structure, Rev. Sci. Instrum. 87 (2016) 053308.
[3] N.S. Ginzburg, N.Y. Peskov, A.S. Sergeev, et al., Theory of free-electron maser with two-dimensional distributed feedback driven by an annular electron beam, J. Appl. Phys. 92 (2002) 1619–1629.
[4] N.S. Ginzburg, N.Y. Peskov, A.S. Sergeev, et al., The use of a hybrid resonator consisting of one-dimensional and two-dimensional Bragg reflectors for generation of spatially coherent radiation in a coaxial free-electron laser, Phys. Plasmas 9 (2002) 2798–2802.
[5] I.V. Konoplev, P. McGrane, A.W. Cross, et al., Wave interference and band gap control in multiconductor one-dimensional Bragg structures, J. Appl. Phys. 97 (2005) 073101.
[6] I.V. Konoplev, A.W. Cross, A.D.R. Phelps, et al., Experimental and theoretical studies of a coaxial free-electron maser based on two-dimensional distributed feedback, Phys. Rev. E 76 (2007) 056406.
[7] I.V. Konoplev, L. Fisher, A.W. Cross, et al., Excitation of surface field cavity and coherence of electromagnetic field scattering on two-dimensional cylindrical lattice, Appl. Phys. Lett. 97 (2010) 261102.
[8] I.V. Konoplev, L. Fisher, K. Ronald, et al., Surface-field cavity based on a two-dimensional cylindrical lattice, Appl. Phys. Lett. 96 (2010) 231111.
[9] I.V. Konoplev, A.R. Phipps, A.D.R. Phelps, et al., Surface field excitation by an obliquely incident wave, Appl. Phys. Lett. 102 (2013) 141106.
[10] N.S. Ginzburg, A.S. Sergeev, N.Y. Peskov, et al., Mode competition and control in free electron lasers with one- and two-dimensional Bragg resonators, IEEE Trans. Plasma Sci. 24 (1996) 770–780.
[11] A.W. Cross, W. He, I.V. Konoplev, et al., Experimental and theoretical study of 2D Bragg structures for a coaxial free electron maser, Nucl. Instrum. Methods Phys. Res. Sect. A-Accel. Spectrom. Dect. Assoc. Equip. 475 (2001) 164–172.
[12] A.W. Cross, I.V. Konoplev, K. Ronald, et al., Experimental studies of two-dimensional coaxial Bragg structures for a high-power free-electron maser, Appl. Phys. Lett. 80 (2002) 1517–1519.
[13] A. Macor, E. de Rijk, S. Alberti, et al., Note: Three-dimensional stereolithography for millimeter wave and terahertz applications, Rev. Sci. Instrum. 83 (2012) 046103.
[14] I.V. Konoplev, L. Fisher, A.W. Cross, et al., Surface wave Cherenkov maser based on a periodic lattice, Appl. Phys. Lett. 96 (2010) 261101.
[15] M. Shevelev, A. Konkov, A. Aryshev, Soft-x-ray Cherenkov radiation generated by a charged particle moving near a finite-size screen, Phys. Rev. A 92 (2015) 14.
[16] K. Lekomtsev, P. Karataev, A.A. Tishchenko, et al., CST simulations of THz Smith-Purcell radiation from a lamellar grating with vacuum gaps, Nucl. Instrum. Methods Phys. Res. Sect. B-Beam Interact. Mater. Atoms 355 (2015) 164–169.
[17] A.W. Cross, I.V. Konoplev, A.D.R. Phelps, et al., Studies of surface two-dimensional photonic band-gap structures, J. Appl. Phys. 93 (2003) 2208–2218.
[18] I.V. Konoplev, A.J. MacLachlan, C.W. Robertson, et al., Cylindrical, periodic surface lattice-theory, dispersion analysis, and experiment, Appl. Phys. Lett. 101 (2012) 121111.
[19] I.V. Konoplev, A.J. MacLachlan, C.W. Robertson, et al., Cylindrical periodic surface lattice as a metadielectric: concept of a surface-field Cherenkov source of coherent radiation, Phys. Rev. A 84 (2011) 013826.
[20] I.V. Konoplev, A.W. Cross, P. MacInnes, et al., High-current oversized annular electron beam formation for high-power microwave research, Appl. Phys. Lett. 89 (2006) 171503.